AD-A170 486 FRACTURE ANALYSIS OF MATRIX CRACKING IN LAMINATED COMPOSITES(U) NATIONAL RESEARCH COUNCIL WASHINGTON DC A S WANG JAN 85 NADC-85118-60 N62269-82-C-0704 1/2

UNCLASSIFIED F/G 11/4 NL

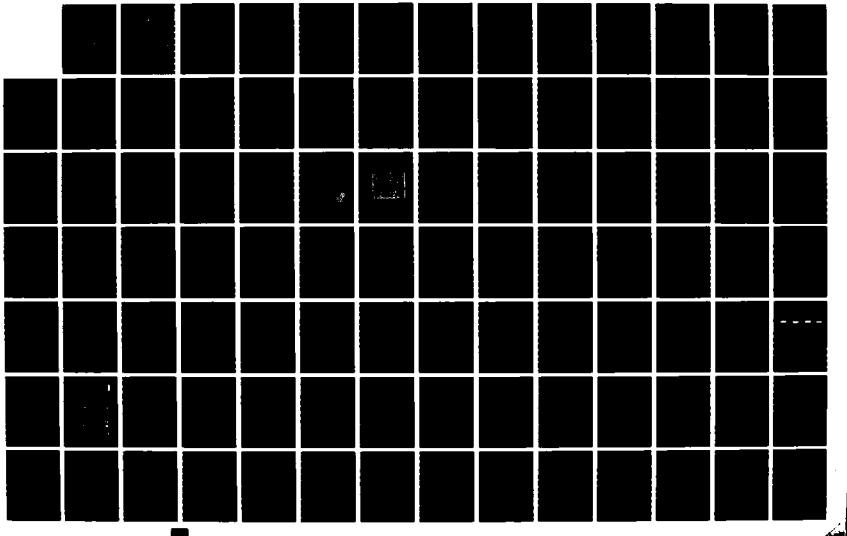

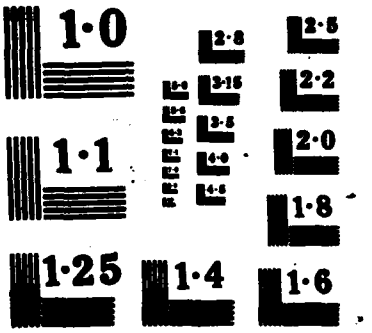
1·0
1·1
1·25
1·4
1·6
1·8
2·0
2·2
2·5

(12)

REPORT NO. NADC-85118-60

AD-A170 486

FRACTURE ANALYSIS OF MATRIX CRACKING IN LAMINATED COMPOSITES

A. S. D. Wang
Senior Research Associate
National Research Council
2101 Constitution Avenue
Washington, DC 20371

JANUARY 1985

FINAL REPORT
Contract No. N62269-82-C-0704

Approved for Public Release; Distribution Unlimited

Prepared for
Aircraft and Crew Systems Technology Directorate
NAVAL AIR DEVELOPMENT CENTER
Warminster, PA 18974

NOTICES

REPORT NUMBERING SYSTEM – The numbering of technical project reports issued by the Naval Air Development Center is arranged for specific identification purposes. Each number consists of the Center acronym, the calendar year in which the number was assigned, the sequence number of the report within the specific calendar year, and the official 2-digit correspondence code of the Command Office or the Functional Directorate responsible for the report. For example: Report No. NADC-78015-20 indicates the fifteenth Center report for the year 1978, and prepared by the Systems Directorate. The numerical codes are as follows:

CODE	OFFICE OR DIRECTORATE
00	Commander, Naval Air Development Center
01	Technical Director, Naval Air Development Center
02	Comptroller
10	Directorate Command Projects
20	Systems Directorate
30	Sensors & Avionics Technology Directorate
40	Communication & Navigation Technology Directorate
50	Software Computer Directorate
60	Aircraft & Crew Systems Technology Directorate
70	Planning Assessment Resources
80	Engineering Support Group

PRODUCT ENDORSEMENT – The discussion or instructions concerning commercial products herein do not constitute an endorsement by the Government nor do they convey or imply the license or right to use such products.

A170486

UNCLASSIFIED
SECURITY CLASSIFICATION OF THIS PAGE

REPORT DOCUMENTATION PAGE

1a REPORT SECURITY CLASSIFICATION UNCLASSIFIED	1b RESTRICTIVE MARKINGS
2a SECURITY CLASSIFICATION AUTHORITY	3 DISTRIBUTION AVAILABILITY OF REPORT Approved for Public Release; Distribution Unlimited
2b DECLASSIFICATION DOWNGRADING SCHEDULE	
4 PERFORMING ORGANIZATION REPORT NUMBER(S)	5 MONITORING ORGANIZATION REPORT NUMBER(S) NADC-85118-60
6a NAME OF PERFORMING ORGANIZATION National Research Council 6b OFFICE SYMBOL (If applicable)	7a NAME OF MONITORING ORGANIZATION Naval Air Development Center
6c ADDRESS (City, State, and ZIP Code) 2101 Constitution Avenue Washington, DC 20371	7b ADDRESS (City, State, and ZIP Code) Warminster, PA 18974
8a NAME OF FUNDING SPONSORING ORGANIZATION Naval Air Development Center 8b OFFICE SYMBOL (If applicable) 6043	9 PROCUREMENT INSTRUMENT IDENTIFICATION NUMBER N62269-82-C-0704
8c ADDRESS (City, State, and ZIP Code) Warminster, PA 18974	10 SOURCE OF FUNDING NUMBERS PROGRAM ELEMENT NO: 61153N PROJECT NO: WR 02303 TASK NO WRO: 2303001 WORK UNIT ACCESSION NO: 133126

11 TITLE (Include Security Classification)

(U) FRACTURE ANALYSIS OF MATRIX CRACKING IN LAMINATED COMPOSITES

12 PERSONAL AUTHOR(S)
A. S. D. Wang

13a TYPE OF REPORT	13b TIME COVERED	14 DATE OF REPORT (Year, Month, Day)	15 PAGE COUNT
Final	FROM _____ TO _____	1985 January	161

16 SUPPLEMENTARY NOTATION
This report was prepared while the author was on sabbatical leave from Drexel University, Phila., PA, during the period 1 October 1983 to 30 September 1984.

17 COSATI CODES			18 SUBJECT TERMS (Continue on reverse if necessary and identify by block number)
FIELD	GROUP	SUB GROUP	Composite Material, Fracture, Fatigue (Materials), Delamination, Matrix-cracks, Crack-growth, Graphite/epoxy, Energy-release-rate, Finite Element Analysis.

19 ABSTRACT (Continue on reverse if necessary and identify by block number)

This report presents an analytical approach to describe the initiation and propagation behaviors of matrix-dominant cracks in laminated composites. A rational analysis method for the phenomenological characteristics of matrix cracking is developed on the basis of ply-elasticity, fracture mechanics and effective material flaw concepts. Emphasis is placed on the basic mechanisms of multiple random cracks formation, delamination growth and interactions among cracks of differing propagation modes. Examples simulating laboratory coupon tests are presented to highlight the analysis method.

20 DISTRIBUTION AVAILABILITY OF ABSTRACT	21 ABSTRACT SECURITY CLASSIFICATION	
☒ UNCLASSIFIED/UNLIMITED ☐ SAME AS RPT ☐ DTIC USERS		
22a NAME OF RESPONSIBLE INDIVIDUAL L. W. Ganse	22b TELEPHONE (Include Area Code) 215-441-1350	22c OFFICE SYMBOL NADC/6045

DD FORM 1473, 84 MAR — 83 APR edition may be used until exhausted. All other editions are obsolete.

SECURITY CLASSIFICATION OF THIS PAGE
UNCLASSIFIED

TABLE OF CONTENTS

PREFACE

Failure analysis of fiber reinforced composite materials is not a simple problem. There is a wide dimensional range in which analytical failure theories can be developed, depending on the viewing scale. Composite materials can be perceived simply as a class of homogeneous elastic media, or as a highly complex structural system. There are a variety of other models proposed in-between. It seems impossible to develop an adequate failure analysis methodology that can be applied over the entire dimensional spectrum of composites as an engineering material.

For a class of epoxy-based structural laminates, failure usually begins with microcracking in the resin or in the resin-fiber interfaces. The dimensions of the microcracks are on the order of the reinforcing fiber diameter. During the course of loading, some of the microcracks may coalesce and form what is known as sub-laminate matrix cracks, whose sizes can be orders of magnitude larger than the microcracks. Despite such large sizes, sub-laminate matrix cracks generally remain localized or propagate stably until reaching a certain late-stage loading, at which time a rapid growth of the matrix cracks occurs. This event usually renders the laminate structurally unsafe.

The purpose of this work is to investigate the formation and propagation mechanisms of some important types of sub-laminate matrix cracks. A phenomenological failure analysis methodology is developed within the dimensional bounds in which these matrix cracks are observed.

It should be mentioned that composite materials possess many unique physical characteristics not previously encountered by the analysts. Thus, it is often necessary to modify the existing analysis methods for each newly encountered situations. This practice may in turn cause the application of the analysis methods with in-sufficient scientific precision and mathematical

rigor. While this work is not an exception to this predicament, it is hoped that it will stimulate new theoretical research in the field.

The author is deeply indebted to his colleaques, former and present students; through whose collaboration much of the results presented here were obtained. He is especially grateful for the financial supports received from the U. S. Air Force Office of Scientific Research, Wright Aeronautical Laboratory and the Naval Air Development Center during the various phases of his research.

This manuscript was prepared while the author was on a sabbatical leave from Drexel University to further pursue these research objectives at the Naval Air Development Center under a program sponsored by the National Research Council from October 1, 1983 to September 30, 1984. Many thanks are due to Mr. Lee W. Gause of NADC for numerous helpful technical discussions on the subject of damages in composites.

Finally, sincere gratitude is expressed to Mrs. Shirley Cheeseman for her patience and expert typing in preparing the manuscript.

A. S. D. Wang
Philadelphia, 1985

NOMENCLATURE

a	linear size of material flaws; a random variable
a_o	linear size of effective flaws in basic 90°-ply
a_i	the ith element in the $\{a_i\}$ set
a_m	flaw size ($= 2a_m$) at maximum energy release rate G_{max}
a_{max}	maximum a_i in the $\{a_i\}$ set
a_n	linear size of effective flaws in n 90°-plies grouped together
$(a_n)_i$	the ith element in the $\{(a_n)_i\}$ set
d	distance from laminate free edge
e_j	elastic ply strain, $j = 1, 6$
e_x	laminate axial strain in the x-direction
$(e_x)_{cr}$	critical laminate strain at onset of an event
$(e_x)_{de}$	laminate strain at onset of delamination
$(e_x)_{sp}$	laminate strain at onset of 0°-ply splitting
$f_{ij}(*)$	a function of variable *
$g_j(*)$	a function of variable *
n	number of plies like fiber orientation grouped together
r	radial coordinate in (r, θ, Z)
s	spacing between two adjacent flaws in 90°-ply
t	thickness of basic material ply ($= 2t$)
u_i	displacement in x-direction of the ith node
v_i	displacement in y-direction of the ith node
w_i	displacement in z-direction of the ith node
x	position along the x-coordinate
x_i	position of the ith effective flaw
z	thickness-wise coordinate
A	area of delamination
C_{ij}	elastic ply stiffness constants
$C_e(a)$	strain energy release rate coefficient due to $\bar{e}_x = 1$
$C_T(a)$	strain energy release rate coefficient due to $\Delta T = -1°F$ or $\Delta T = -1°C$
$C_{eT}(a)$	strain energy release rate coefficient due to coupled $\bar{e}_x$ and ΔT
E_L	longitudinal ply modulus
E_T	transverse ply modulus
E_Z	thickness-wise ply modulus
E_x	laminate axial modulus
F_{ij}, F_i	ply strength parameters, $i, j = 1, 6$
F_x	nodal force in the x-direction
F_y	nodal force in the y-direction
F_z	nodal force in the z-direction
$F_n(a)$	cumulative Weibull function for flaw size a in n-grouped plies

G, $G(\ )$	strain energy release rate
G_c	critical strain energy release rate of material
$G^o(\ )$	strain energy release rate of a single crack without the influence of shear-lag
G_I, G_{II}, G_{III}	energy release rate of modes I, II and III
G_{IC}	critical energy release rate in mode-I
G_{LT}	ply shear modulus in LT plane
G_{LZ}	ply shear modulus in LZ plane
G_{TZ}	ply shear modulus in TZ plane
K_i	stress intensity factors, i = I, II and III
L	material coordinate longitudinal to the fibers
M	number of effective flaws in a unit length of 90°-ply
$P_n(\sigma)$	failure probability in strength σ in n-grouped plies
$R(\ )$	stress energy release rate retention factor
S	material surface energy
T	material coordinate transverse to the fibers
U(a)	total strain energy in an elastic body containing a crack of size a
V	volume of a unit material ply
α_o	Weibull shape parameter for flaw distribution in basic 90°-ply
α_n	Weibull shape parameter for flaw distribution in n grouped plies
α_L	longitudinal ply thermal expansion coefficient
α_T	transverse ply thermal expansion coefficients
α_Z	thickness-wise ply thermal expansion coefficient
β_o	Weibull position parameter for flaw distribution in basic 90°-ply
β_n	Weibull position parameter for flaw distribution in n grouped plies
ν	ply Poisson ratio
ν_{LT}	ply Poisson ratio in T due to axial load in L
ν_{TL}	ply Poisson ratio in L due to axial load in T
σ_i	ply elastic stress, i = 1,6
σ_L	longitudinal ply tensile strength
σ_T	transverse ply tensile strength
σ	applied far-field stress
σ_x	applied laminate stress in x-direction
$(\sigma_x)_{cr}$	critical laminate stress at onset of a cracking event
τ, τ_{xy}	ply shearing stress; shearing stress in xy plane
θ	angular coordinate in (r, θ, Z)
Δa	incremental linear crack extension
ΔT	temperature difference
ΔV	minimum representive value of a material ply
ΔW	incremental work done
Φmm	constants

CHAPTER I. MATRIX CRACKS IN COMPOSITE LAMINATES

One major class of structural composites is fabricated using unidirectional plies of resin-impregnated fibers (prepreg tape). These prepreg plies may be stacked in a certain prescribed orientation sequence to achieve the required structural properties when pressed to a laminate. Ideally, the fibers would be orientated primarily in the principal loading directions with the resin material serving only to bind the fibers and the various plies together. Experiences have shown, however, that material failure in this class of laminates seldom begins with breaking of the load-carrying fibers. Rather, small micro-cracks first occur in the resin or in the resin-fiber interfaces. Under sustained loading, these microcracks can form in increasing density and grow larger in size. At stress critical locations, coalescence of the microcracks can take place, forming what is known as matrix cracks.

Because of the laminate's internal reinforcement structure, matrix cracks are generally inhibited from monotonic propagation, but they tend to form a cracking pattern which is characteristic to the laminate in question.

Experiments on laboratory coupons (see, e.g. [1]) have established that matrix cracking patterns are generic to the ply fiber orientations and stacking sequence of the laminate. The patterns are essentially reproducible in laminate replicates subjected to similar loading conditions. It has often been suggested that the basic mechanisms of matrix cracking and the associated characteristic cracking pattern are amenable to some form of analytical description based on the principles of mechanics [2].

From the viewpoint of material strength, a crack formed in fibrous composites signifies that the limit of local material strength has been exceeded. An analysis of strength should therefore be conducted at the microscopic scale where the composite is distinctly a multi-phase material. If this view is

followed, not only should the individual mechanical properties of the fibers the matrix and the fiber-matrix interfaces be included among the important factors determining the strength behavior, but local anomalies of either geometrical or material origins, or any other such quantities whose dimensions are comparable to the fiber diameter should also be considered. One major difficulty with this viewpoint is that material anomalies are random in nature, rendering fruitless efforts to include their identity and effects in any deterministic form of analysis.

Yet, microflaws do exist in composites and they remain the primary cause of matrix cracking. Their presence, or at least their effects, must in some way be included in the analysis.

An alternative approach is to look upon the matrix cracking process as a phenomenological event. Typically, the individual material plies are regarded as homogeneous anisotropic bodies, in which the actual fiber-matrix microstructure as well as the micro-defects all become indistinguishable. Material property distinction is maintained between plies of differing fiber orientations. Thus, a transition is made from a microscopic to a macroscopic description, with the requirement that important factors in the microscopic regime be retained in the macroscopic regime. In this context, the presence and the effects of material microflaws on matrix cracking are represented by a distribution of "effective" material flaws, with the effective flaw distribution characterized as an inherent property of the material ply. In order to develop a methodology based on this approach, however, a physical understanding of the matrix cracking mechanisms at both the microscopic and the macroscopic scale is essential.

1.1 Physical Characteristics of Matrix Cracks

Because of the unique internal reinforcement structure of the considered class of laminates, there are only two basic forms of matrix cracking when viewed at the macroscale. Suppose that the stresses in each ply of the laminate are three dimensional [3]; then there are three in-ply stresses and three interply stresses, as shown in Figure 1.1. Under certain conditions, the in-ply stresses may initiate and propagate matrix cracks parallel to the fibers in that ply, known commonly as transverse cracks, Figure 1.2. On the other hand, the interply stresses may initiate and propagate matrix cracks parallel to the plane of the ply, or in the interface between two plies. The latter is labeled as delamination, Figure 1.3.

The modal behavior of laminate matrix cracking clearly depends on the relative dominance between the in-ply stresses and the interply stresses. In many instances, the state of the ply stresses changes as local cracks form. Then, a combination of the two different cracking forms can be induced.

Multiplicity is another unique character of matrix cracking. This phenomenon is again due to the laminates internal reinforcement. Because of the filamentary structure in each ply and the layering structure in the laminate, a matrix crack cannot, generally, undergo monotonic propagation. The crack is likely to be arrested or blunted at some reinforcement boundary. This crack-arresting mechanism permits the applied load to increase without causing the crack to propagate. The result is that another matrix crack is initiated elsewhere in the laminate. In this manner, a load-dependent multiple crack formation process is developed.

Thus, it is clear that the physical character of matrix cracking is influenced strongly by the laminate's internal and external geometries, including ply fiber orientations, ply thicknesses, ply stacking sequence and

laminate shape feature, etc. Consequently, any anayltical approach to this problem must include implicitly or explicitly these geometrical factors.

1.2 Statistical Homogeneity and Ply Elasticity

The mathematical transition from a microscopic description to a macroscopic description of the composite laminate is made through the concept of a statistically homogeneous body [4]. This concept applies to fibrous composites in general and to the unidirectional material systems in particular. It is assumed that the constitutive properties of a unidirectional ply having arbitrary finite volume V can be determined from the same material having a smaller representative volume ΔV. However, in order for the determined properties to be statistically representative of those in volume V, the minimum size of ΔV must be large enough to include all possible variations of the composite microstructure, including fiber packing patterns, presence of microflaws, etc.; see Figure 1.4.

Within this context, two mutually equivalent approaches can be taken to characterize the constitutive properties of the unidirectional ply. The first approach is to apply the methods of micromechanics which describe the mechanical behavior of the composite of volume ΔV in terms of the properties of the fiber and the matrix phases as well as the geometrical configurations of the fiber-matrix microstructure. An average is then taken for the stresses and the strains in ΔV, whereby a set of effective constitutive properties is obtained. By virtue of the statistically homogeneous body postulation, these effective properties are regarded as the same for the entire material system of any arbitrarily large volume.

The other approach is to determine phenomenologically the effective properties of the material ply in a large volume V by direct experimental measurement. Then, owing to the statically homogeneous body postulate, these

effective properties are assumed the same for any arbitrarily small volume of the material, including those in ΔV.

Traditionally, the effective elastic properties determined by the two different approaches have been treated as mutually equivalent. But, extension of this equivalence to material strength properties, and especially its implications on the mathematical failure criteria have not been critically investigated.

Consider for example a typical graphite-epoxy system. Figure 1.5 shows a cross-sectional view of the fiber-matrix microstructure enlarged 500x. The thickness of the individual material ply is in the order of 125 μm, whereas the fiber diameter is about 8 μm. From the statistically homogeneous body concept discussed above, the minimum dimension of a representative volume ΔV should contain several fiber cross-sections (say, 10). If so, the linear dimension of ΔV is about 20% the thickness of the material ply. It is thus seen that the physical size of ΔV is quite large compared to the ply thickness. This raises the serious question as to whether the ply homogeneity assumption can adequately reflect the discrete field (microscopic) effects when a crack-like failure propagates inside the thickness of the ply, such as in the transverse cracks shown in Figure 1.1. Some of the questions regarding the ply homogeneity assumption and the use of the fracture mechanics approach do, indeed, pose conceptual difficulties.

Consider the theory of ply elasticity [5], an important derivative of the statistical homogeneous body concept. The theory assumes linear elasticity for the material ply, in addition to the homogeneity assumption. Specifically, the generalized Hookes Law is assumed to govern the ply constitutive relations:

$$\sigma_i = C_{ij}\, e_j \quad ; \quad i,j = 1,6 \tag{1.1}$$

where the stiffness constants C_{ij} are determined either from a micromechanics analysis method for a representative volume ΔV (see, e.g. [4]), or by a set of experimental test methods for a large volume V of the ply material (see, e.g. [6]). In either manner, the determined constants C_{ij} are assumed a uniform property for the unidirectional material system.

For laminates fabricated by stacking plies of different fiber orientations, the analysis allows the ply material constants to change abruptly across the ply interfaces. Then, assuming a perfect bonding at the interfaces, an exact analysis of the laminate stress field based on the ply elasticity theory can be performed [3]. Such an analysis provides the stress distribution in each of the plies from which a suitable ply failure criterion is applied to determine whether or not any of the plies is failed by the applied load. Typically, the ply failure criterion is derived from the conventional point-stress concept. For example, material ply failure occurs at a point in the ply if the stress state satisfies the following criterion [5],

$$F_{ij}\,\sigma_i\,\sigma_j + F_i\,\sigma_i = 1 \quad ; \quad i,j = 1,6 \tag{1.2}$$

The implication of this type of criteria is that the strength parameters such as F_{ij} and F_i in (1.2) are constant throughout the material ply. Consequently, ply failure can occur only as a stationary event, without regard to any possible modal and/or propagative behaviors.

This is clearly contradictory to the observed behavior of matrix cracks in laminates as matrix cracking is not a stationary event. Moreover, matrix cracking can occur as multiple events within one given ply at different ply stress levels [1, 7]. Therefore, some new concept of failure is needed, from which a criterion appropriate for matrix cracking in laminates can be addressed.

1.3 The Concept of Effective Flaws

In order to include the non-uniform ply strength property in modeling laminate matrix cracking, one frequently followed approach is to assume a characteristic strength distribution for the ply [8]. Strength estimation for multiple failures in the ply can then be formulated based on some probabilistic stress redistribution arguments. However, this approach still does not relate the modal or the propagative nature of matrix cracking.

As discussed before, the physical source of multiple matrix cracks is attributed to inherent material flaws which distribute randomly throughout the material plies. Through the homogeneity assumption made in ply elasticity, the physical identity of the flaws are lost and their effects on ply failure are not properly retained.

An alternative approach, however, is to represent the physical material flaws by a hypothetical effective flaw distribution at the macroscopic level [9 - 13]. In this way, the basic stress analysis scheme can still be conducted based on ply elasticity, but the elastic medium now contains imaginary flaws.

From this concept, it is assumed that a characteristic distribution of effective flaws having random sizes and locations can be determined as a macroscopic property of the basic material ply. It is required that the assumed effective flaws and their distributional character must yield an aggregate effect on ply failure similar to that observed in laminate matrix cracking. In this manner, failures in the individual plies are now governed by the conditions under which the effective flaws individually become matrix cracks; the ensuing modal behavior of crack propagation and the multiplicity of the cracking events then constitute the observed phenomena at the micro-scale.

As it will be demonstrated later in some example problems, the effective flaw distribution in a given material system can be rationally characterized by a simple test. The characterization includes the form, size and location of each of the flaws.

When the form, size and location of an effective flaw in a laminating ply are known, the mathematical conditions governing flaw initiation and propagation as a matrix crack are then formulated on the basis of classical fracture mechanics.

Let an effective flaw of known form in a considered ply be of size a and location x. The stress state surrounding the flaw can be determined in terms of the applied laminate stress $\bar{\sigma}$ by means of the ply elasticity theory. The critical incidence at which the flaw becomes a matrix crack is now derived from classical fracture mechanics. It will be assumed that the flaw/crack transition is governed by the fracture quantity, the strain energy release rate G, at the flaw tip. Given the form and location of the flaw, G can be calculated in terms of the applied laminate stress $\bar{\sigma}$ and the flaw size a [14]. The condition for the flaw to propagate into a matrix crack is given by the Griffith criterion [15]:

$$G(\bar{\sigma}, a) = G_c \tag{1.3}$$

where G_c is an appropriately determined material toughness for the particular mode of the crack propagation.

The critical laminate stress $\bar{\sigma}_{cr}$ at the incidence of flaw/crack transition is determined from Equation (1.3), given a and G_c. As for the propagation stability, it is then governed by the inequality (see also [15]):

$$\frac{\partial G(\sigma, a)}{\partial a} \geq 0 \tag{1.4}$$

Since the size and location of an effective flaw are actually random variables, and since the use of Equation (1.3) in matrix cracking problems is limited to a known crack individually, use of Equation (1.3) in multiple matrix cracks can lead to some time-dependent stochastic processes. But, before a stochastic simulation procedure is developed, some basic questions regarding the application of fracture mechanics need to be discussed.

1.4 Application of Fracture Mechanics to Matrix Cracks

It is well known that the classical fracture criteria expressed in Equations (1.3) and (1.4) apply only to brittle cracks undergoing stable and self-similar propagation [15]. Whether or not the general class of matrix cracks considered here fulfills these requirements needs careful analysis. Most structural composites are made of brittle matrix material, such as epoxy resin. Cracks in these materials can be considered brittle at both the microscopic and the macroscopic scales [11]. In addition, an in-ply matrix crack will always remain parallel to the fibers of that ply, while an interply matrix crack, or a delamination crack, remains parallel to the ply interface and propagates more or less in the same plane [11]. Thus, it would seem that the basic requirements in applying Equations (1.3) and (1.4) to brittle, self-similar matrix cracking can be fulfilled in the main.

However, use of the fracture criteria, particularly Equation (1.3), requires consistency between the mathematical quantity $G(\bar{\sigma}, a)$ and the physical quantity G_c. Some details relating to this question will be discussed in the following.

Consider first the right-hand side of (1.3). G_c is a material toughness property against matrix rupture, which is determined by some suitable phenomenological experiments. As such, the measured G_c for a given material system may vary with a number of factors. Specifically, G_c for unidirectional

fibrous composites changes with the local matrix-fiber packing geometry as well as the presence of microflaws along the path of the crack [16]. But these influencing factors exist at the microscopic level and are not identifiable at the macroscopic level. As a result, the macroscopically measured G_c exhibits two peculiar characteristics. The first is the dependence of G_c on the direction of matrix crack propagation relative to the ply fiber direction [11]; and the second is the dependence of G_c on crack extension increment, as the crack propagates intermittently rather than continually in real situations [16]. Apparently, both characteristics stem from the microscopically heterogeneous nature of the composite system.

The dependence of G_c on crack growth direction relative to the fibers has been demonstrated in two experiments of mode-I delamination in unidirectional laminates [17, 18]. Figure 1.6 shows a delamination crack propagating in the fiber direction, while Figure 1.7 shows a delamination crack propagating normal to the fiber direction. Although the two types of delamination crack occur essentially in the same interface plane, their corresponding fracture surfaces show different morphology when viewed at the microscopic scale. Hence, when G_c is deduced from a macroscopic measurement, the difference is also considerable. The multi-valued nature of G_c for a crack propagating in the same plane but in different directions is not generally found in conventional metallic materials.

As for the intermittent, stop-and-go behavior of matrix crack propagation, this is due to the fact that the crack path is often wandering around many fiber diameters. Others have also attributed the phenomenon to the viscoelastic behavior of the matrix material. In any event, G_c would have a stable value only if it is averaged over a finite crack extension Δa. The latter can be as large as several fiber diameters and can be interpretated as

the effective crack extension. Such a character is inherent to the fibrous material system; no theoretical value for Δa is available. Perhaps, Δa discussed here and ΔV discussed in Section 1.2 have some common relationship.

Now, the left-hand side of (1.3) pertains to the mathematically computed $G(\bar{\sigma}, a)$. The origin of G is traced to the theory of Griffith [19], who postulated that in a strained elastic body containing a small crack of size a, the stored elastic strain energy U will decrease if the crack extends stably. The decreased amount of the strain energy is equal to the increased free surface energy of the extended crack. Thus, if S denotes the total surface energy of the crack, a balance of energy at the incipient crack extension leads to the following condition,

$$-\frac{\partial U}{\partial a} = \frac{\partial S}{\partial a} \tag{1.5}$$

In common practice, the right-hand side of (1.5) is interpreted as the irrecoverable energy dissipated at the incipient crack extension [15]. The term would then include such non-elastic quantities as local plastic yielding, viscoelastic dissipation, etc. Then, the resultant quantity becomes measurable only by phenomenological experiment. This quantity is commonly known as the critical energy release rate G_c, which is mentioned earlier in Equation (1.3).

The left-hand side of (1.5) is calculated mathematically by means of some elasticity boundary-value solution methods (e.g. [14]), which give rise to the definition of

$$G(\bar{\sigma}, a) = -\partial U/\partial a \tag{1.6}$$

The mathematical implication of (1.5) or (1.6) is that U is a continuous function of the continuous variable a. And, at least the first and the second derivatives of the function U exist for $a > 0$ [20].

But, this implication contradicts the actual physics of matrix cracks. As mentioned before, matrix cracks extend intermittently with increments Δa usually in the order of several fiber diameters [16]. Furthermore, G_c could be measured only as an average over the finite crack extension Δa.

In view of the above, it seems that $G(\bar{\sigma}, a)$ in (1.6) may be more appropriate if defined as

$$G(\bar{\sigma}, a) = - \frac{U(a + \Delta a) - U(a)}{\Delta a} \tag{1.7}$$

and the stability criteria in (1.4) as

$$\frac{G(\bar{\sigma}, a + \Delta a) - G(\bar{\sigma}, a)}{\Delta a} < 0 \tag{1.8}$$

where Δa is chosen appropriately given the actual fibrous system.

It is noted that between the definitions in (1.6) and (1.7), the original physical meaning is more or less preserved. But, mathematically, the right-hand side of (1.6) is the tangent of $-U(a)$ at a, while that in (1.7) is now the secant of $-U(a)$ from a to $a + \Delta a$; see Figure 1.8. The numerical difference between the two could be significant depending on the form of $U(a)$ and on the size of Δa.

Clearly, use of (1.7) rather than (1.6) for the definition of $G(\bar{\sigma}, a)$ can result in considerable controversy. For instance, the traditional concepts of crack-tip singularity and stress intensity factor K as a fracture quantity [21, 22] may now require reinterpretation.

It is known that the development of the K-concept was based on the equivalence between K and G for brittle crack in an elastic continuum [21, 22]. The meaning of K represents the intensity of the singular stress field near the closest vicinity of the crack-tip through the general relationship

[21];

$$\sigma_{ij}(r, \theta) = \frac{K_i}{\sqrt{r}} f_{ij}(\theta) \quad ; \quad i,j = 1, 2, 3 \tag{1.9}$$

where K_1, K_2 and K_3 are associated with the three modes of crack propagation, while (r, θ) are the polar coordinates measured from the crack-tip; see Figure 1.9.

The stress intensity factors K_i can be determined in explicit terms of the applied load $\bar{\sigma}$ and the crack size a, in the general form

$$K_i(\bar{\sigma}, a) = \bar{\sigma}\, g_i(a) \tag{1.10}$$

The form of $g_i(a)$ depends only on the geometry of the crack and the physical details of the strained body in consideration (see e.g. [23]).

Under the assumption of infinitesimal local response at the crack-tip, the stress intensity factors K_i are then related to the energy release rate G in the general form [20],

$$G(\bar{\sigma}, a) = \Phi_{mn} K_m(\bar{\sigma}, a) K_n(\bar{\sigma}, a) \quad ; \quad m,n = 1, 2, 3 \tag{1.11}$$

where Φ_{mn} are functions of the material stiffness constants C_{ij} only. Hence, if G_c is a material property, the quadratic combination of K_c's must also be a material property.

Use of K as a quantity for crack growth implies that material separation at the crack-tip region is determined solely by the elastic stress field which exists locally; and, this stress field is adequately represented by the singular function in the general form of (1.9).

Now, when applied to matrix cracking, use of K may need reinterpretation. The reasons are as follows. First, since the physical justification for the K-concept stems from the G - K equivalence, their mathematical relationship as expressed in the general form in (1.11) becomes invalid if $\bar{G}(\sigma, a)$ takes on

the definition of (1.7) instead of (1.6). Secondly, since K signifies the intensity of a singular stress field near the considered crack tip region, which is often very small in size, say about a single fiber diameter, the meaning of K may contradict the basic requirements of a finite crack extension Δa as well as the statistically homogeneous postulation. Thus, in order to describe the macroscopic behavior of the composite system, use of the K-concept for matrix cracking may also require some new interpretation from both a physical and a mathematical consideration.

1.5 Cracks in Bi-Materials Interface

A related question concerns a crack that occurs in the interface between two plies of different fiber orientations. According to ply elasticity, this is a crack propagating in the interface of bonded dissimilar materials. The question relates to the stress singularity at the tip of the crack. In this case, the singular stresses will contain oscillatory components (see [20]). Consequently, the stress intensity factor K or the strain energy release rate G cannot be computed exactly in the classical manner. The oscillatory nature of the crack-tip stress field implies material penetration, which is physically inadmissible. A modification of the classical definition for K is possible if a partial crack-tip closure is included in the calculation [24]. Since the oscillatory part of the stress field exists only on a small scale, the importance of its influence on the physical quantity G near the crack-tip is usually negligible [20].

The existence of crack-tip oscillatory stresses is attributed to the impossibility of satisfying the zero-load boundary conditions near the crack-tip point [20]. The problem seems to be inherent to the theory of linear elasticity. The oscillatory part of the singular stress field near a bi-material crack tip would disappear if a non-linear theory of elasticity is

assumed for the materials [25].

In order to bring some further clarification to this problem, a recent paper [26] has examined a case where an adhesive layer of finite thickness is introduced in the interface of two dissimilar plates. A delamination crack is made to propagate inside the adhesive layer. If the adhesive layer is elastic and homogeneous, then the crack-tip stress singularity will contain no oscillatory components. The strain energy release rate G in this case can be computed in the conventional manner provided the various material interface conditions are incorporated in the computation. When the adhesive layer thickness is reduced to nearly zero, the computed G uniformly approaches a finite quantity, see Figure 1.10. It would thus seem that the oscillatory stress field of a bi-material crack is not an issue for delamination analysis, particularly in view of the requirement of the statistically homogeneous body concept.

As demonstrated in [26], for a delamination crack between two plies of different fiber orientations, the mixed-mode energy release rate G can also be adequately calculated by a finite element method which disregards the stress singularity altogether.

1.6 The Finite Element Procedures

From the classical fracture mechanics viewpoint, both the G-concept and the K-concept are equally applicable to brittle crack propagation problems. Relative ease in computation is often the reason dictating which one of the concepts is employed. In the case of crack in metals, the K-concept has traditionally been preferred.

When a crack is situated in a body of complex boundaries, numerical procedures such as the contemporary finite element techniques are frequently used. In this case, the computation of G is usually simpler than the computa-

tion of K. In either case, uncertainties over numerical accuracy often arise because of the numerical technique used to approximate the singular stress field.

These concerns, however, are largely removed if the discrete form for G as expressed by (1.7) is computed. But the practical question remains as to the proper definition for the effective crack extension, Δa. This question is related to the inherent character of the physical material system. It can be answered only by experience and experiment. Except for the uncertainty over the choice of Δa, the finite element technique is a useful and direct means for computing G, as expressed in the form of (1.7).

Figure 1.11 shows the finite element representation of a plane crack in a 2-dimensional solution field. Here, the tip of the crack of length a is at node c. Given the applied far-field load $\bar{\sigma}$, the entire elastic stress field can be determined within the framework of the finite element method. The solutions not only include the stresses and displacements (at the nodes) but also the total strain energy stored in the body, U(a). Then, by a properly chosen incremental crack extension Δa in the direction of the original crack, the node c is opened up into two separate nodes f and g, whereby the crack tip advances to node h. With this new crack configuration and by keeping the far-field conditions unchanged, a new solution is obtained which yields the displacements (u, v, w) for nodes f, g and h, as well as the stored strain energy $U(a + \Delta a)$. This step readily yields the strain energy release rate $G(\bar{\sigma}, a)$ as defined in (1.7).

If the finite crack extension Δa is closed by requiring the nodes f and g to return to the original position of node c, the finite element solution yields the nodal forces (F_x, F_y, F_z) needed to close nodes f and g together. The work done in closing the crack extension Δa is then given by

$$\Delta W = 1/2\ [F_x(u_f - u_g) + F_y(v_f - v_g) + F_z(w_f - w_g)] \qquad (1.12)$$

According to the work-energy equivalence principle [22], the strain energy release rate during the finite crack extension Δa can be alternatively defined as

$$G(\bar{\sigma}, a) = \Delta W/\Delta a \qquad (1.13)$$

Expression (1.13) gives the same results as (1.7). But, the advantage of the expression in (1.13) is that it also gives the modal components in G if the crack propagation is in mixed-mode. Thus, by way of (1.12), Equation (1.13) takes the form,

$$G(\bar{\sigma}, a) = G_I(\bar{\sigma}, a) + G_{II}(\bar{\sigma}, a) + G_{III}(\bar{\sigma}, a) \qquad (1.14)$$

where

$$G_I(\bar{\sigma}, a) = F_z\ (w_f - w_g)/2\Delta a$$

$$G_{II}(\bar{\sigma}, a) = F_y\ (v_f - v_g)/2\Delta a \qquad (1.15)$$

$$G_{III}(\bar{\sigma}, a) = F_x\ (u_f - u_g)/2\Delta a$$

By successive opening and closing of the nodes along the crack propagation path, the quantity $G(\bar{\sigma}, a)$ can be calculated as a function of the crack length a.

This technique was apparently first applied to delamination cracks in laminates by Rybicki and Kanninen [27]. It was later extended to simulate transverse cracks [9] and contoured delamination in 3-dimensional stress field by Wang, et. al [28].

1.7 Summary

In this chapter, several basic physical and mathematical concepts have been discussed. These are pertinent to a consistent development of a failure

analysis methodology for matrix cracks in composite laminates. At this point, a summary discussion of these concepts is briefly presented below:

(1) Matrix cracks, their initiation, propagation and interaction constitute a complex failure process in fibrous composite materials. For the class of laminates that are made by stacking unidirectionally fiber reinforced plies of different fiber orientations, the matrix cracking patterns are generic to the lamination geometry and the nature of the applied load. The general cracking process is seen to follow a certain mechanistic rule, and the problem appears to be amenable to some form of analytical description.

(2) When viewed at the macroscopic scale, a matrix crack can be classified as one of two fundamental forms. The in-ply crack which separates through the thickness of a ply is confined to propagate parallel to the fibers in that ply. The interply crack, known also as delamination, is propagated in a plane parallel to or inside of ply interfaces. Both may be considered as self-similar propagating cracks at the macroscale.

(3) When viewed at the microscopic scale, i.e. with precise fiber-matrix structure taken into account, matrix cracks are thought to originate from material flaws which exist randomly either in the matrix phase or on the fiber-matrix interfaces. The individual propagation and mutual coalescence of these flaws lead to matrix cracks of large proportion, which are then observeable at the macroscale. The initiation and growth behaviors of matrix cracks at the macroscale depend intrinsically on the local details of flaw growth and flaw coalescence. These local details, however, cannot be practically modelled because of the multiplicity and the probabilistic nature of the material flaws.

(4) The accepted theoretical basis for stress and failure analysis of composite laminates has been the concept of statistically homogeneous body,

From this concept, the theory of ply elasticity has traditionally been derived and applied. But, this theory compromises the presence and the effects of the material flaws on failure. Consequently, these microscopic effects cannot be recovered rationally in the ensuing stress and failure analyses in the conventional manner.

(5) In order to overcome the predicament caused by micro-macro translocation of the material flaws, an alternative approach is followed. The approach is to work within the realm of ply elasticity, but to include the presence and the effects of the material microflaws in the form of assumed effective flaws. Specifically, given a finite volume of the basic ply material, it assumes that a characteristic distribution of effective flaws can be identified which has the equivalent effects as the intrinsic flaws that exist at the microscale. Although the existence of the effective flaws is hypothetical, they nevertheless provide a viable alternative for modelling matrix cracks at the macroscale. As such, the assumed effective flaw distribution represents a macroscopic ply property.

(6) The introduction of the assumed effective flaw distribution not only retains the probabilistic and the multiplistic characteristics of the matrix cracking process as a whole, it also enables the description of the propagative behavior of the individual matrix cracks themselves. Specifically, the individual flaw is treated as a crack whose propagation mechanisms is governed by the criteria derived from the theory of linear elastic fracture mechanics; the collective behavior of a distribution of random flaws is then treated by a method of stochastic processes.

(7) Within the logical context outlined above, two problems of fundamental nature arise. The first is related to the actual characterization of the effective flaw distribution, given a finite volume of the ply material. By

definition, this distribution can be characterized only by phenomenological means. And, as such, a considerable amount of empiricisms would be involved in the characterization. This will undoubtedly pose uncertainties as to the uniqueness and the reliability of the determined flaw distribution as a ply material property.

The second problem concerns the consistency between the physics and the mathematics associated with the crack propagation criteria used. On one hand, the theory of elastic fracture mechanics assumes that crack propagation is governed by conditions which exist in the closest vicinity of the crack-tip, where the dimension of the region of interest is often smaller than the diameter of a single fiber, or the actual size of a microflaw. On the other hand, the actual physics of matrix cracking seems to indicate that microscopic activities near the crack-tip may extend over a region larger than several fiber cross-sections.

(8) To alleviate these difficulties, a modification of the classical criteria of crack propagation is proposed. Namely, only the effective fracture quantities are defined and used. In particular, a discrete form, or an averaged value of the strain energy release rate G over a finite crack extension Δa is defined, see Equation (1.7). The choice for the proper size of the crack extension Δa will depend on such factors as the size of material heterogeneity (e.g. fiber diameter, microflaws, etc.) in the actual composite system and the lamination fabrication variables.

Using the concepts presented above, the fracture description for matrix cracks may be augmented by a numerical finite element simulation. Against this background, an analytical methodology is presented and applied to several matrix cracking problems. Concurrent experiments have been conducted to adjudicate the theory. Most of the details are presented in the following chapters.

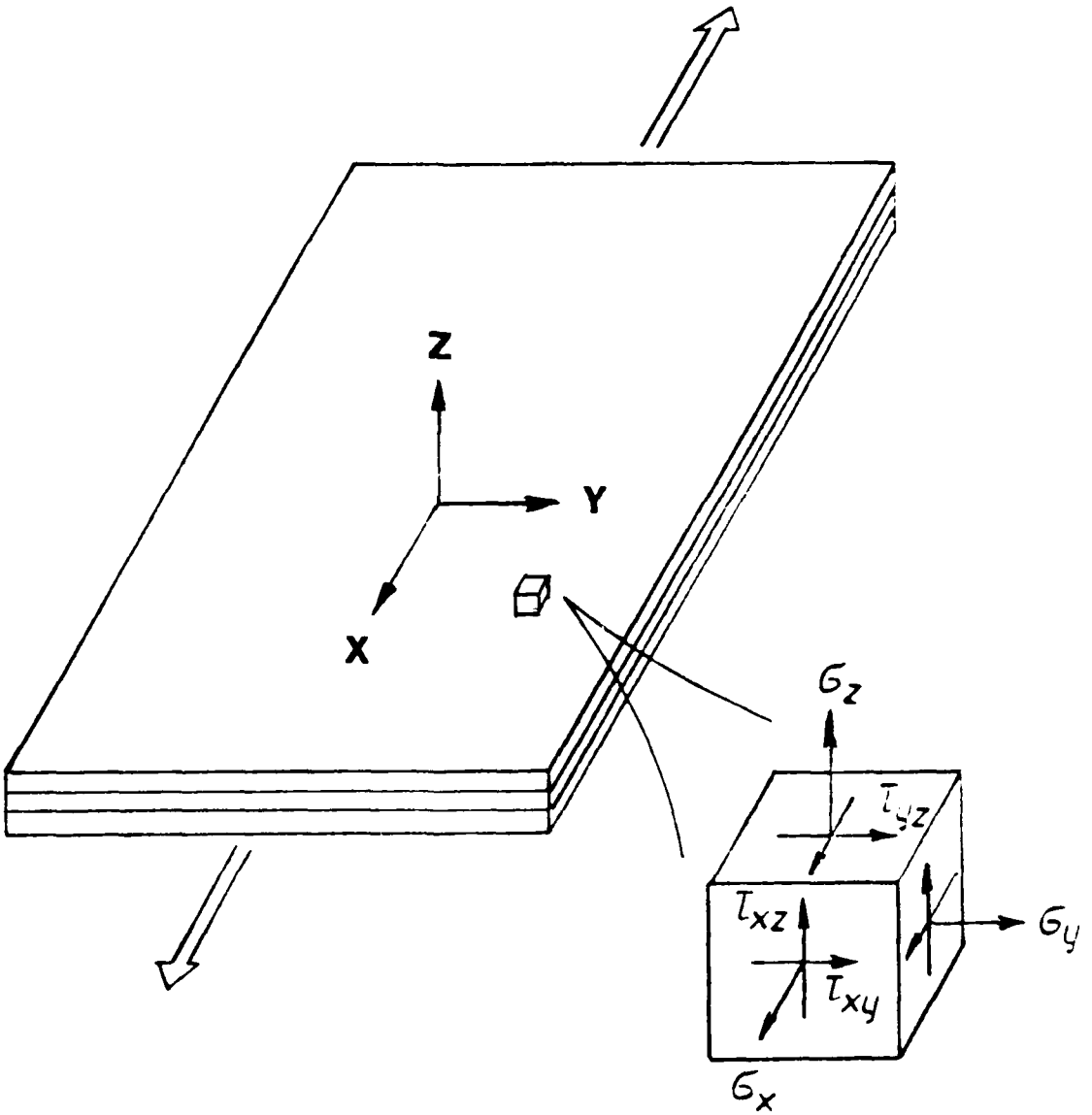

Figure 1.1 Laminate Coordinate and Stress Field.

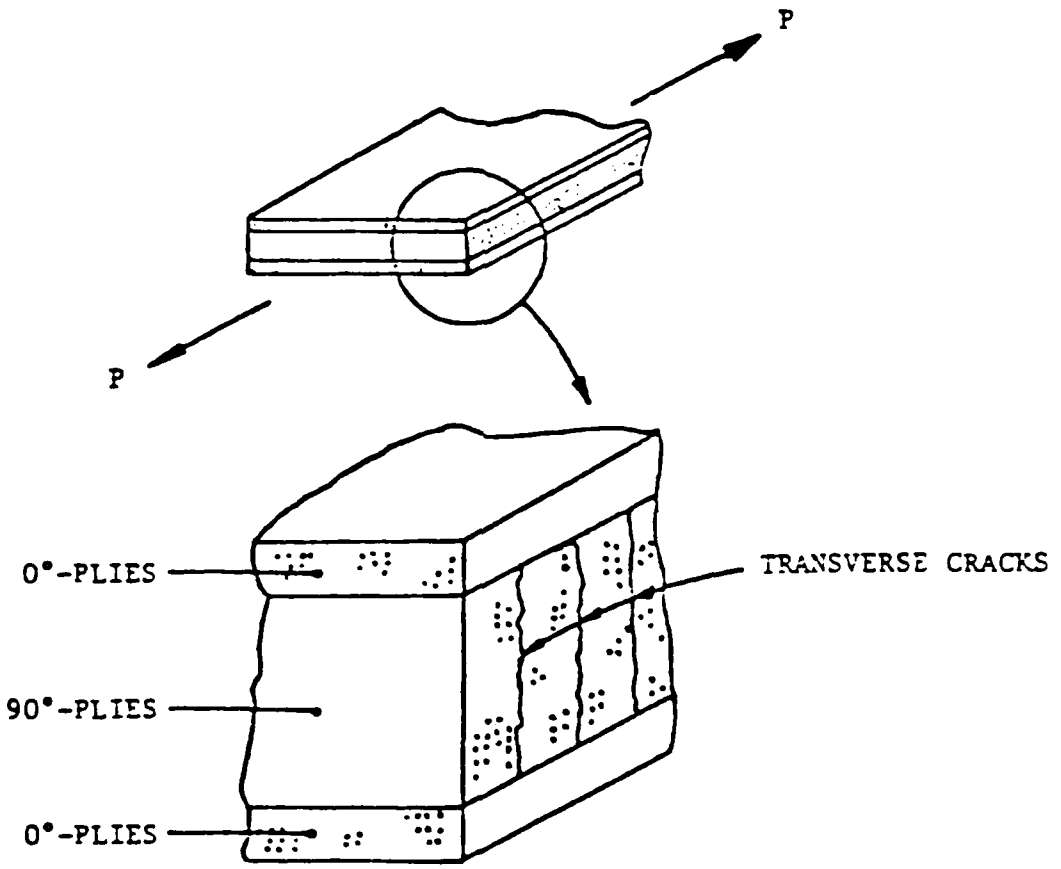

Figure 1.2 Intraply Cracking (Transverse Cracks) in a Cross-Ply Laminate.

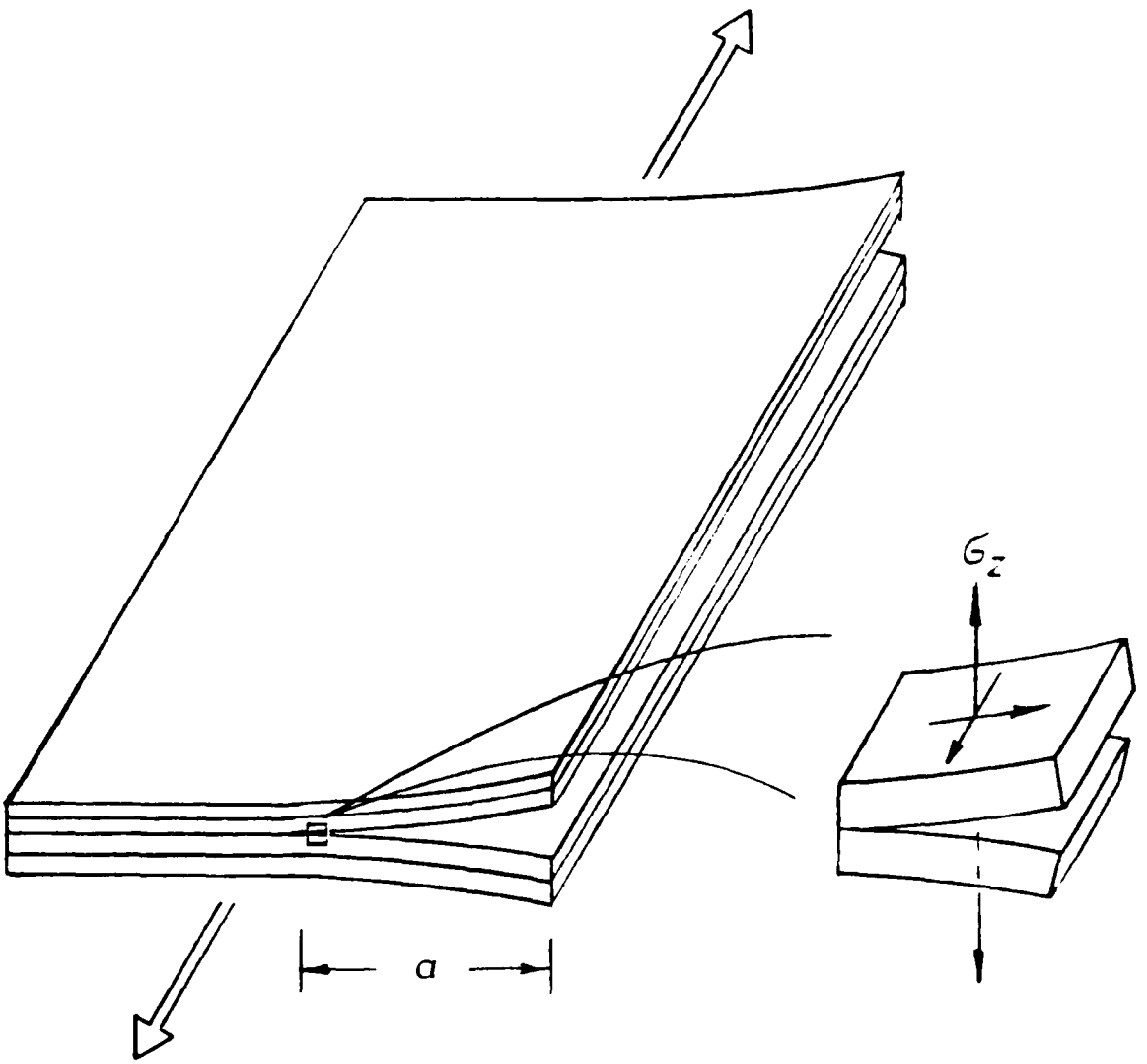

Figure 1.3 Interply Cracking (Edge Delaminate) in a Multi-Ply Laminate.

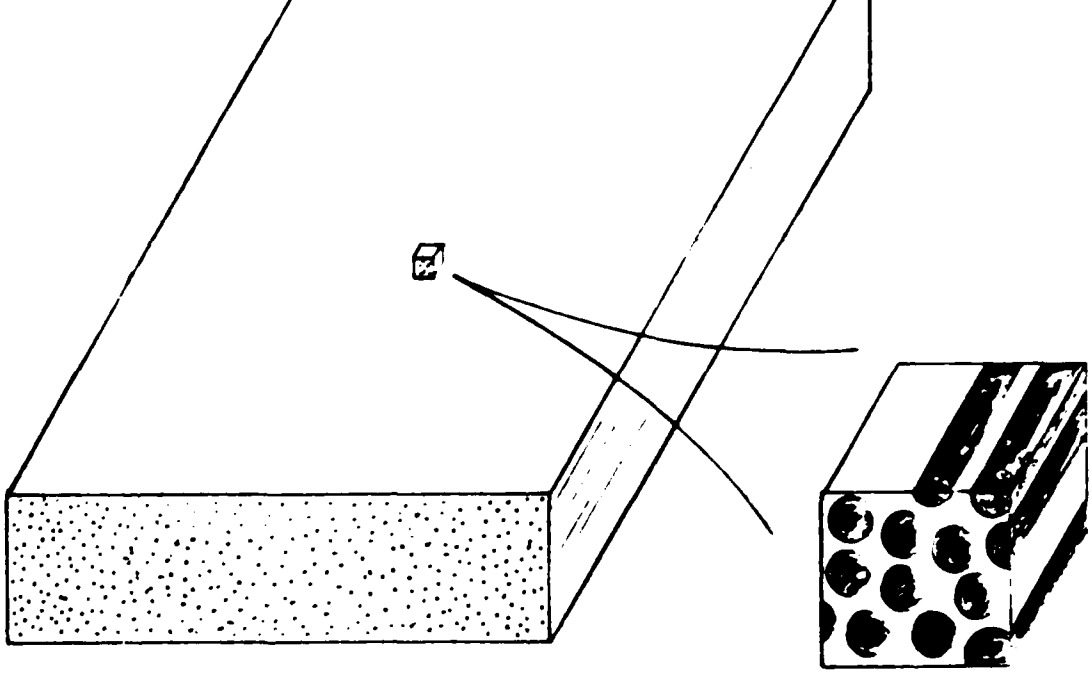

Arbitrary Volume V **Representative Volume ∇V**

Figure 1.4 A Microscopic View of the Unidirectional System.

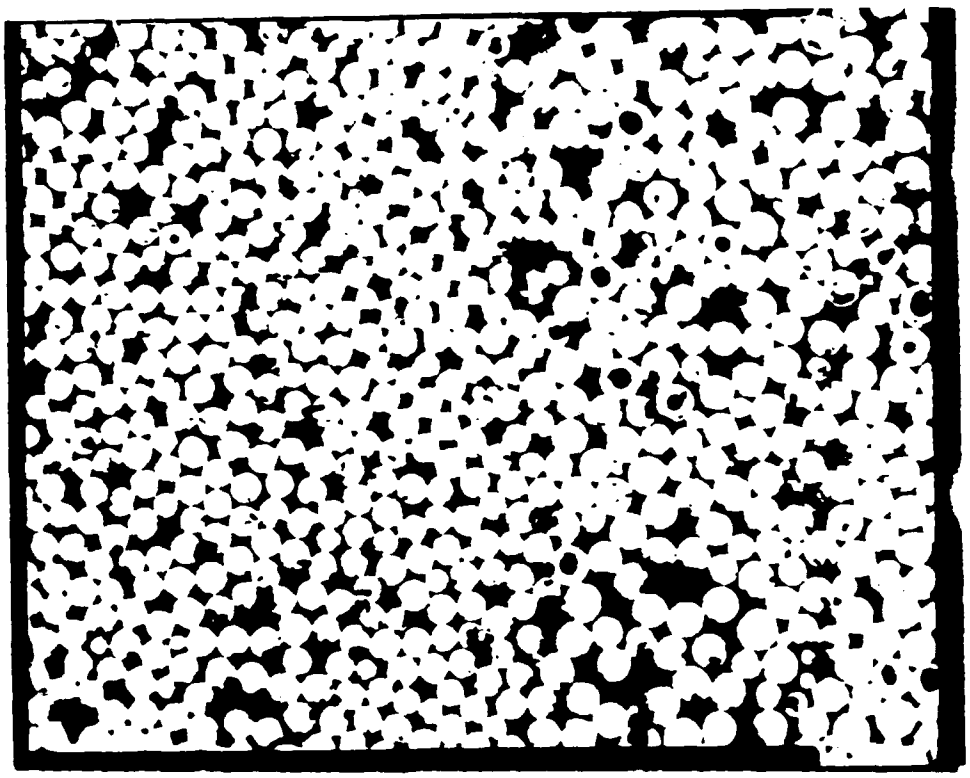

Figure 1.5 Cross-Sectional Photomicrograph of a Graphite-Epoxy Unidirectional System.

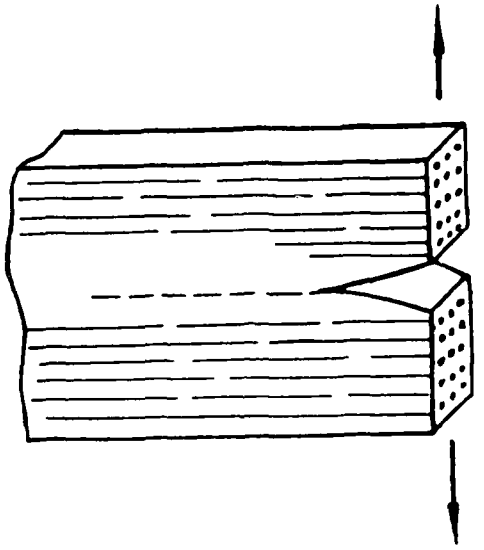

Figure 1.6 Matrix Crack Propagating Parallel to the Fibers.

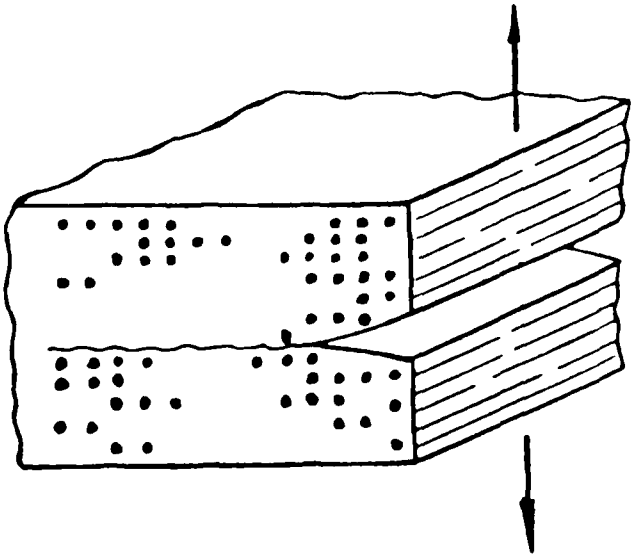

Figure 1.7 Matrix Crack Propagating Normal to the Fibers.

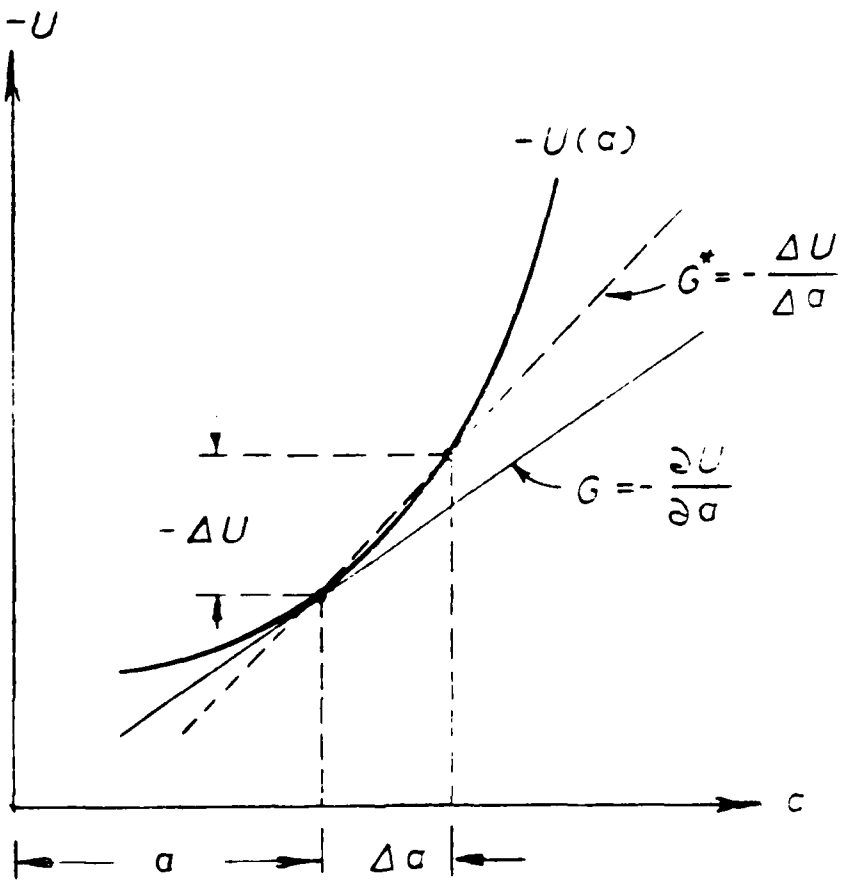

Figure 1.8 Classical Definition of G versus G* for Finite Δa.

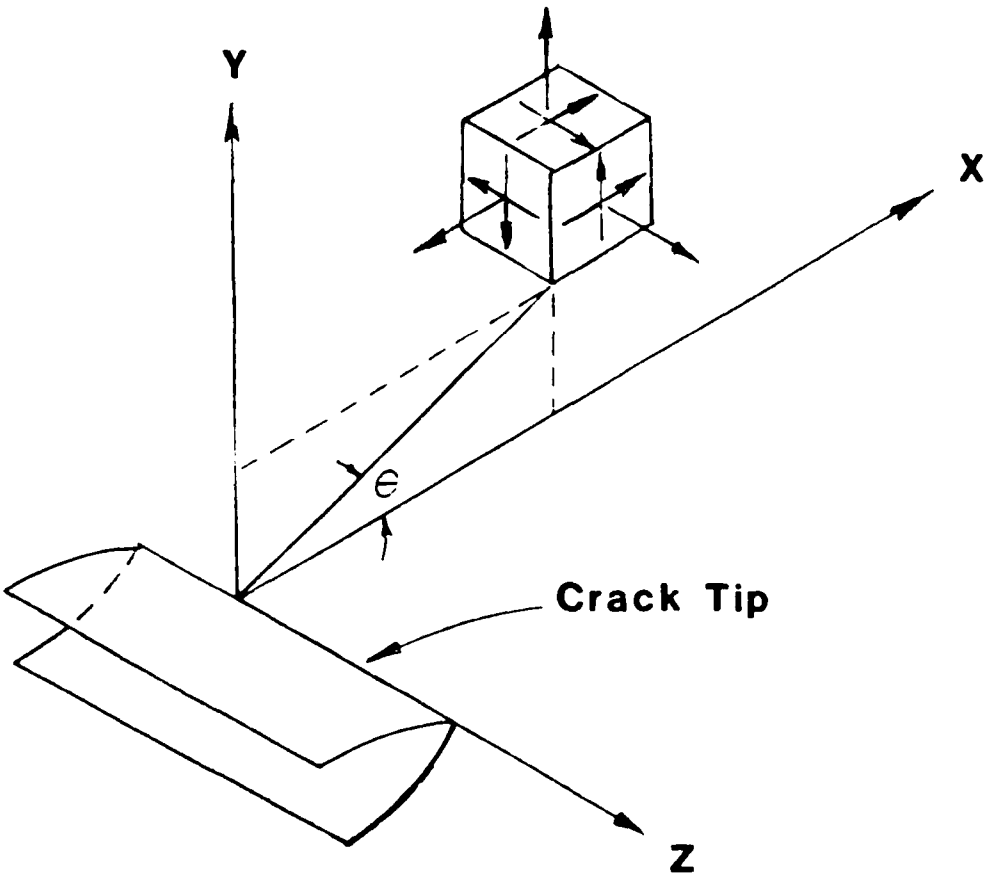

Figure 1.9 Crack-Tip Coordinates for a Crack Propagating in the x-y Plane.

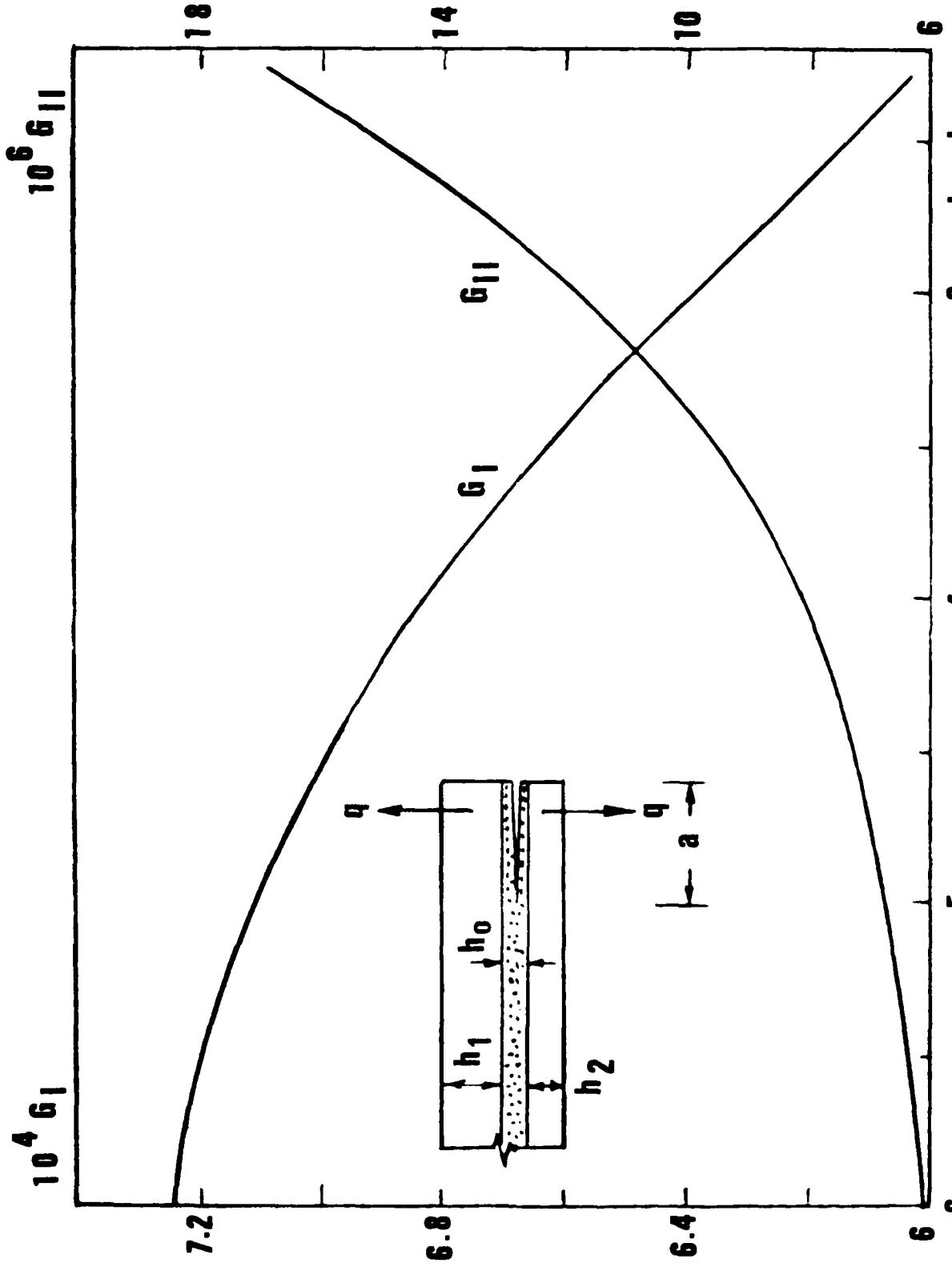

Figure 1.10 Mixed-Mode Energy Release Rate as a Function of the Thickness of the Adhesive Layer in a Bi-Material Interface [26].

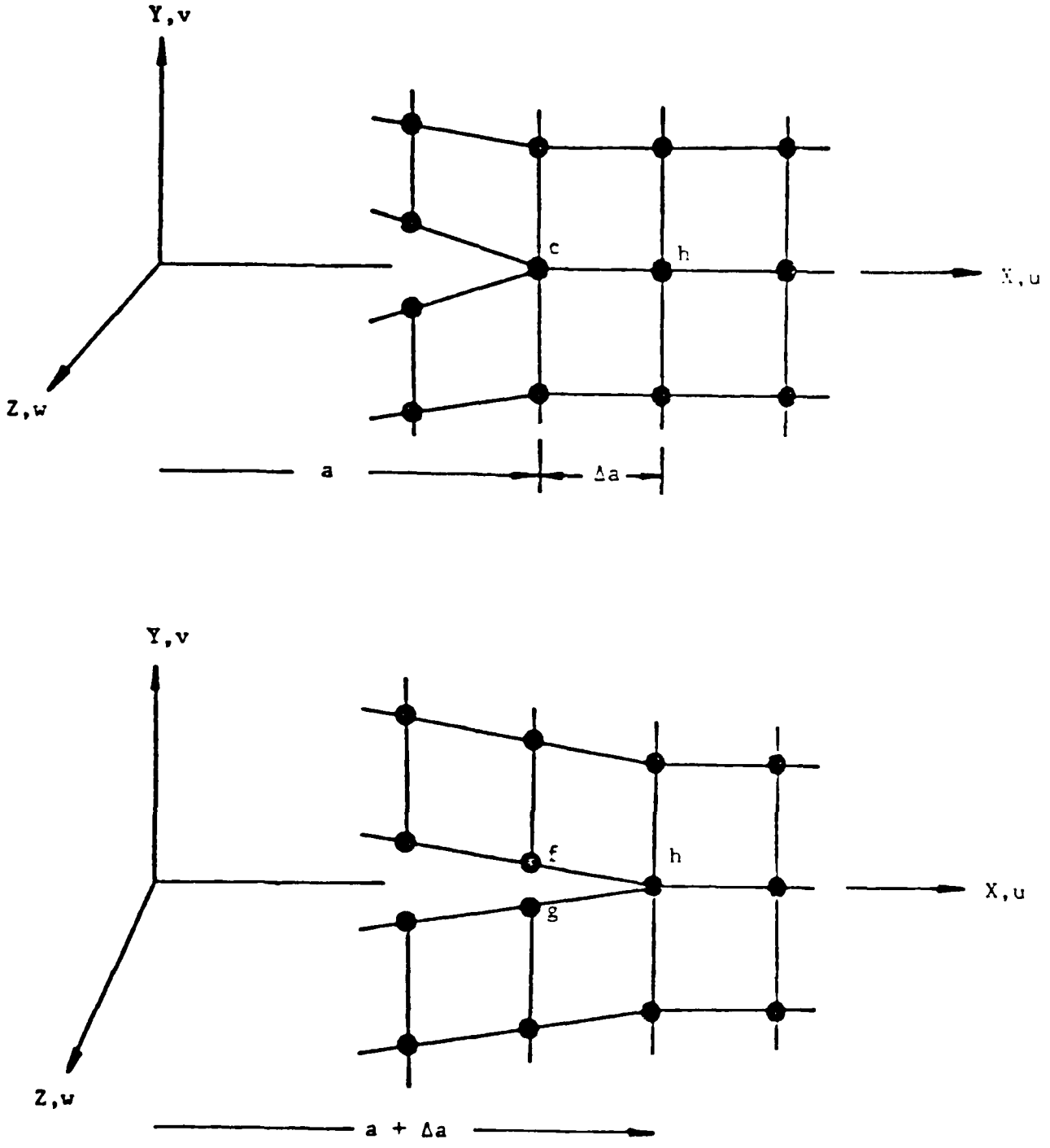

Figure 1.11 Finite Element Representation for a Crack Propagating in the x-y Plane.

CHAPTER II. ANALYSIS OF INTRAPLY CRACKING

2.1 Intraply Versus Interply Matrix Cracks

As was seen in the previous chapter, structural composites made from laminated unidirectional plies frequently suffer matrix cracks well before final laminate rupture. These matrix cracks can develop into damage zones of various degrees of severity under service loading.

To visualize the physical nature of matrix cracks at the macroscale, it is useful to examine the sketch in Figure 2.1. Individually, each unidirectional ply is highly anisotropic. For example, the ply stiffness in the fiber direction, E_L, can be orders of magnitude larger than the stiffness normal to the fiber direction, E_T. Similar differences also exist between the in-ply Poisson ratios ν_{LT} and ν_{TL}, the thermal expansion coefficients in the longitudinal direction α_L, and the transverse direction, α_T, etc. Table II-1 shows the disparity between the fiber dominated and the matrix dominated effective ply properties of a typical graphite-epoxy unidirectional system.

Clearly, the in-plane property mismatch between plies of different fiber orientations can cause complex in-ply and interply stresses when the plies are laminated together. The thermal expansion mismatch between plies in laminates cured at high temperature will result in considerable thermal residual stresses upon cooling to ambient temperature. Likewise, a mismatch of stiffness and Poisson ratio between plies complicates the laminate stress field when external service load is applied.

Since the ply tensile strength transverse to the fibers is usually orders of magnitude smaller than the strength in the fiber direction, (see e.g. Table II-1), matrix cracks due to in-ply tension σ_T or interply tension σ_z frequently occurs first. But, whether an intraply matrix crack occurs before an interply matrix crack in a given laminate depends on the laminate geometry and

the exact nature of loading. Particularly, geometrical factors profoundly influence the laminate's in-ply and interply stress fields.

To illustrate, compare the following two cases between the $[0/90]_s$ and the $[\pm 25/90]_s$ laminate coupons:

The $[0/90]_s$ Tensile Coupon. Assume that the $[0/90]_s$ laminate coupon is long and is loaded uniformly in axial extension. Under such a condition, the laminate stress field is independent of the axial coordinate x and the three-dimensional laminate stresses can be analyzed by a two-dimensional generalized plane strain formulation in the y-z plane. This problem has originally been treated by Pipes and Pagano [30]; and a later treatment using a sepcial finite element method was carried out by Wang and Crossman [31].

Now, let the material system be T300/934 graphite-epoxy system (see Table II-1 for ply properties) and consider the stress field induced by an applied far-field strain, $\bar{e}_x = 1$ με. The dominant in-ply and interply stresses in the 90°-ply are sketched in Figure 2.2. It is seen that the tensile σ_x stress is due to the applied tension, while a compressive σ_y stress is caused by the Poisson ratio mismatch between the 0°-ply and the 90°-ply. On the other hand, the tensile σ_z and the shearing τ_{yz} stresses are effected by and concentrated near the laminate free edge [30]. Figure 2.3 shows the σ_z distribution on the laminate mid-plane (90/90 interface) as a function of distance from the free edge. Note the sharp rise in magnitude for σ_z near the laminate free edge.

In this example, the numerical value of the in-ply stress σ_x in the 90°-ply is about 11.7 Kpa per με, while the maximum σ_z stress near the free edge is less than 2 Kpa per με. It is clear by comparison that in-ply matrix cracks (transverse cracks) caused by σ_x are likely to occur in the 90°-ply before the edge stress σ_z induced interply delamination.

The $[\pm 25/90]_s$ Tensile Coupon. Now, consider the $[\pm 25/90]_s$ coupon under similar situation. In this case, the $\pm 25°$-plies as a unit has a smaller axial stiffness, but has a larger in-plane Poisson ratio ν_{xy}. Consequently, both the in-ply and the interply stresses near the free edge region are considerably altered, especially the interply stress σ_z near the free edge region which increases dramatically in value. As seen in Figure 2.4, the value of σ_z at the free edge is about 20 Kpa per με, a ten-fold increase from the previous example.

On the other hand, the in-ply tensile σ_x stress in the 90°-ply remains about the same at 11.7 Kpa per με. Hence, it may be inferred that interply cracks in the form of edge delamination in the 90°/90° interface occurs before the transverse cracking in the 90°-ply.

As both the in-ply matrix crack and the interply matrix crack are localized failures, the occurrance of one may precipitate the occurrance of the other. In the following, however, the basic mechanisms of these two basic forms of matrix cracking shall be examined separately.

2.2 Physical Characteristics of Intraply Cracking

Consider first the physical characters of intraply matrix cracking. Take, for example, the $[0/90]_s$ type tensile coupon discussed above. Because of the relatively small interlaminar edge stresses, formation of matrix cracks is largely, if not exclusively, inside the thickness of the 90°-plies in the form of transverse cracks. It is thus possible to use this example and examine the cracking events without regard to the influence of laminate free edge effects.

The Onset and Growth Characteristics. When viewed at the macroscopic scale, the formation of a transverse crack in the 90°-ply is simply a sudden separation of the collimated fibers that lie normal to the applied tension.

Within a single specimen, numerous such cracks could form as a sequence of load-dependent events; onset of the first crack occurs when the applied load reaches a certain critical value, and similar successive cracks emerge as the applied load increases. Experimental records by x-radiographs are shown in Figure 2.5 for a $[0/90]_s$ coupon under monotonic tension. The pictures show the emergence of transverse cracks as a function of the applied load. From the photographs of this kind, a plot of the transverse crack density (cracks per unit coupon length) versus the applied tension can be obtained.

Figure 2.6 shows a family of such experimental plots from tests of T300/934 $[0/90_n/0]$ laminate series with n = 1, 2, 3 and 4 [32]. Except for the laminate of n = 1 for which no visible transverse crack was detected before final laminate rupture, all three cases (n = 2, 3, 4) yielded distinctive transverse crack density vs. applied tension relationships. This data shows that the 90°-ply transverse cracking process possesses both a probabilistic and a deterministic character. Specifically, the occurrence of any one individual crack is highly probabilistic, while the overall crack development process, including the initiation load and the crack density vs. load relationship as a whole are deterministic.

Several geometrical factors were found to influence the characteristics of the cracking process [32]. In addition to the laminate stacking sequence, the actual thickness of the 90°-plies (or the number n) also influences the cracking behavior. This can be seen from the data in Figure 2.6, which shows that a thinner 90°-layer is capable of reaching a higher crack density than a thicker 90°-layer. Also, the critical tensile strain $\bar{e}_{cr}$ for the onset of the transverse crack process decreases with increased 90°-layer thickness, see Table II-2.

The Kinematics of Crack Propagation. In order to develop a descriptive model for intraply cracking, the kinematics of the individual crack propagation must first be understood. Despite numerous experiments, the exact nature of the 90°-ply transverse crack propagation is unclear. From macroscopic observations, it has been suggested that the crack might initiate from a cluster of flaws which lie thickness-wise in the 90°-ply. As load reaches the critical value, a sudden coalescence occurs accompanied by audible acoustic emissions (see e.g. [33]). This dynamic character may be due to the very rigid axial stiffness of the 0°-plies constraining the flaws in the 90°-ply to propagate primarily in the thickness direction. The propagation is, however, immediately arrested or blunted at the 0/90 interface, see illustration in Figure 2.7.

The thickness-wise crack propagation is merely conjecture, though it conforms to the phenomenonological behavior observed experimentally. This conjecture provides a basis for defining and characterizing the "effective" flaws, as well as for simulating the multiple cracks propagation process.

2.3 Representation of the Effective Flaws

For practical purpose, assume that the in-ply "effective" flaws are one-dimensional, being orientated in the ply thickness direction as illustrated in Figure 2.8. The linear size of an individual flaw is denoted by 2a, which is bounded by the total thickness of the 90°-plies, 2nt. The relative spacing between any two adjacent flaws is denoted by s, which can be determined by their relative positions $(x_{i+1} - x_i)$. Hence, both a and s are real, positive random variables. Given the laminate, the distribution function f(a) and the distribution function f(s) are sufficient to define the characteristics of the flaws in the 90°-plies.

As will be shown next, the distribution function f(a) and f(s) in

laminates with grouped 90°-plies can be obtained in terms of the flaw distribution functions of a single 90°-ply through a statistical volume-theory. Then, it is necessary only to characterize the flaw distribution functions of the single 90°-ply as a basic ply property.

Effective Flaws in Single Material Ply. Let 2t be the nominal thickness of the basic 90°-ply. For a unit length of the 90°-ply, say 1 cm long, let there be M effective in-ply flaws which lie thickness-wise and distribute randomly along the 1 cm length, Figure 2.8. If the half size of the ith flaw is denoted by $(a_o)_i$ and its location is denoted by $(x_o)_i$, then the sets $\{(a_o)_i\}$ and $\{(x_o)_i\}$, i = 1, M characterize the in-ply flaws of the 90°-ply of unit length (1 cm).

Now, let the set $\{(a_o)_i\}$ be represented by a Weibull distribution of the continuous variable a_o in the form [34],

$$F_1(a_o) = 1 - \exp\left[-(a_o/\beta_o)^{\alpha_o}\right] \tag{2.1}$$

where α_o and β_o are the shape and the scale parameter of the cumulative distribution $F_1(a_o)$.

In the mathematical form of (2.1), the variable a_o extends from 0 to ∞. But, as a practical matter, a_o must be bounded between 0 and t. For instance, the 1-percentile of a_o should be greater than 0 and the 99-percentile of a_o be smaller than t. Then the following constraints on the values of α_o and β_o may be imposed:

$$\begin{aligned} &\left[(0.01)^{1/\alpha_o}\right]\beta_o > 0 \\ &\left[(4.6)^{1/\alpha_o}\right]\beta_o < t \end{aligned} \tag{2.2}$$

The characterization of the in-ply flaw size distribution then reduces to determining the number M and the parameters α_o and β_o, subjected to the possible constraints in (2.2).

As it will be shown next, the distribution functions f(a) and f(s) in laminates with grouped 90°-plies can be obtained in terms of the flaw distri-

As for the flaw spacing distribution f(s) or the location set $\{(x_o)_i\}$, i = 1, M, it is often sufficient to select a suitable random number generator that gives a set of M random values between the interval (0, 1). These random values then constitute $\{(x_o)_i\}$.

Effective Flaws in Grouped Plies. In laminates of more than one 90°-ply grouped together as in the $[0/90_n/0]$ family when n > 2, the effective flaws in the grouped 90°-plies are not the same size as those in the single 90°-ply. A simple scheme may be used to determine the effective flaw sizes in the grouped 90°-plies, given the flaw size distribution of the single 90°-ply.

The scheme is based on a statistical consideration of increased volume [34]. It may be perceived at the first glance that the grouped 90°-plies would behave as n individual plies arranged in parallel, similar to a bundle of threads loaded in uniform tension [35]. However, because the plies are laminated together, failure of any one 90°-ply may lead to unstable propagation through the thickness of the grouped 90°-plies. Consequently, failure of the grouped 90°-plies more likely behaves as n plies arranged in series.

Assume that for every unit length (1 cm long) of the 90°-ply, there exists a discrete tensile strength distribution, $\{(\sigma_o)_i\}$ i = 1, M; the set $\{(\sigma_o)_i\}$ is assumed to be related one-to-one with the effective flaws $\{(a_o)_i\}$ through the linear fracture mechanics law:

$$(\sigma_o)_i = K/\sqrt{(a_o)_i} \; ; \; i = 1, M \tag{2.3}$$

where K is some constant.

Now, let the $\{(\sigma_o)_i\}$ set be represented by a Weibull failure probability function of the continuous variable σ_o,

$$P_1(\sigma_o) = 1 - \exp\left[-(\sigma_o/\beta_o)^{\bar{\alpha}}_{o}\right] \tag{2.4}$$

The parameters $\bar{\alpha}_o$ and $\bar{\beta}_o$ in (2.4) are implicitly related to α_o, β_o and K in (2.1) through the relationship of (2.3).

When n 90°-plies grouped together, the probability of failure based on a in-series arrangement is given by,

$$P_n(\sigma_o) = 1 - [1 - P_1(\sigma_o)]^n \tag{2.5}$$

which, upon substitution of $P_1(\sigma_o)$ in the form of (2.4), leads to the Weibull function:

$$P_n(\sigma_o) = 1 - \exp\left[-(\sigma_o/\bar{\beta}_n)^{\bar{\alpha}_n}\right] \tag{2.6}$$

where

$$\bar{\alpha}_n = \bar{\alpha}_o \text{ and } \bar{\beta}_n = \bar{\beta}_o(1/n)^{1/\bar{\alpha}_o} \tag{2.7}$$

The second result in (2.7) suggests that the characteristic failure parameter $\bar{\beta}_n$ of n 90°-plies in group is determined by $\bar{\alpha}_o$ and $\bar{\beta}_o$ of the single ply strength distribution in (2.4). In fact, the same result for $\bar{\beta}_n$ can be obtained if the grouped plies are assumed to behave like a bundle arranged in-parallel if the number n in the bundle is small, say $n < 6$ [36].

In view of the specific relationship between the strength σ_o and flaw size a_o, Equation (2.3), it may be assumed that the effective flaw size distribution in grouped plies obeys a volume-rule similar to (2.7). Thus, let the effective flaws of n 90°-plies in group be represented by the random variable a_n; and a_n is determined from a_o and α_o of the single ply by the relationship,

$$a_n = a_o(n)^{2/\alpha_o} \tag{2.8}$$

As for the location distribution $\{(x_n)_i\}$, it is assumed unchanged for any number of 90°-plies grouped together.

It should be emphasized that the volume-law (2.8) for effective flaw size distribution in grouped 90°-plies is only empirical and should therefore be regarded as tentative. Its usefulness remains to be experimentally verified. Further, research based on microscopic examination and statistical mechanics is needed in order to define a flaw representation scheme on more rigorous grounds.

2.4 Shear-Lag Effect on Crack Spacing

When a 90°-ply transverse crack is formed, the local tensile load formally carried by the 90°-ply is now transferred to the adjacent 0°-plies. Because of the interface bonding strength between the 0° and the 90° plies, an interlaminar shear stress τ_{xz} is developed near the transverse crack termini, see Figure 2.9. This shear stress is in fact singular at the crack root but decays exponentially a distance away. As the shear stress decays, the in-situ tensile stress σ_x in the 90°-ply regains its far-field magnitude. The "size" of this local load-transfer zone, known also as the shear-lag zone, is roughly proportional to the total thickness of the 90°-plies which contain the transverse crack. For the $[0/90]_s$ type tensile coupons considered in this section, the shear-lag zone is about 3 times the total thickness of the 90°-plies [37].

The effect of the 90°-ply transverse crack is that it alters the stress state locally. If a 90°-ply flaw is located near the transverse crack, or lie inside its shear-lag zone, the flaw will become less likely to initiate and propagate into a crack. If the flaw is located outside the shear-lag zone, then the presence of the neighboring transverse crack will not have any effect on the behavior of the flaw. Hence, the shear-lag effect indirectly regulates the spacing of transverse cracks. This effect can be seen from the crack density versus load relationships, e.g. shown in Figure 2.6.

Clearly, it is important to include this shear-lag effect either implicitly or explicitly in the predictive model for multiple cracks.

2.5 Formulation of the Simulation Model

The essence of the predictive model is that the transverse cracking process is regarded as a sequence of local events which occur during the course of loading. Each event is a fracture propagation problem involving the growth of a certain effective flaw into a transverse crack. The conditions governing the individual flaw growth depend on the local stress state surrounding the flaw. This also includes the effects of shear-lag zones and the concurrent cracking state in the 90°-ply. Since the sizes $\{a_i\}$ and locations $\{x_i\}$ of the flaws are random, the exact order of the cracking events is actually stochastic in nature.

In what follows, a probabilistic simulation procedure derived from the Monte-Carlo search technique is presented for the transverse cracking process.

Onset of the First Crack. Consider the $[0/90]_s$ type laminate coupon under uniaxial tension. Assume that there are M effective flaws in a unit length of the grouped 90°-plies. The sizes of the flaws ($= 2a_i$) are represented by the set $\{a_i\}$ and their locations by $\{x_i\}$; $i = 1, M$. In this case, all flaws are one-dimensional and lie thickness-wise in the 90°-plies, as shown in Figure 2.8.

Under the applied laminate tension, say a uniform tensile strain $\bar{e}_x$, the largest flaw in $\{a_i\}$, a_{max}, will be the first to propagate into a transverse crack located at x^*. The critical value of $(\bar{e}_x)_{cr}$ for this to happen thus defines the onset load of the transverse crack events.

The determination of $(\bar{e}_x)_{cr}$ is essentially a fracture mechanics problem. As postulated earlier, the individual effective flaw would behave as a small crack. Under the applied tension $\bar{e}_x$ and possibly also a uniform temperature

drop, ΔT, due to laminate curing, the flaw of size $2a_i$ would undergo mode-I propagation. The energy release rate G_I^o which is available at the flaw-tip can be calculated by means of the 2-dimensional generalized plane strain finite element crack-closure procedure as outlined in [11]. Thus,

$$G_I^o(\bar{e}_x, \Delta T, a_i) = [\sqrt{C_e} \cdot \bar{e}_x + \sqrt{C_T} \cdot \Delta T]^2 \, (2t) \tag{2.9}$$

where C_e, and C_T are coefficients depending on the value of a_i and the properties of the particular laminate in question; they are independent of the loads $\bar{e}_x$ and ΔT. The quantity (2t), which is the thickness of one ply, represents the linear scale of the finite element model. That is, in the finite element model, ply thickness is set to a unity.

Onset of flaw propagation is governed by the criterion (1.3), yielding,

$$G_I^o(\bar{e}_x, \Delta T, a_i) = G_{Ic} \tag{2.10}$$

If ΔT is given, it follows that the critical $(\bar{e}_x)_{cr}$ for the formation of the first transverse crack is determined from (2.10) by setting $a_i = a_{max}$, yielding

$$(\bar{e}_x)_{cr} = \frac{\sqrt{G_{Ic}/2t} - \sqrt{C_T} \cdot \Delta T}{\sqrt{C_e}} \tag{2.11}$$

The Propagative Nature of Transverse Crack. In order to see the propagative behavior of a flaw from its initial size $2a_i$ to a full transverse crack, it is useful to examine the behavior of G_I^o in (2.9), which is a function of a. Figure 2.10 shows the mode-I energy release rate, G_I^o, plotted against a, typically for $[0/90]_s$ laminates under uniaxial tension.

It is seen that the available crack-tip energy release rate is a nonlinear function of a. The general behavior is that it increases sharply from initial value of a_i and reaches a maximum at about 3/4 the half thickness of

the 90°-plies (= nt). After this point, a decrease in G_I^o is effected as the crack propagates near the 0/90 interface. Presumably, the crack is then arrested at the interface.

If the initial size a_1 is smaller than 3/4 of (nt), onset of propagation is determined by equating $G_I^o(a_1)$ to G_{Ic} according to (2.10). When the flaw size starts to increase from a_1, the available G_I^o becomes larger than G_{Ic}. Consequently, the propagation is unstable, according to the stability criterion of (1.4).

The excess energy (the shaded area in Figure 2.10) released during the unstable propagation may result in local damages at the 0/90 interface near the crack termini. This subject will be further discussed in a later chapter. But, it is noted that the amount of the excess energy increases with the number of the 90°-plies, n. It may thus be inferred that the level of damage following the transverse crack arrestment at the 0/90 interface increases with the number of the 90°-plies grouped together.

Simulation of Multiple Cracks. In the foregoing, the conditions for determining the critical onset load for the first transverse crack have been established. After the formation of the first crack, all future cracks will form from the remaining flaws. But, the sizes of the remaining flaws are smaller than the first, and some of the flaws may now be under the influence of the shear-lag effect from the first crack. Now, let G_I^o be the available energy release rate at the tip of a flaw if it is outside the influence of shear-lag, while G_I be the energy release rate if it is inside the shear-lag zone. Then, the value of G_I is smaller than G_I^o and G_I is expressible in the form

$$G_I(\bar{e}_x, \Delta T, a) = R(s) \cdot G_I^o(\bar{e}_x, \Delta T, a) \qquad (2.12)$$

where R(s) is a reduction factor representing the effect of shear-lag. Depending on the distance s between the flaw and the first crack, R(s) has a value in the interval (0, 1), see Figure 2.11.

The curve shown in Figure 2.11 can be numerically generated by the same finite element procedure by including the presence of a transverse crack in the calculation of G for the considered flaw; see inset of Figure 2.11.

Hence, for all the remaining flaws in $\{a_i\}$, minus a_{max}, the one flaw that gives the largest G_I will be the next to propagate into a transverse crack. This is accomplished most routinely by a computer search [12]. Then, the corresponding applied laminate tension, $\bar{e}_x$, for this flaw to propagate is determined again from the fracture condition,

$$G_I(\bar{e}_x, \Delta T, a) = G_{IC} \tag{2.13}$$

given the values of ΔT and a associated with the flaw.

Note that $\bar{e}_x$ determined from (2.13) is larger than $(\bar{e}_x)_{cr}$ determined for the first crack, because a is smaller than a_{max} and the flaw may be under the influence of the shear-lag of the first crack.

As for subsequent cracks, they can be similarly determined from the remaining flaws. The corresponding laminate strains are found through solving equations similar to (2.13). However, a flaw located between two adjacent transverse cracks, will be subjected to a shear-lag effect from each crack. In such cases, the available energy release rate at the flaw tip is expressed as

$$G_I(\bar{e}_x, \Delta T, a) = R(s_\ell) \cdot G_I^o(\bar{e}_x, \Delta T, a) \cdot R(s_r) \tag{2.14}$$

where s_ℓ and s_r are distances from the flaw to the left crack and to the right crack, respectively.

Successive searches for the most energetically possible flaws to become transverse cracks provide a load-sequence for the multiple cracks formation process. The searching procedure mimicks the cracking process as it would occur naturally. Since each simulation begins by generating a set of M random numbers used to define the flaws in the 90°-plies, the random number set may be considered in a sense as a test specimen. Generations of several random number sets can be used to simulate replicate test specimens. In this manner, the scattering property of transverse cracks in a sample of replicates can also be simulated.

2.6 Illustrative Examples

With the modelling procedure outlined in the preceding section, the method can now be illustrated by several experimental examples. Consider first the T300/934 laminate family $[0/90_n/0]$, n = 1, 2, 3 and 4 under uniaxial tension. The basic ply properties of the unidirectional system have been previously given in Table II-1, and the growth data for multiple cracks under increasing laminate tension were shown earlier in Figure 2.6. From this crack growth data, the experimental onset load for transverse cracking for each value of n can be determined. These are listed in Table II-2.

Determination of Effective Flaw Distributions. The first step in the modelling is to determine the effective flaws in the basic 90°-ply as a ply property. To do so, a correlation is performed between the predicted and the experimental crack-density versus applied load relationships. From Figure 2.6, it is noted that in the case of n = 1 there was no noticeable transverse cracks formed prior to laminate final rupture. But for n = 2, 3 and 4, sufficient number of transverse cracks are recorded. For the illustrative examples to be discussed in this section, the effective flaw distribution in the 90°-ply will be determined using the data curve for n = 2. It will be

assumed here that two (2) 90°-plies grouped together shall be a basic unit; the flaws in its thickness are denoted by the set $\{(a_2)_i\}$. Then, according to the volume-law proposed in Equation (2.8), the flaw sizes for n = 3 and n = 4 are represented by

$$(a_n)_i = (a_2)_i \, (n/2)^{2/\alpha_2} \; ; \quad n = 3, \, 4 \tag{2.15}$$

where α_2 is the shape parameter of the distribution function for $\{a_2\}$.

Now, assume there are M flaws in each unit length of the basic 90°-ply; and there are M locations $\{x_i\}$ in a unit length. The set of flaw locations, $\{x_i\}$, is obtained from a suitable random number generator that yields M values in the interval (0, 1). These same values are also used in conjunction with the assumed flaw distribution function of the Weibull form, Equation (2.1), in the following way: by letting F equal to each of the discrete values of $\{x_i\}$ and by guessing the parameters α_2 and β_2 (the subscript 2 denotes two 90°-plies grouped together), a discrete set $\{(a_2)_i\}$, i = 1, M, is obtained from solving (2.1).

With $\{x_i\}$ and $\{(a_2)_i\}$ defined, simulation of the transverse crack process may begin. Detailed calculations in the simulation will be presented later in this section; but it is sufficient to state here that correlations between the simulated results and the experimental data finalize the values of α_2 and β_2 and the value of M. For the data shown for n = 2 in Figure 2.6, this procedure yielded, by best fit, for the following values:

$$\begin{aligned} &M = 32 \text{ crack/cm} \\ &\alpha_2 = 4; \; \beta_2 = 0.96t \end{aligned} \tag{2.16}$$

Now, let the largest flaw in $\{(a_2)_i\}$ be in the top 3% rank, or the 97-percentile in the flaw size cumulative function (2.1); it follows that

$$(a_2)_{max} = 1.31t \tag{2.17}$$

Using the volume-law of (2.15), the maximum flaw size for the cases of n = 3 and n = 4 are represented respectively by:

$$\begin{aligned}(a_3)_{max} &= 1.61t \\ (a_4)_{max} &= 1.85t\end{aligned} \tag{2.18}$$

Determination of Onset of Transverse Cracking. By using the ply stiffness properties of the T300/934 graphite/epoxy system listed in Table II-1, the strain energy release rate coefficients C_e and C_f that appear in Equation (2.9) are generated numerically for each value of n. These coefficients are shown, respectively, in Figures 2.12 and 2.13 as functions of the half flaw size a. To predict the critical tensile load for onset, Equation (2.11) is used in which the coefficients C_e and C_f take their values at $a = a_{max}$. These values are listed in Table II-3. Note that for the case of n = 1, a_{max} could not be determined; so the maximum available energy release rate G_{max} is used for prediction.

Finally, by assigning $2t = 132 \times 10^{-6}$m, $\Delta T = 125°C$ and $G_{Ic} = 228$ J/m^2 (Table II-1) solving Equation (2.11) yields the critical strain $(\bar{e}_x)_{cr}$ for each case of n. The predicted results and those found experimentally (see Table II-2) are compared below:

n	$(\bar{e}_x)_{cr}$, Predicted	$(\bar{e}_x)_{cr}$, Experiment
1	1.05%	(> 1.0%)
2	0.68%	0.66%
3	0.58%	0.61%
4	0.52%	0.52%

For all practical purposes, the prediction is satisfactory both in magnitude and in trend.

Simulation of Multiple Cracks. Since the results shown in Figure 2.6 are from the initial portion of the transverse cracking process, it is insufficient for a complete simulation. Instead, the experimental data reported recently in Reference [38] will be used next. In that experiment, a series of T300/934 graphite-epoxy laminates in the form of $[0_2/90_{2n}/0_2]$, n = 1, 2 and 4, were tested under uniaxial tension. This family of laminates is identical in stacking sequence as the $[0/90_n/0]$ family considered in the earlier examples, but the thicknesses of the layers of like fiber orientation are now doubled. As it will be shown shortly, the doubling of the layer thickness permits early onset of transverse cracks in the 90°-plies. Consequently, complete development of transverse cracks is obtained before the other complicating failure modes occur.

Figure 2.14 shows the experimental crack density versus the applied laminate stress $\bar{\sigma}_x$ curves for each n in the $[0_2/90_{2n}/0_2]$ family. For each n, there were four replicate specimens tested; and a finite-width scatter band is obtained and displayed. Note that for each n, a transverse crack density saturation limit is reached before final laminate failure. The random search procedure outlined earlier will now be used to simulate this result.

The T300/934 Graphite-epoxy ply constants listed in Table II-1 are used in all computations. In fact, the energy release rate curves for G_e and G_f shown in Figures 2.12 and 2.13 are also used in the present $[0_2/90_{2n}/0_2]$ cases. Since layers of like fiber orientation are now doubled, the curves in Figures 2.12 and 2.13 can be used to compute G_I^o in equation (2.9) by replacing 2t by 4t. Then, all other equations remain unchanged, except the size distribution function for the effective flaws.

As the effective flaws in the basic plies (two 90°-plies grouped together) were already determined, see (2.16), it is necessary only to follow the volume-law to define the flaw sizes in 90°-layers of more than two plies.

Note that in this laminate series, with n = 1, 2, and 4, the numbers of the grouped 90°-plies are, respectively, 2, 4, and 8. The effective flaw size for the cases of n = 1, 2 and 4 should now be determined by,

$$(a_{2n})_i = (a_2)_i \, (n)^{2/\alpha_2} \quad ; \quad n = 1, 2 \text{ and } 4 \tag{2.19}$$

It will be assumed that for each case of n, there are M = 32 flaws per 1 cm as before. The flaw locations are again represented by a set of M random values in the interval (0, 1). To include the shear-lag effect, the energy reduction factor R(s) must be generated independently. The R(s) factor for $[0_2/90_{2n}/0_2]$ is represented by a single function in terms of s and n:

$$R(s, n) = 1 - 1.0056 \exp [-0.3888s/n\ t] \tag{2.20}$$

Equation (2.20) is graphically displayed in Figure 2.15.

Now, all the elements for the simulation are now given: the value of M, the flaw size distribution $\{a_i\}$ for any value of n, the flaw location distribution $\{x_i\}$, the energy release rate coefficients C_e, and C_T and the energy reduction factor R(s, n). By following the outlined search procedure, 90°-layer crack development is simulated as a function of ascending laminate stress $\bar{\sigma}_x$, or strain $\bar{e}_x$. The computer routine utilized incorporates a Monte-Carlo type search procedure, the detail of which has been described in [12].

For each $[0_2/90_{2n}/0_2]$ laminate type, four or five replicate simulations are performed (each simulation represens a specimen). Because of the discrete nature of the random numbers, specimens so represented are slightly different from one another. Consequently, repeated simulations also give rise to a

scatter band in the results.

Figure 2.16 shows the simulated transverse crack density versus the applied (tensile) laminate stress $\bar{\sigma}_x$ for four specimens of n = 1. It is seen that the simulated results form a narrow scatter band and agree closely with the band obtained by actual experiment.

Similar comparisons for the laminates of n = 2 and 4 are displayed in Figure 2.17 and Figure 2.18, respectively. Here, again, the simulated results agree reasonably well with the experiment both in trend and in scatter. Note that the scatter band in the simulated results stems from the random numbers scheme used, whereas the scatter band in the experimental data is due to physical factors such as the random property of the basic composite material system and the randomness in the laminate curing procedure, specimen handling practice, the test method, etc. In the illustrations shown in Figures 2.16 to 2.18, no special effort was made to correlate in any way the scatter between the simulated and the experimental results.

2.7 Effects of Thermal Residual Stresses

In the example problems considered so far, the effects of thermal residual stresses have been included implicitly in the analysis. It is interesting to examine these effects explicitly in some detail. Figure 2.19 shows the in-situ tensile stress σ_x in the 90°-plies at the onset of the first transverse crack for each n value in the $[0/90_n/0]$ family. The calculated σ_x stress contains the contributions from both the thermal cooling of ΔT and the mechanical loading, $\bar{e}_x$.

It is seen that the total in-situ σ_x is not constant with respect to n, but decreases sharply with increasing n. Although the in-situ σ_x is directly responsible for the formation of transverse cracking, it is not a useful strength measure for the 90°-ply. Thermal cool down following fabrication

curing induces about 25% to 40% of the total in-situ σ_x, depending on the value of n.

The thermal stress contribution to the total strain energy release rate is associated with the coefficients G_T in Equation (2.9). Note that G_I^o is composed of three parts: G_e, G_T and G_{eT} representing, respectively, the energy due directly to the applied tension $\bar{e}_x$, the temperature drop ΔT and the coupled energy involving both $\bar{e}_x$ and ΔT. Figure 2.20 displays the values of the parts G_e, G_T and G_{eT} for the considered laminate family when the first crack is formed. Note that, at onset of the crack, G_I^o is equal to G_{IC} and G_{IC} is independent of n.

Since the sum of G_T and G_{eT} is attributable to the thermal effects, its share in the total energy release rate can be as much as 40% to 65%, depending on the value of n.

Clearly, the thermal effects are important and must be included in the cracking analysis. Furthermore, the thermal stress effect and the applied stress effect on the total strain energy required for cracking are not simply additive. This is fundamentally different from the failure criterion based on strength. In the latter, thermal and mechanical stresses are linearly additive.

2.8 Summary

In this chapter, an analysis method was presented for the formation process of intraply matrix cracks in the form of 90°-ply transverse cracking.

The underlining assumption of the method is that successive cracks in the 90°-ply under transverse tension are due to the propagation and the arrestment of material flaws which distribute randomly in the 90°-ply. The analysis entails two essential elements, the first being the proper representation of the material flaws as an inherent ply property, and the second being the

establishment of a logical criterion determining the exact loading condition at which a particular flaw becomes a transverse crack.

The representation of material flaws is based on a set of assumed effective flaws for the basic material ply. As such, the effective flaws do not have real physical identity but their effect results in the macroscopic characteristics of the multiple cracking observed in experiment.

Once the effective flaw distribution for a 90°-ply having a reference thickness is known, the effective flaws in several 90°-plies grouped together can be determined by means of a statistical volume-law. The law suggested by Equation (2.8), while plausible, is essentially empirical. Further research is needed in order to formulate a volume-law on more rigorous grounds.

As for the formation of transverse cracks, the classical fracture mechanics criterion is employed. It is assumed that each of the effective flaws behaves like a small crack. Onset of its propagation defines the transition from a flaw to a transverse crack; and its arrestment at the 0/90 interface completes the formation.

The calculation of the strain energy release rate associated with a flaw/crack propagating in the thickness of the 90°-plies is accomplished by a finite element procedure based on ply elasticity. The procedure is a numerical alternative for problems having complex geometrical constraints, along with other peculiarities such as the inclusion of thermal effect, shear-lag effect, etc.

Because the effective flaws in the 90°-plies are random in size and location, successive flaw/crack transitions under the applied load constitute a stochastic process. A search procedure is used for the simulation of multiple cracks as a function of continued loading.

In addition to the logical development of the analytical model, the influence of the lamination parameters on the model are also addressed. These parameters are found to play an important role in the crack formation processes. For example, the effects of lamination stacking sequence, the actual ply thickness, etc., are implicitly contained in the predictive model. By varying these parameters both in the model simulation and in the experiments, their influence can be quantified and the reliability as well as the generality of the analytical model can be evaluated.

At the conclusion of this chapter, it is noted that the effective flaw concept results in physically correct behavior although the actual representation of the flaws remains a subject for further refinement. This also includes the empirically derived volume-law for flaws in grouped 90°-plies.

TABLE II-1

Material Constants for T300/934 Unidirectional Ply*

Property	SI Unit	English Unit
E_{LL}	144.8 Gpa	21×10^6 psi
E_{TT}, E_{zz}	11.7 Gpa	1.7×10^6 psi
ν_{LT}, ν_{Lz}	0.3	0.3
ν_{Tz}	0.54	0.54
G_{LT}, G_{Lz}	6.5 Gpa	0.94×10^6 psi
G_{Tz}	3.5 Gpa	0.5×10^6 psi
α_T, α_z	28.8×10^{-6}/°C	16.10^{-6}/°F
α_L	$0.36.10^{-6}$/°C	0.2×10^{-6}/°F
σ_L, long. tensile strength	1720 mpa	250 ksi
σ_T, trans. tensile strength	44 mpa	6.5 ksi
2t, nominal ply thickness	0.132 mm	0.0052"
ΔT, temperature drop	125°C	225°F
G_{Ic} (0/0 interface)**	158 J/m^2	0.9 in-lb/in^2
G_{Ic} (90/90 interface)**	228 J/m^2	1.3 in-lb/in^2
$G_{(I,II)c}$, $G_{II}/G_I = 0.5$**	288.75 J/m^2	1.65 in-lb/in^2

*Data taken from Reference [29].

**See discussions in Reference [11].

TABLE II-2

Onset of Transverse Cracking in $[0/90_n/0]$ Laminate Family*

Laminate	Experimental Axial Stiffness	Experimental Onset Stress	Experimental Onset Strain
[0/90/0]	95.8 GPa	>950 MPa	>1.00%
$[0/90_2/0]$	78.2 GPa	520 MPa	0.66%
$[0/90_3/0]$	64.9 GPa	400 MPa	0.61%
$[0/90_4/0]$	55.8 GPa	290 MPa	0.52%

*Data taken from Reference [32]

TABLE II-3

Maximum Flaw Size and Energy Release Rate for $[0/90_n/0]$

n	a_{max}	G_e, $10^9 J/m^3$	G^T, $J/m^3/c^2$
1	--	9.4*	6.5*
2	1.31t	17.0	11.5
3	1.61t	22.0	14.0
4	1.85t	25.0	15.2

*Maximum value is used.

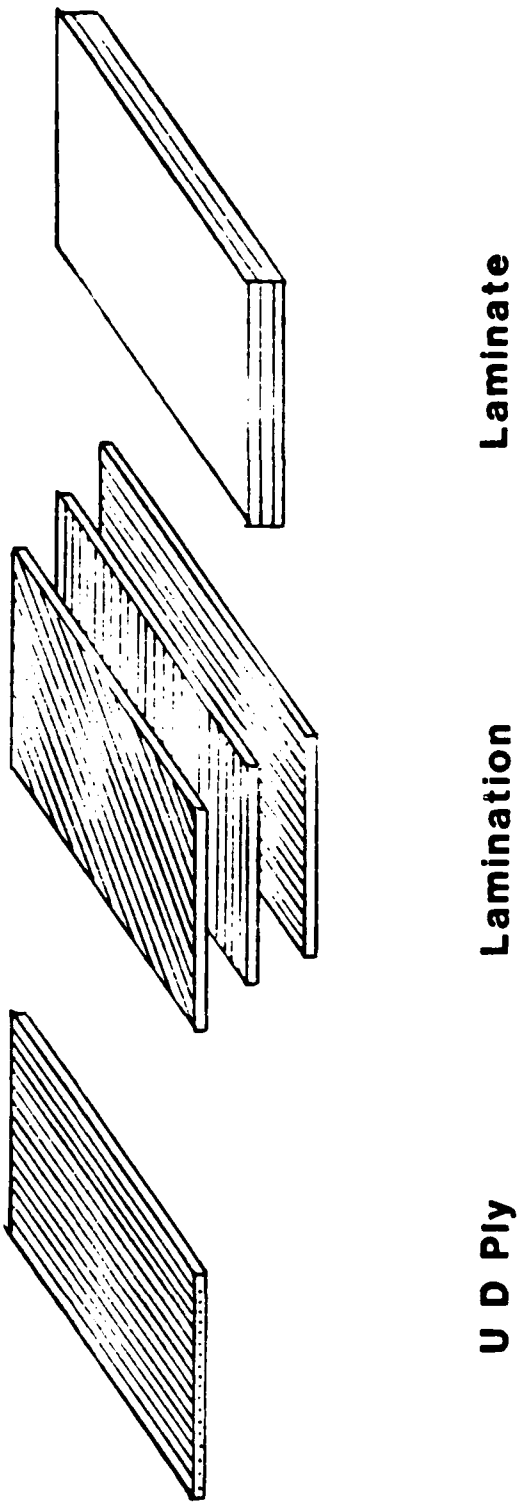

Figure 2.1 The Reinforcement Structure of Laminates Made of Unidirectional Plies.

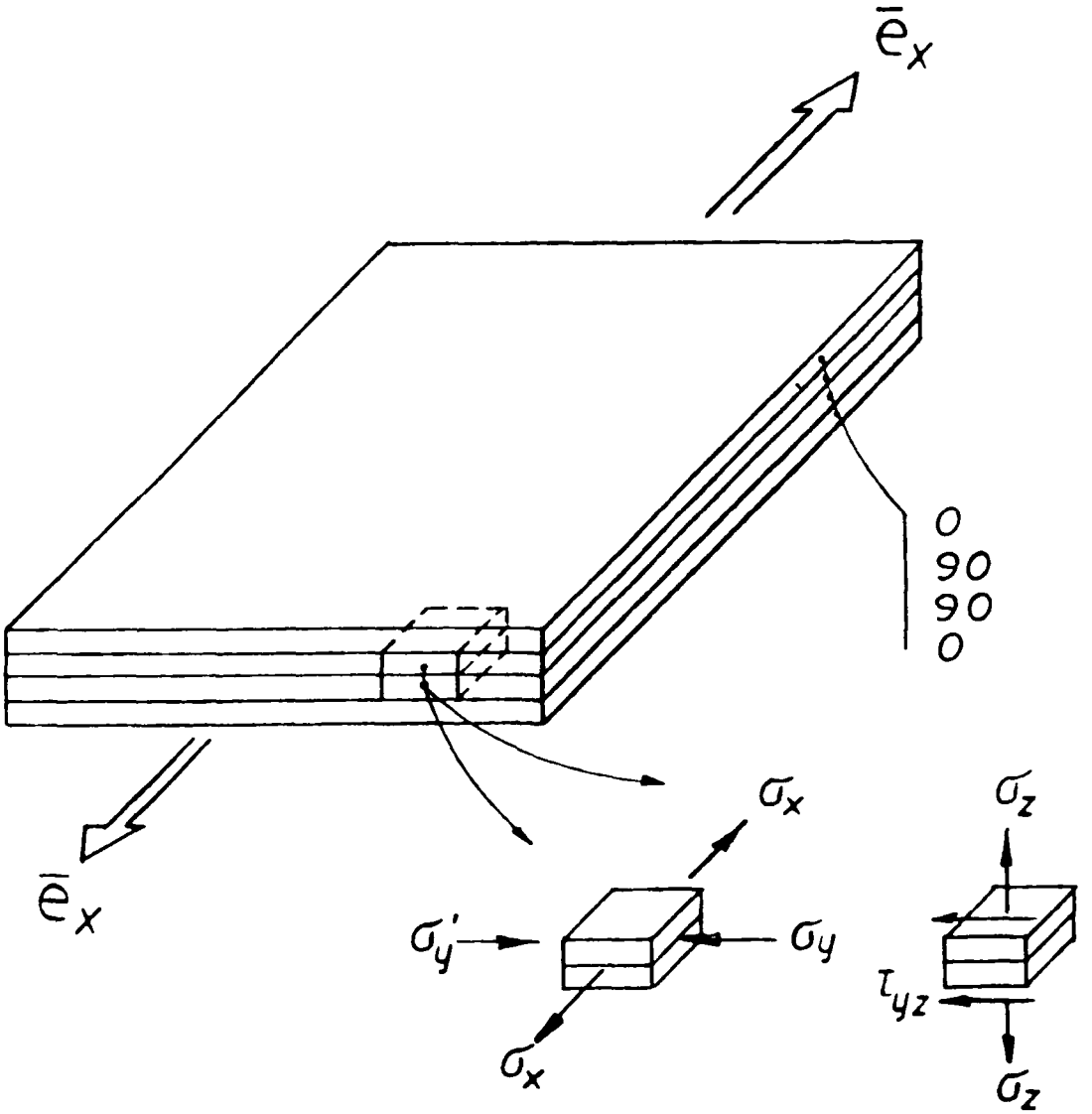

Figure 2.2 In-Ply and Interply Stresses Near the Free Edge of the $[0/90]_s$ Laminate Under Tension.

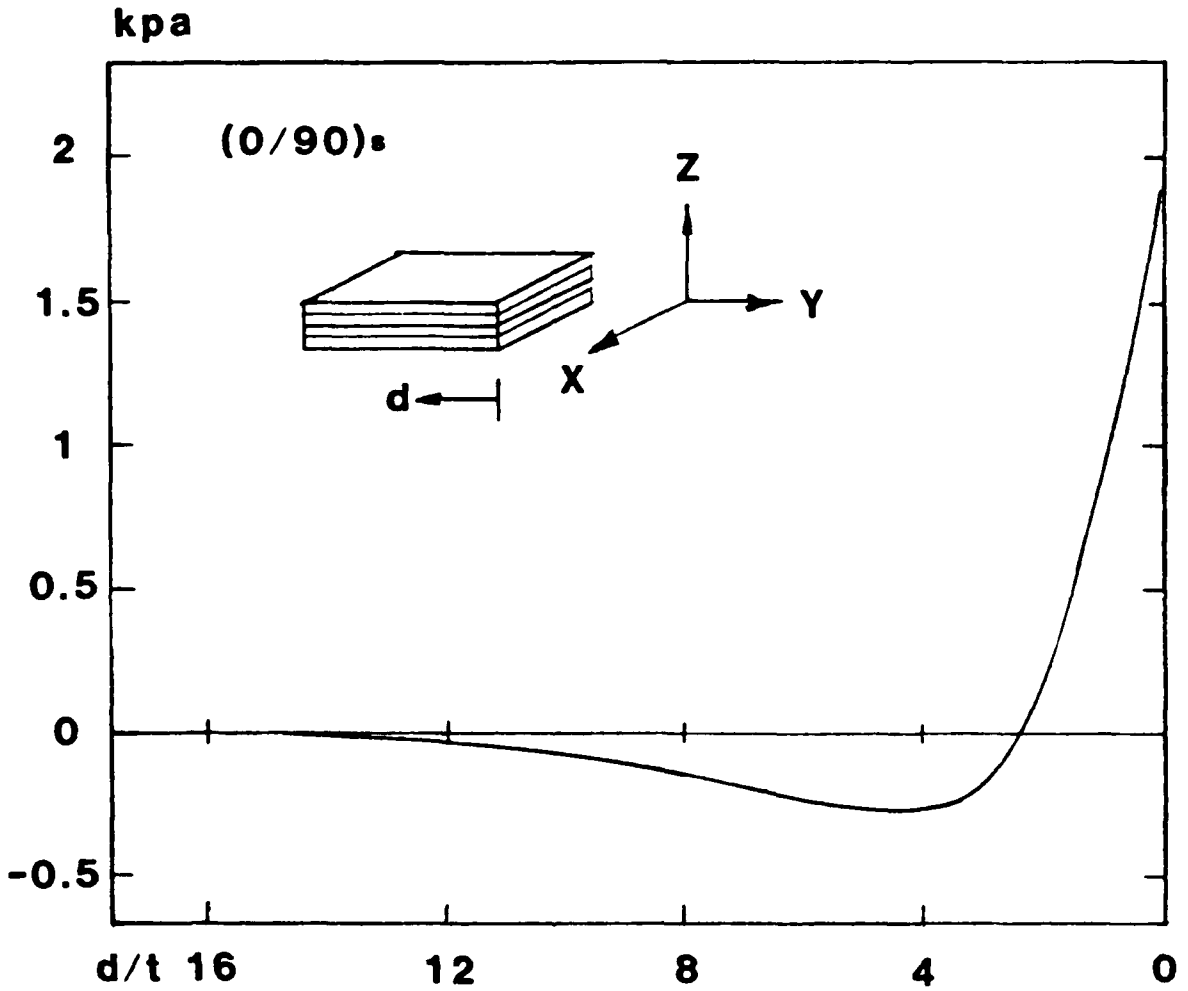

Figure 2.3 Interlaminar σ_z (in kpa/με) on Laminate Mid-Plane as a Function of Distance From Free Edge $[0/90]_s$.

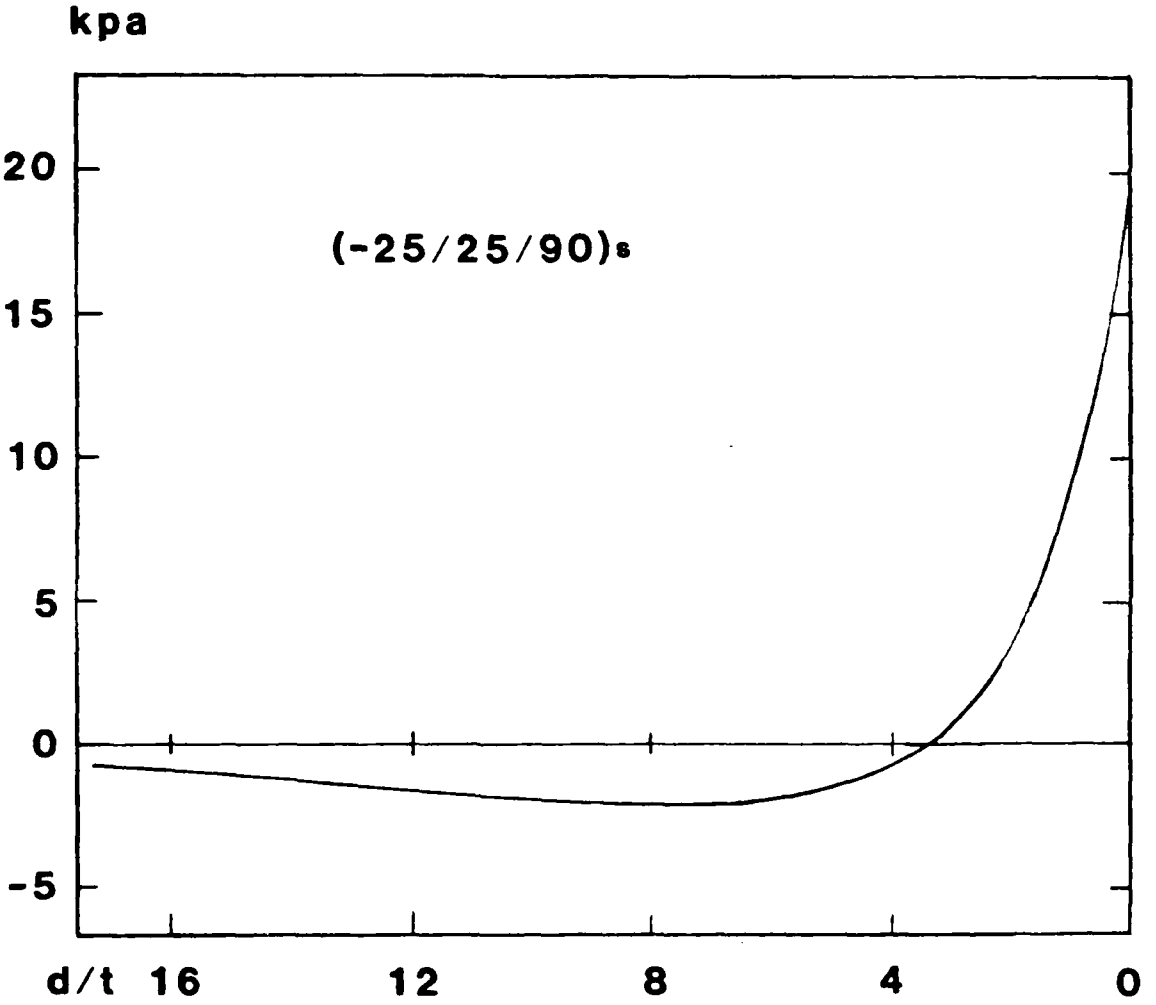

Figure 2.4 Interlaminar σ_z (in kpa/με) on Laminate Mid-Plane as a Function of Distance From Free Edge $[\pm 25/90]_s$.

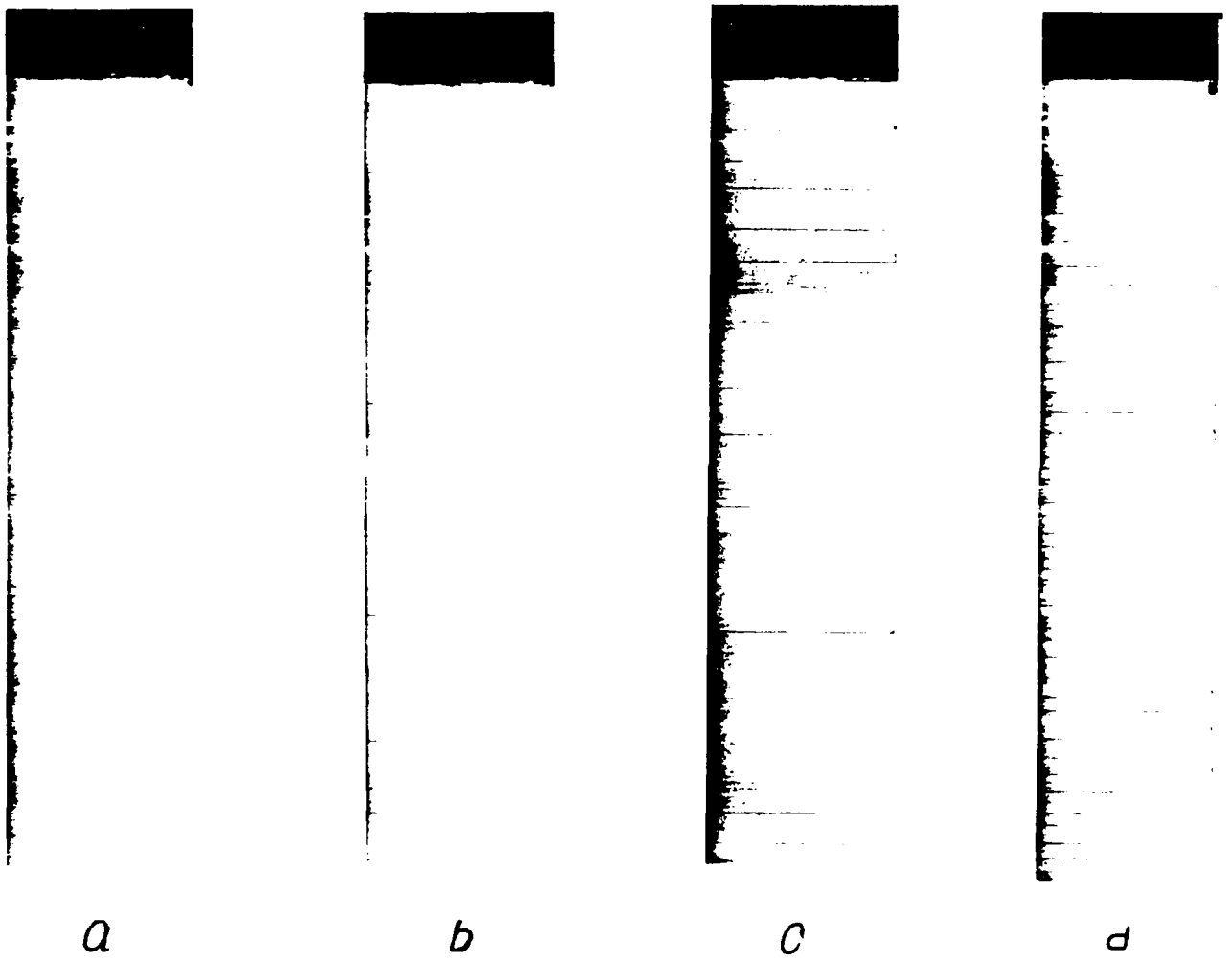

Figure 2.5 X-Radiographs Showing Transverse Cracks Formation Under Increasing Tension.

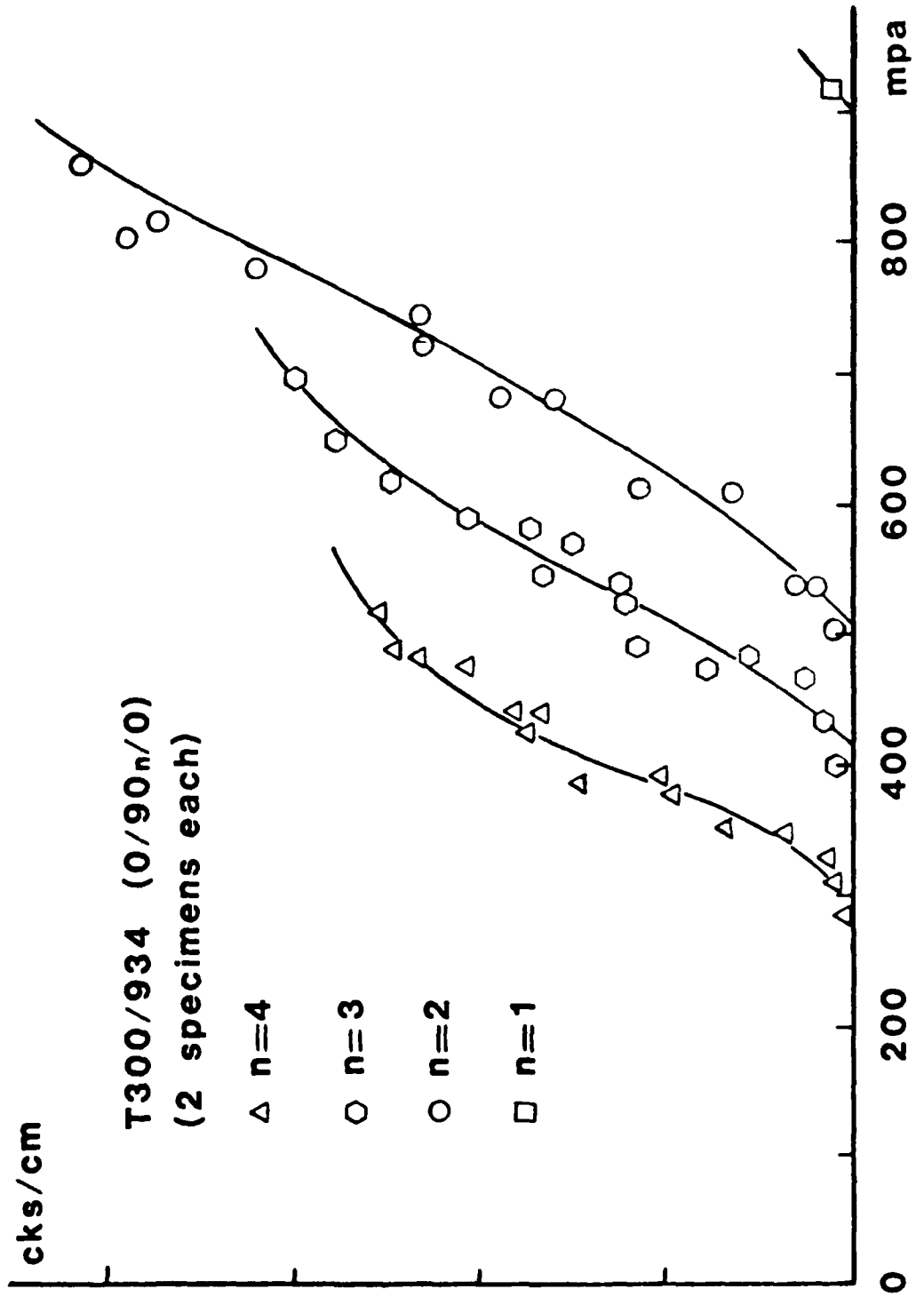

Figure 2.6 Experimental Crack-Density versus Laminate Tension Relations for the $[0/90_n/0]$ Laminate Family.

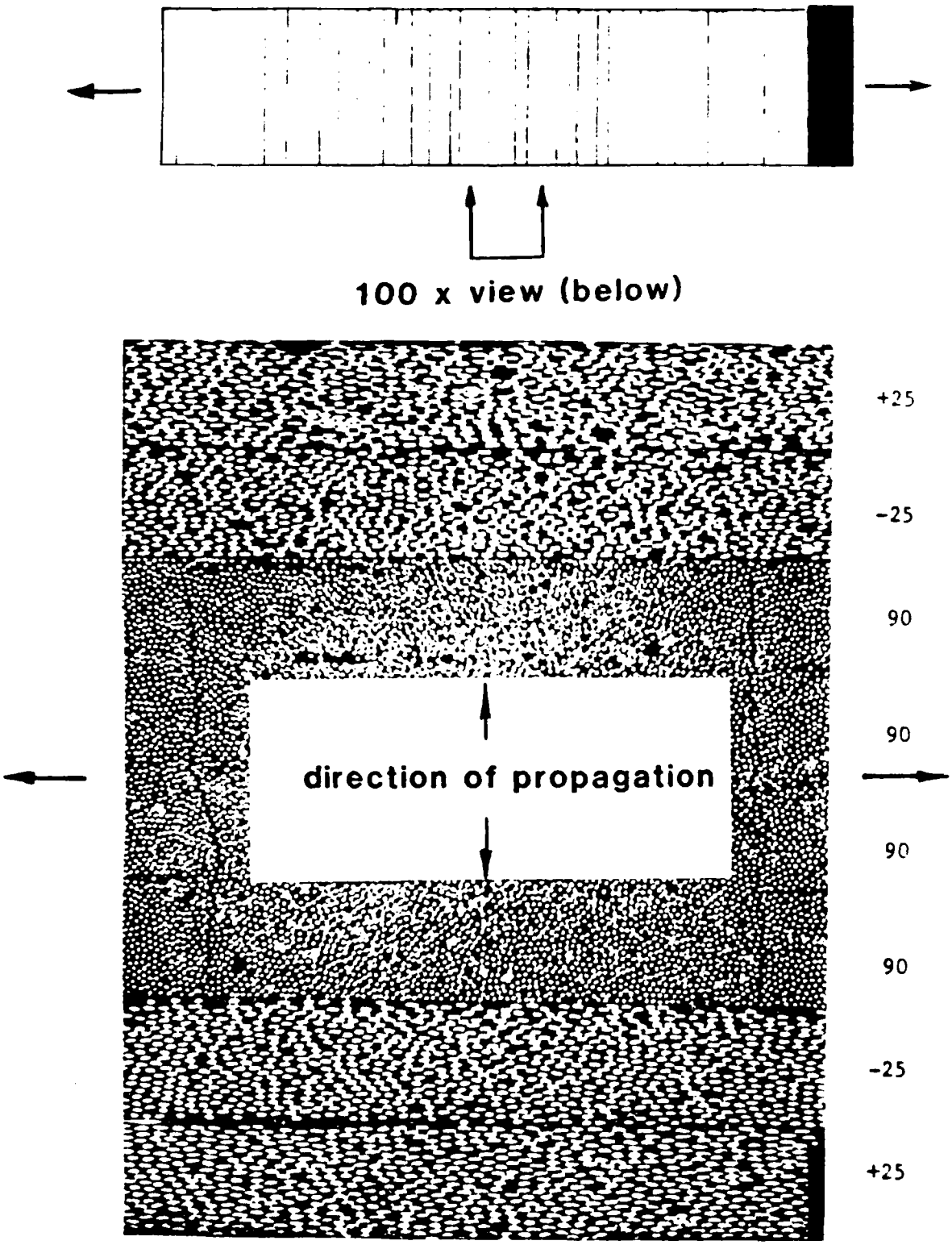

Figure 2.7 An X-Radiograph and a Thickness View Photo-Micrograph of Transverse Cracks in a $[\pm 25/90_2]_s$ Laminate.

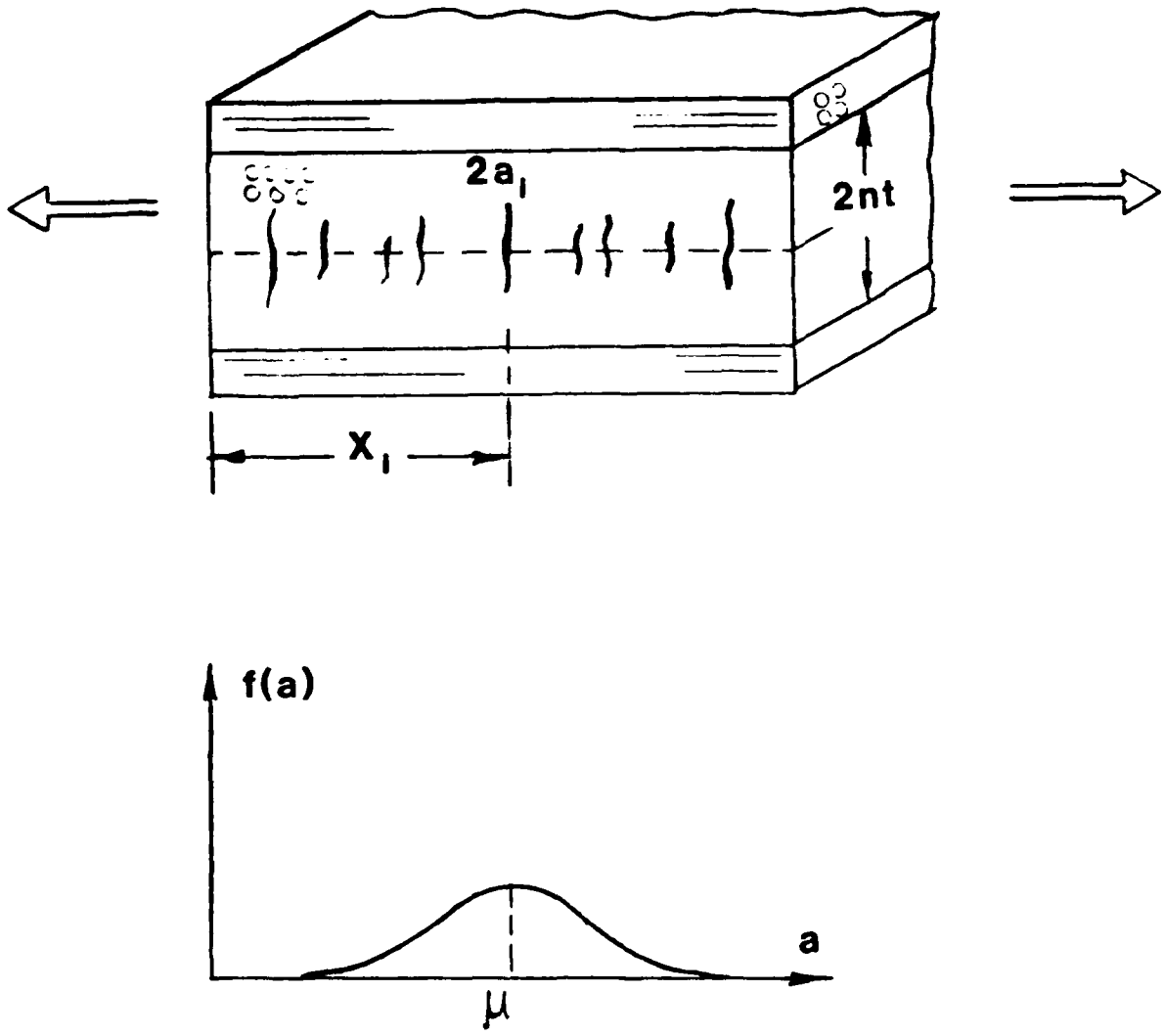

Figure 2.8 The Distribution of Effective Flaws in the $[0/90_n/0]$ Laminate Family.

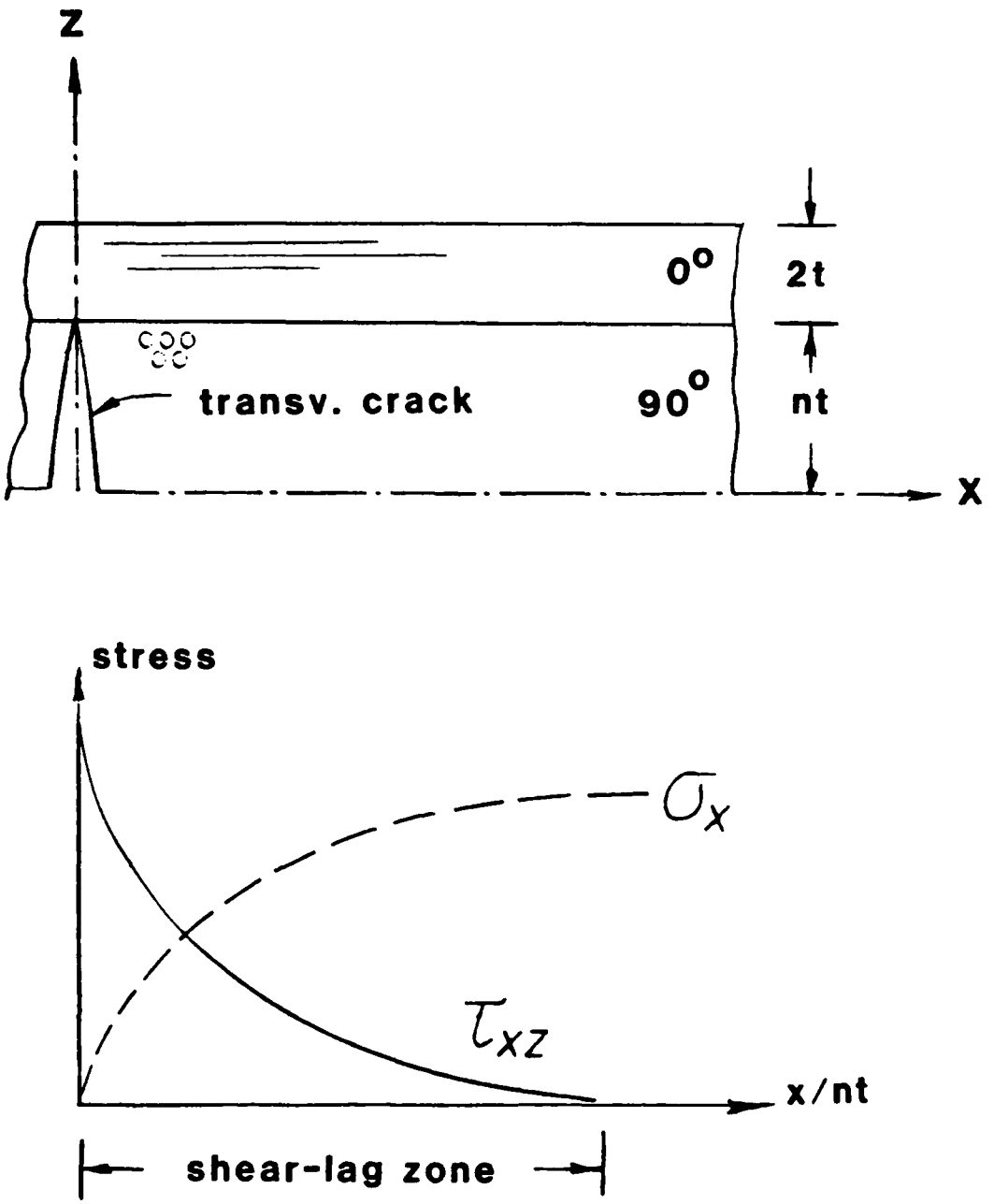

Figure 2.9 The Formation of Shear-Lag Zone.

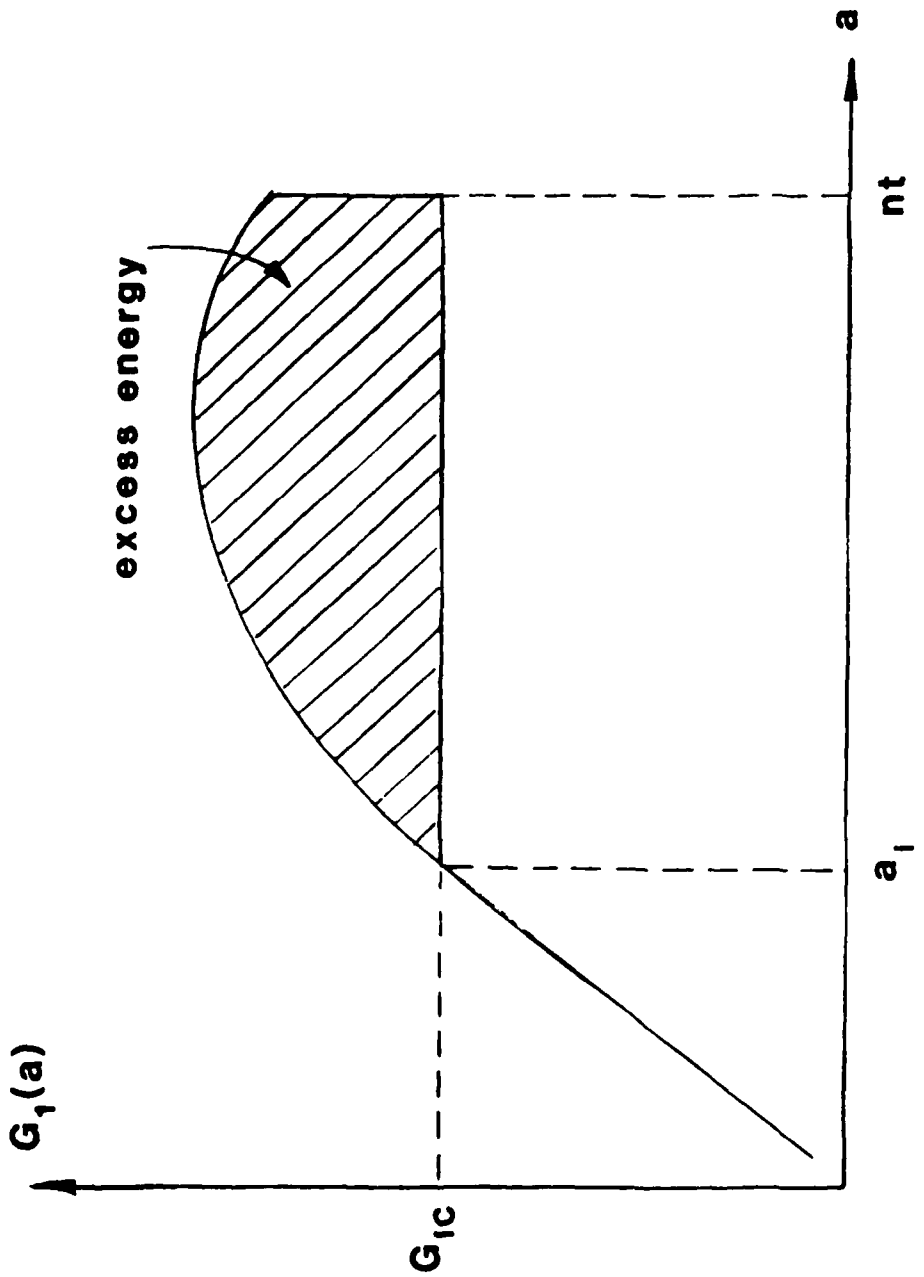

Figure 2.10 Excess Energy Release Rate Given Off by a Transverse Crack Propagating in Thick 90°-layer.

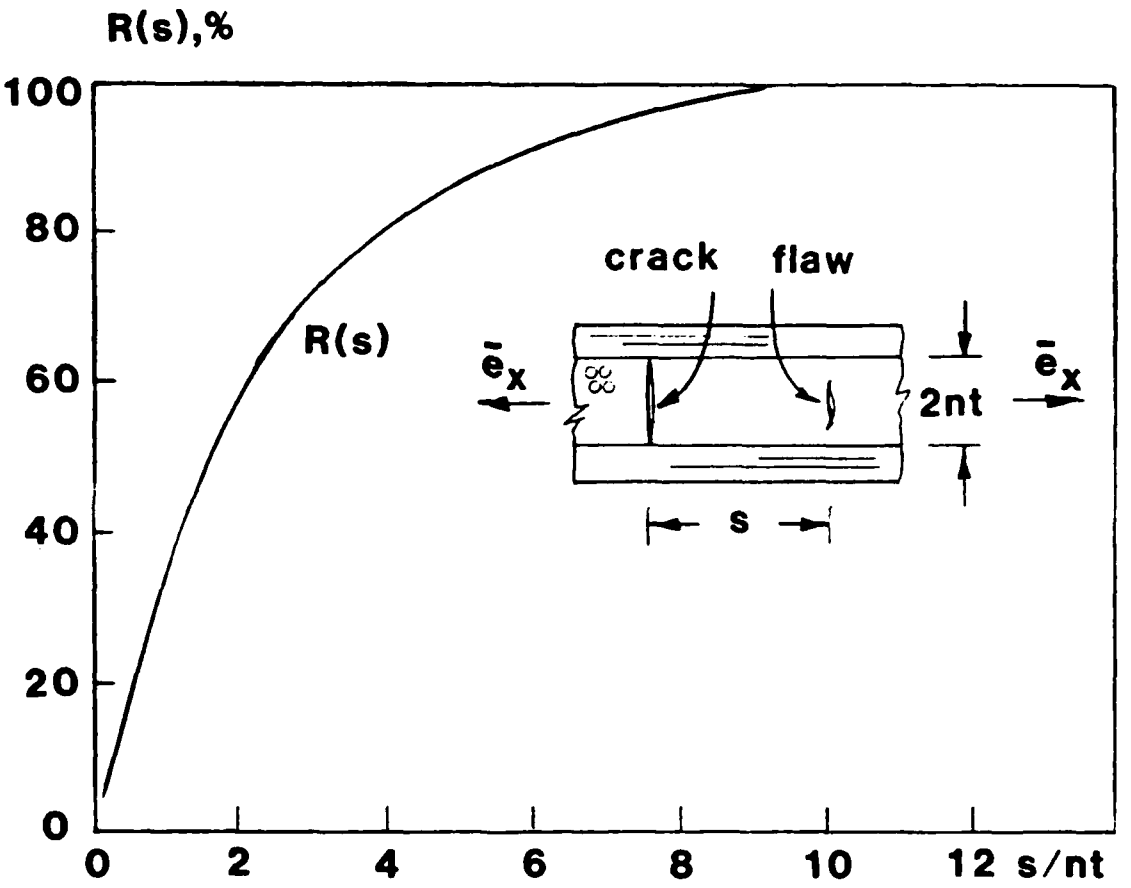

Figure 2.11 Energy Release Rate Retention Factor R(S) for the $[0/90_n/0]$ Laminate Family.

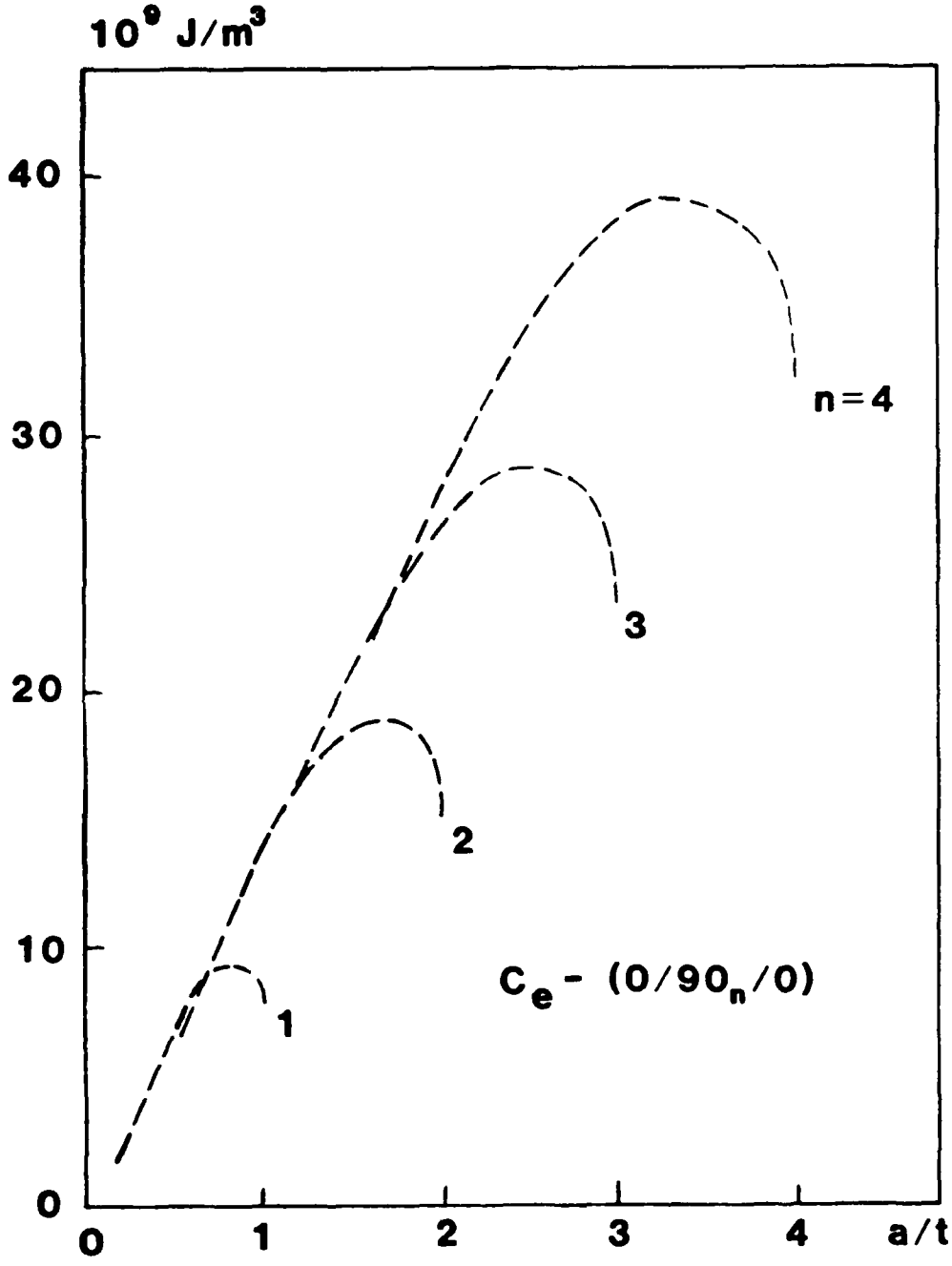

Figure 2.12 Energy Release Rate Coefficient C_e for the $[0/90_n/0]$ Laminate Family.

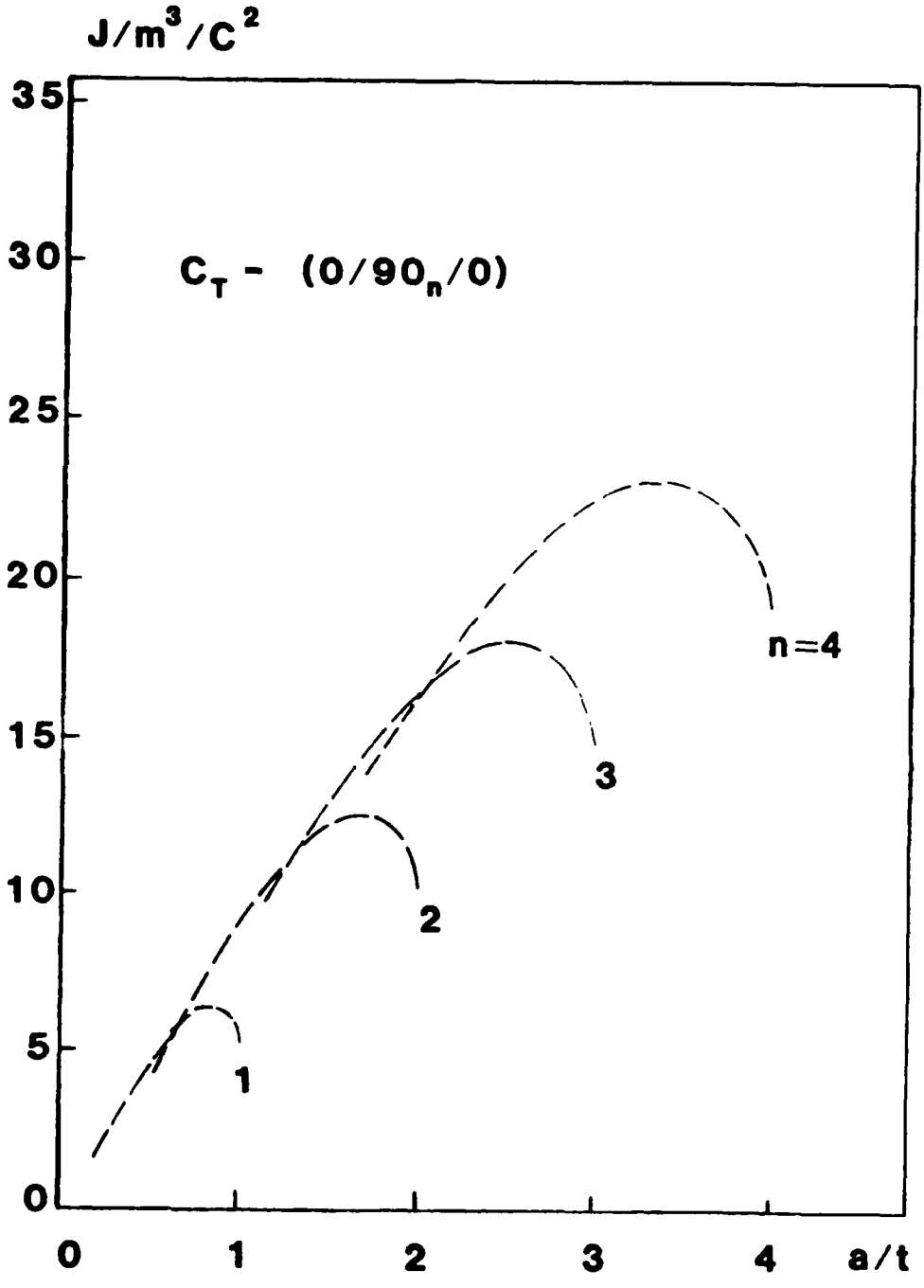

Figure 2.13 Energy Release Rate Coefficient C_T for the [0/90$_n$/0] Laminate Family.

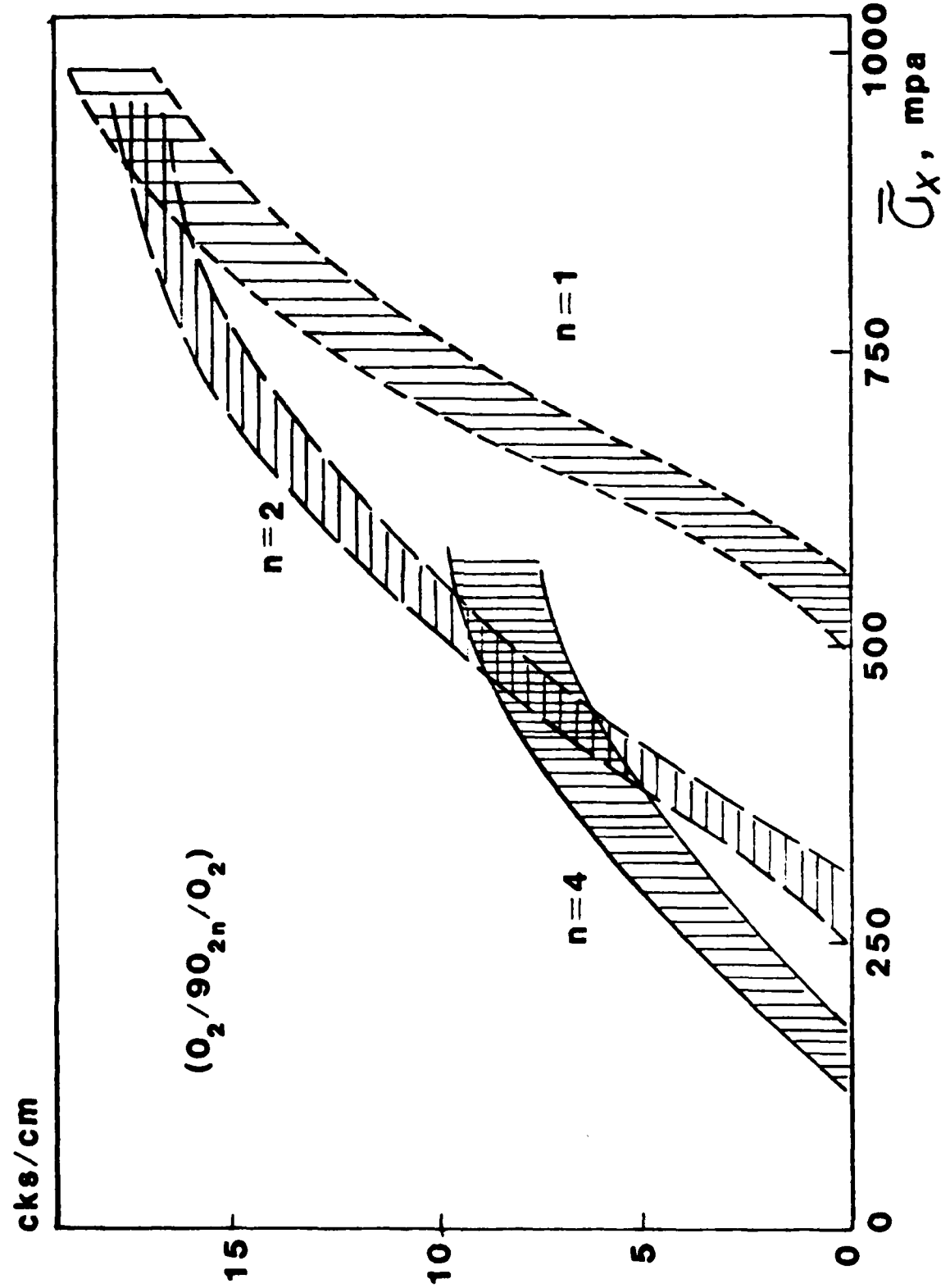

Figure 2.14 Experimental Crack-Density versus Lamination Relations for the $[0_2/90_n]_s$ Laminate Family.

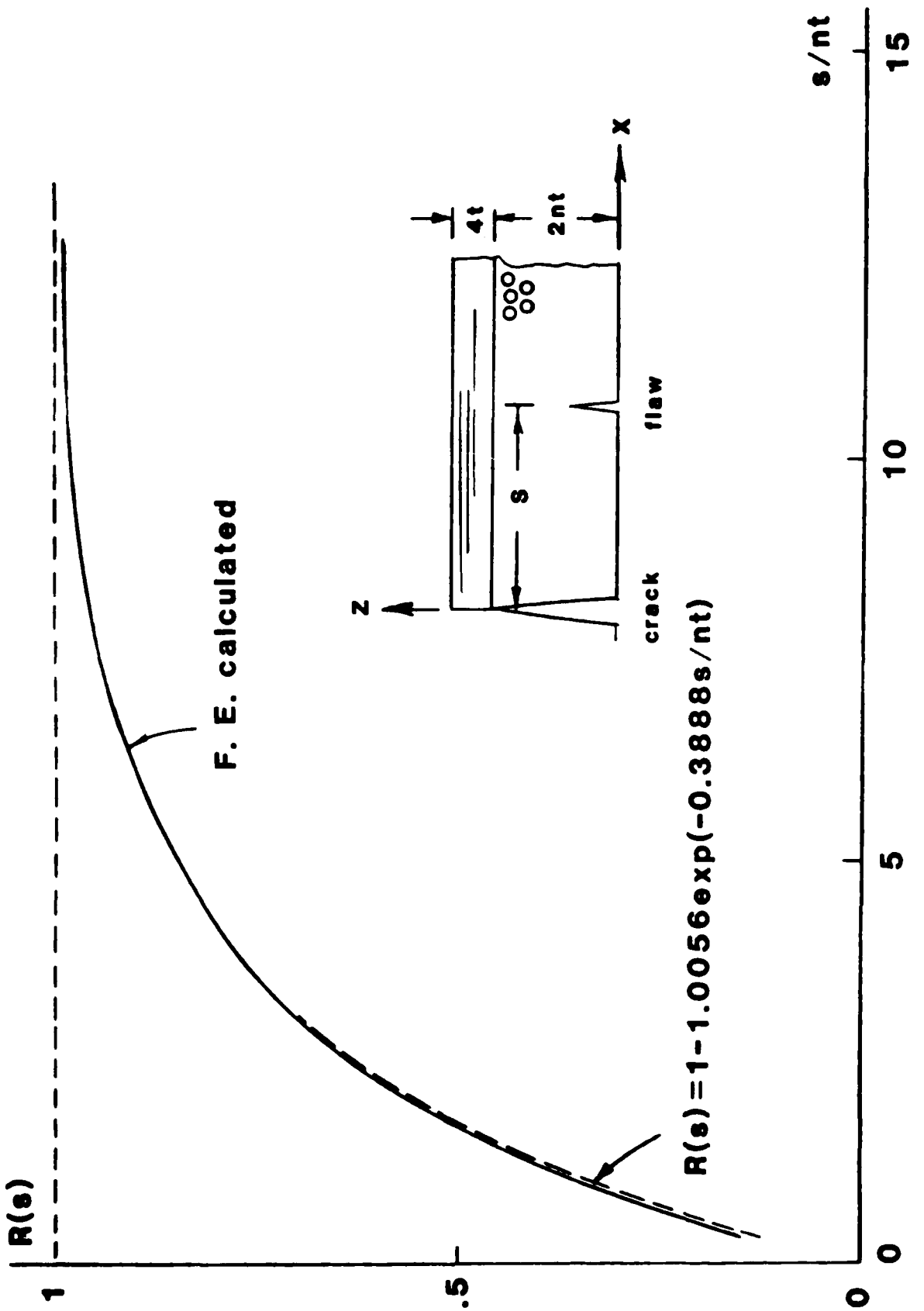

Figure 2.15 Energy Release Rate Retention Factor R(S) for the $[0_2/90_n]_s$ Laminate Family.

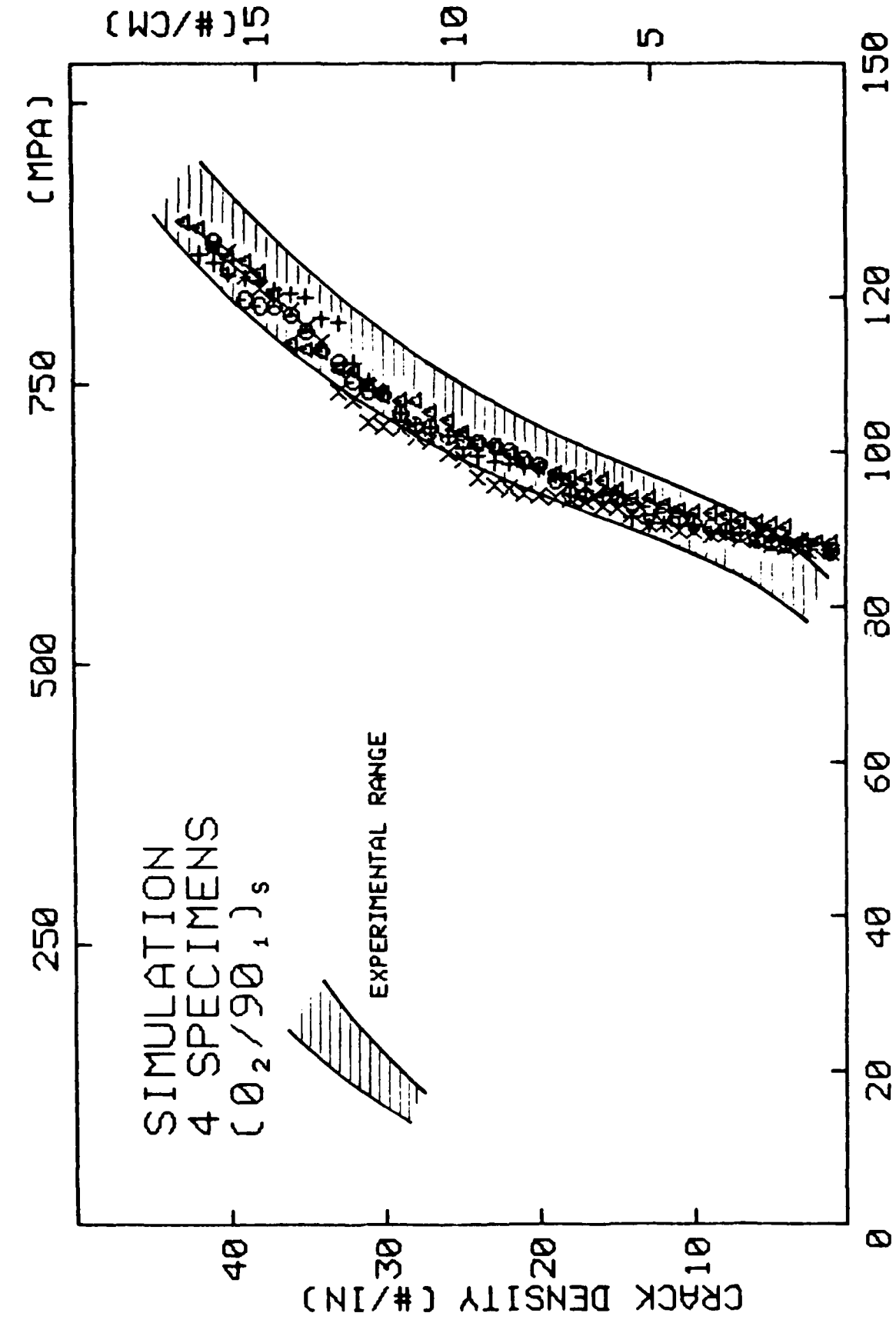

Figure 2.16 Comparison Between the Simulated and the Experimental Crack-Density versus Laminate Tension Relations $[0_2/90]_s$.

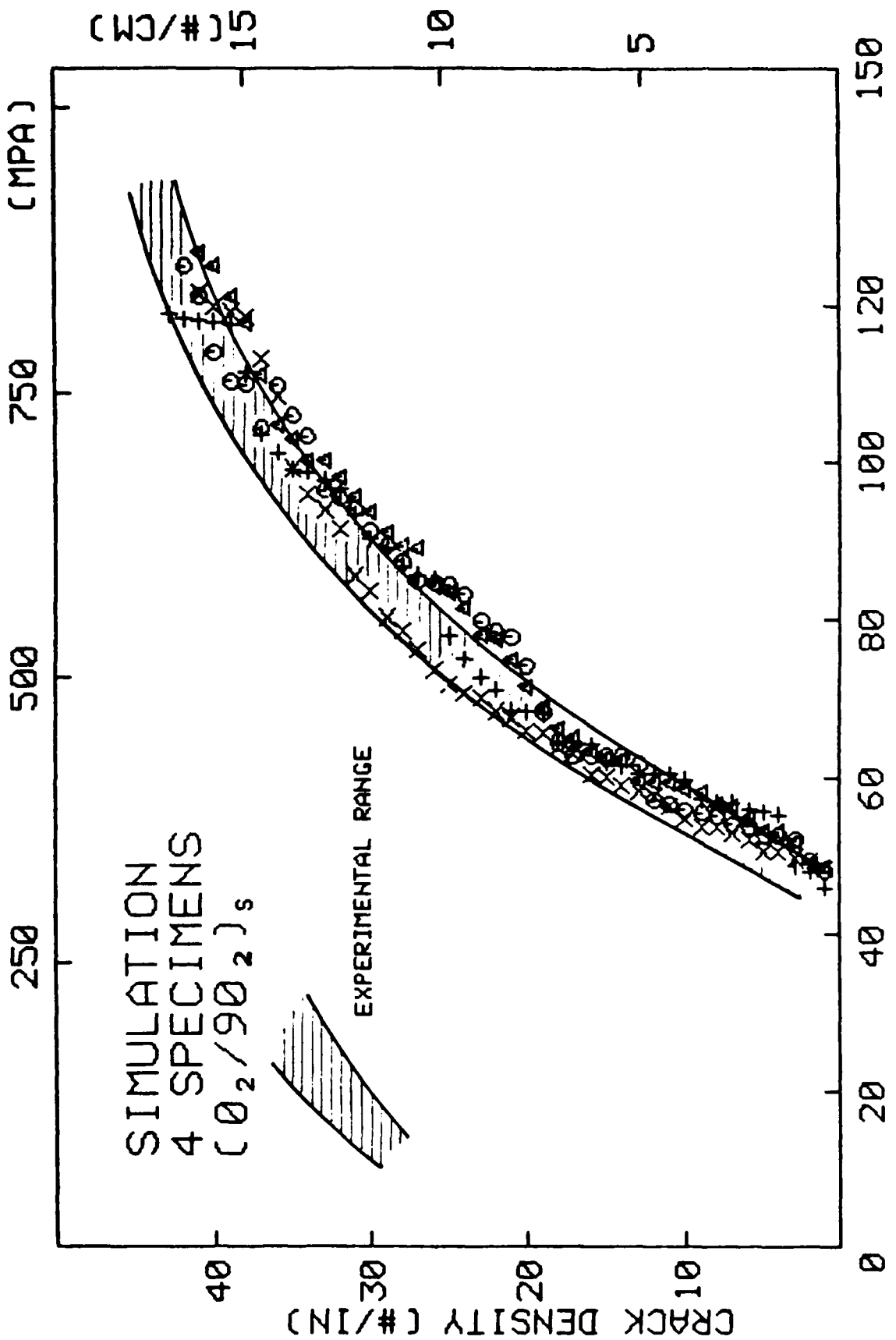

Figure 2.17 Comparison Between the Simulated and the Experimental Crack-Density versus Laminate Tension Relations $[0_2/90_2]_s$.

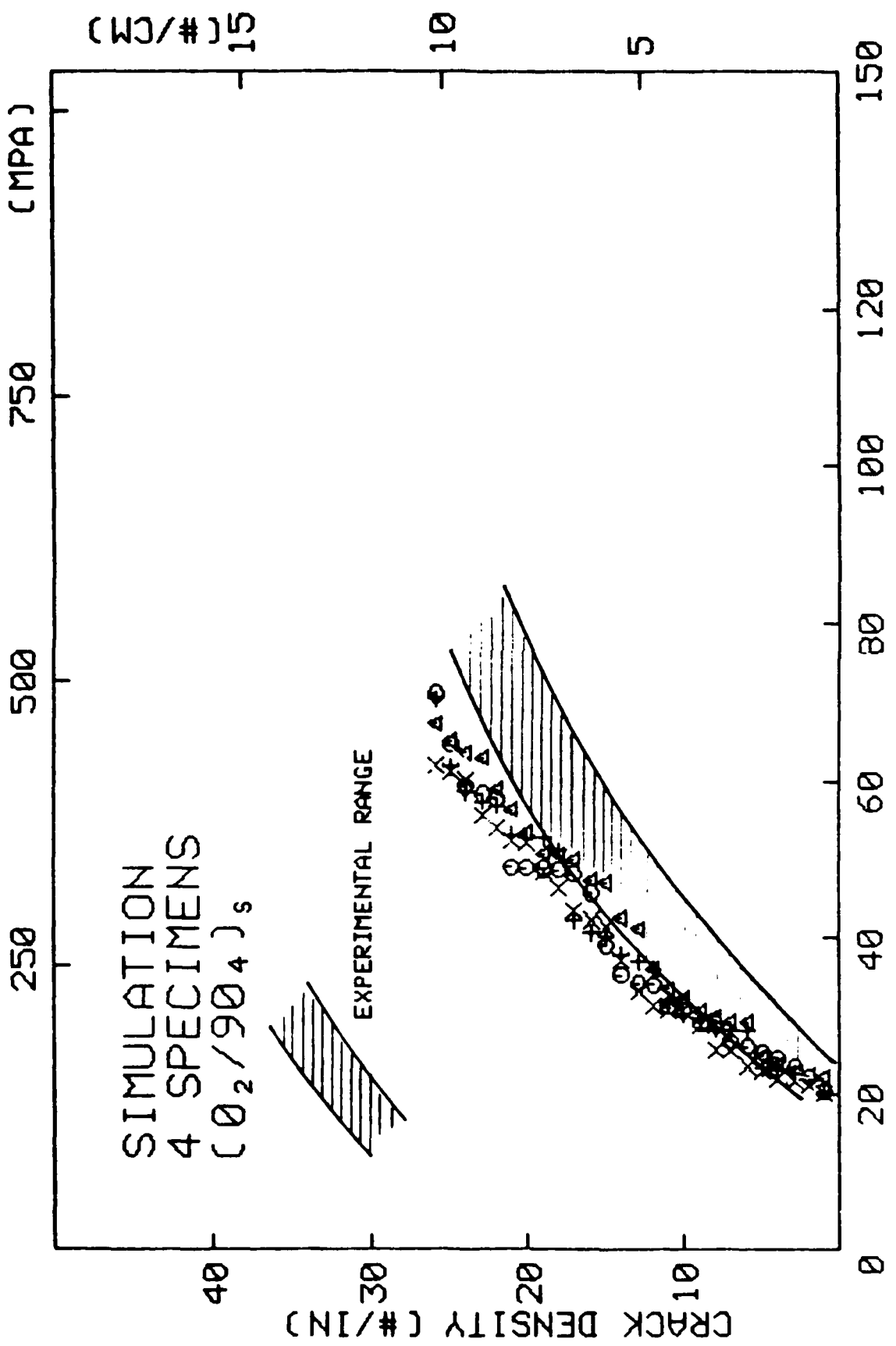

Figure 2.18 Comparison Between the Simulated and the Experimental Crack-Density versus Laminate Tension Relations $[0_2/90_4]_s$.

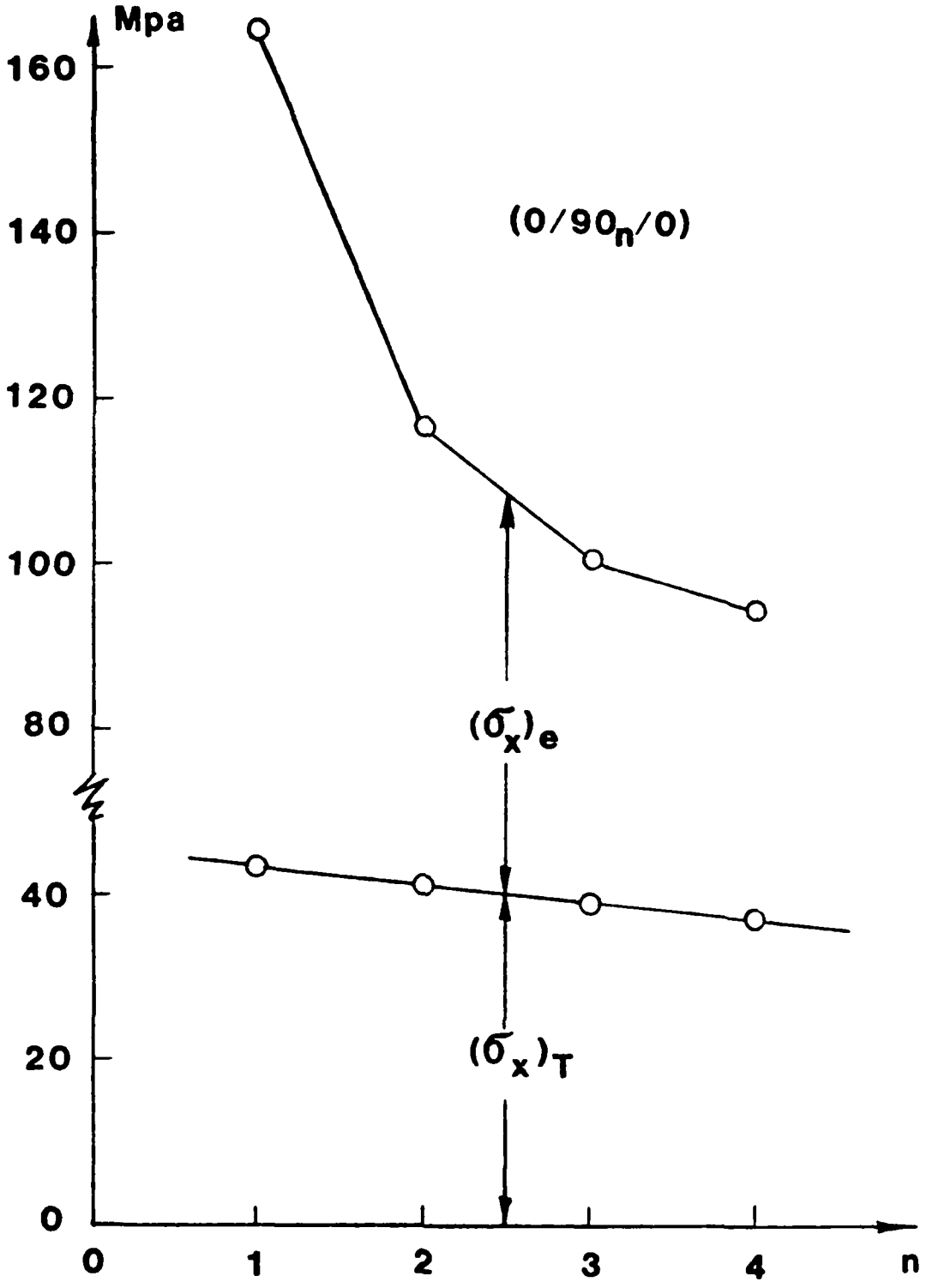

Figure 2.19 In-Situ Tensile Stress σ_x in the 90°-Plies at Onset of Transverse Cracking.

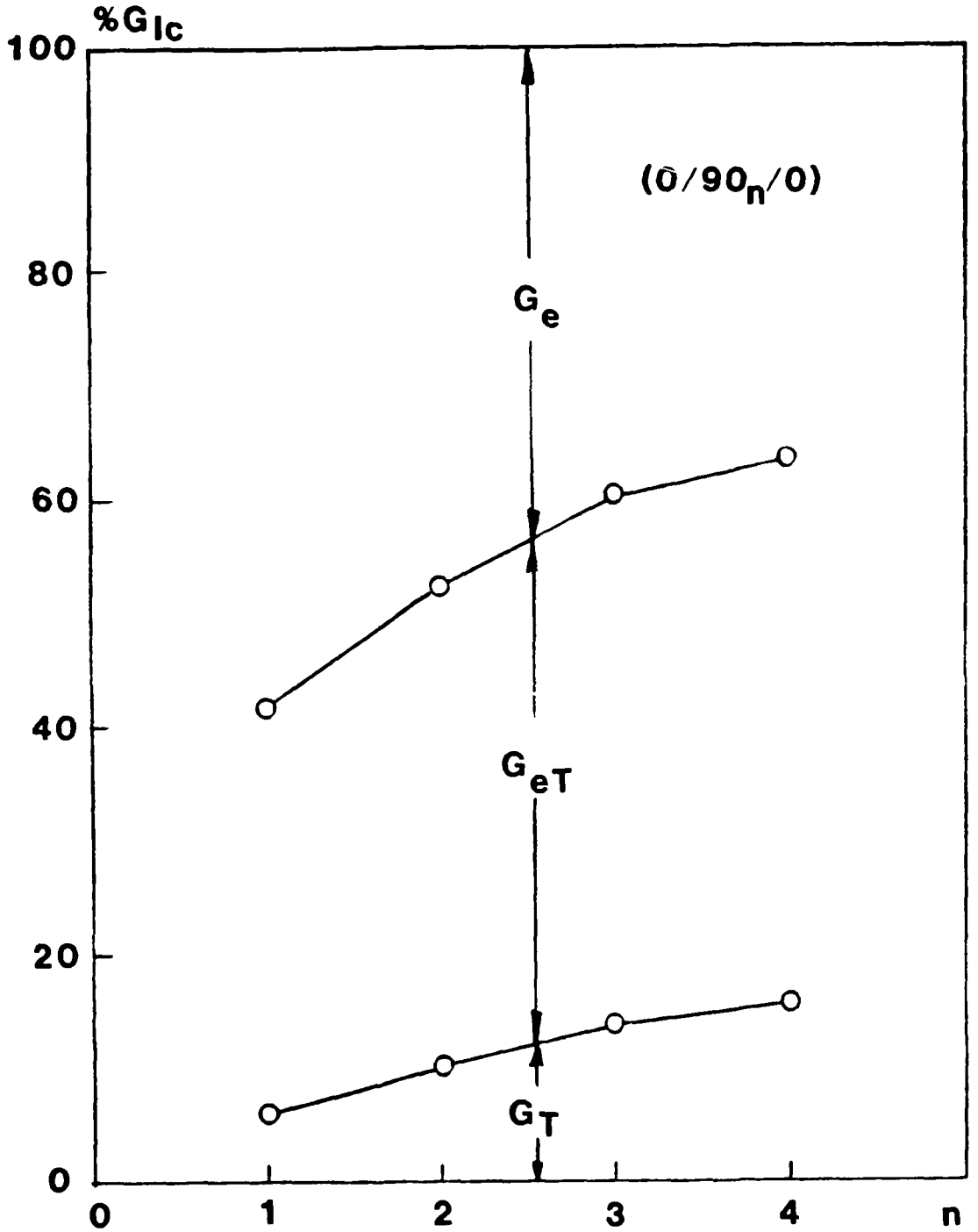

Figure 2.20 Percent of G_e, G_{eT} and G_T in Total Energy Release Rate at Onset of Transverse Cracking.

CHAPTER III. ANALYSIS OF INTERPLY CRACKING

3.1 Physical Characteristics of Interply Cracking

In Chapter II, the mechanics of intraply cracking in the form of transverse cracks was investigated. Intraply cracking is labeled as the first basic form of matrix crack, which occurs primarily because of the in-ply stresses, σ_x, σ_y, and τ_{xy}. The second basic form of matrix crack is interply crack, or delamination. Delamination is a plane crack which initiates and propagates in a plane parallel to or inside of an interface between two adjacent plies. The primary cause is the interlaminar stresses σ_z, τ_{xz} and τ_{yz} that exist in the delaminating plane.

In practice, most structural laminates are designed to withstand in-plane loads. Interlaminar stresses occur near locations of geometric discontinuity, such as laminate free edge, bolt-hole, surface cut, inclusion, internal defect, or some intraply cracks that already occurred, etc. Hence, interlaminar stresses are localized or concentrated stresses.

The severity of the various localized interlaminar stresses depends on the nature of the particular geometrical discontinuity. Similarly, the initiation and propagation characteristics of interply cracking also vary with the same geometrical factor.

In this section, an effort is made to delineate the physical behaviors of some commonly observed delaminations in engineering terms, and to set a logical procedure for an analytical treatment.

Free Edge Delaminations. Consider first the free edge delamination problem. This problem has attracted research interests ever since the advent of composite laminates. As far back as in the late 1960's, laboratory coupon tests already established that the tensile strength of a laminate coupon depends on whether or not free edge delamination occurs prior to final coupon

rupture. In this regard, it was found that the laminate's ply stacking sequence greatly influences the behavior of the observed free edge delamination [39]. Bjeletich, et. al [29] showed, for example, the uniaxial tensile strength of the graphite-epoxy $[\pm 45/0/90]_s$ coupon was much lower than the $[0/90/\pm 45]_s$ coupon. The reason is that the former can develop extensive free edge delamination prior to final failure, while the latter cannot. Free edge stress analysis based on ply elasticity reveals that large tensile σ_z stress is concentrated along the free edge of the $[\pm 45/0/90]_s$ coupon, while a compressive σ_z stress is concentrated along the edge of the $[0/90/\pm 45]_s$ coupon. Hence, the former is prone to delamination; the latter is not.

Actually, stacking sequence is not the only factor affecting the behavior of free edge delamination. Other factors have been identified. For instance, Rodini, et. al [40] were the first to experimentally document the dependence of delamination growth on ply thickness. They showed that the critical laminate tensile strain $\bar{e}_x$ at the initiation of edge delamination in a $[\pm 45_n/0_n/90_n]_s$, n = 1, 2, 3, laminate family varied approximately inversely with the value of $\sqrt{n}$. A more systematic study of ply thickness effect on matrix cracking in general was reported recently by Crossman, et. al [41].

Experimental documentation of free edge delamination has traditionally been conducted using both macroscopic and microscopic damage inspection techniques. Optic opaque penetrant enhanced x-radiography is among the techniques used at the macroscale, while microphotography in conjunction with scanning electronic microscopy is a method for detecting material damage at the microscale.

Figure 3.1a shows an x-radiograph in plane view of free edge delamination in a $[\pm 45/0/90]_s$ graphite-epoxy coupon subjected to uniaxial tension. In this particular laminate coupon, a uniform delamination was initiated along both

edges of the laminate at about 90% the laminate ultimate strength. The growth behavior was essentially stable. Near total delamination, other matrix cracking modes developed and caused final failure of the test coupon.

Microscopic examination of the same delaminated coupon gives a more detailed view. Figure 3.1b is an edge view of the delamination magnified at 80 times. This picture was taken after the onset of edge delamination, but before the laminate failure. It is seen that the crack is not confined in any one given ply-to-ply interface. Rather, it wanders in the thickness of the 90°-plies with a zig-zagged path. The zig-zagged crack surface may be explained by the fact that the 90°-plies near the free edge region are subjected both to a tensile σ_z normal to the laminate plane and to a tensile σ_x in the loading direction. The tensile σ_x tends to cause transverse cracks in the 90°-ply, while the tensile σ_z causes delamination.

As the applied tensile load increases, the delamination propagates further toward the center of the laminate. The growth is sometimes concurrent with multiple transverse cracks in the 90°-ply. Figure 3.2 shows an 80x thickness-view of the same $[\pm 45/0/90]_s$ coupon taken just before its final failure. Note that in addition to delamination in the 90°-plies, there are also delaminations in the ± 45 interfaces and the -45/90 interfaces. Moreover, intraply cracks in the ± 45 plies are also visible. Clearly, at this stage of loading, laminate matrix cracking involves several modes of failure that occur at several interfaces. For the laminate shown here, however, onset of edge delamination at 90% of the laminate ultimate strength appears to be the first event in the matrix cracking process.

As mentioned, growth of delamination causes secondary cracks in other plies. Figure 3.3 shows a set of free edge delamination photographs taken from a $[\pm 25/90/\mp 25]$ tensile coupon. Here, a free edge crack is seen to have

formed initially in the 90°-ply, but then branched onto the 25/90 interface as it propagated inward. The branching is probably caused by the secondary skewed cracks that occur ahead of the delamination. The skewed secondary cracks in the 90°-ply thickness is clearly the result of multi-axial tensile stresses that develop near the delamination front. In this particular instance, the thickness of the 90°-ply is thin and the threshold condition for a pure 90°-ply transverse cracking is not reached before edge delamination. However, the tensile σ_x is significant enough to alter the initial delamination growth direction.

Finally, Figure 3.4 displays an x-radiograph of free edge delamination for a $[90_2/0_2/\pm 45_2]_s$ laminate coupon subjected to uniaxial compression [42]. In this case, a tensile σ_z stress is developed in the $\pm$45°-plies near the free edge. This caused free edge delamination in the 45/-45 interface. Note that the delamination contour is not as uniform along the free edge, due possibly to the constraint from the grips at the coupon's end-tabs. Although the test specimen was very short length-wise to prevent global buckling, local ply buckling still occurred subsequent to delamination. The latter had resulted in transverse cracks in the 45°-plies, as can be seen in Figure 3.4.

Other Types of Delamination. The foregoing discussions focussed on the physical nature of free edge delaminations as observed in some laboratory coupon tests. Generally free edge delamination is not a concern in applications. In practical problems, delaminations usually occur near laminate defects where the stress concentration is much more severe than the free edge induced stress concentration.

Figure 3.5 shows an x-radiograph taken from a graphite-epoxy $[45/0_2/-45/0_2/90]_s$ laminate tensile coupon having a through hole. In this test coupon, both the straight edge and the curved edge around the hole caused

interlaminar stresses. Indeed, delamination cracks can be seen to form along both the straight edges and around the hole. However, the contour of delamination around the hole is more complicated than that along the free edge, because the stress field around the hole is more complex.

Another example of complicated ply delamination is shown in Figure 3.6, where a T300/934 graphite-epoxy tensile coupon having $[0_2/90_3]_s$ lamination was subjected to uniaxial tension. Purely 90°-ply transverse cracks are induced long before any delamination. Upon increased loading, the transverse cracks acted like local defects which cause localized interlaminar stresses. This results in the development of localized delaminations. As can be seen from Figure 3.6, these delaminations grew with the increasing load and their coalescence precipitated a massive 0/90 interface separation. This last event is believed to have caused the final specimen failure.

Finally, Figure 3.7 is an x-ray picture of a graphite-epoxy laminate subjected to low velocity impact. The localized damage caused by the impacting object involved primarily matrix cracks in the various plies and ply interfaces. Post-impact strength is adversely affected by the damage propagation upon re-loading.

These laboratory examples are cited to portray the complex characters of interply cracking. Though the basic cause of delamination is attributable to the existence of interlaminar stresses, the exact distribution of these stresses cannot always be determined. Since interply cracking and intraply cracking often mutually interact, the interacting mechanisms also remain perplexing.

In the following, an effort is made to idealize and simplify the delamination mechanisms, yet to retain all the essential influencing factors. In this context, a descriptive model is formulated for the initiation and growth

of some important delamination problems, as seen from a macroscopic viewpoint.

3.2 The Energy Model for Free Edge Delamination

As has been previously stated, the physical complexities of interply cracking are far from being fully clarified, especially the mechanisms associated with crack interactions. But, for the simpler problem of free edge delamination which propagates without crack interactions, a reasonably accurate analysis of the phenomena at the macroscopic level is possible. The analysis approach will be the same fracture mechanics concept applied to the intraply cracking problems. Some preliminary considerations for the model formulation are given in the following.

Kinematics of Free Edge Delamination. Consider the case of a long laminate coupon having straight edges. Let the laminate ply stacking sequence and the manner of loading be such that free edge delamination occurs exclusively at a known ply interface. For simplicity, assume that the initiation and propagation of the delamination is the only matrix crack event during the course of loading. Under such circumstances, the delamination growth contour will be uniformly advancing along the edges; the growth may be treated as one-dimensional and self-similar. This idealization permits the representation of the delamination as a line crack propagating in the cross-sectional plane of the laminate, as illustrated schematically in Figure 1.3.

Effective Interlaminar Flaws. For definiteness, let the laminate be of finite width 2b and subjected to the uniaxial tensile laminate strain $\bar{e}_x$. Then, given the geometrical lay-up of the laminate, all free edge stresses including the interlaminar σ_z, τ_{xz} and τ_{yz} can be calculated based on ply elasticity. In order to render a prediction for delamination initiation, it is necessary to introduce a certain effective interface flaw near the free edge. Upon loading, the flaw is under the influence of the free edge stress

field. Delamination of macroscopic dimension will result from the growth of the flaw once the edge stress field reaches a critical state.

Once again, the size of the effective flaw is unknown; some heuristic arguments about micro-macro transition are necessary to justify its presence and to estimate its size, as was done in the intraply cracking problems.

For the present case, let it be assumed that an "effective" interlaminar flaw of uniform width "a_o" is situated in some ply interface near the straight edge of the laminate. This effective flaw is regarded as a small interply crack which begins propagation when the stress state surrounding the flaw-tip reaches the critical value. This incident then defines the onset of delamination, with a physical crack detectable at the macroscale.

Condition for Onset of Delamination. The transition from an effective flaw to a physical crack is governed by the criterion of fracture growth. Since the particular interface in which edge delamination occurs is assumed known, then the flaw-tip energy release rate $G(\bar{e}_x, a_o)$ for a given effective flaw of size a_o can be calculated. The finite element crack-closure procedures outlined previously is again applicable. The calculated G can be conveniently expressed as a function of a_o, given the stacking sequence of the laminate, the ply elastic constants and the applied tension $\bar{e}_x$.

Figure 3.8 shows a typical G-curve plotted against the flaw size a_o. It is seen that G rises sharply from zero at $a_o = 0$ and reaches a limiting value G_{max} at about $a_o > a_m$. The fact that G initially increases linearly with the flaw size a_o is a behavior similar to the classical crack problems. But as a_o approaches a_m, the crack driving force G becomes non-linear and reaches eventually an asymptote. This behavior of G indicates that the delamination growth is basically a stable process when its size exceeds the quantity a_m.

The physical meaning of a_m is not fully understood at the present time. Its numerical value for most laminates is of the order of the thickness of the material plies which contains the delamination crack. For example, a_m equals about 4t (2 ply thickness) in the $[\pm 45/0/90]_s$ laminate; it equals about 8t in the $[\pm 45_2/0_2/90_2]_s$ laminate [32]. Hence, the value of G_{max} is similarly affected by the same ply thickness factor.

The calculated G function can be expressed again in explicit terms of the applied tension $\bar{e}_x$:

$$G(\bar{e}_x, a) = C_e(a) \cdot 2t \cdot \bar{e}_x^2 \tag{3.1}$$

where $C_e(a)$ is a coefficient dependent only on the delamination size (denoted as a); and t is a chosen length parameter (2t = ply thickness). Note that the functional shape of C_e is similar to G(a) shown in Figure 3.8, given t and $\bar{e}_x$.

Similarly, if the laminate is subjected to a known uniform temperature drop, ΔT, and if the thermally induced stresses surrounding the flaw-tip also effect delamination growth in similar manner, then the associated flaw-tip energy release rate due to ΔT is expressible as

$$G(\Delta T, a) = C_T(a) \cdot 2t \cdot \Delta T^2 \tag{3.2}$$

where $C_T(a)$ is also a function of the delamination size a only. The functional behavior $C_T(a)$ is similar to that of C_e, see [32].

When the mechanical load and the temperature load both effect crack growth at the same time, the total energy release rate is expressible as

$$G(\bar{e}_x, \Delta T, a) = [\sqrt{C_e} \cdot \bar{e}_x + \sqrt{C_T} \cdot \Delta T]^2 \, (2t) \tag{3.3}$$

Now, if the initial size of the effective edge flaw a_o is known, then the condition for its propagation (i.e. onset of delamination) is governed by

$$G(\bar{e}_x, \Delta T, a) = G_c; \qquad a = a_o \tag{3.4}$$

In order to execute a solution for (3.4), one question must now be answered and two quantities defined. The question is on which ply interface is the delaminaton to occur; and the two quantities to be defined are the values of G_c and a_o.

The Range Of Effective Flaw Size. The question regarding the delamination site and the value of G_c will be examined in more detail latter in this section. Now, examine first the possible values of a_o. Note from Equation (3.4) that a one-to-one relationship between the applied tension $\bar{e}_x$ and the flaw size a_o exists, given ΔT and G_c. Figure 3.9 shows a schematic plot of Equation (3.4) in the $\bar{e}_x$ versus flaw size plane. It is seen that if a range of values is given for the edge flaw size a_o, then a corresponding range for the onset tension $\bar{e}_x$ can be determined. In particular, if for all probability, the effective flaw size a_o is of the order of a_m or larger, then the range of the onset tension $\bar{e}_x$ is very narrow. Actually, Equation (3.4) predicts a constant $\bar{e}_x$ for all $a_o \geq a_m$ because G then reaches its asymptote. In fact, this constant $\bar{e}_x$ is the minimum possible laminate strain predicted for which onset of delamination could occur.

As discussed before, the numerical value for a_m in many practical laminate stacking sequence is less than 4t, or about 2 ply thicknesses. It is entirely possible that the largest effective interply flaw size may even be greater than 4t. In any event, a lower bond for the onset load $(\bar{e}_x)_{cr}$ can always be obtained by setting $a_o \geq a_m$ or $a_o \sim 4t$, whichever is smaller.

Location of Delamination. To determine the exact delamination site by an analytical means is not straight-forward, because given a multi-layered laminate coupon there are always several ply interfaces possible for delamination.

Consider for example the T300/934 graphite-epoxy $[\pm 25/90]_s$ laminate under uniaxial tension examined earlier in Chapter II. As was pointed out then, a strong tensile σ_z is concentrated near the free edge. So, free edge delamination is expected before 90°-ply transverse cracking. The interlaminar σ_z distribution along the mid-plane (90/90 interface) was shown earlier in Figure 2.4. It was inferred that it is this stress which is responsible for edge delamination.

Actually, σ_z is not the only strong interlaminar stress near the free edge; nor is it limited to act only on the laminate mid-plane. In fact, there is a high shear τ_{xz} acting both on the 25/-25 and the -25/90 interfaces along with a tensile σ_z. Figure 3.10 shows the through-the-thickness distribution of τ_{xz} near the free edge, while Figure 3.11 shows the through-the-thickness distribution for σ_z. It is seen that τ_{xz} are singular on the 25/-25 and the -25/90 interfaces. Likewise, σ_z is singular and tensile on the -25/90 interface.

From the interlaminar stress distributions, it would appear that the 25/-25, -25/90 and 90/90 interfaces are all possible delamination sites. Owing to the lamination symmetry, delamination in the 90/90 interface is predominantly in mode-I (opening mode); delamination in the 25/-25 interface is in mode-III (anti-plane shear) and delamination in the -25/90 interface is mixed with mode-I and mode-III, as both τ_{xz} and σ_x act on that interface. From such a stress analysis, however, it is still not possible to determine for sure on which of the ply interfaces delamination will initiate. Clearly, a suitable quantity is needed to explicitly distinguish the delamination conditions on the various possible interfaces.

To this end, examine the computed strain energy release rate available in each of the possible interfaces. Since on each ply interface an effective

interlaminar flaw of size a_o is assumed, the available total G at the flaw-tip in each of the interfaces may be calculated individually in terms of a_o and the applied tension $\bar{e}_x$.

Figure 3.12 shows two curves for the total energy release rate coefficient $C_e(a)$, one for a flaw residing in the mid-plane (90/90 interface) and the other for a flaw in the -25/90 interface. Note that $C_e(a)$ for the mid-plane flaw contains exclusively mode-I energy, while $C_e(a)$ for the flaw in the -25/90 interface (dotted line) contains mode-I and mode-III energies. The ratio between mode-III and mode-I in the latter is about 0.8.

Similarly, Figure 3.13 shows the energy release rate coefficients $C_T(a)$ for delamination in the same two interfaces. The corresponding $C_e(a)$ and $C_T(a)$ curves for delamination in the 25/-25 interface (predominantly mode-III) are omitted because of their relatively small magnitudes.

From Figures 3.12 and 3.13, it can be seen that propagation of a flaw in the mid-plane releases more energy than a flaw of same size propagating in the -25/90 interface. However, whether or not a mid-plane delamination will occur before a -25/90 interface delamination is determined by the specific delamination resistances G_{IC} for mode-I and $G_{(I, III)C}$ for mixed-mode. As was discussed in Chapter I, different cracking modes may mean different microscopic failure processes, which in turn give rise to different macroscopically measured material energy release rates.

Dependence of G_c on Delamination Modes. In several recent experiments on graphite-epoxy composites [43 - 45], the total energy release rate G_c for mixed-mode delamination has been found to be generally greater than G_{IC} for mode-I delamination. In fact, in one case the total G_c for mixed mode crack growth was found to increase with the ratio G_{II}/G_I [45]. Figure 3.14 shows the measured total G_c for mixed-mode (I and II) delamination plotted as a

function of G_{II}/G_I ratio (the material used was the T300/934 composite system). It shows that the total G_c is always greater than G_{IC}; and there seems to exist a limiting value at large G_{II}/G_I. This limiting value may be construed as the value of G_{IIC}.

The reason for the dependence of the total strain energy dissipated in mixed-mode crack on the G_{II}/G_I ratio may be explainable at the microscale. Some have attributed the increased energy to crack-tip matrix yielding under shearing deformation [44]; others attempted to explain it from the crack surface morphology [43]. Whatever the exact cause, the macroscopic G_c is multiple-valued in mixed-mode crack growth. When used in the context of Equation (3.4), it becomes necessary to know the G_{II}/G_I ratio of the delamination growth, so as to select a proper value for G_c-total. For this reason, a functional curve for each material system, such as shown in Figure 3.14, must be experimentally determined.

Alternative mixed-mode crack growth criteria have been suggested (see, e.g. [46]), requiring material resistances such as G_{IIC} and/or G_{IIIC}. But many questions need to be settled concerning both the existence of and test methods for measuring G_{IIC} and G_{IIIC} as applied to delamination in composite laminates. For the time being the criterion in Equation (1.3) will be used in conjunction with a variable fracture toughness property, such as displayed in Figure 3.14 for the T300/934 system. As further research clarifies the many uncertainties surrounding the problem of mixed-mode matrix cracking in composites, a more precise and direct delamination criterion may be developed.

3.3 Illustrative Examples for Free Edge Delamination

In this section, two example problems will be discussed. All are related to free edge delamination. But, the loading factor and lamination geometry factors will be varied to see how good or bad the predictive model is.

$[\pm 25/90]_s$ T300/934 Tension Coupon. Consider the $[\pm 25/90]_s$ tension coupon made of T300/934 discussed earlier. A prediction can now be made as to which interface an edge delamination will first initiate. If the fracture criterion (3.4) is used in conjunction with the total G_c curve for mixed-mode delamination shown in Figure 3.14, it may be concluded definitely that free edge delamination will occur in the mid-plane of the laminate coupon, based on the calculated energy release rate curves shown in Figures 3.12 and 3.13.

As for the critical applied tension $(\bar{e}_x)_{cr}$ for the onset of the mid-plane (mode-I) delamination, assume that the effective interface flaw has an initial size $a_o \sim 4t$ or larger. Then, the maximum values of G_e and G_T in Figures 3.12 and 3.13 are taken:

$$(G_e)_{max} = 29.6 \times 10^9 \text{ J/m}^3$$
$$(G_T)_{max} = 4.0 \text{ J/m}^3/c^2 \qquad (3.5)$$

From Table II-1, use $\Delta T = 125°C.$, $t = 0.066$ mm and $G_{IC} = 227.5$ J/m^2. Substituting these values into Equations (3.3) and (3.4), it follows that the critical laminate tensile strain $(\bar{e}_x)_{cr}$ at onset of delamination should be equal to or greater than,

$$(\bar{e}_x)_{cr} \geq 6.17 \times 10^{-3} \qquad (3.6)$$

This prediction agrees with the experimental finding reported in References [32] and [41]. Four replicate specimens were tested and delamination onset occurred at laminate strain $\bar{e}_x$ ranging from 5.8 to 6.1 x 10^{-3}. The average was $\bar{e}_x = 5.95 \times 10^{-3}$.

In predicting $(\bar{e}_x)_{cr}$ in (3.6), G_{IC} was assumed to have the constant value 227.5 J/m^2. This value represents the upper bound value for mode-I (90/90) interface delamination, see Table II-1. For the present problem, the actual

AD-A170 486 FRACTURE ANALYSIS OF MATRIX CRACKING IN LAMINATED COMPOSITES(U) NATIONAL RESEARCH COUNCIL WASHINGTON DC A S WANG JAN 85 NADC-85110-60 N62269-82-C-0704 2/2

UNCLASSIFIED F/G 11/4 NL

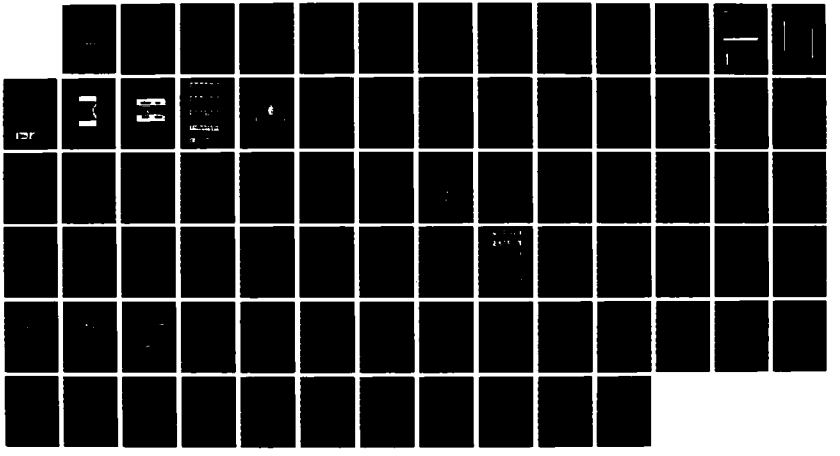

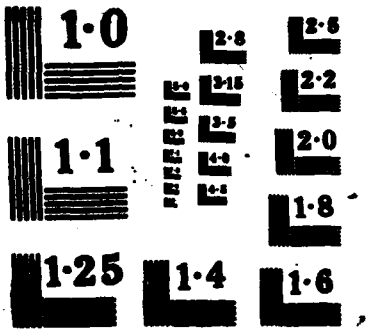
1·0
1·1
1·25
1·4
1·6
1·8
2·0
2·2
2·5
2·8
3·15
3·5
4·0

G_{IC} should be somewhat smaller. Then, the prediction and the experiment would agree even closer.

Quasi-Isotropic Laminates Coupon Under Compression. To further illustrate the utility of the energy release rate method, consider the following laminate coupons of different lamination stacking geometries: $[90_2/0_2/\pm 45_2]_s$, $[0_2/90_2/\pm 45_2]_s$ and $[(0/90)_2/(\pm 45)_2]_s$. Note that these laminates are macroscopically identical in the elastic responses to in-plane laminate loading except for the free edge effect. Specifically, the stacking sequence of each laminate causes tensile interlaminar normal stress σ_z, shearing stresses τ_{xz} and τ_{yz} near the free edge under uniaxial compressive load. Of course, the magnitudes of the free edge stresses will differ with the different stacking sequences.

In Reference [42], laminates of these stacking sequences were made using AS-3501-06 graphite-epoxy. Basic ply properties are given in Table III-1. The laminates were tested in room temperature under monotonic uniaxial compression. In all test cases, free edge delamination in the laminate mid-plane was recorded, see Figure 3.4.

Figure 3.15 shows the experimentally measured free edge delamination growth plotted against the applied laminate compressive stress $\bar{\sigma}_x$ for each of of the three types of laminate coupons. These delamination growth curves indicate that onset of delamination is followed by relatively rapid growth, and the growth may have precipitated localized ply buckling failure.

Note the onset load for delamination. As can be seen from Figure 3.15, this varies with the laminate stacking sequence. The final failure load is also affected by the stacking sequence factor.

In order to explain these observed differences, an edge stress field analysis was performed using the finite element routine. Figures 3.16 - 3.18

show the isometric view of σ_z distributions on the coupon cross-section (first quadrant section) for, respectively, $[90_2/0_2/\pm45_2]_s$, $[0_2/90_2/\pm45_2]_s$ and $[(0/90)_2/(\pm45)_2]_s$. Similarly, Figures 3.19 - 3.21 show the shearing stress τ_{xz} for the same three coupon types. The other shearing stress, τ_{yz}, is not shown due to its relatively small magnitude.

From these edge stress displays, it appears that both the laminate mid-plane and the 45/-45 interface are possible delamination sites. It is not immediately clear, however, as to why the onset loads for delamination should be different, and why the delamination sites should all be at the mid-plane.

To answer these questions, an energy release rate analysis was performed. The energy release rate coefficient function $G_e(a)$ computed by assuming an interply effective flaw of size a_o in the laminate mid-plane, and in the 45/-45 interface are shown respectively in Figures 3.22 and 3.23. The G_T-curves due to residual thermal loading were neglected because of their small values.

The mid-plane delamination again contains purely mode-I action, while in the 45/-45 interface it contains both opening (mode-I) and anti-plane shear (mode-III) actions. The mixed-mode ratio G_{III}/G_I varies from 0.1 to 0.3 amongst the three types of laminates, see Reference [42]. The G_e-curves in Figure 3.23, however, are for the total energy release rate.

From the computed G_e-curves, it can be inferred that mode-I (mid-plane) delamiantion should occur in all the three types of laminates. This is because the computed G_e-curves for mid-plane delamination are all higher than the corresponding G_e-curves for delamination in the 45/-45 interface plane. In addition, for the material system used, G_{IC} is lower than mixed-mode G_c total, see Table III-I.

The actual onset loads are predicted using the maximum values of the corresponding G_e-curves for mid-plane delamination. As was done in the previous example, Equations (3.3) and (3.4) are used to predict the minimum

possible onset strain $\bar{e}_x$ for each case considered. The results are as follows:

Laminate Type	Minimum Onset $\bar{\sigma}_x$ (= $\bar{e}_x\bar{E}_x$)
$[90_2/0_2/\pm45_2]_s$	-303 Mpa (-44 ksi)
$[0_2/90_2/\pm45_2]_s$	-352 Mpa (-51 ksi)
$[(0/90)_2/(\pm45)_2]_s$	-407 Mpa (-59 ksi)

The corresponding experimental loads are determined from Figure 3.15. Because of the data scatter, load-ranges are obtained yielding, respectively, 290 - 310 Mpa; 331 - 358 Mpa; and 400 - 427 Mpa. The predicted results are within the experimental scatter ranges. In particular, the difference in the onset loads caused by the difference in stacking sequences is also correctly predicted.

In the examples discussed in this section, the question regarding the effective flaw size a_o is treated indirectly. The assumption used is simply that along the free edge of the laminate, the interface flaw has a probable size equal or greater than a_m (a_m is of the order of 4t or the layer thickness in which the assumed delamination is contained). In this manner, the prediction is made using the maximum available energy release rate, yielding a lower bound for the delamination onset load.

3.4 Two-Dimensional Delamination Growth

In the preceding sections, the energy release rate method has been applied to describe a number of free edge delamination problems. The laminates studied were so designed and loaded as to induce delamination without significant interactions with other cracking modes. Furthermore, the delamination was either actually confined or theoretically assumed to grow uniformly along the free edges of the test coupon. So, it could be treated as a one-

dimensional, self-similar crack growth problem. Under such circumstances, the kinematics of the crack propagation is simplified and crack growth is represented in a two-dimensional plane. The crack size then has a linear magnitude "a" and the propagation is simply along a line. This simplification makes possible a two-dimensional stress field solution in which the crack-tip energy release rate function $G(\bar{\sigma}, a)$ is computed. Within the general confines of the classical fracture mechanics, the problem is treated, at least conceptually, without recourse to empirical formulisms.

Generally speaking, one-dimensional delamination growth in laminates is a very special case, it can probably happen only under ideally controlled conditions. Most of the delamination problems encountered in practice are caused by laminate defects much more severe than free edges. The growth of delamination near a local defect is almost always mixed-mode and multi-directional in nature.

For example, consider the laminate with a through-hole shown in Figure 3.5. Upon loading, localized delamination and other modes of matrix cracking are induced near the curvilinear edge of the hole. In this case, the resulting delamination crack front is actually a plane contour. Because the associated growth is two-dimensional, the progression of the crack must be represented both in terms of the instantaneous delamination area and the delaminated shape.

Clearly, this problem not only requires a three dimensional stress analysis but also a two-dimensional fracture growth treatment. Among the most difficult tasks analytically are (1) how to calculate the crack front energy release rate $G(\bar{\sigma}, \tilde{a})$, in which $\tilde{a}$ is some line contour; and (2) how to set up a fracture growth criterion appropriate for the instantaneous mixed-mode and multi-directional crack growth behavior.

If the line contour of a local delamination is prescribed and its instantaneous growth shape assumed, the crack front energy release rate $G(\sigma, \tilde{a})$ can be calculated by a three-dimensional finite element routine [28]. Of course, the calculated $G(\bar{\sigma}, \tilde{a})$ remains as an effective, or averaged quantity in the same context as discussed in Chapter I, Section 1.5. As for a criterion suitable for contoured crack propagation in a given plane, little information is available at the present time. So, rather than attempt a rigorous treatment encompassing all these fundamental questions, consider the following example problem in light of the analytical developments thus far.

An Example for Contoured Delamination. Earlier in Section 3.3, free edge delaminations in three similar quasi-isotripic laminates induced by axial compression were examined. In a related but separate experiment [42], one of the laminate coupons, $[0_2/90_2/\pm45_2]_s$, was fabricated with a pre-implanted delamination in its mid-plane, see inset in Figure 3.24. The experimental details regarding the fabrication and test procedures were reported in Reference [42]. Figure 3.24 shows the test results in terms of the delamination size versus the applied laminate compression for specimens with and without the implanted delamination. These laminates display strikingly different growth behaviors. Specifically, the laminates with the implant underwent contoured delamination emanating from the corner of the implant edge, while the laminate without the implant experienced more or less uniform, one-dimensional free edge delamination as discussed before. The contoured growth in the laminate with implant was comparatively slower and more stable; but its early initiation and subsequent growth actually led to premature laminate final failure.

In what follows, a prediction will be attempted for the onset of the contoured delamination growth with the aid of the 3-D finite element simula-

tion routine developed in [28].

But before proceeding with the growth simulation, it is useful to examine the stress field near the implant at the coupon's free edge. For in this region a severe stress concentration is present. The particular point of interest is the interface corner where the implanted delamination intersects the free edge of the test coupon. This point is labeled "interface corner" in Figure 3.25.

Recall that laminates without the implant developed a tensile interlaminar σ_z stress near the laminate free edge. The largest value of σ_z near the free edge (acting on the mid-plane) was about 14 kpa (2 psi) per far-field strain $\bar{e}_x = -10^{-6}$; see Figure 3.16. In contrast, for laminates with the implant, the distribution of σ_z on the laminate mid-plane is shown in Figure 3.25, where the magnitude of σ_z near the "interface corner" is in the order of 60 kpa (8 psi) per $\bar{e}_x = -10^{-6}$. In fact, σ_z at the point is theoretically unbounded.

Since the implant is situated in the laminte mid-plane, the initial delamination growth is primarily of mode-I.

To predict the associated delamination onset, it is necessary to calculate the crack-front strain energy release rate. Assume that the expected initial delamination will start from the interface corner point and grow with a certain known contoured front. This growth contour is represented by a prescribed sequence of nodal releases in the finite element mesh. Specifically, Figure 3.26(a) shows the intended nodal release sequence that unlocks the delamination growth in a discrete fashion. The actual number labeled for each node represents the order of its release. In this manner, the energy release rate coefficient G_e can be computed as a function of the delaminated area associated with the prescribed growth contour. This is shown in Figure 3.26(b).

It is seen that the delamination growth is most energetic along the implant edge, represented by the nodes numbered 1, 2, 3, 5, 6, 8, etc. As the delaminated area becomes larger, the available energy release rate becomes smaller. This implies that the growth process is essentially stable, as observed in the experiment.

To obtain a reasonable prediction, the maximum value of G_e in Figure 3.26(b) is used to calculate the onset load for delamination. In this case, thermal effect on delamination is ignored as G_T is relatively small. Then, the maximum strain energy release rate associated with the prescribed initial delamination contour can be expressed as:

$$G_{max} = (G_e)_{max} (\bar{e}_x)^2 (2t) \tag{3.7}$$

where the value of $(G_e)_{max}$ corresponds to the release of node 6 in Figure 3.26(b).

Using G_c = 175 J/m^2 (1.0 in-lb/in^2) for mode-I delamination along the fiber direction and 2t = 0.13 mm (0.005 in.) from Table III(-1, the calculated minimum onset load in terms of the applied far-field strain ($\bar{e}_x$) is found to be

$$(\bar{e}_x)_{min} = 2.89 \times 10^{-3} \tag{3.8}$$

For the laminate considered, the axial stiffness is $\bar{E}_x$ = 50.1 Gpa (7.27 msi), so that the predicted (minimum) onset far-field laminate stress is about

$$(\bar{\sigma}_x)_{min} = 145 \text{ Mpa } (21.0 \text{ ksi}) \tag{3.9}$$

This predicted value is almost the same as the experimental value extracted from Figure 3.25.

Up to this point, reasonable analytical rigor could be maintained. But, what to do when the delamination growth becomes larger is not at all clear. Not only is the exact crack front unknown but the growth also becomes mixed-mode.

3.5 Summary

In this chapter, the basic mechanics of interply cracking has been discussed from both an experimental and an analytical view point. Several examples belonging to the class of free edge induced delaminations were studied by means of the energy release rate method in conjunction with a three dimensional ply stress analysis. On the whole, the energy method is a useful technique to describe some of the essential characteristics found experimentally in free edge delaminations.

The basic mechanisms of interply cracking seem to be more intricate than intraply cracking. Since an interply crack is propagating parallel (albeit macroscopically) to the laminate plane, the applied in-plane load required to propagate an interply crack is usually higher than that required to propagate an intraply crack. For this reason, interply cracking almost always interacts with other matrix cracking events in practical cases.

Even in the special case of free-edge delamination, such as those examples studied in this chapter, one cannot always create a pure delamination growth without concurrent interactions with other cracking modes. To model such interactions would necessarily add uncertainties both in physical reasoning and in analytical modeling.

An equally troublesome aspect in the delaminaton problem is the lack of a suitable mixed-mode growth criterion. Because of the anisotropic nature of the composite plies, an interface crack would always propagate in mixed-mode. And, for the same reason, the material resistance against crack propagation

also depends on the ply geometry (e.g. fiber orientations) as well as the particular microstructures that exist on the interface.

All these difficulties make it seemingly impossible to treat the problem on a more rigorous basis. Nonetheless, further analytical developments remain promising. As will be demonstrated in the next chapter, the energy-release-rate method, as outlined here, continues to provide a reasonable analytical description for matrix crack interactions that emerge at higher applied load levels.

TABLE III-1

Material Constants for AS-3501-06 Unidirectional Ply*

Property	SI Unit	English Unit
E_{LL}	140.0 Gpa	20.4×10^6 psi
E_{TT}, E_{zz}	11.0 Gpa	1.6×10^6 psi
ν_{LT}, ν_{Lz}	0.29	0.29
ν_{Tz}	0.3	0.3
G_{LT}, G_{Lz}	5.5 Gpa	0.8×10^6 psi
G_{Tz}	5.5 Gpa	0.8×10^6 psi
α_T, α_z	28.8×10^{-6}/°C	16.10^{-6}/°F
α_L	$0.36.10^{-6}$/°C	0.2×10^{-6}/°F
σ_L, long. tensile strength	1325 mpa	190 ksi
σ_T, trans. tensile strength	50 mpa	8.6 ksi
2t, nominal ply thickness	0.132 mm	0.0052"
ΔT, temperature drop	155°C	310°F
G_{Ic} (0/0 interface)**	175 J/m^2	1.0 in-lb/in^2
G_{Ic} (90/90 interface)**	228 J/m^2	1.3 in-lb/in^2

*Data taken from Reference [42].

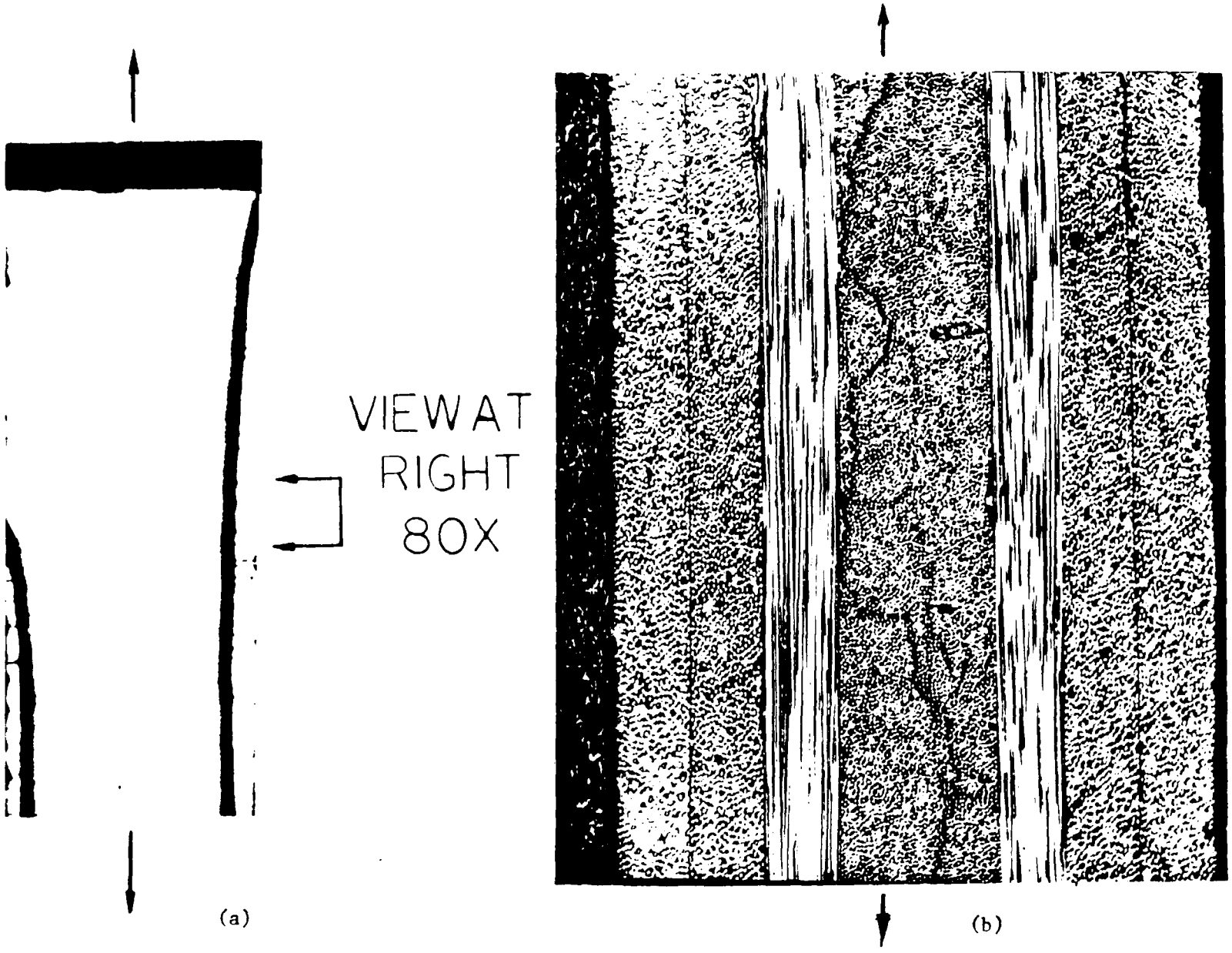

Figure 3.1 X-Radiograph (left) and Micrograph (right) Showing Free Edge Delamination in a $[\pm 45/0/90]_s$ Tensile Coupon.

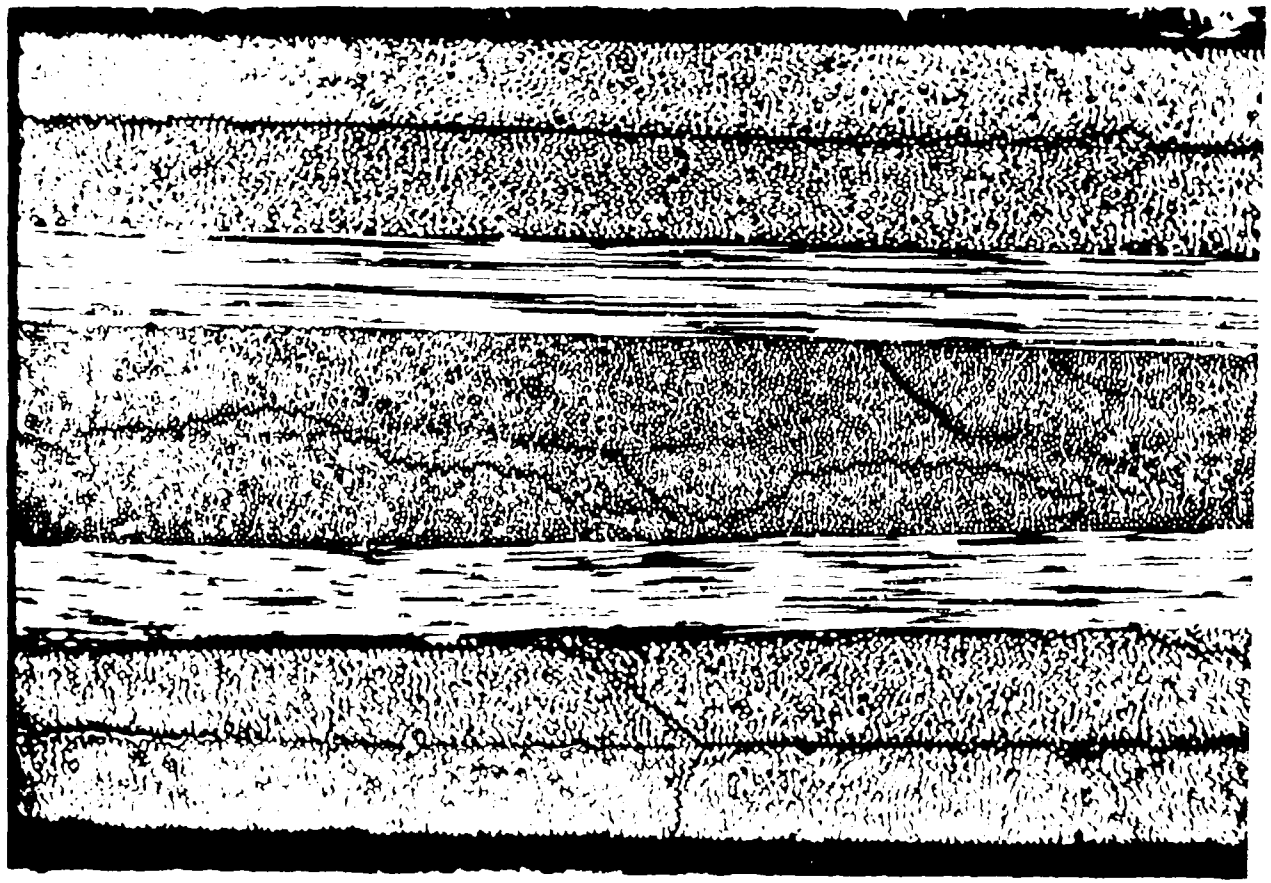

Figure 3.2 An Edge View Micrograph Showing Multiple Delaminations in a $[\pm 45/0/90]_s$ Tension Coupon During Late-Stage Loading.

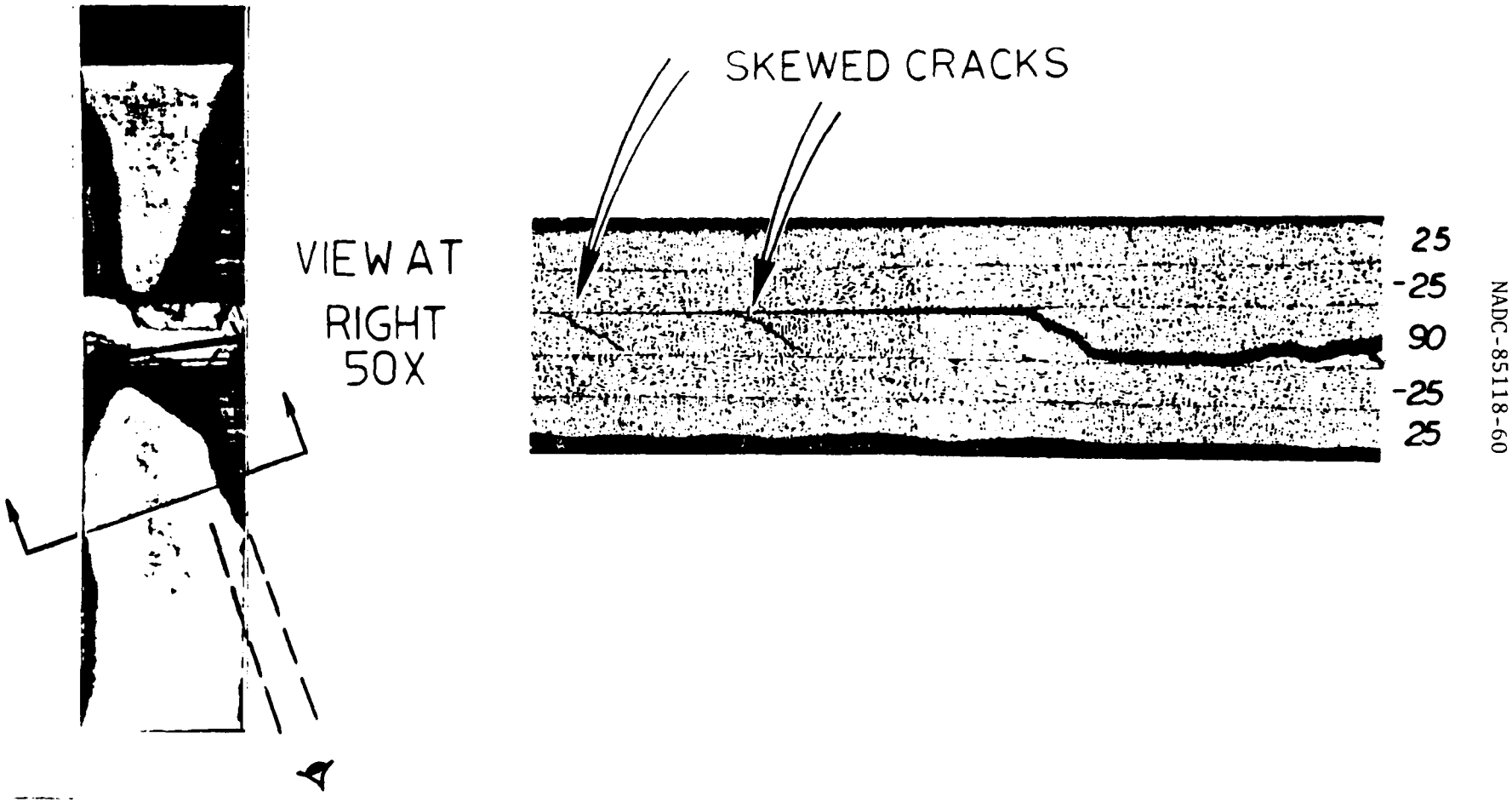

Figure 3.3 X-Radiograph (left) and Micrograph Showing a Cross-Sectional View of Edge Delamination in a [±25/90/±25] Tensile Coupon.

Figure 3.4 X-Radiograph Showing Edge Delamination in a $[90_2/0_2/\pm45_2]_s$ Compression Coupon.

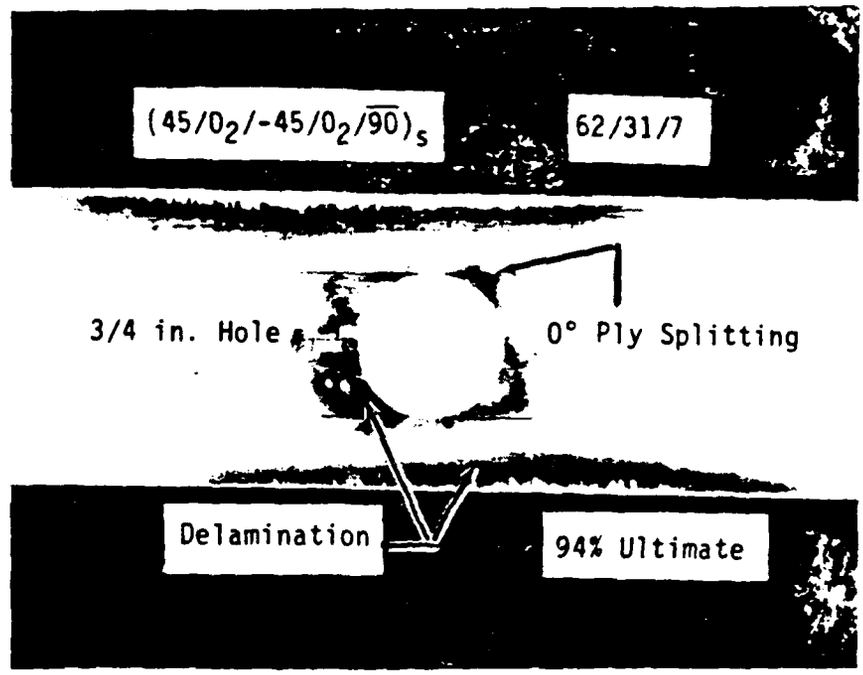

Figure 3.5 X-Radiograph Showing Matrix Cracking Around a Hole in a $[45/0_2/-45/\overline{90}]_s$ Tensile Coupon.

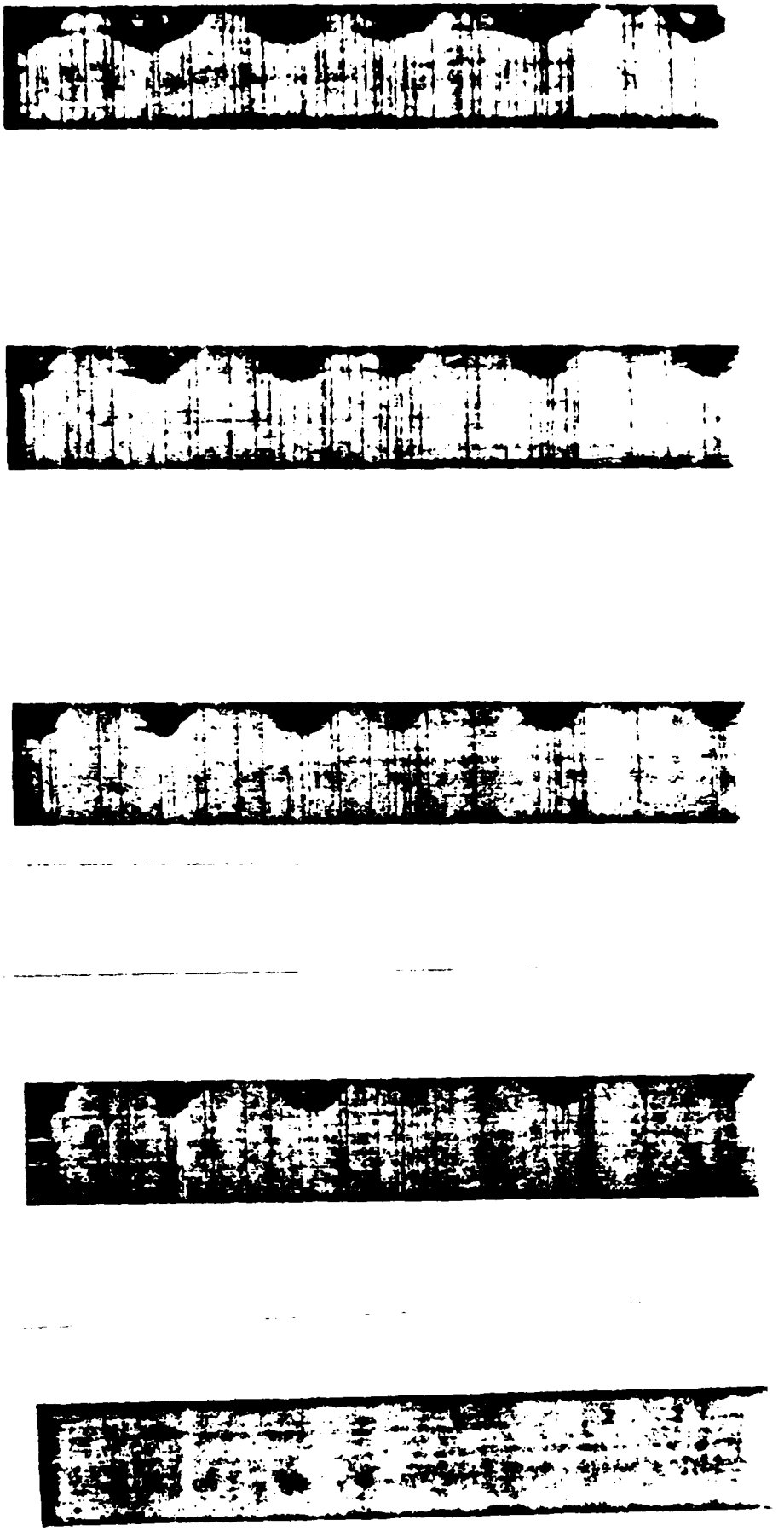

Figure 3.6 Load-Sequence of X-Radiographs Showing Formation of Localized Delaminations in a $[0_2/90_3]_s$ Tensile Coupon.

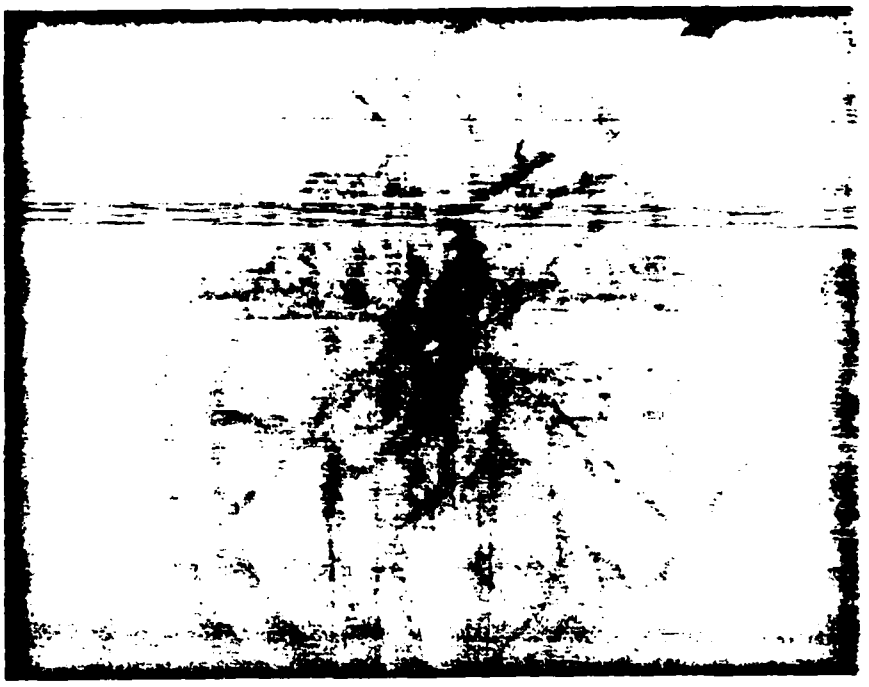

Figure 3.7 X-Radiograph of Post-Impact Damages in a 48-Ply Quasi-Isotropic Laminate.

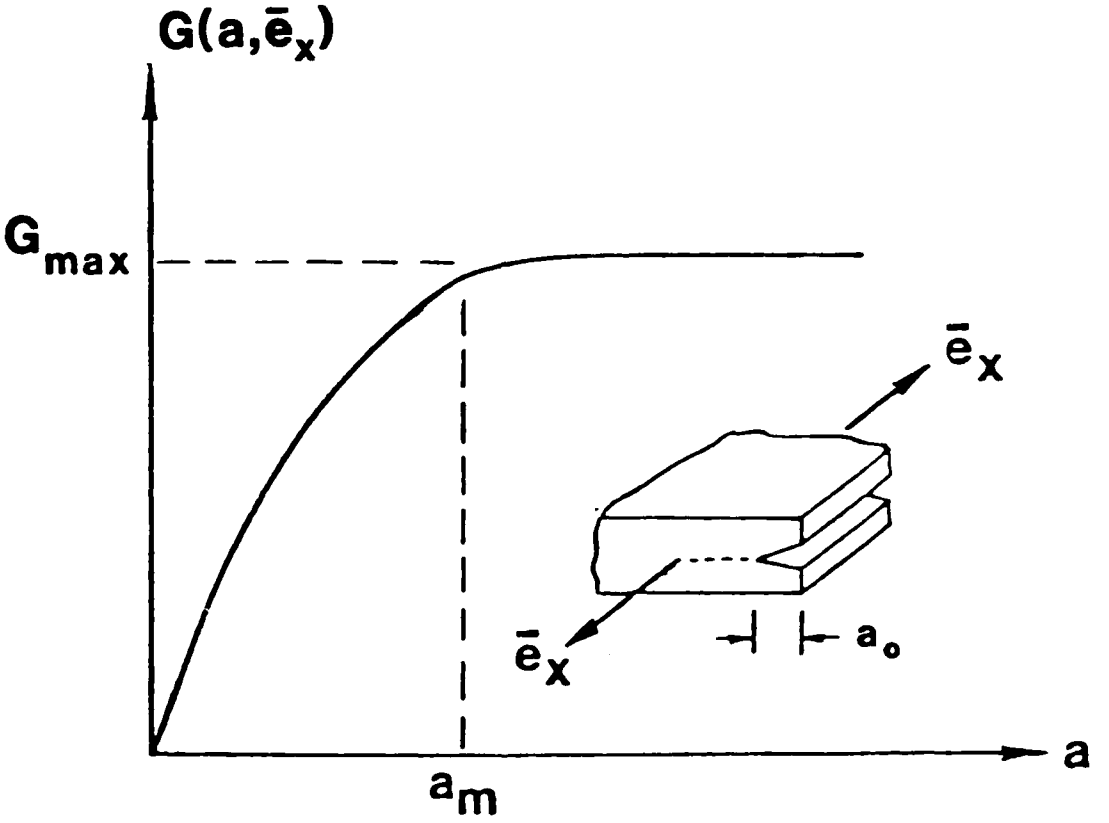

Figure 3.8 Typical Behavior of Energy Release Rate for Edge Delamination.

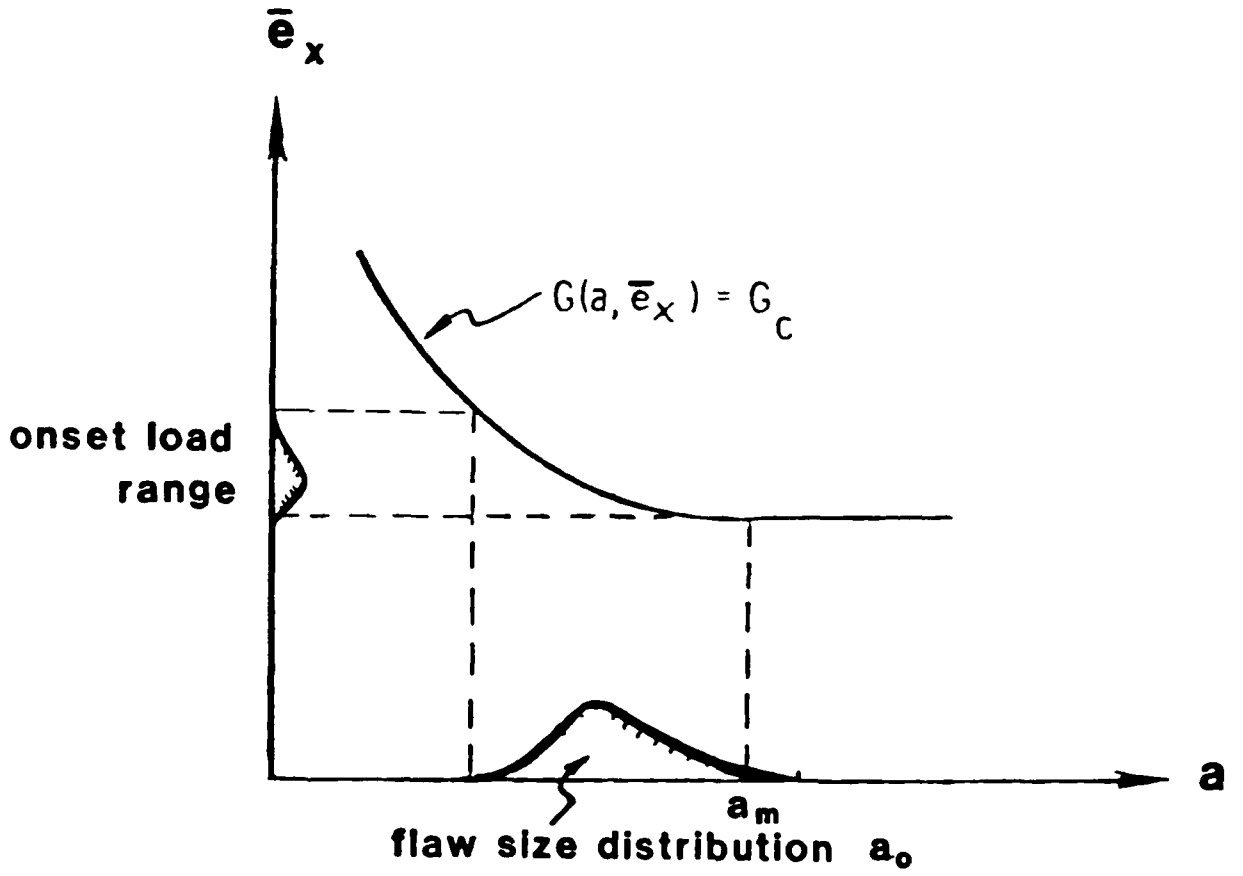

Figure 3.9 Load-Flaw Size Relationship for Edge Delamination Based on Griffith Type Fracture Criterion.

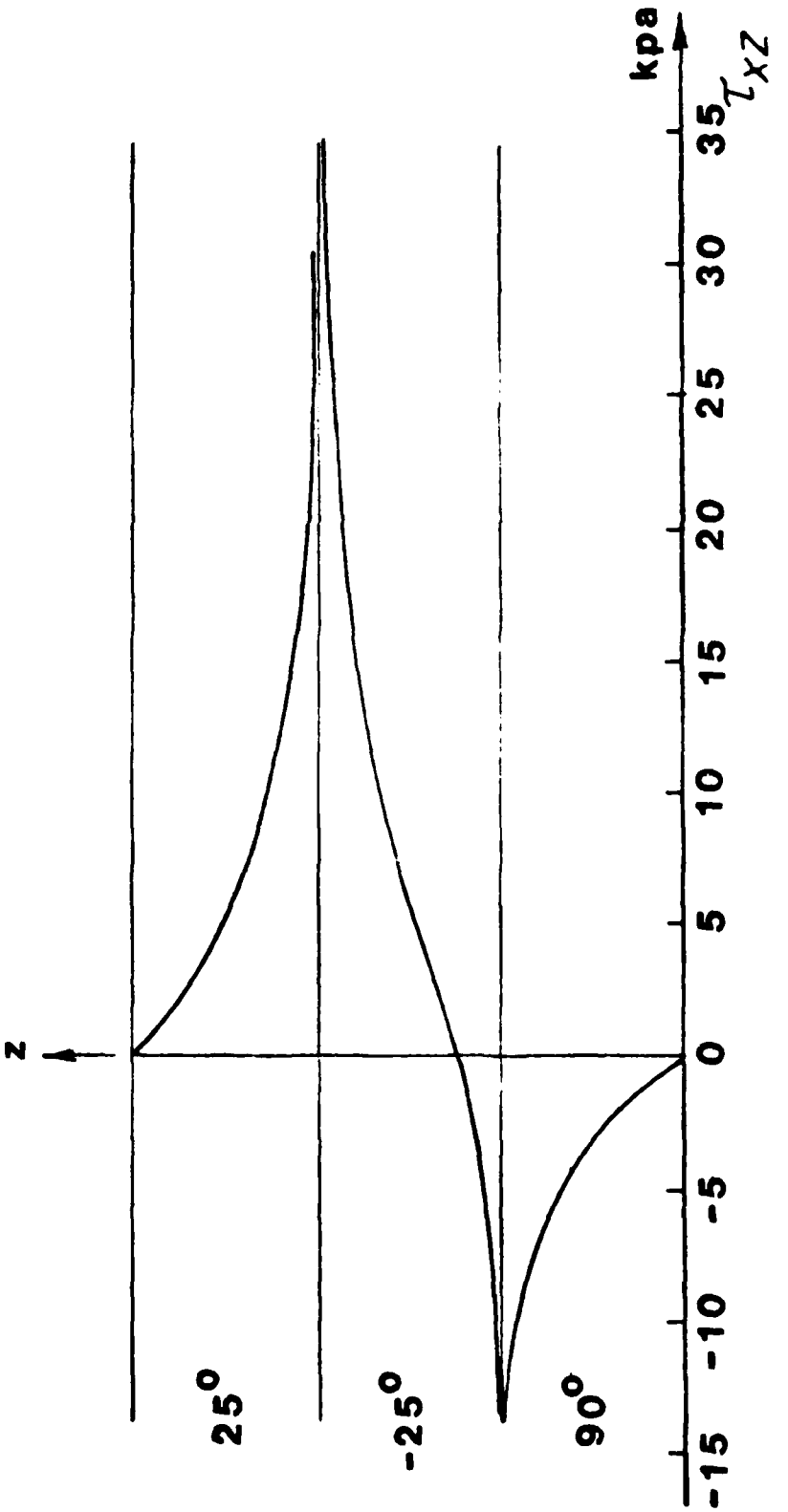

Figure 3.10 Through-Thickness Distribution of τ_{xz} Near the Free Edge of a $[\pm 25/90]_s$ Tensile Coupon.

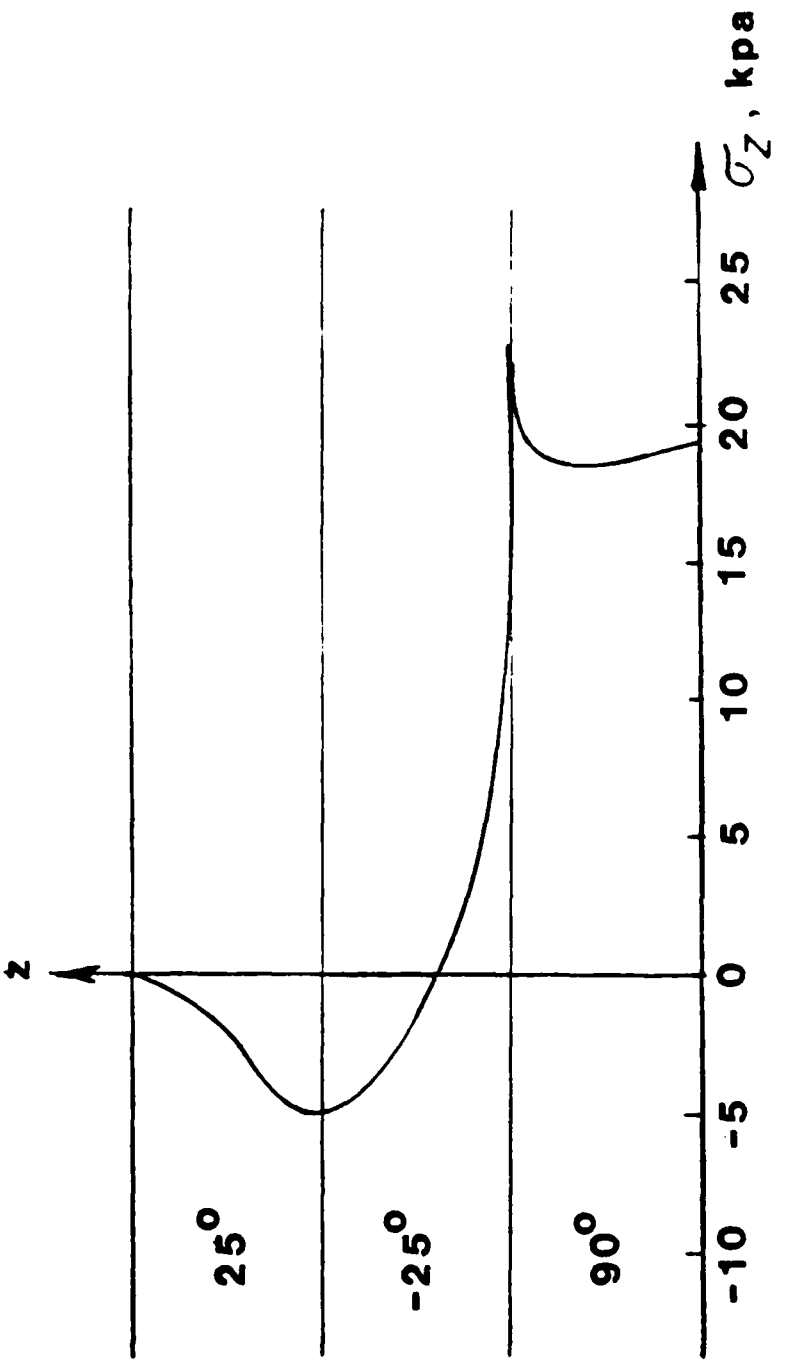

Figure 3.11 Through-Thickness Distribution of σ_z Near the Free Edge of a $[\pm 25/90]_s$ Tensile Coupon.

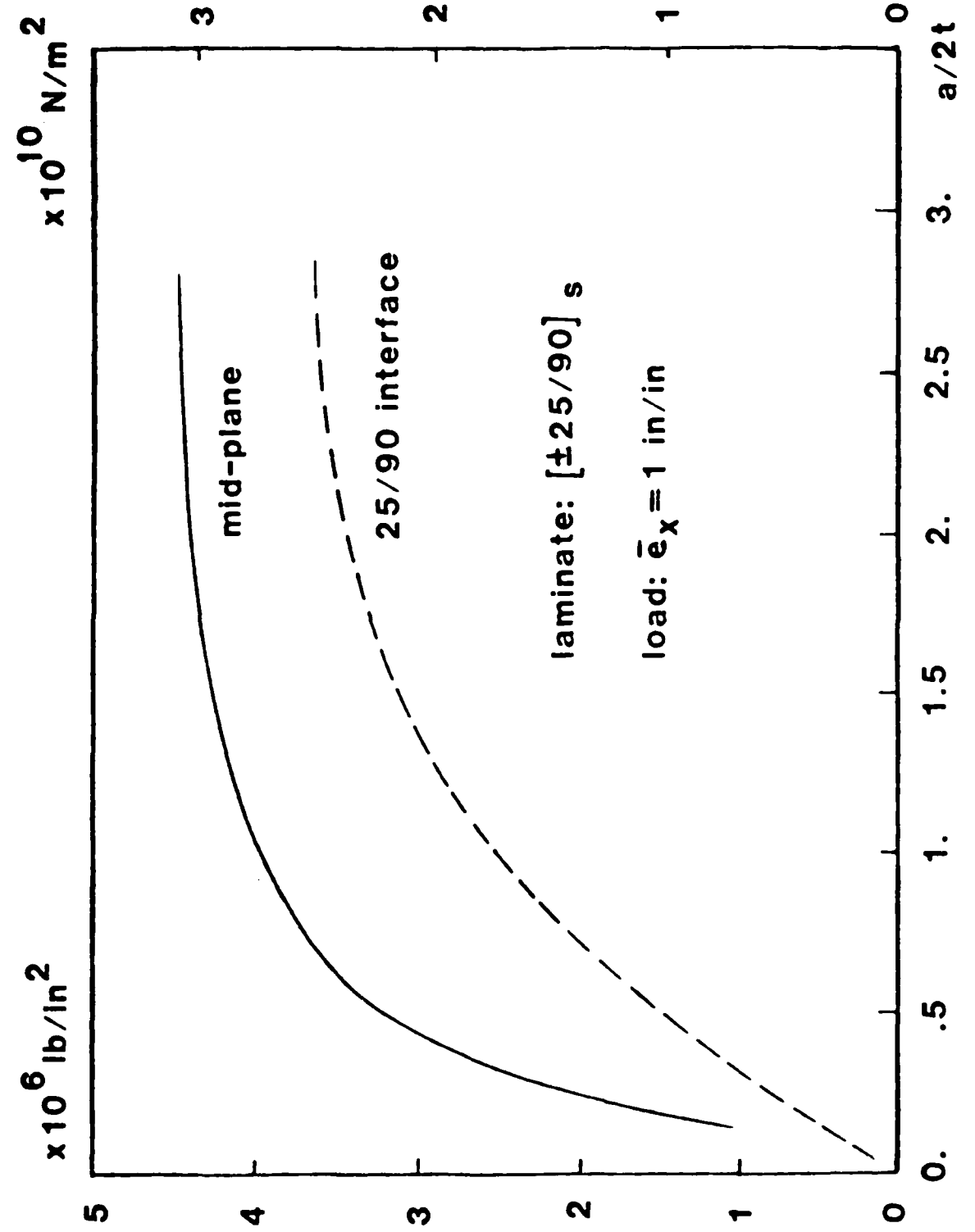

Figure 3.12 Computed Energy Release Rate Coefficient $C_e(a)$ for the $[\pm 25/90]_s$ Tensile Coupon.

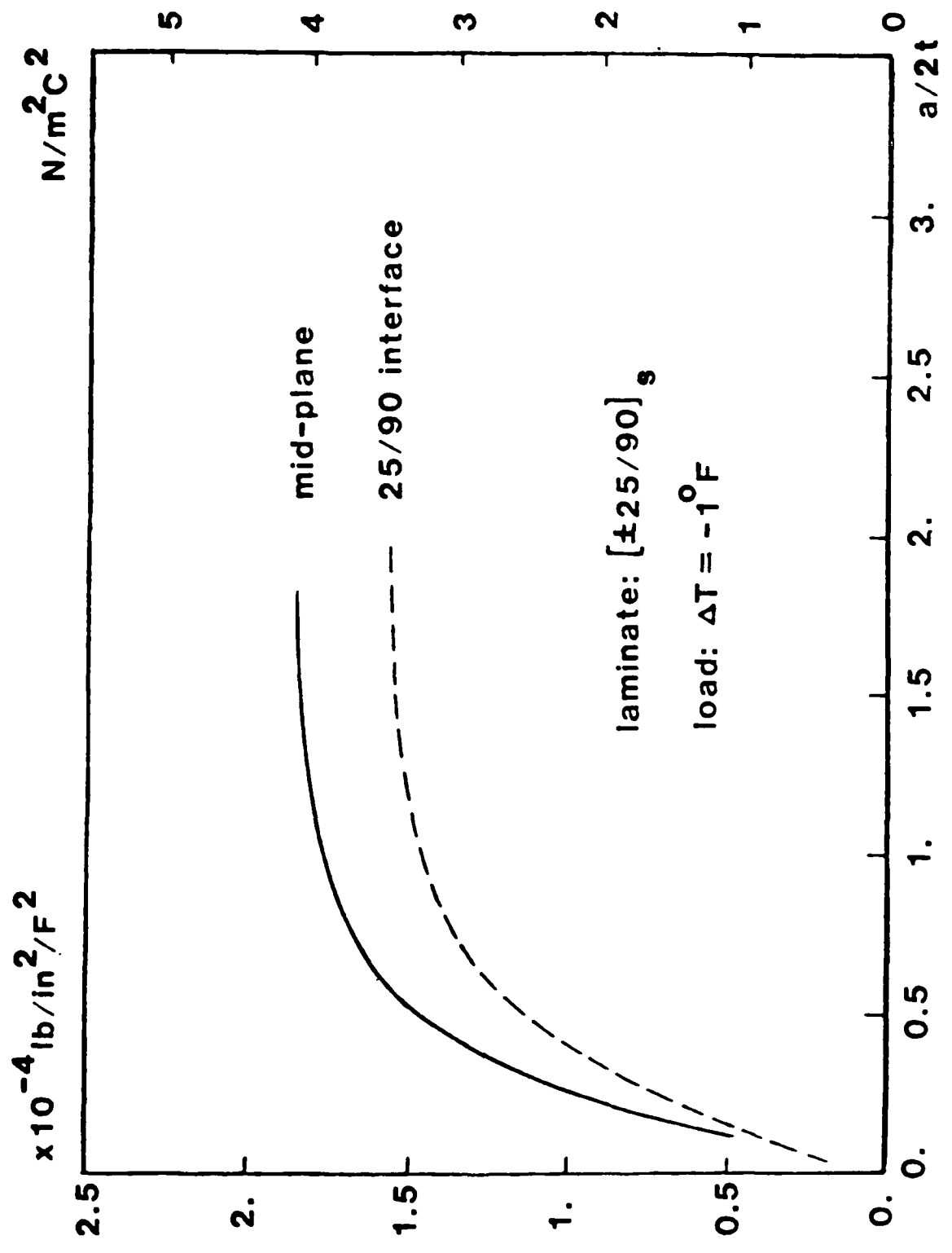

Figure 3.13 Computed Energy Release Rate Coefficient $C_T(a)$ for the $[\pm 25/90]_s$ Tensile Coupon.

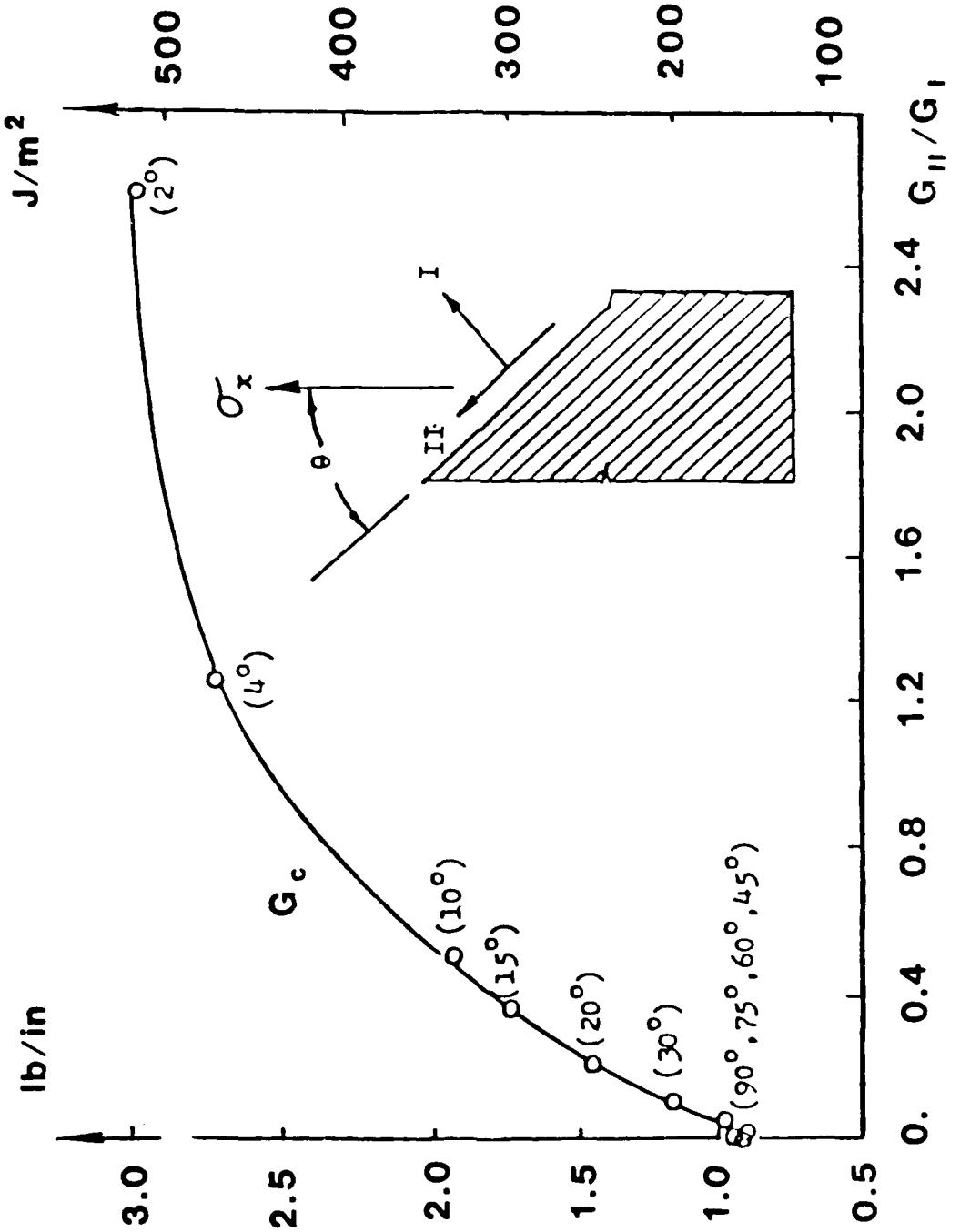

Figure 3.14 Total Critical Energy Release Rate G_c as a Function of the Ratio G_{II}/G_I T300/934

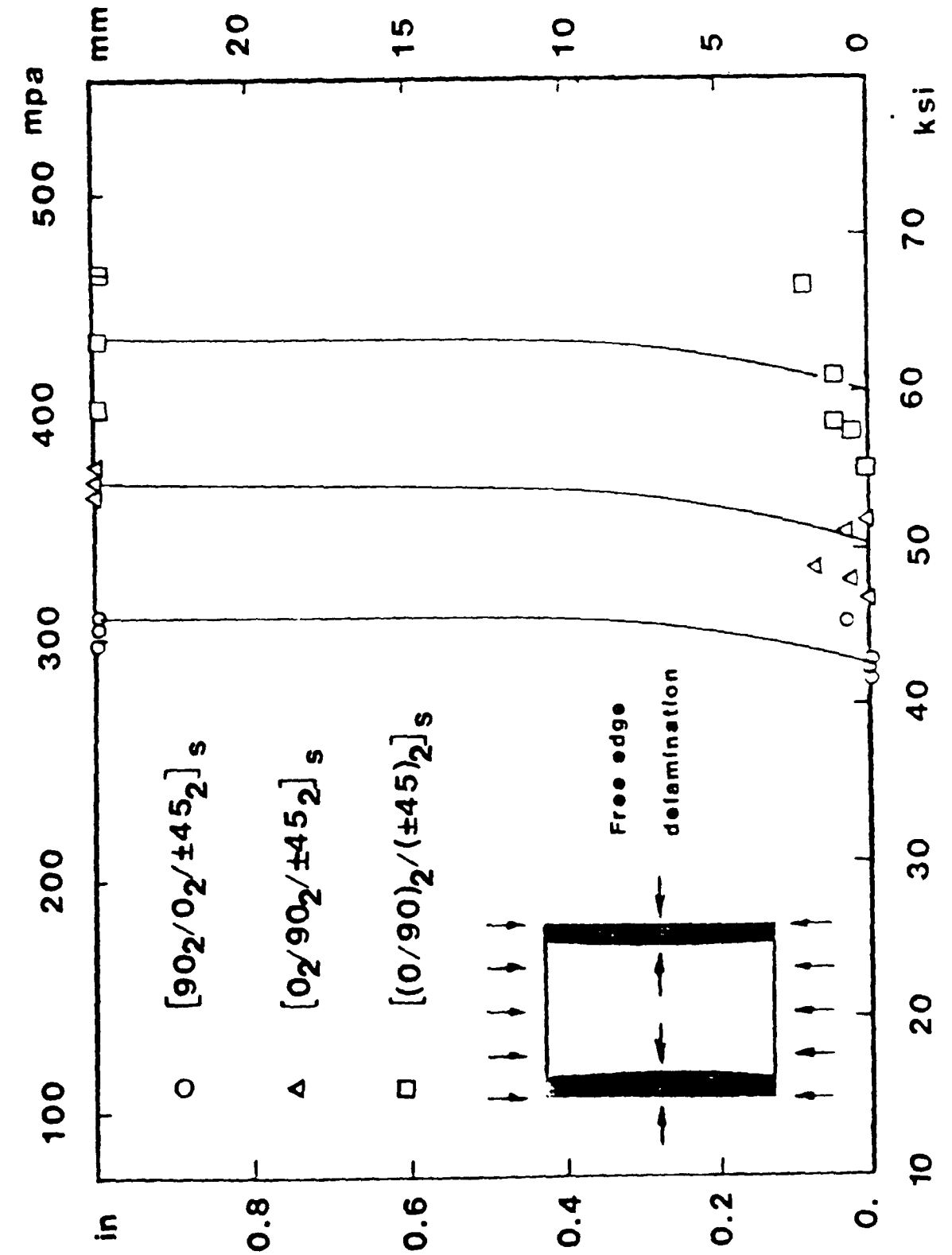

Figure 3.15 Experimental Free Edge Delamination Growth Plotted Against the Applied

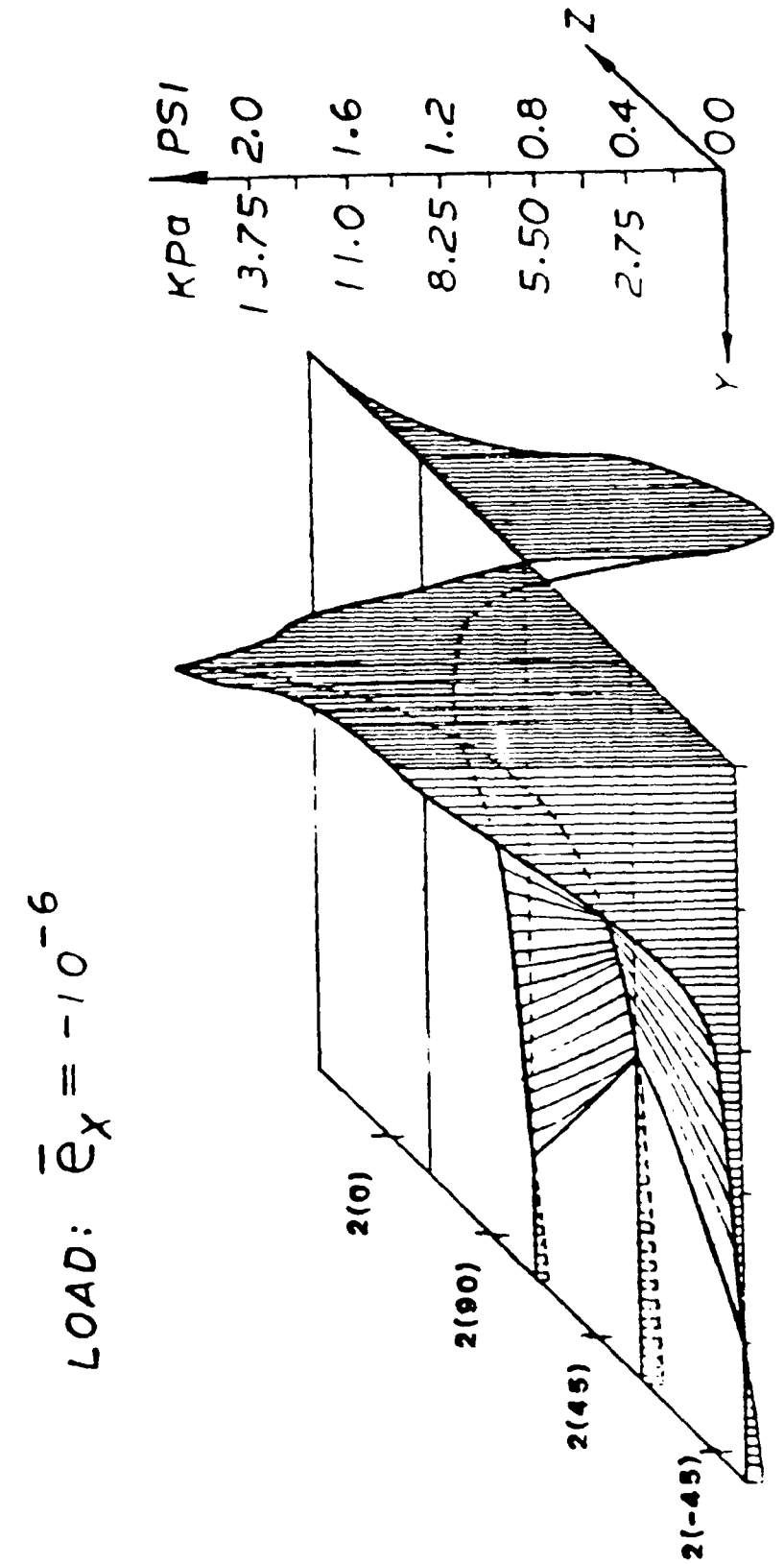

Figure 3.16 Cross-Sectional View of σ_z Distribution in the $[0_2/90_2/\pm45_2]_s$ Compression Coupon.

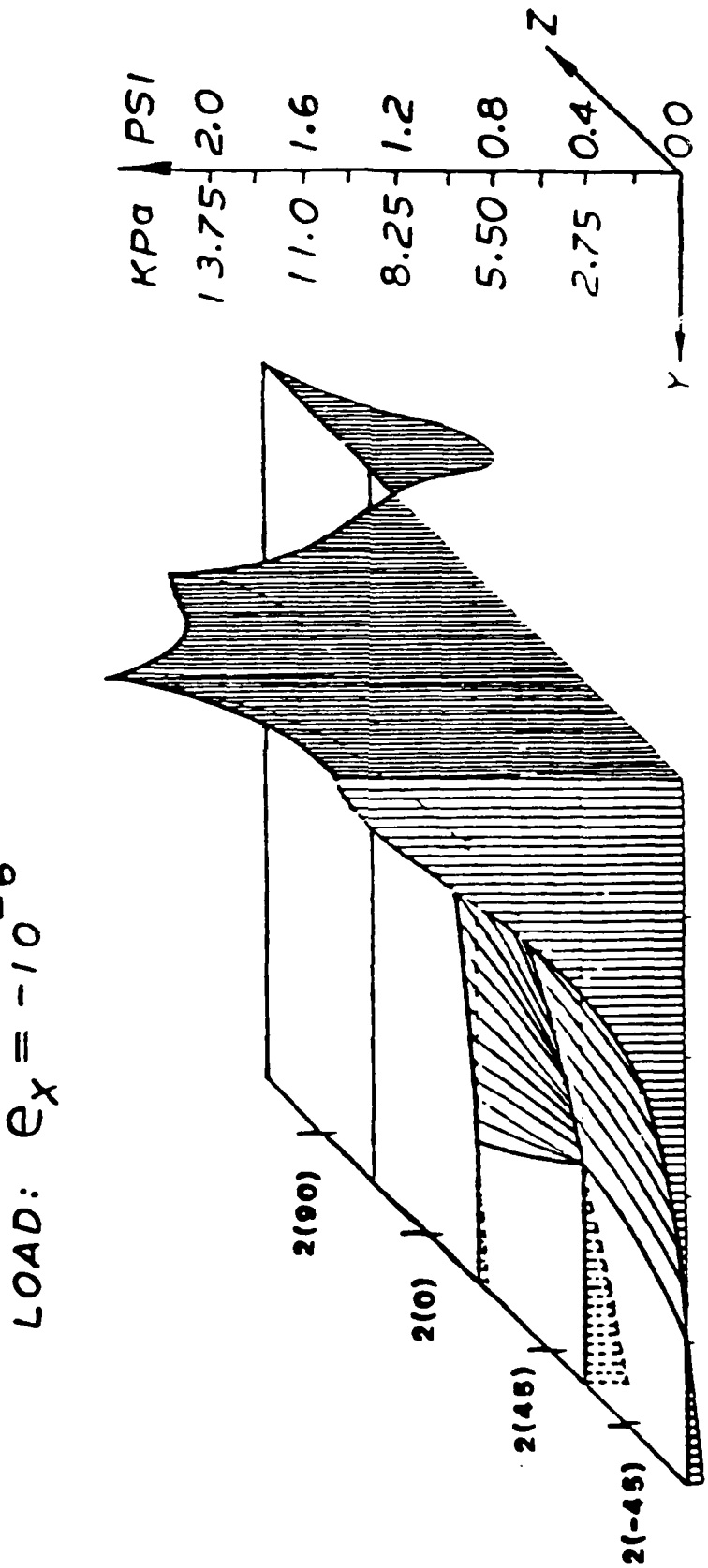

Figure 3.17 Cross-Sectional View of σ_z Distribution in the $[90_2/0_2/\pm 45_2]_s$ Compression Coupon.

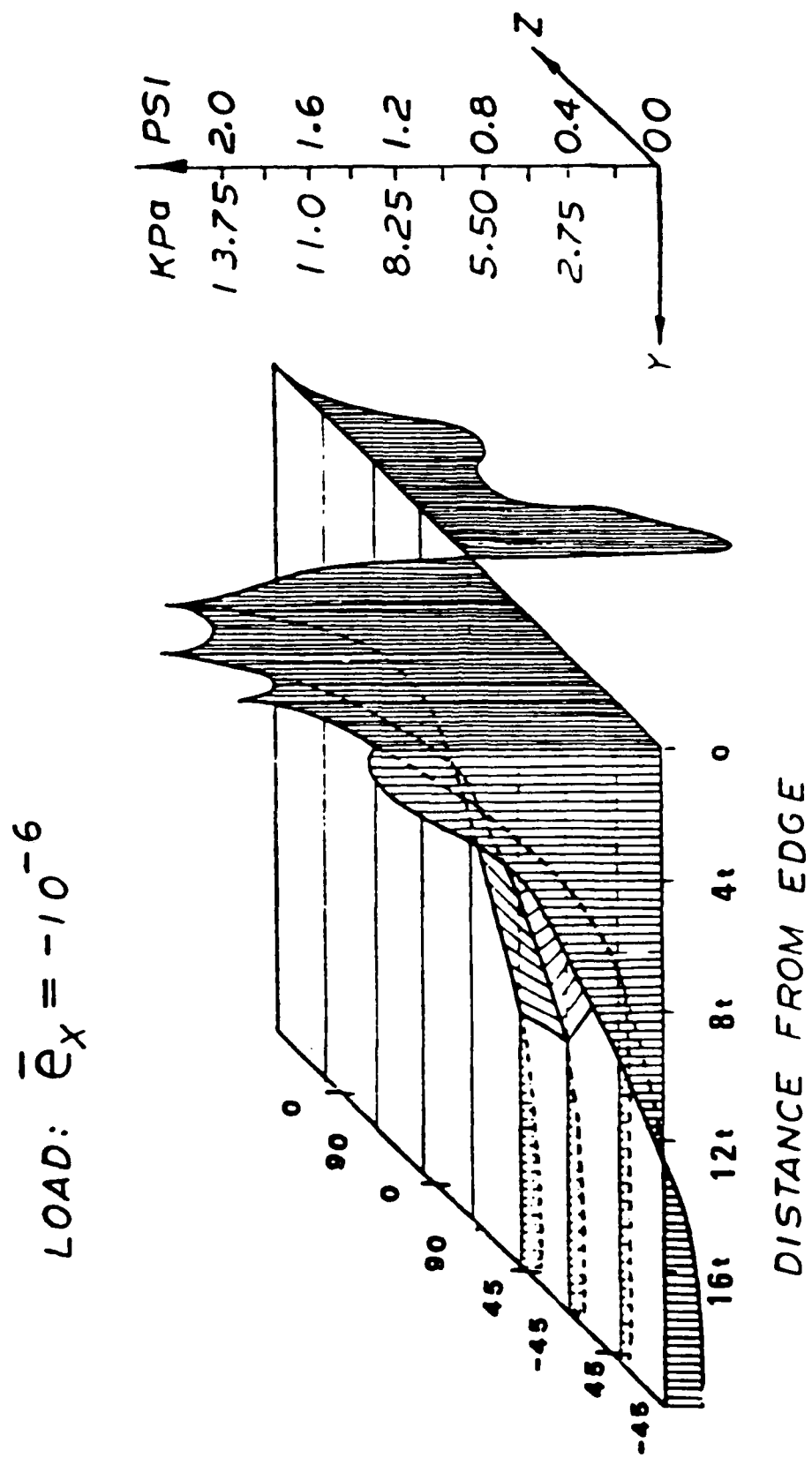

Figure 3.18 Cross-Sectional View of σ_z Distribution in the $[(0/90)_2/(\pm 45)_2]_s$ Compression Coupon.

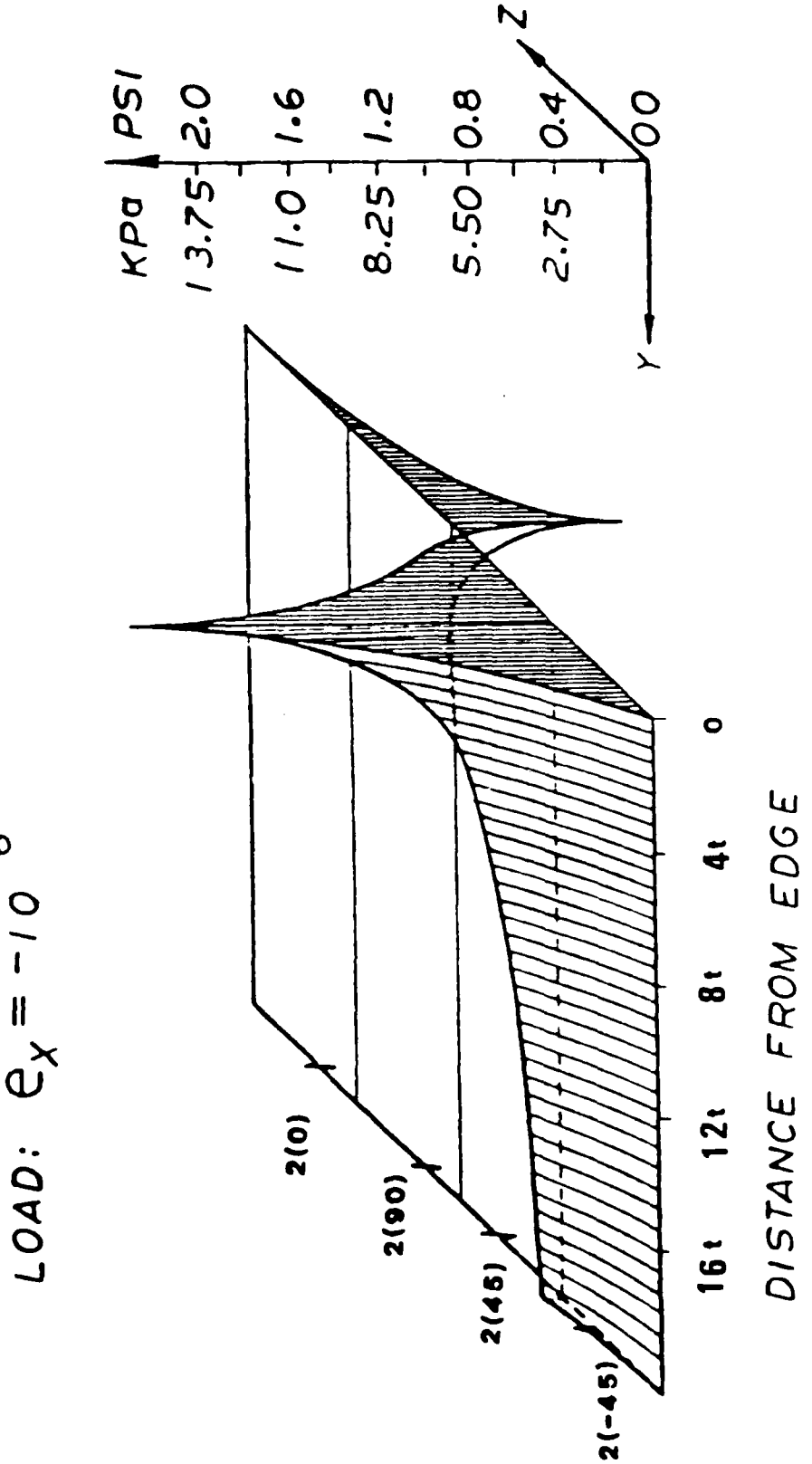

Figure 3.19 Cross-Sectional View of τ_{xz} Distribution in the $[0_2/90_2/\pm 45_2]_s$ Compression Coupon.

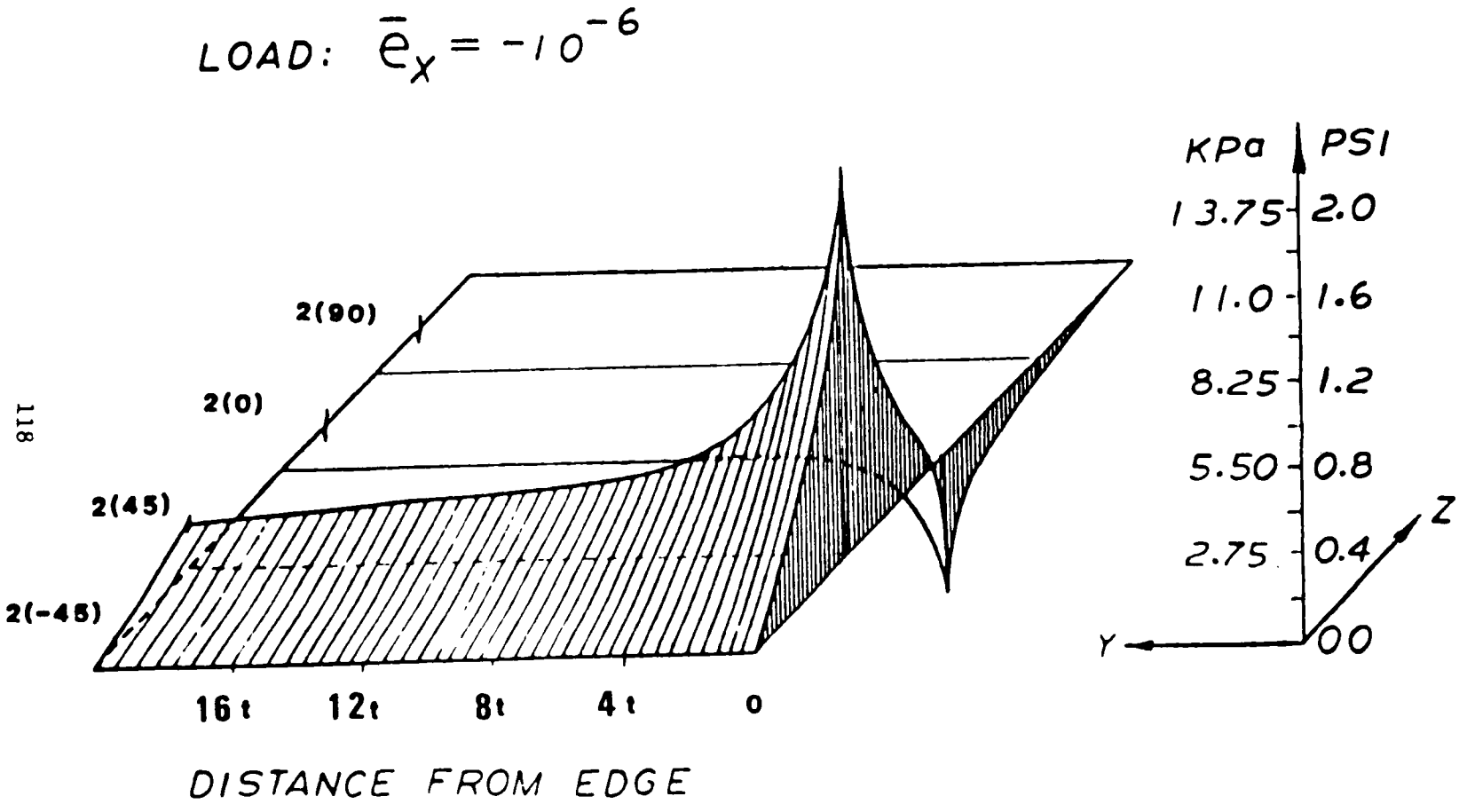

Figure 3.20 Cross-Sectional View of τ_{xz} Distribution in the $[90_2/0_2/\pm45_2]_s$ Compression Coupon.

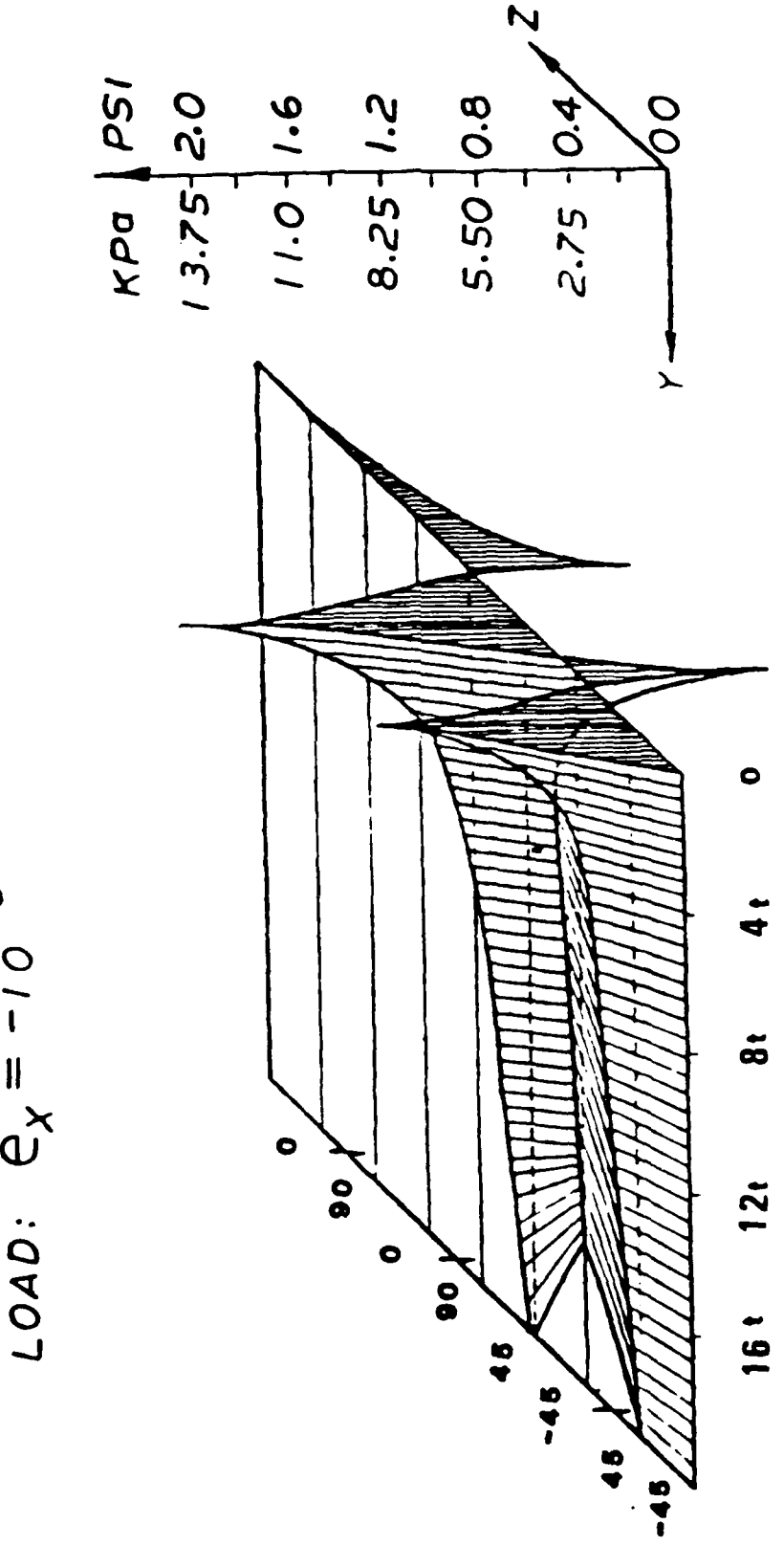

Figure 3.21 Cross-Sectional View of τ_{xz} Distribution in $[(0/90)_2/(\pm 45)_2]_s$ Compression Coupon.

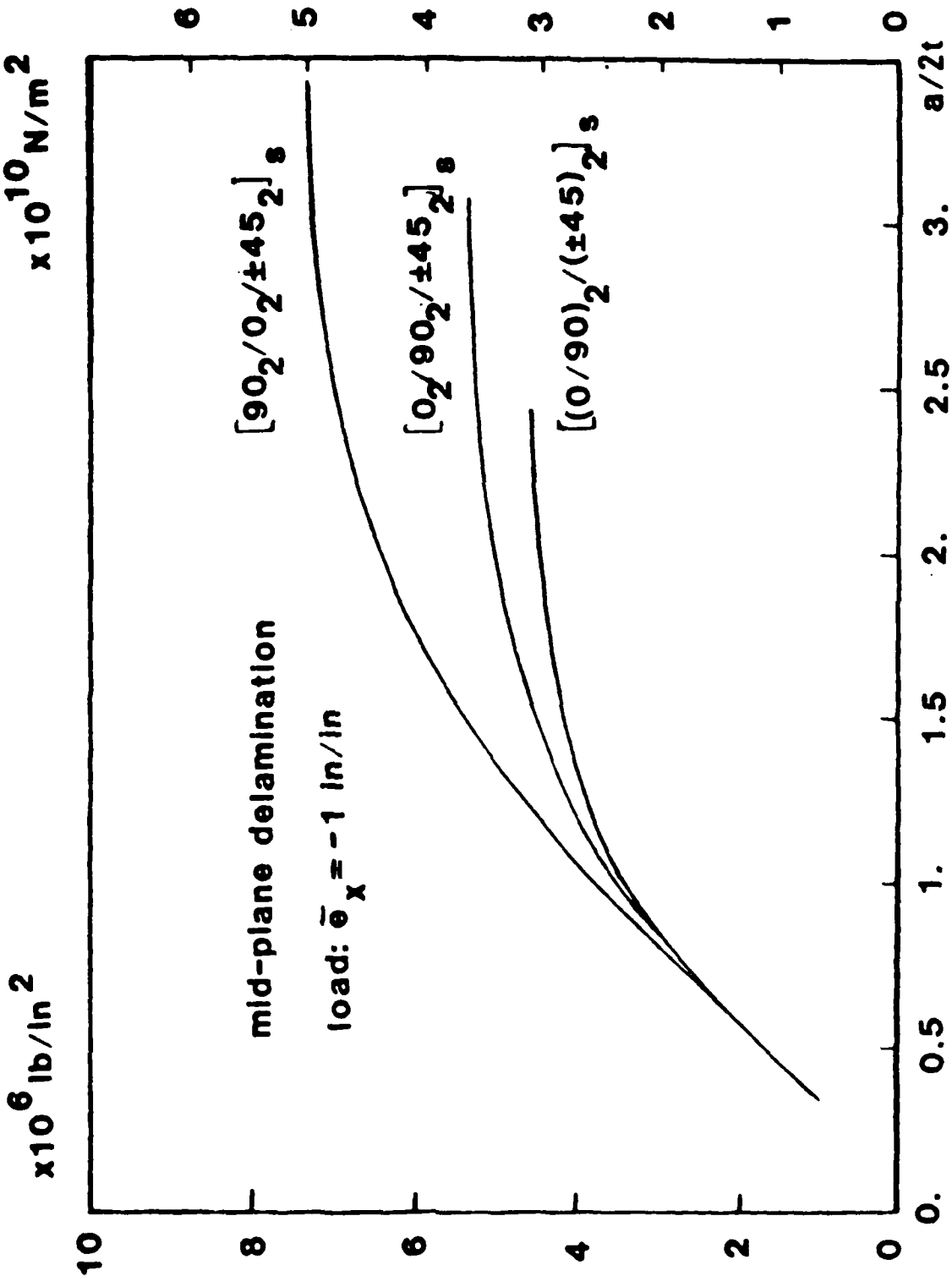

Figure 3.22 Mode-I Energy Release Rate Coefficient $C_e(a)$ for all Three Compression Coupons.

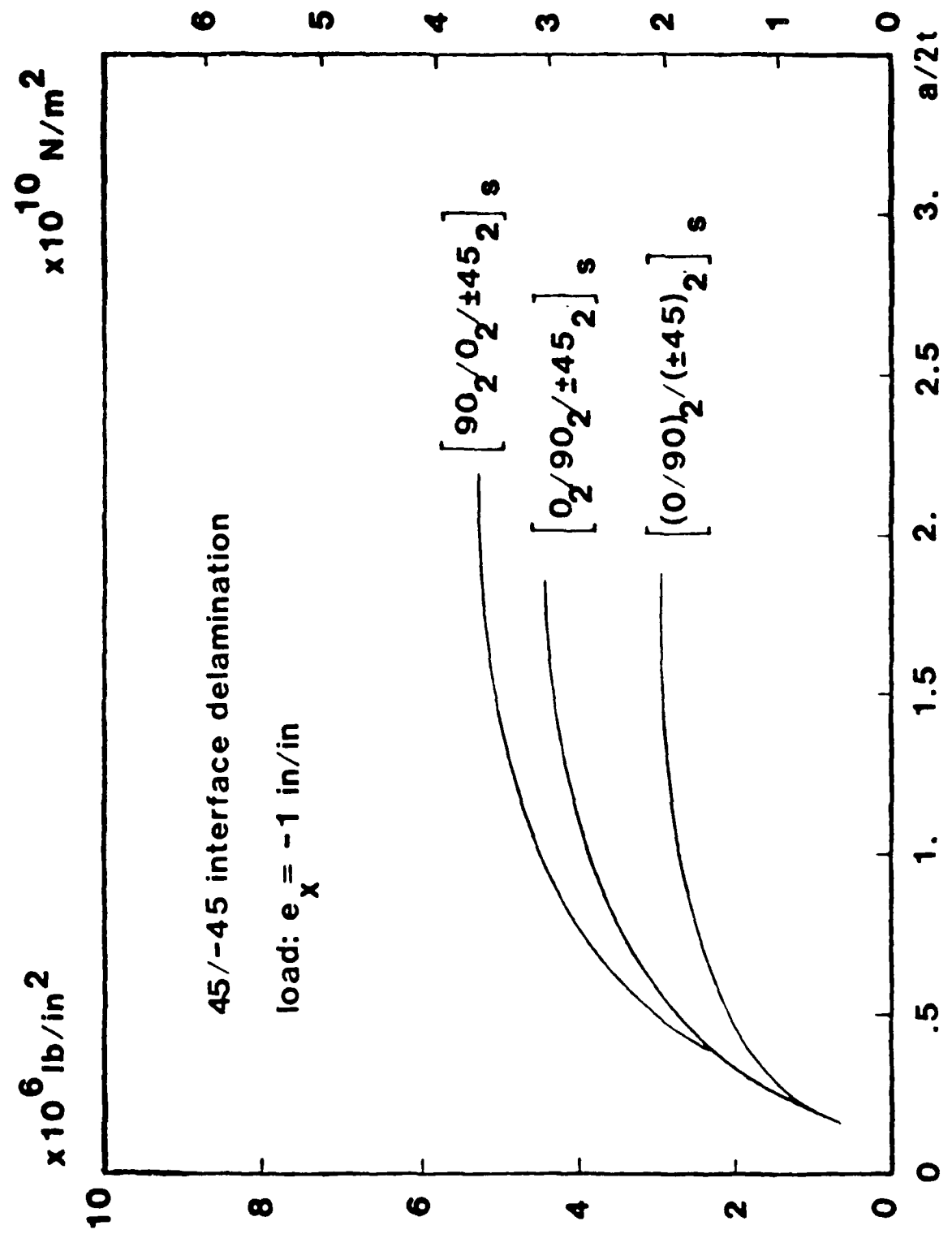

Figure 3.23 Mixed-Mode Energy Release Rate Coefficient $C_e(a)$ for all Three Compression Coupons.

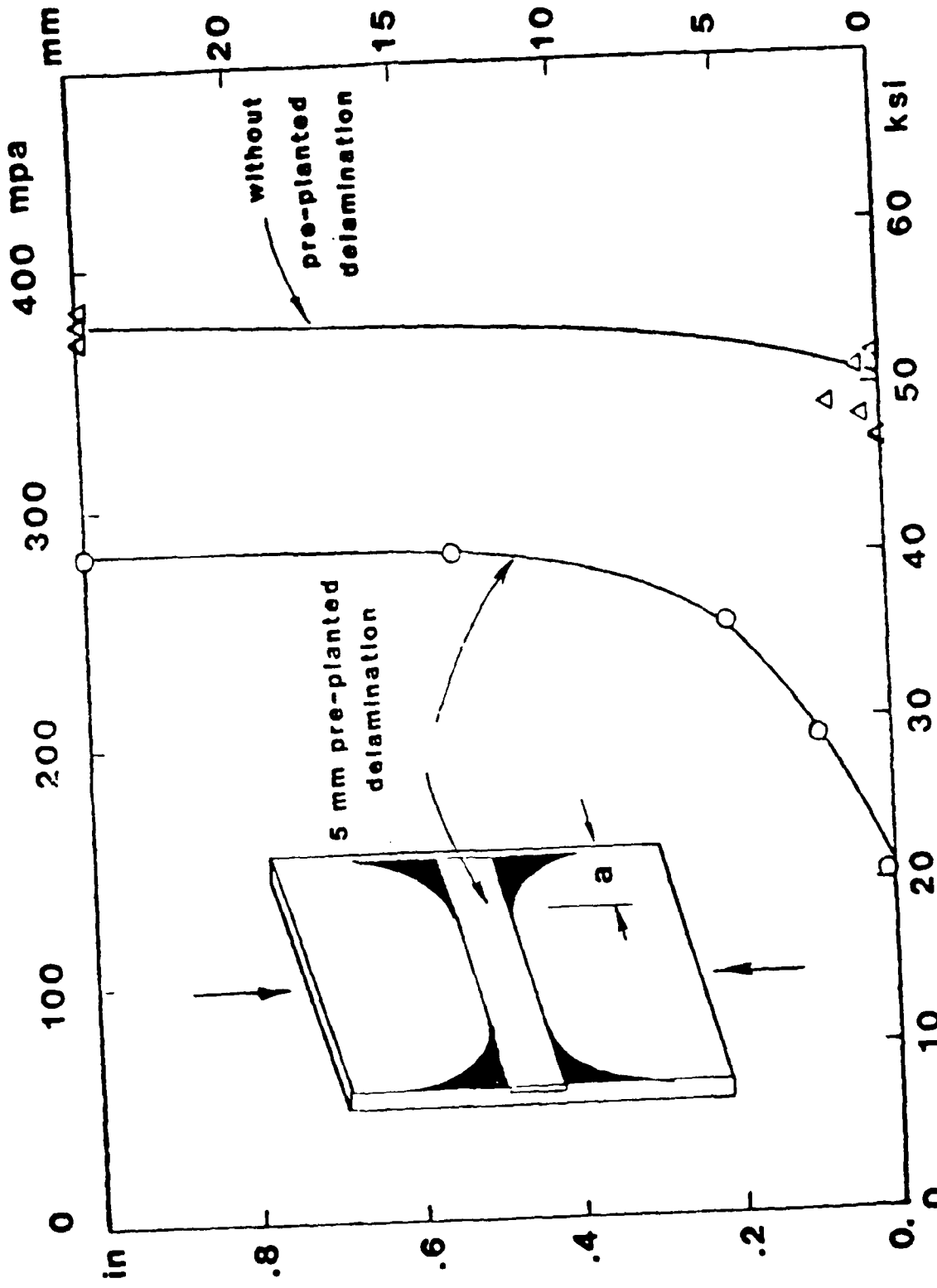

Figure 3.24 Experimental Delamination Growth Plotted Against the Laminate Stress in $[0_2/90_2/\pm45_2]_s$ Compression Coupons with and without Preplanted Delamination.

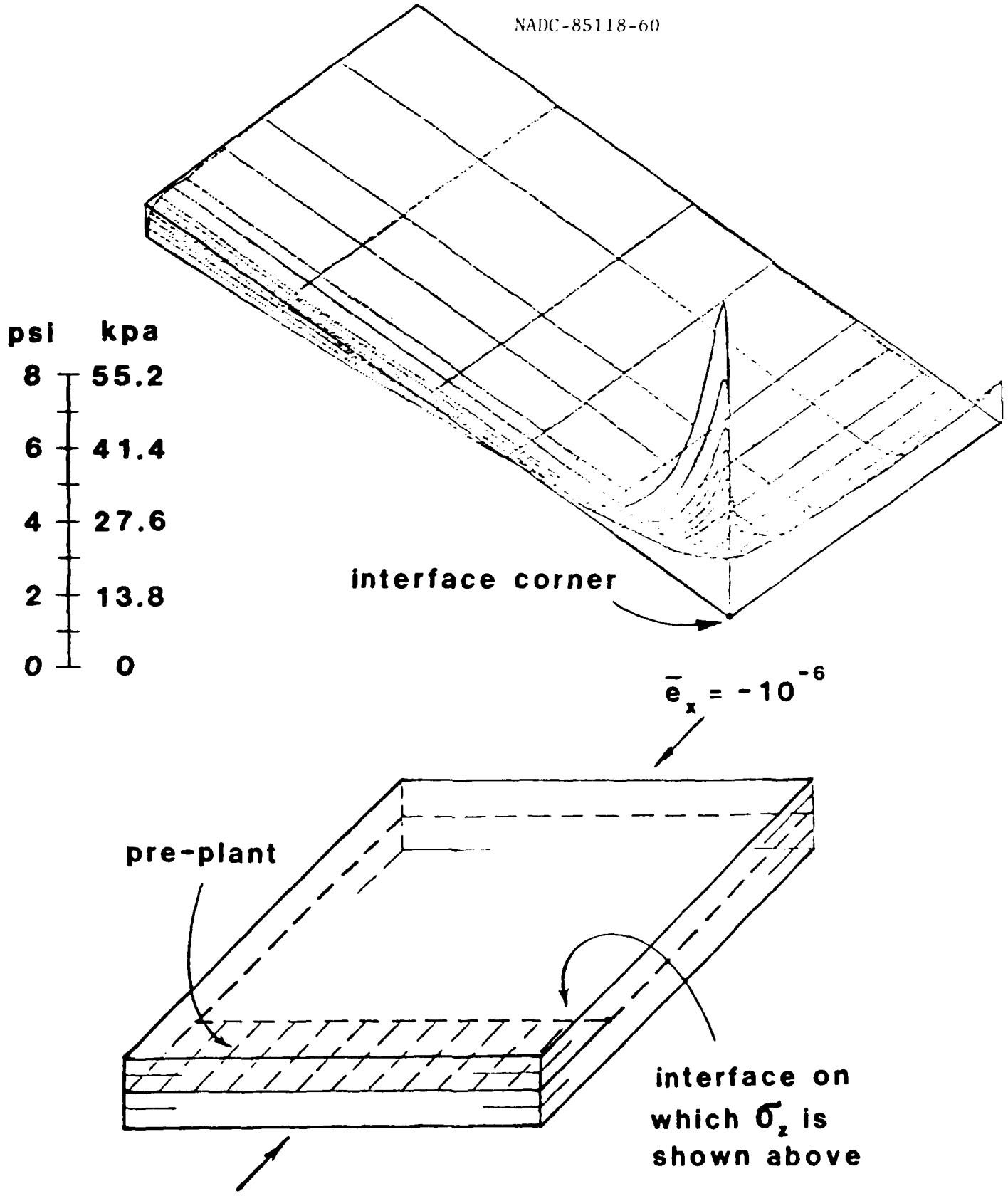

Figure 3.25 An Interface Plane View of σ_z Distribution in the $[0_2/90_2/\pm45_2]_s$ Compression Coupon with the Implant.

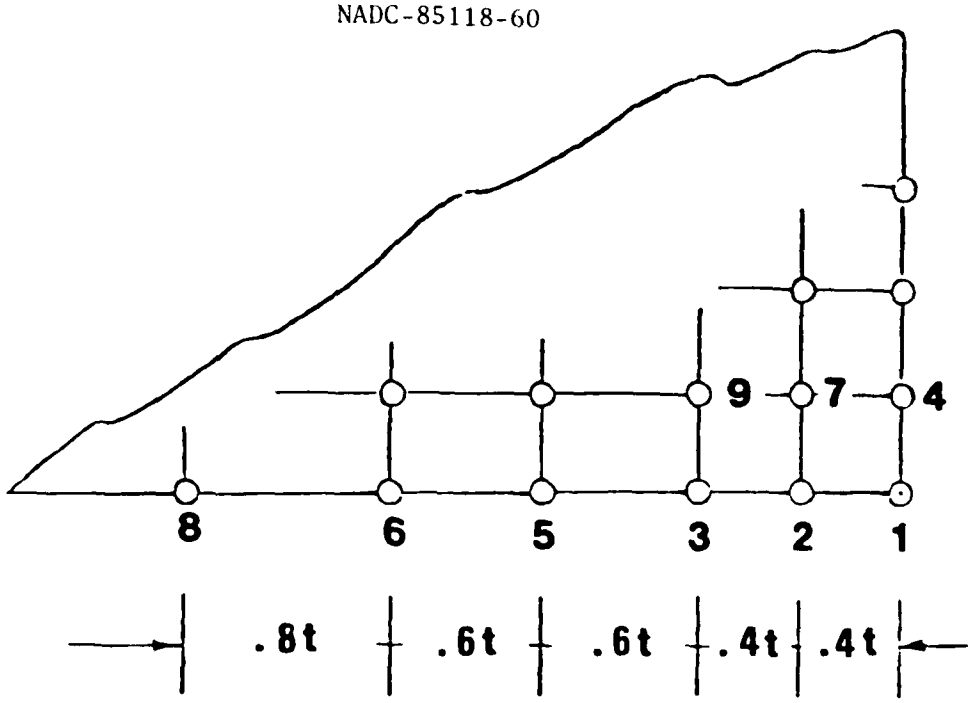

(a)

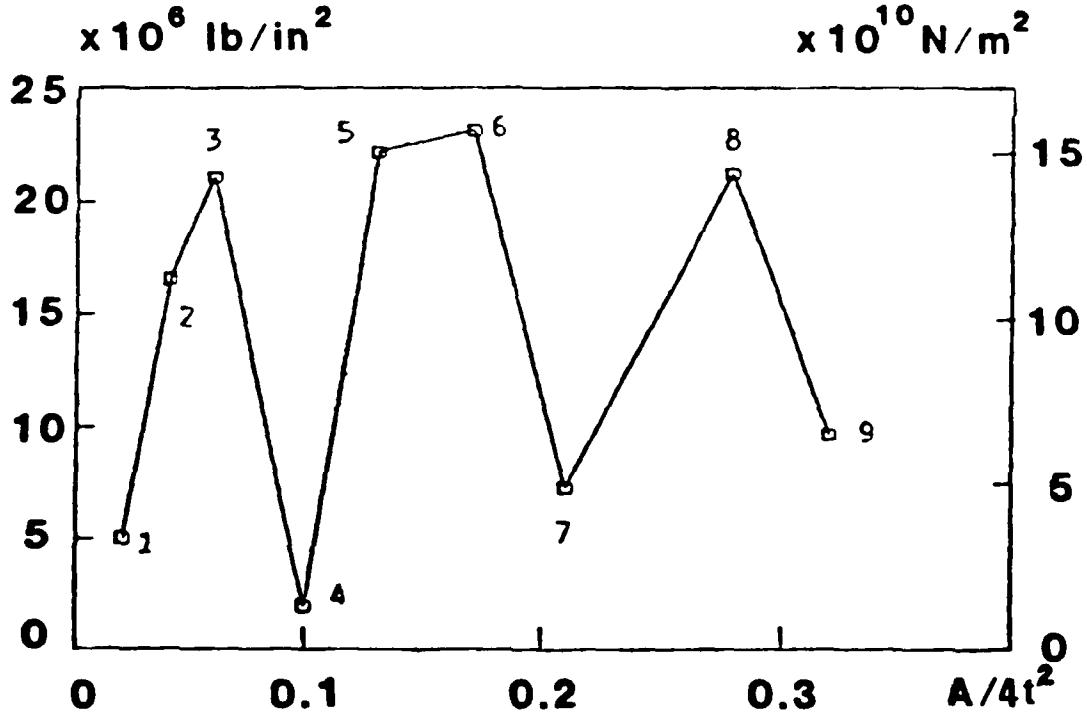

(b)

Figure 3.26 The Proposed Initial Delamination Nodal Release Sequence (above) and the Computed Energy Release Rate Coefficient $C_e(A)$.

CHAPTER IV. ANALYSIS OF LATE-STAGE MATRIX CRACKING

4.1 Matrix Cracks at High Load Levels

From the analysis in the previous chapters, it may be concluded that matrix damage begins generally with the formation of intraply cracks in the secondary or non-loading plies. In one example discussed in Chapter II, the cross-ply $[0_2/90_4]_s$ laminate suffered sporadic transverse cracks in the 90°-plies at laminate strains as low as 0.2% to 0.3%. Since many laminates designed for practical usage can reach ultimate tensile strains in excess of 1%, early stage intraply cracking in the secondary plies is often tolerated as benign service-related defects.

In some instances, interlaminar matrix cracking in the form of delamination can occur before intraply cracking. Such occurrences are mostly confined to localized areas, such as near the laminate free edges, around man-made notches or at the leading edges of internal damages, where high concentration of interlaminar stresses is present.

In any event, both types of matrix cracking are undesirable from the laminate reliability and durability viewpoint. This is because matrix cracks in secondary plies can precipitate matrix cracks into the load-carrying plies, under either monotonically increasing or cyclically applied loads.

In the cross-ply laminates discussed in Chapter II, for instance, transverse cracks in the 90°-plies did not seem to affect the structural performance of the laminate until about 90% the ultimate load [38]. Toward the late-stage of loading, however, in-ply matrix splits in the 0°-plies were found throughout the interior of the laminates. The splits are orientated parallel to the applied tension and cross-over the 90°-ply transverse cracks that formed early. As soon as a 0°-ply split formed and crossed over a 90°-ply transverse crack, localized delamination in the 0/90 interface was found near

the crossing. Subsequent rapid propagation of many of the cross-cracks induced delaminations eventuated a massive 0/90 interface separation. This event was followed almost immediately by catastrophic failure of the 0°-plies. The last failure event involved fiber breaking in the split 0°-plies. Figure 4.1 shows a sequence of x-ray photographs that illustrate the matrix cracking proliferation process of a $[0_2/90_3]_s$ laminate during its late-stage loading. These photographs clearly demonstrate that matrix cracks in non-loading plies can become detrimental to the load-carrying plies at high load levels.

Laminates of more practical lay-ups suffer similar late-stage matrix cracking, though the sequence of events may not be the same [47]. Experiments using small coupons confirmed that late-stage matrix cracking patterns are usually generic to the lamination geometry (stacking sequence, ply thickness, etc.) and the nature of loading [47, 48]. The same factors that are important in the early-stage matrix cracking continue to play a dominate role during the late-stage matrix cracking.

The objective of this chapter is to investigate some of the basic mechanisms associated with late-stage matrix cracking. The basic macromechanics/ply elasticity approach discussed in the previous chapters is followed. Since the cracks concerned involve three dimensional and localized stress fields, the finite element routine developed in Reference [28] is employed in the analysis.

In order to achieve a cohesive discussion, emphasizing mechanisms rather than the analysis method, a specific family of laminates will be analyzed. Namely, the T300/934 tensile coupons $[0_2/90_n]_s$, $n = 1, 2, 4$ are investigated again for late-stage matrix cracking. A complete documentation of damage accumulation up to final laminate failure is available in Reference [38]; so a comparison between the analysis and experiment can be made.

4.2 Stress Field Near a Transverse Crack Terminus

Consider again the $[0_2/90_n]_s$ laminate coupon series under monotonic axial tension. Transverse cracks in the 90°-plies are formed during the early-stage loading. The effect of these cracks on damage development during the late-stage loading can be qualitatively studied by examining the behavior of the stress fields near the transverse crack termini.

Figure 4.2 shows a tensile coupon which already suffered 90°-ply transverse cracks. For the purpose of presentation only, consider the section of the laminate that contains only one transverse crack. Due to lamination symmetry, only one-eighth of this section needs to be modeled, see Figure 4.2. Details of the finite element sizing, mesh generation and other computational aspects are found in Reference [28] and will not be discussed here.

The computed stress field near the transverse crack terminus is complex, but the stresses can still be separated in two groups. The first group consists of the interlaminar stresses σ_z, τ_{xz} and τ_{yz} acting on the 0/90 interface. These stresses are responsible for delamination. The second group consists of the in-ply stresses σ_x, σ_y and τ_{xy} acting in the 0°-plies. These stresses may cause matrix damage in the 0°-ply, such as length-wise splitting, as well as fiber breaking.

Interlaminar Stresses. Figures 4.3 to 4.5 show, respectively, the interlaminar σ_z, τ_{xz} and τ_{yz} distributions on the 0/90 interface. In each display, the x-y plane coincides with the 0/90 interface; the x-axis coincides with the free-edge of the coupon, while the loci of the transverse crack terminus fall on the y-axis. One of the corner points labeled in Figure 4.2 is located at the x-y origin.

In each display, stresses for the $[0_2/90_2]_s$ and $[0_2/90_4]_s$ coupons are shown. The magnitude of the stresses is due to an applied laminate strain $\bar{e}_x = 1$ με. It is noted that the interlaminar stress fields for $n = 2$ and

n = 4 show similar distributional features, but with noticeable difference in magnitudes and in areas of concentration. In particular, the interlaminar normal stress σ_z is tensile in both cases, concentrated along the x and the y axes. This peculiar distribution is effected by both the free edge and the transverse crack in the 90°-layer.

The tensile σ_z and the shearing stresses τ_{xz} and τ_{yz} could cause delamination in the 0/90 interface, emanating from the corner point and growing into a delta-shaped contour as illustrated in Figure 4.6. An analysis of that problem will be presented in the next section.

In-Plane Stresses in 0°-Plies. As for the in-ply stress group - σ_x, σ_y and τ_{xy}, especially those existing in the 0°-plies, their intensities are also affected by the presence of the free edge and the transverse crack.

First, consider the distributional characteristics of these stresses in a plane parallel to the 0/90 interface, or the x-y plane. Figures 4.7 to 4.9 show, respectively, σ_x, σ_y and τ_{xy} distributions in the 0°-ply near the 0/90 interface. A severe stress concentration occurs near the transverse crack terminus and a less severe concentration occurs along the free edge in all cases. The 90°-layer thickness, or the value of n, is seen to influence both the stress concentration intensity and the size of the stress concentration zone.

Of the three in-plane stresses, the magnitude of τ_{xy} in Figure 4.9 is relatively small, though its distributional behavior is quite dramatic near the corner point. However, σ_x and especially σ_y, magnified significantly by the presence of the transverse crack, will cause damage in the 0°-ply. In particular, both stresses are in tension throughout the field and each can cause a different mode of failure of the 0°-ply.

The thermal residual stresses due to thermal mismatching of the 0° and 90° plies are also significant. For reasons of brevity, they are not shown,

but their distributional features are similar to those displayed in Figures 4.3 to 4.5, and 4.7 to 4.9. When coupled with the applied load, the role of the thermal stresses in matrix damage development cannot be ignored.

The distributional behavior of σ_x and σ_y in the 0°-layer near the transverse crack terminus cannot be fully revealed by displays such as Figures 4.7 and 4.8. Both stresses also vary dramatically throughout the thickness of the 0°-layer.

Figure 4.10 shows the σ_x distribution in the 0°-layer thickness above the transverse crack terminus (see figure inset). Note that the part due to the applied tension, $\bar{e}_x = 1\ \mu e$, is tensile throughout the thickness and is highly concentrated approaching the 0/90 interface. The part due to thermal cooling, $\Delta T = -1°F$, is compressive, except near the transverse crack root region where it becomes tensile with significant magnitude. The combined σ_x near the transverse crack terminus region displays varied degree of concentration, depending on the thickness of the 90°-layer in which the transverse crack is situated.

It is apparent that concentrations of σ_x near the transverse crack sites may have a profound effect on the breaking strength of the 0°-ply fibers. Several recent experiments [47, 48] found broken fibers in the 0°-plies at locations where adjacent 90°-ply transverse cracks had occurred.

Figure 4.11 displays a similar distribution for σ_y, which is an in-plane stress normal to the fibers of the 0°-ply. It is seen that the part of σ_y due to $\bar{e}_x = 1\ \mu e$ and the part due to $\Delta T = -1°F$ are both tensile throughout the thickness of the 0°-layer. Both are magnified in intensity near the 90°-ply transverse crack terminus. The near-field σ_y distribution is seen to vary again with the 90°-ply thickness or the value of n. The high tensile stress is capable of causing matrix cracks in the 0°-layer in the form of longitudi-

nal splits. The splits occur in much the same manner as the 90°-ply transverse cracks discussed in Chapter II.

4.3 Damage Modes Effected by Transverse Cracks

From the preceding section, it may be summarized that the presence of transverse cracks in the $[0_2/90_n]_s$ laminates can cause three possible damage modes, all of which are localized near the transverse crack termini. Of the three possible modes, the 0/90 interface delamination and the 0°-ply longitudinal splitting are matrix-dominated cracks, while 0°-ply fiber breaking is something different fundamentally. The subject of fiber breaking requires a different theoretical treatment and is outside the scope of this discussion. Hence, only the localized delamination and 0°-ply splitting are analyzed in this section.

Onset of Delamination at Transverse Crack Terminus. The physical reason for delamination at a transverse crack terminus is quite clear. The major stresses causing delamination in the 0/90 interface are the concentrated tensile σ_z and shearing τ_{xz}. The other shear stress τ_{yz} appears to be negligible, see Figures 4.3 to 4.5. These stresses attain their highest magnitude at the corner point where interactions take place between the transverse crack and the free edge, see Figure 4.6. Thus, if a delamination is to occur, it would probably start from this point and propagate into a plane contour as shown in the figure.

In order to make a prediction for the onset and the growth behavior of the contoured delamination, a small interface effective flaw will again be assumed, located near the corner point. This assumption is in accordance with the effective flaw concept discussed earlier. Then, under the applied tension, the assumed flaw starts to propagate and becomes a local delamination. Following the energy release rate methodology outlined before, the

growth of the crack front can be mimicked by a sequence of nodal-point releases (Figure 4.6) in the finite element net-work, shown in Figure 4.2. As each finite element node is released, the corresponding delamination area as well as the strain energy lost can be approximately computed (for details, see References [28]). In this manner, a relationship between the delaminated area and the strain energy release rate is obtained for the assumed delamination growth.

Figure 4.12 shows the computed energy release rate coefficient C_e (for $\bar{e}_x = 1$) plotted against the assumed delamination area contour for the $[0_2/90_2]_s$ laminate. Note that C_e consists of all three modal components of cracking. In this case, the mode-I (z) component is slightly larger than the mode-II (y) component, while the mode-III (x) component is negligible.

Figure 4.13 shows the C_T coefficient for the laminate subjected to $\Delta T = -1°F$ (or $-0.65°C$). The general character of C_T and its three modal components of cracking are similar to those of C_e. The calculated C_e and C_T coefficients are based on the assumed nodal release sequence (shown in Figure 4.6), which may not be the best representation for the actual delamination growth. But, the general trend of these coefficient functions indicates that the initial delamination growth is basically stable, as is the case observed in experiment.

Now, assume that the starting size of macroscopically observable delamination is about $4t^2$ (where 2t is one ply thickness) so that when such a delamination is induced, it defines the onset of the contoured delamination. Then, by taking the values of C_e and C_T from Figures 2.12 and 2.13 at $A/t^2 = 4$, the total energy release rate $G(\bar{e}_x, \Delta T)$ can be computed via Equation (3.3). Let, as before, $\Delta T = 125°C$ and $G_c = 289\ J/m^2$ for mixed-mode crack growth, see Table II-1. It follows from Equation (3.4) that the predicted threshold tensile

strain for the onset of the contoured delamination for n = 2 is:

$$(\bar{e}_x)_{de} = 11.0 \times 10^{-3} \tag{4.1}$$

Similarly, the computed C_e and C_T coefficient functions for $[0_2/90_4]_s$ are shown in Figures 4.14 and 4.15, respectively. It is seen that the values of C_e and C_T are significantly increased as a result of doubling the number of the 90°-plies. Consequently, the predicted threshold strain for onset of the assumed contoured delamination in this laminate is:

$$(\bar{e}_x)_{de} = 7.8 \times 10^{-3} \tag{4.2}$$

Since the breaking strain of the 0°-ply is normally at about 10×10^{-3}, it may be inferred that the assumed contour delamination would not occur in the $[0_2/90_2]_s$ laminate, but would occur in the $[0_2/90_4]_s$ laminate.

Indeed, in the experiment reported in Reference [38], no such delamination was detected until after laminate failure in $[0_2/90]_s$ and $[0_2/90_2]_s$. For $[0_2/90_4]_s$, however, delta-shaped delamination were found at laminate strain about 7.5×10^{-3}. This compares closely with the predicted value in (4.2).

Onset of 0°-Ply Splitting. As was discussed in the previous section, the basic mechanisms in 0°-ply splitting are much the same as in 90°-ply transverse cracking. However, the normal-to-the-fiber tension, σ_y, in the 0°-ply is more concentrated near the transverse crack terminus. In addition, along the length of the laminate such concentrations occur periodically, coinciding with the regularity of the 90°-ply transverse cracks. This makes it difficult to predict how a 0°-ply split initiates.

Let it be assumed that an effective in-ply flaw in the 0°-ply exists and lies fiber-wise in the ply. Then, the growth conditions for the effective flaw can be formulated based on the same concept of energy release rate. As

in the case of the 90°-ply transverse cracking, the size of the assumed effective flaw is not known. But, by computing the maximum possible energy release rate available along the growth path of such a flaw, a minimum possible onset load for the flaw growth can be obtained. The actual computational procedure is identical to the transverse cracking cases discussed in Chapter II; therefore, the details of the computation will be omitted here. Instead, only the final results will be given. Namely, longitudinal splits in the interior of the 0°-ply will probably occur over the transverse cracks when the applied tensile strain $\bar{e}_x$ exceeds the following critical values:

$$\text{for } n = 2, \qquad (\bar{e}_x)_{sp} = 10.5 \times 10^{-3} \tag{4.3}$$

$$\text{for } n = 4, \qquad (\bar{e}_x)_{sp} = 7.8 \times 10^{-3} \tag{4.4}$$

According to this prediction, 0°-ply splitting cannot occur in the $[0_2/90_2]_s$ before laminate failure; but may occur in the $[0_2/90_4]_s$ laminate because the approximate threshold breaking strain for 0°-ply fiber is about 10×10^{-3}.

Note that the threshold strain for 0°-ply splitting in the $[0_2/90_4]_s$ laminate is about the same as the threshold strain for the 0/90 delaminations induced near the transverse crack/free-edge corner points, see Equation (4.2). Or, these two types of matrix cracks may occur at the same load level. This was actually observed in the $[0_2/90_3]_s$ laminates shown in Figures 3.6 and 4.1. In Figure 3.6, local delaminations occurred near the free edge, while in Figure 4.1 0°-ply splits occurred in the interior; both types of matrix cracking occurred at about the same applied load level. In the experiment reported in [38], longitudinal splitting was also found in $[0_2/90_2]_s$ at the laminate strain of 9.2×10^{-3}, while in $[0_2/90_4]_s$ at the laminate strains of less than 8×10^{-3}. These numbers are in general agreement with the predictions in Equations (4.3) and (4.4).

4.4 Delamination at Two Crossing Cracks

When a splitting crack is formed in the 0°-ply, it makes a cross with the transverse crack in the 90°-ply as illustrated by Figure 4.16. In the close vicinity of the crossing point, a severe stress concentration is developed. Both interlaminar and in-plane stresses are present. The interlaminar stresses in particular will cause localized delamination such as shown by the shaded area in Figure 4.16. (See also Figure 4.1.)

Figure 4.17(a) shows the 0/90 interface plane, with the x-axis parallel to the 0°-ply split and the y-axis parallel to the 90°-ply transverse crack. The axis origin is the intersection point of the two crossing cracks.

The stress field near the intersection point is highly amplified. In particular, the interlaminar normal stress σ_z is tensile due both to the applied tension and thermal cooling.

To determine the threshold condition for delamination caused primarily by the interlaminar stresses, a crack growth simulation is performed using the same finite element nodal release procedure. The simulated delamination follows the nodal release sequence shown in Figure 4.17(b). The point-by-point energy release rate coefficients G_e and G_T are shown in Figures 4.18 and 4.19 for $[0_2/90_2]_s$ and in Figures 4.20 and 4.21 for $[0_2/90_4]_s$, respectively.

From the energy release rate coefficient curves, it is apparent that the behavior of the delamination is mixed-mode. The total energy release rate slightly decreases with the delaminated area A, indicating a stable growth behavior at least initially.

Comparing the four energy release rate curves with those shown in Figures 4.12 to 4.15, a close similarity is seen between the delamination occurring at the crossing cracks and at the transverse crack/free-edge corner points.

However, the calculated energy release rate for delamination at the cross cracks is slightly higher.

Using the same procedure as before for the threshold strain at onset of delamination, the predicted laminate strains are as follows:

$$\text{for } n = 2 \qquad (\bar{e}_x)_{de} = 10.9 \times 10^{-3} \tag{4.5}$$

$$\text{for } n = 4 \qquad (\bar{e}_x)_{de} = 7.5 \times 10^{-3} \tag{4.6}$$

This shows that delamination at the cross cracks occurs at about the same load as the 0°-ply splitting. Experimentally, however, the splitting occurred first, while the delamination followed immediately [38]. Since the analysis involved considerable approximations, both in numerical computation and in setting the threshold conditions for flaw growth, the close agreement achieved between the prediction and experiment was rather surprising.

From these results, the energy release rate concept coupled with the effective flaw postulate is shown to be useful in predicting a threshold load for matrix cracking that takes place at high loads.

4.5 Effects of Matrix Cracking on Laminate Strength

As has been shown, matrix cracks and crack interactions in laminates can occur in multiple plies under high loads. These cracks may severely reduce laminate strength if the laminate's internal microstructure (e.g. ply stacking sequence) allows them to grow, either by self-propagation or by mutual coalescence. For example, matrix cracks in off-axis plies, such as 90°-ply transverse cracks, are initial laminate damages. In time, or at high loads, these cracks cause secondary matrix cracks in the load-carrying plies which trigger catastrophic laminate failure. Since matrix cracking is influenced greatly by the lamination geometry, material system and loading environment, even a qualitative understanding of their inter-relationships is useful for optimum

laminate design. It is shown here that these factors can be explicitly accounted for in the predictive models. In the examples presented, it seems that the energy method can be an effective means to analyze certain matrix cracking processes and their contribution to the final failure of the load-carrying plies.

Up to now, most practical design analysts have ignored the detailed matrix cracking patterns in the off-axis plies. They assume that all loads will eventually be taken by the 0°-plies. This practice is typified by the so-called discount method, which ignores any internal crack interactions. Such approximation techniques may over-predict the laminate strength.

Ultimate failure in laminates occurs when the fibers are broken. Matrix cracks precede and influence this process. Hence, a predictive model for fiber breaking should include the influence of matrix cracks. As fiber strength modeling was outside the scope of this effort, it is only proper to point out here that the mechanisms of fiber breaking and matrix cracking must be merged to provide a complete description of the laminate failure process.

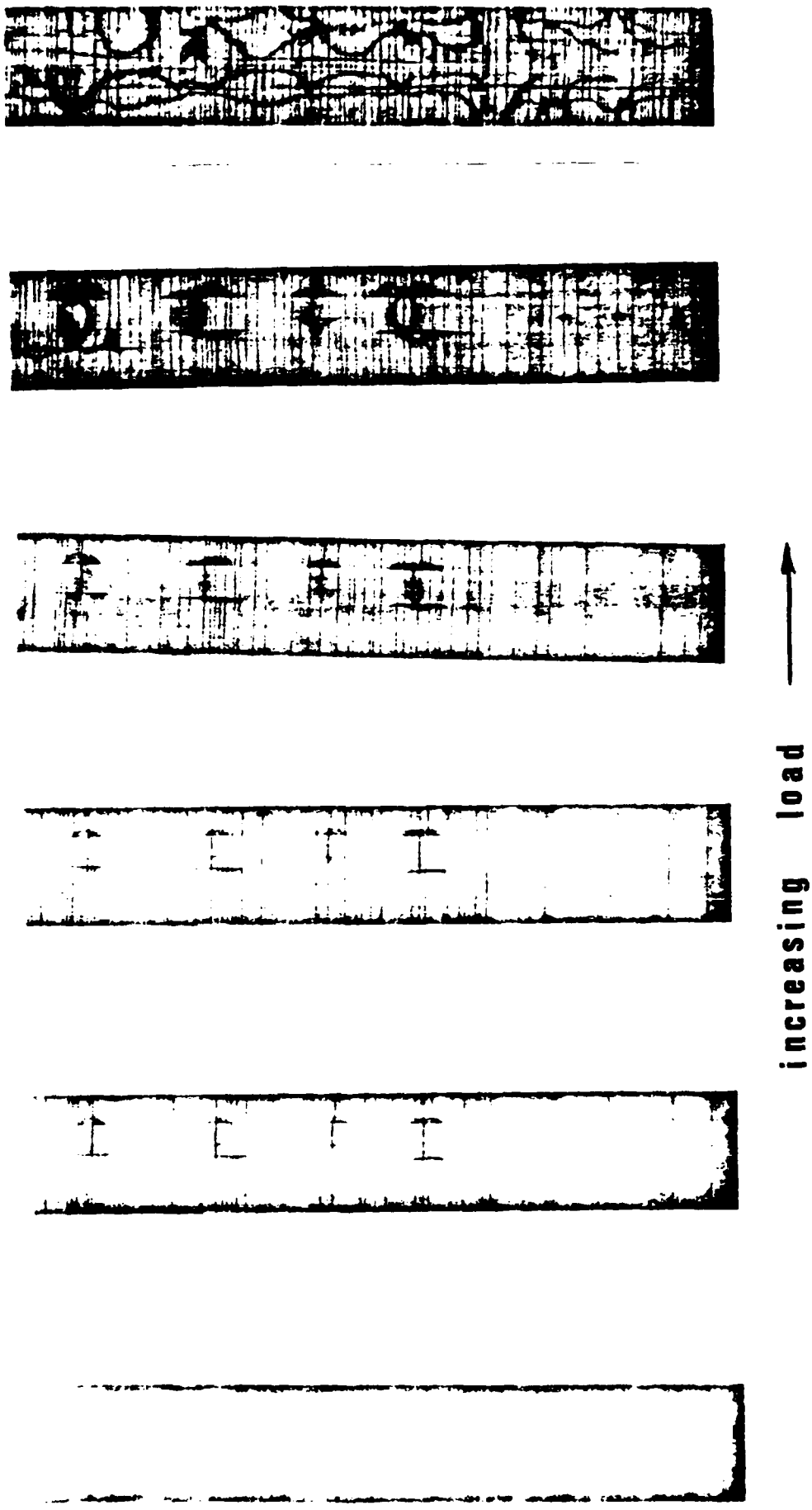

Figure 4.1 Load-Sequence of X-Radiographs Depicting Localized Delaminations at Cross-Cracks.

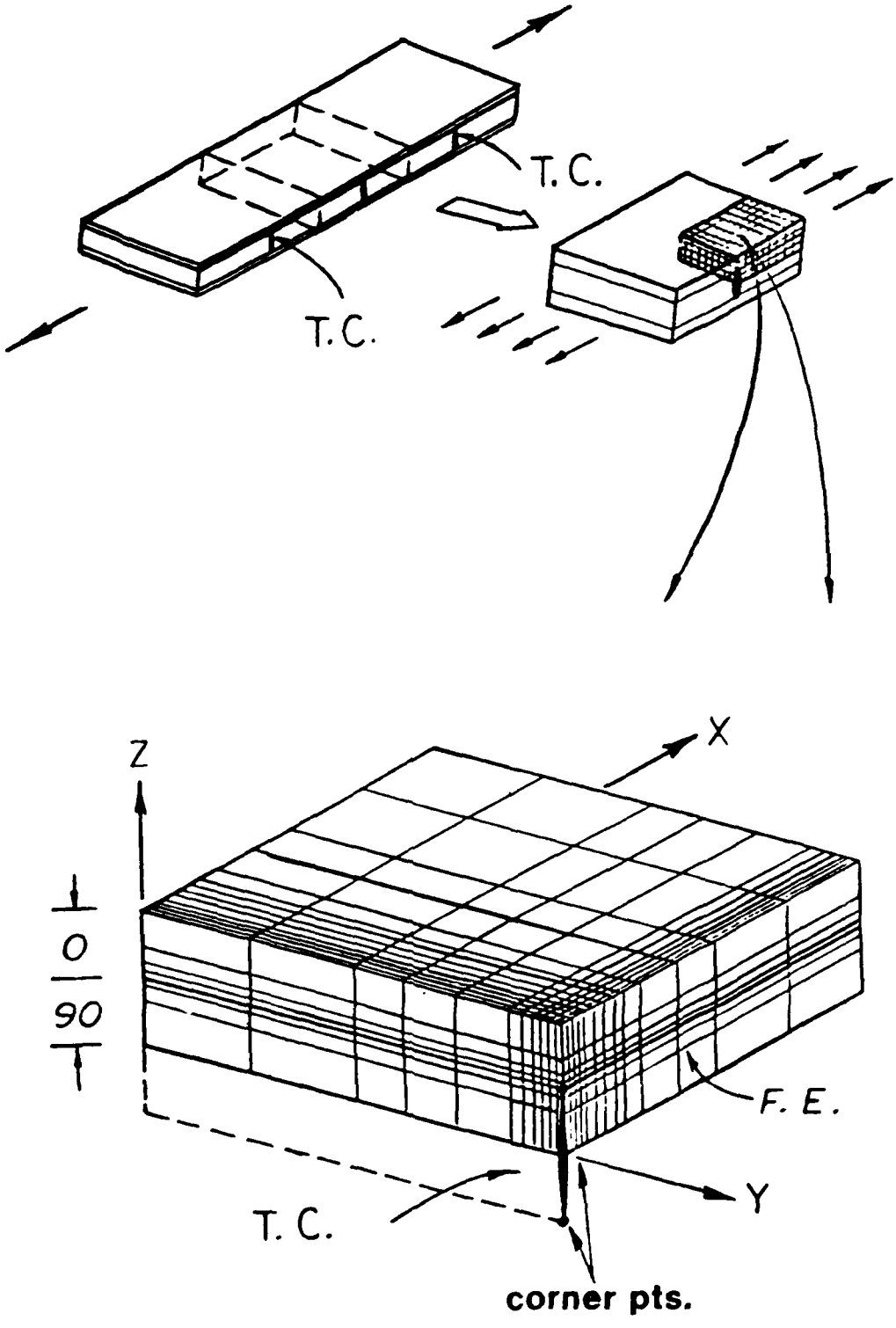

Figure 4.2 Finite Element Model for $[0/90]_s$ Laminates Containing Transverse Cracks.

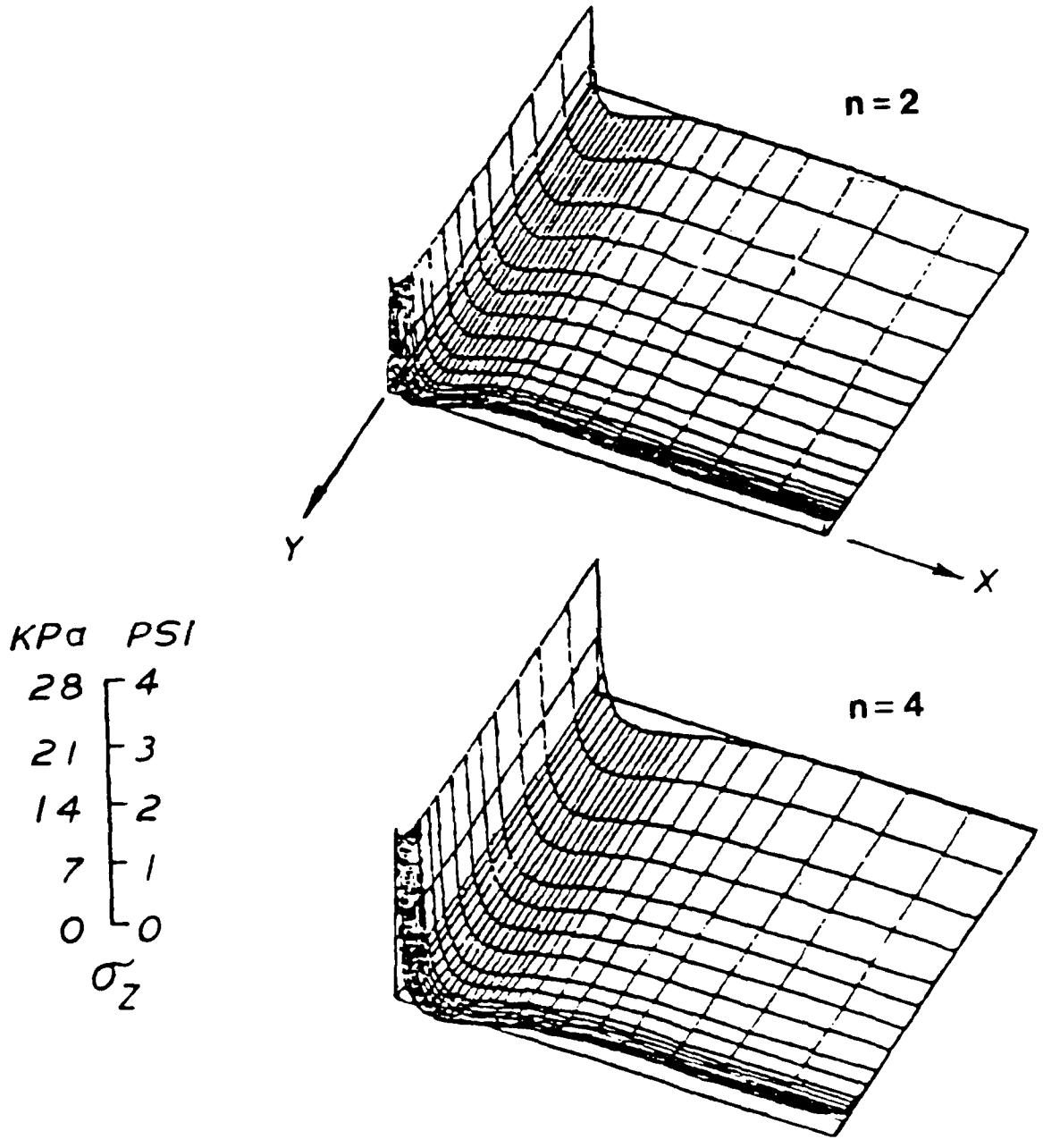

Figure 4.3 σ_z Distribution on 0/90 Interface Near a Transverse Crack.

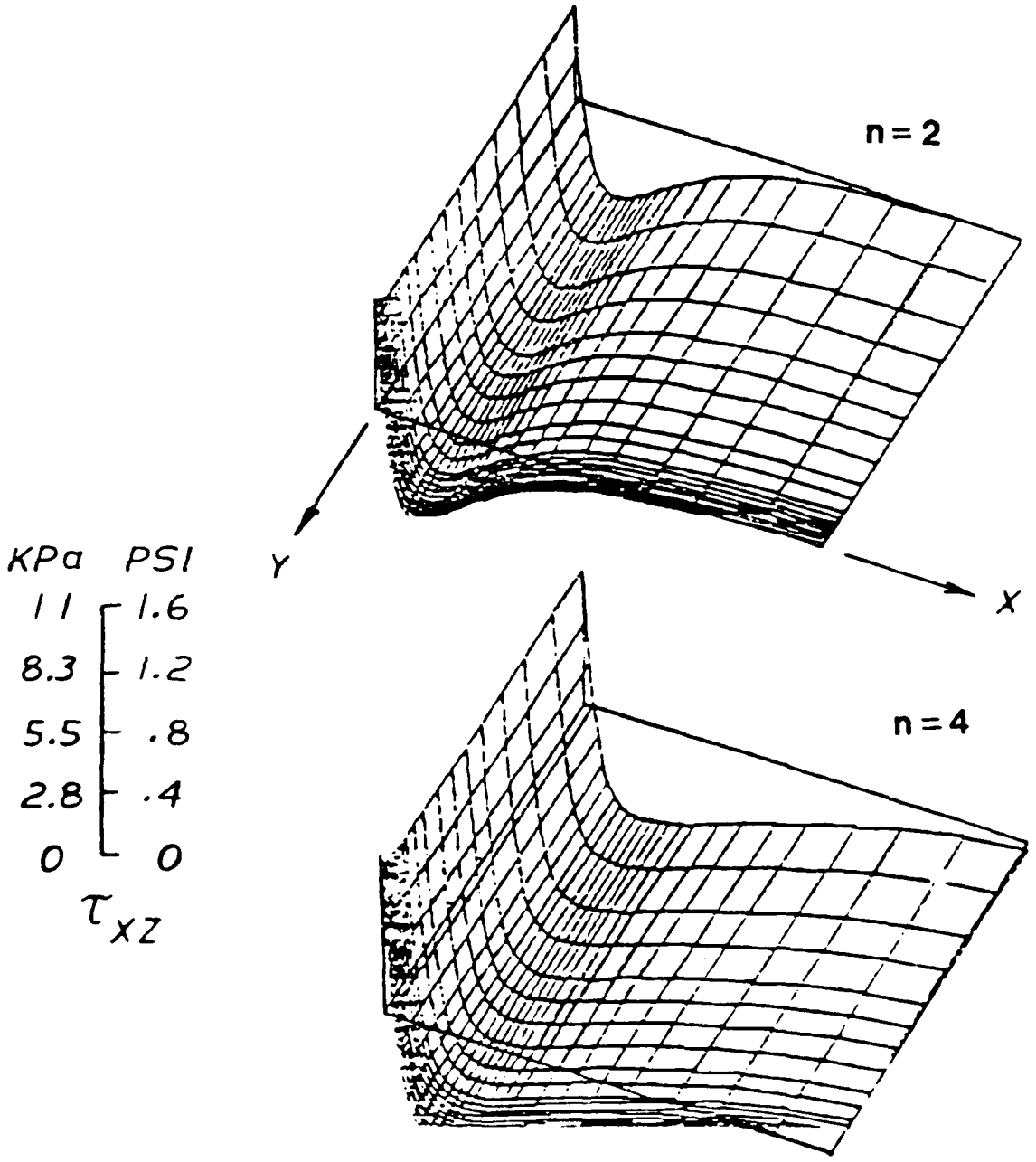

Figure 4.4 τ_{xz} Distribution on 0/90 Interface Near a Transverse Crack.

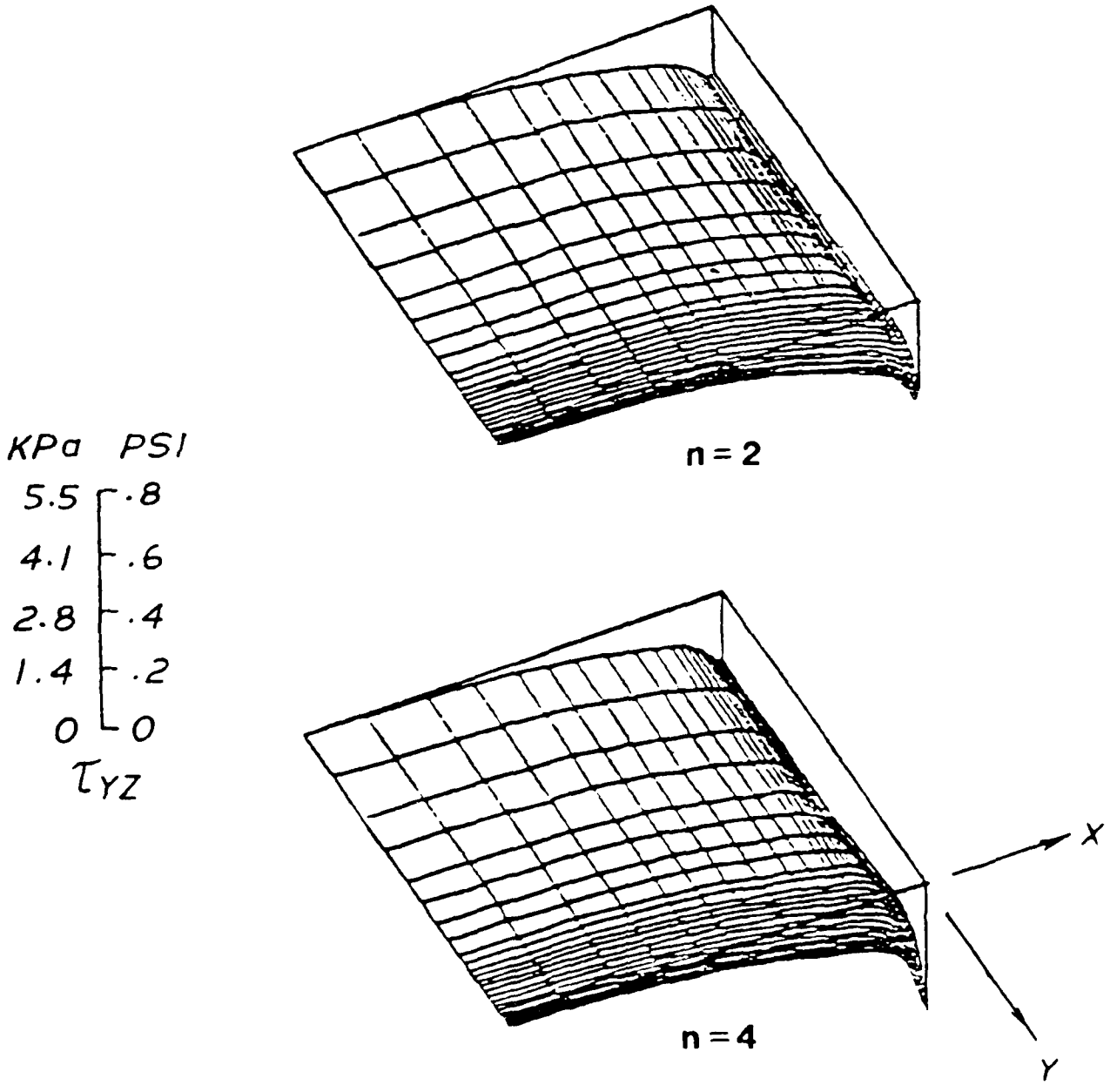

Figure 4.5 τ_{yz} Distribution on 0/90 Interface Near a Transverse Crack.

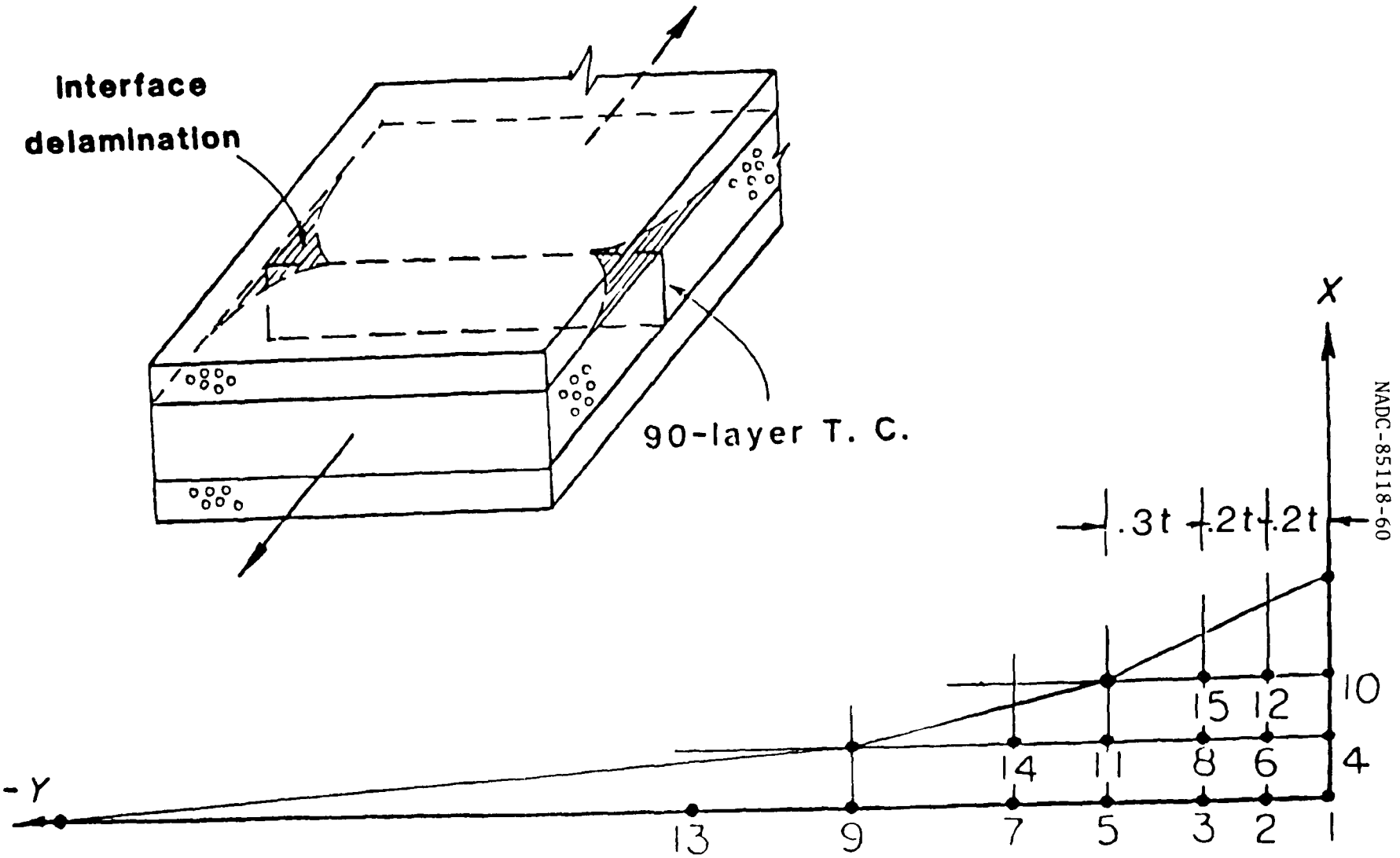

Figure 4.6 Free Edge/Transverse Crack Induced 0/90 Interface Delamination (above); and the Nodal Release Sequence for Simulation.

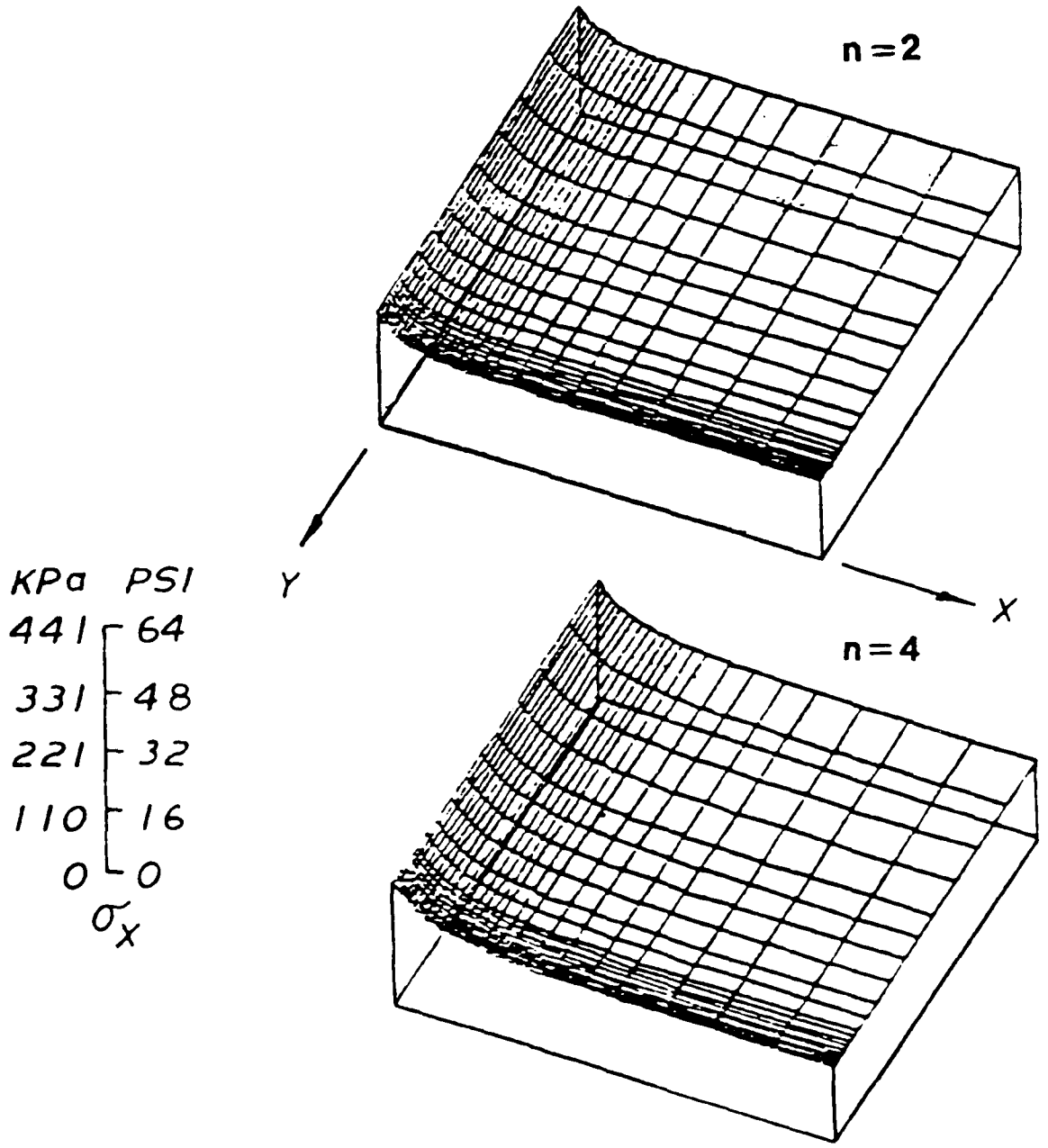

Figure 4.7 σ_x Distribution in the 0°-ply Near 0/90 Interface.

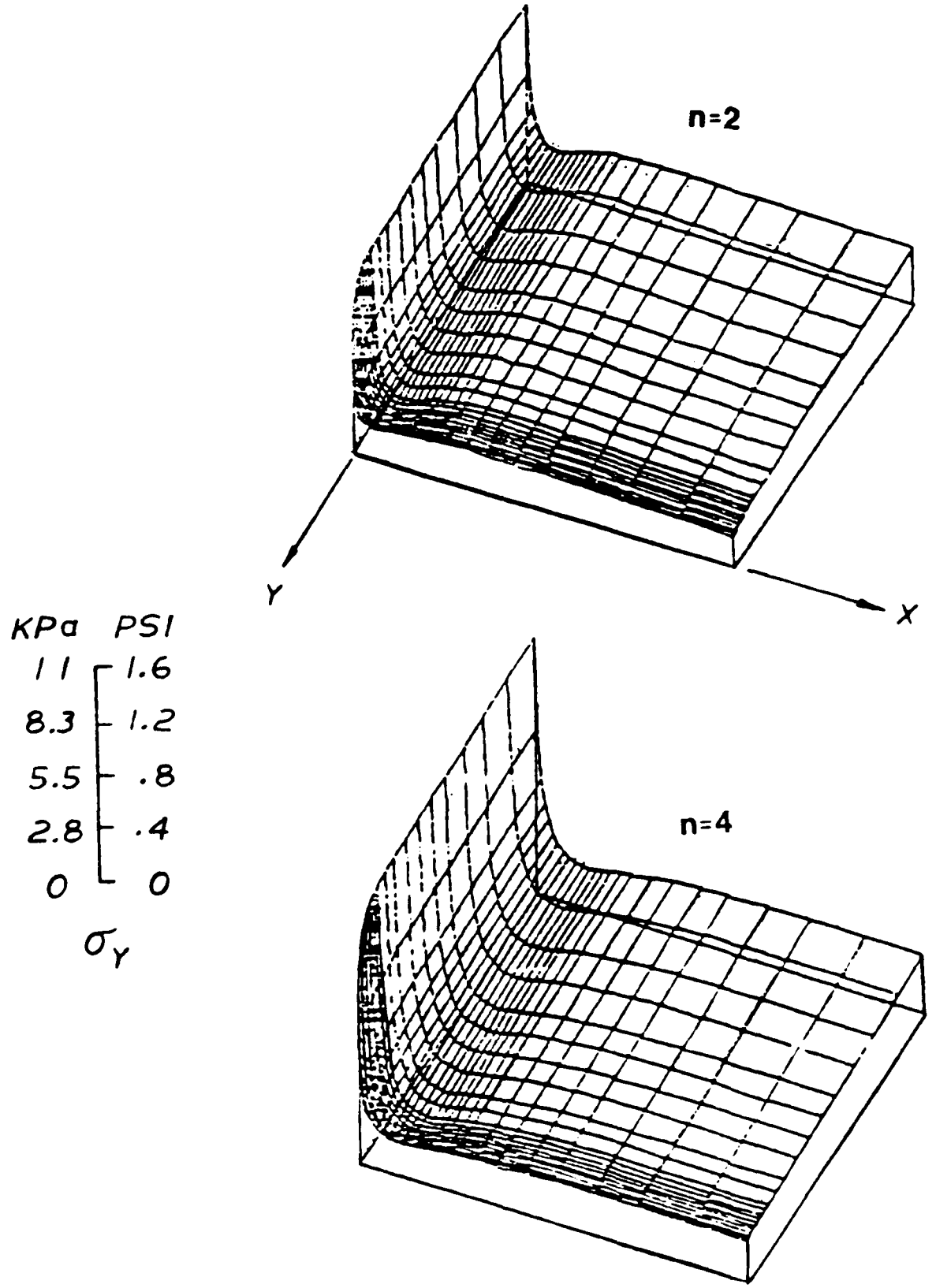

Figure 4.8 σ_y Distribution in the 0°-ply Near 0/90 Interface.

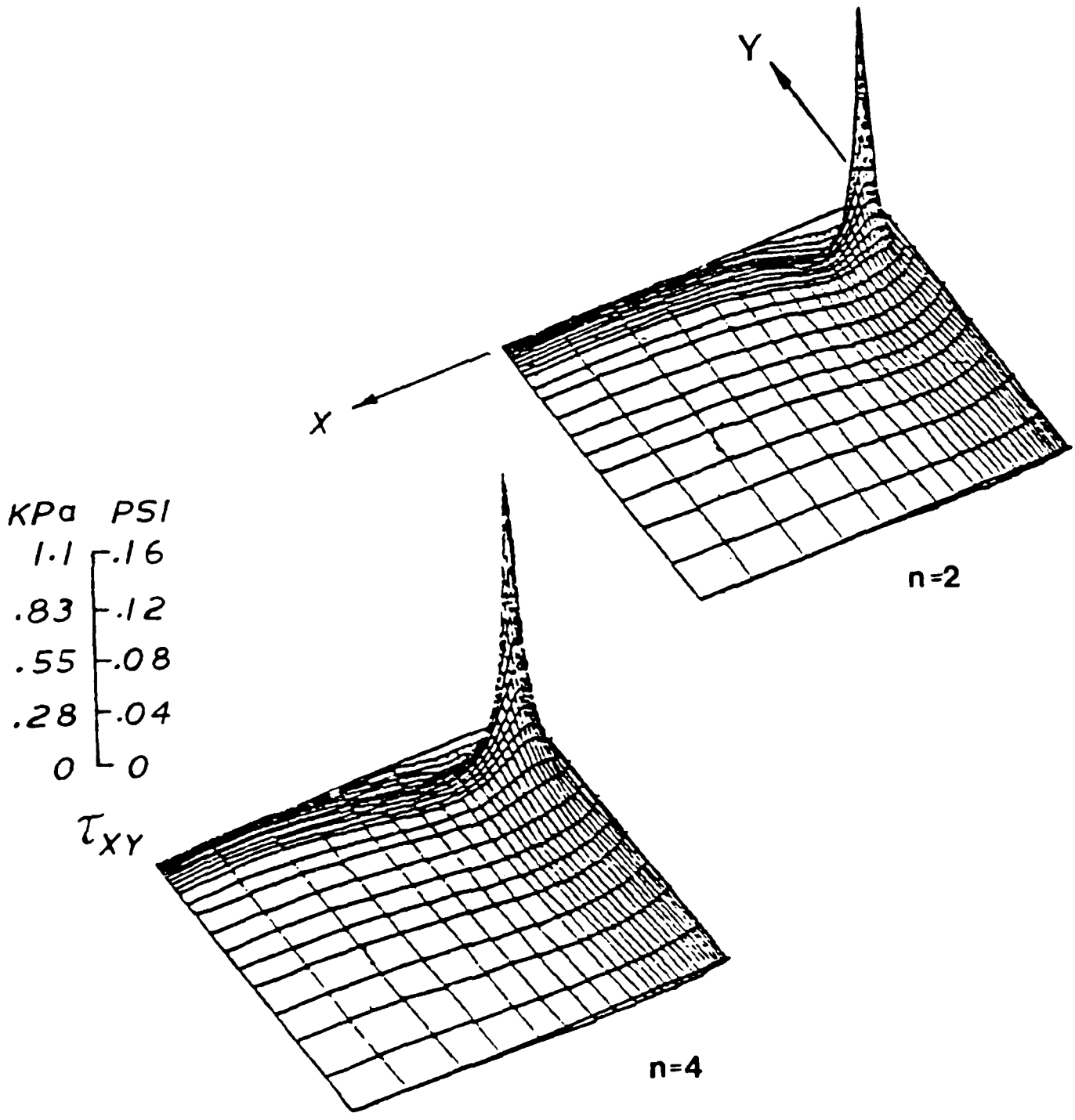

Figure 4.9 τ_{xy} Distribution in the 0°-ply Near 0/90 Interface.

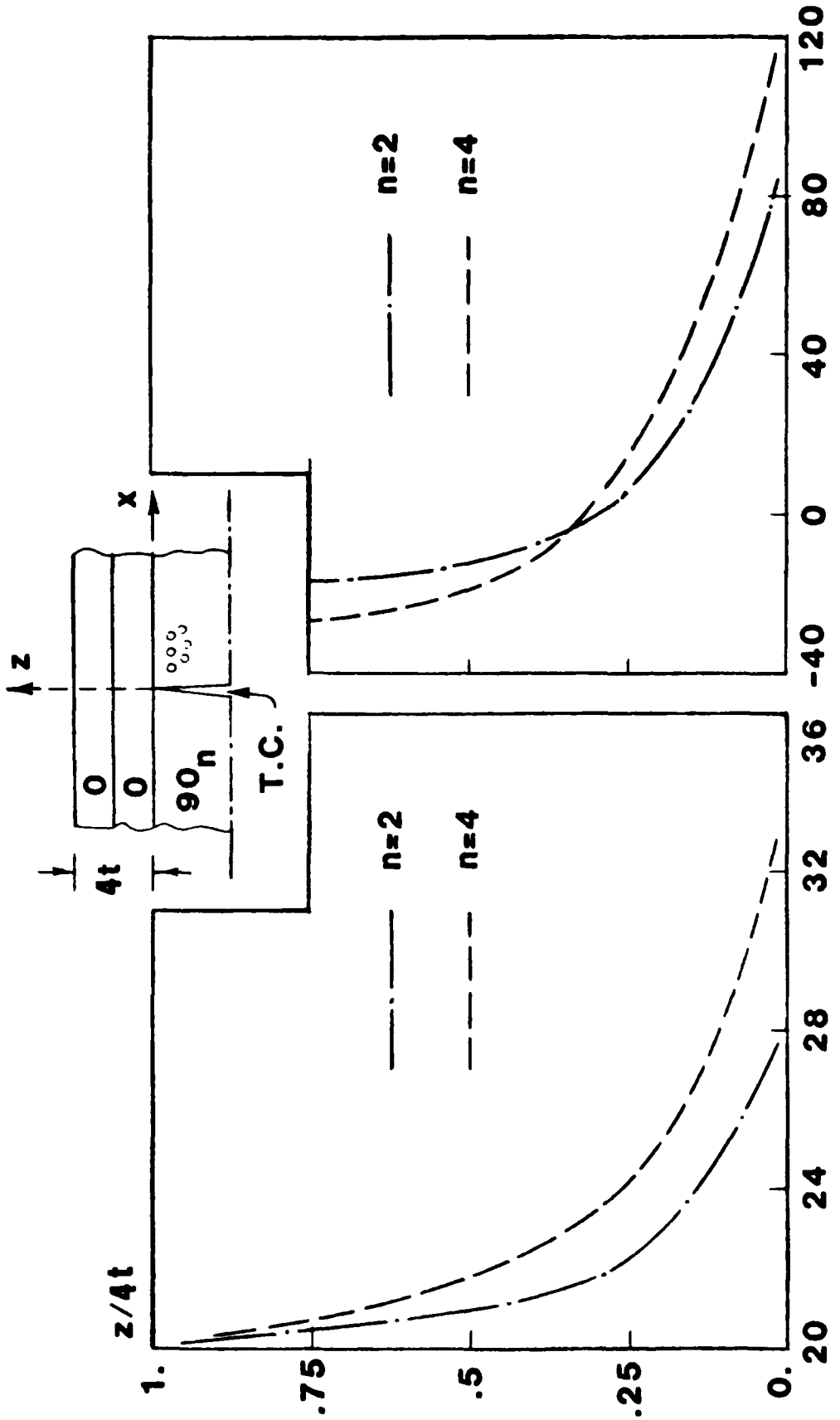

Figure 4.10 Through-Thickness Distribution of σ_x in the 0°-ply Near a Transverse Crack.

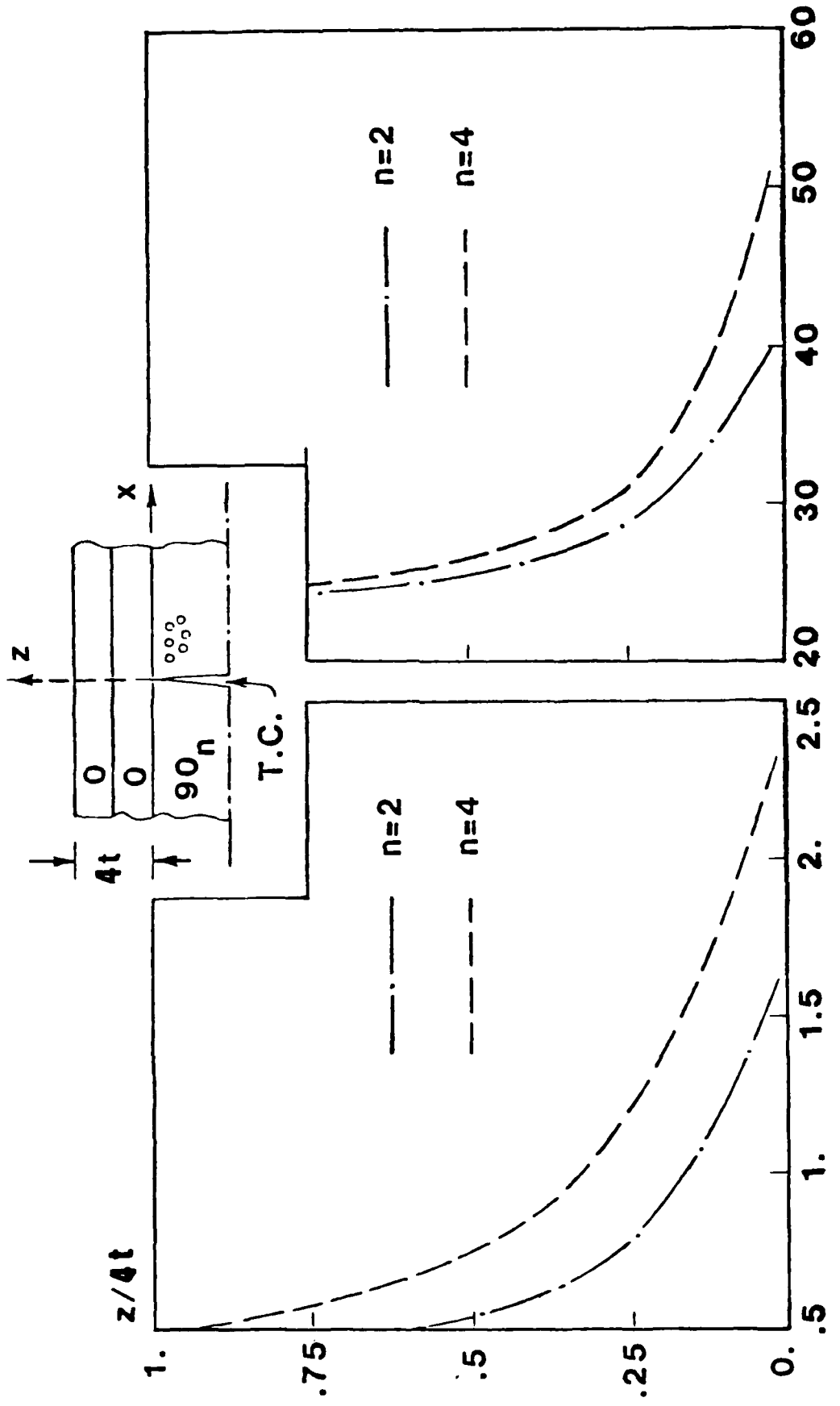

Figure 4.11 Through-Thickness Distribution of σ_y in the 0°-ply Near a Transverse Crack.

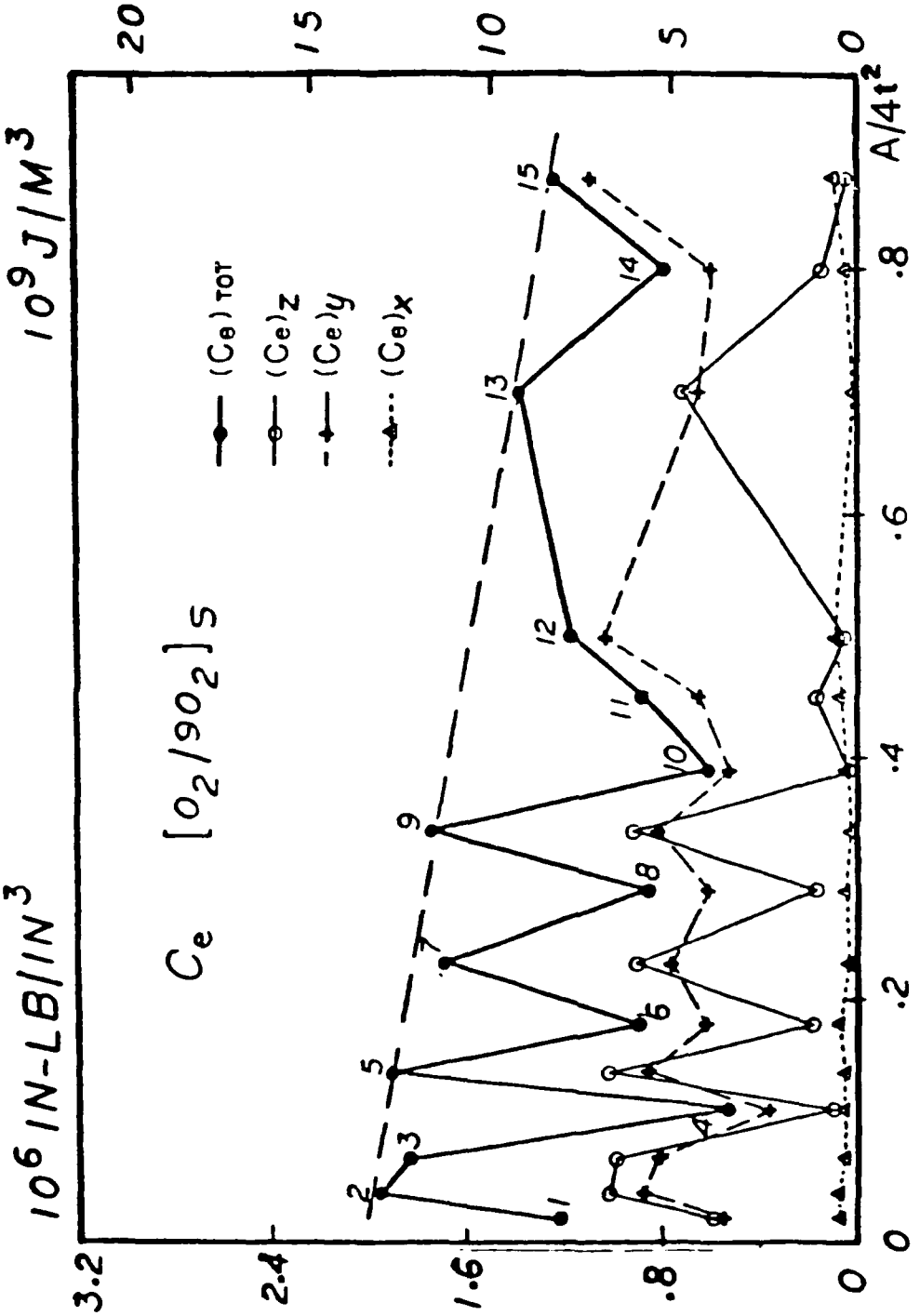

Figure 4.12 Strain Energy Release Rate Coefficient, C_e, for Delamination at Corner Point $[0_2/90_2]_S$.

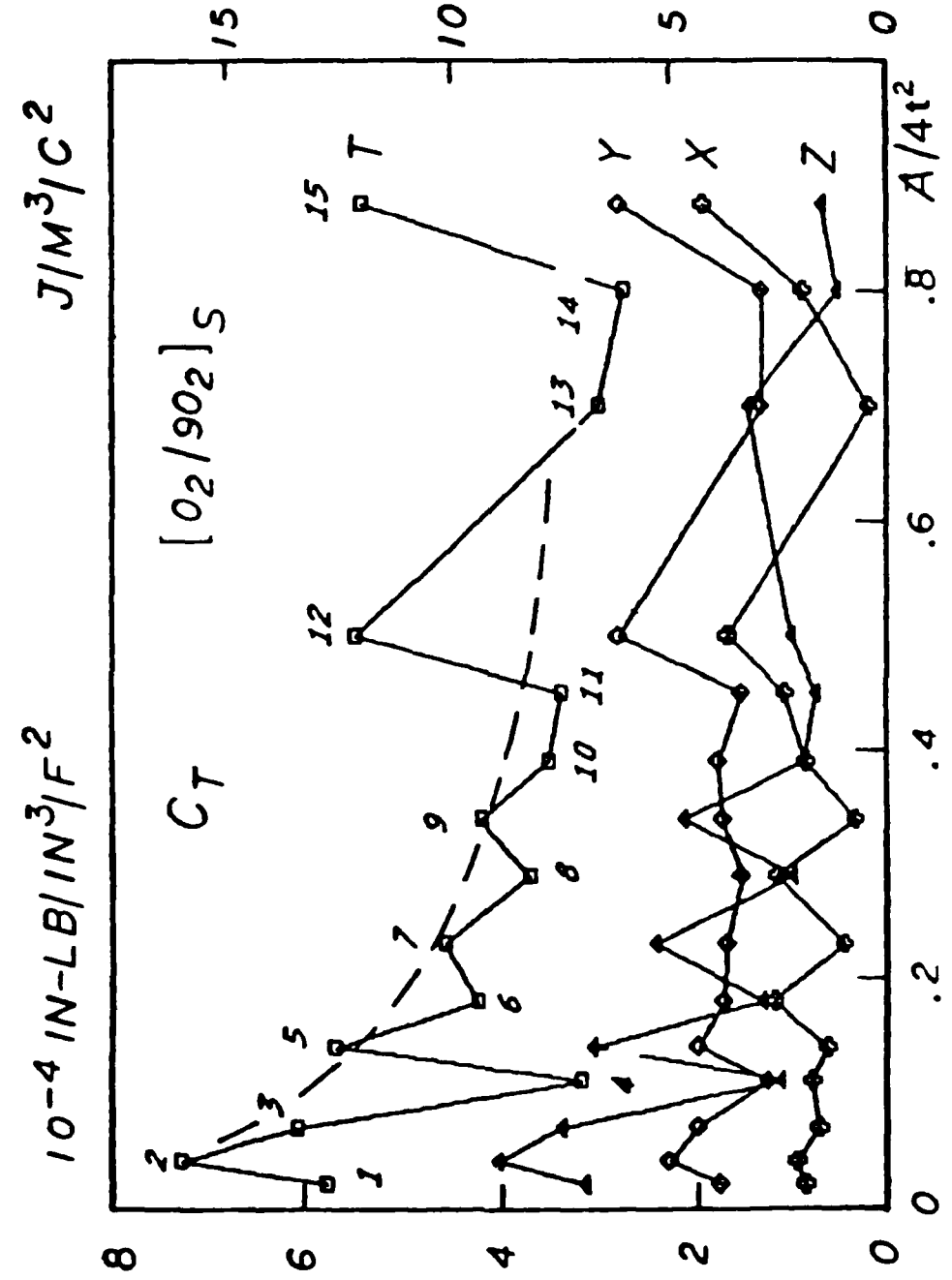

Figure 4.13 Strain Energy Release Rate Coefficient, C_T, for Delamination at Corner Point $[0_2/90_2]_S$.

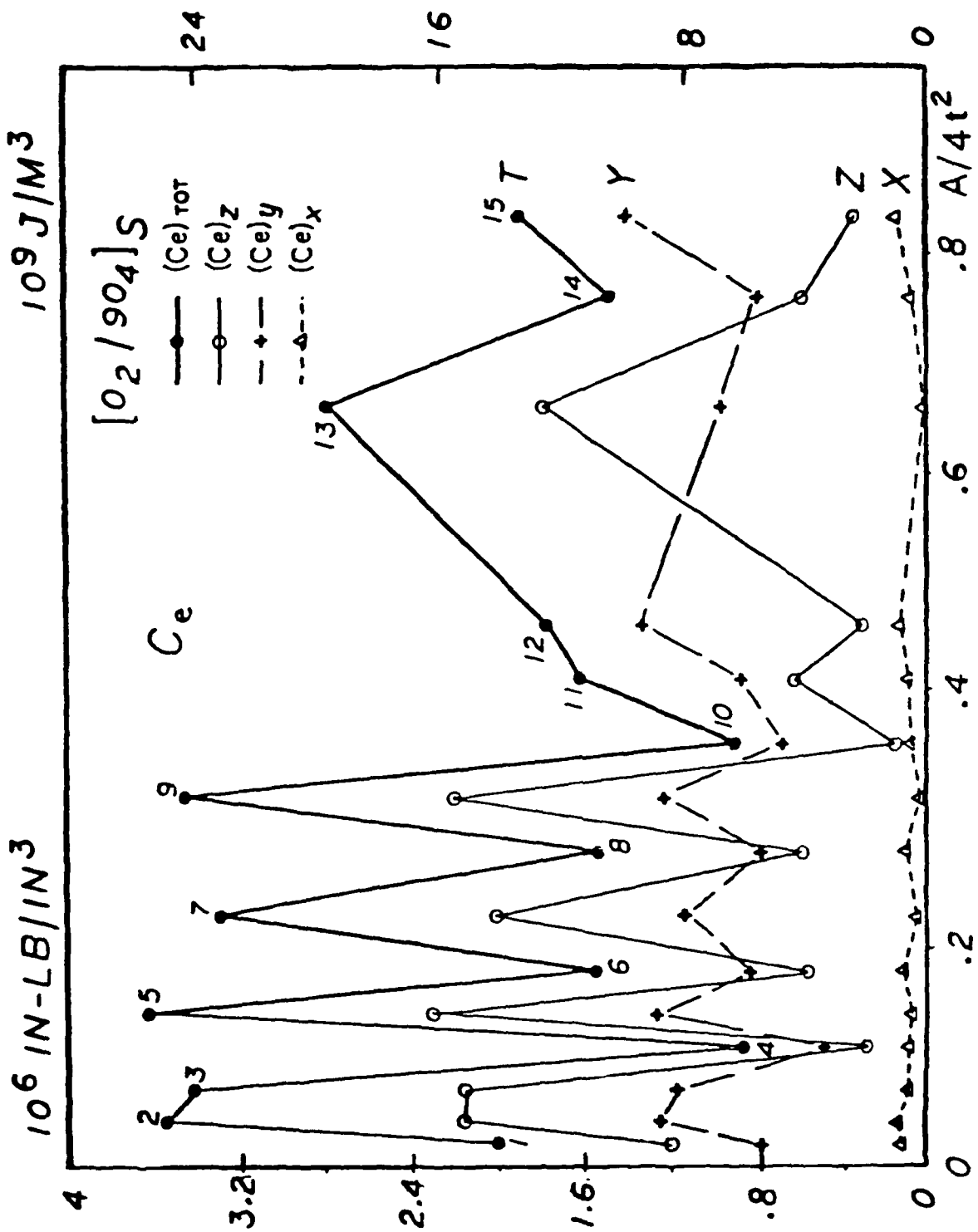

Figure 4.14 Strain Energy Release Rate Coefficient, C_e, for Delamination at Corner Point $[0_2/90_4]_S$.

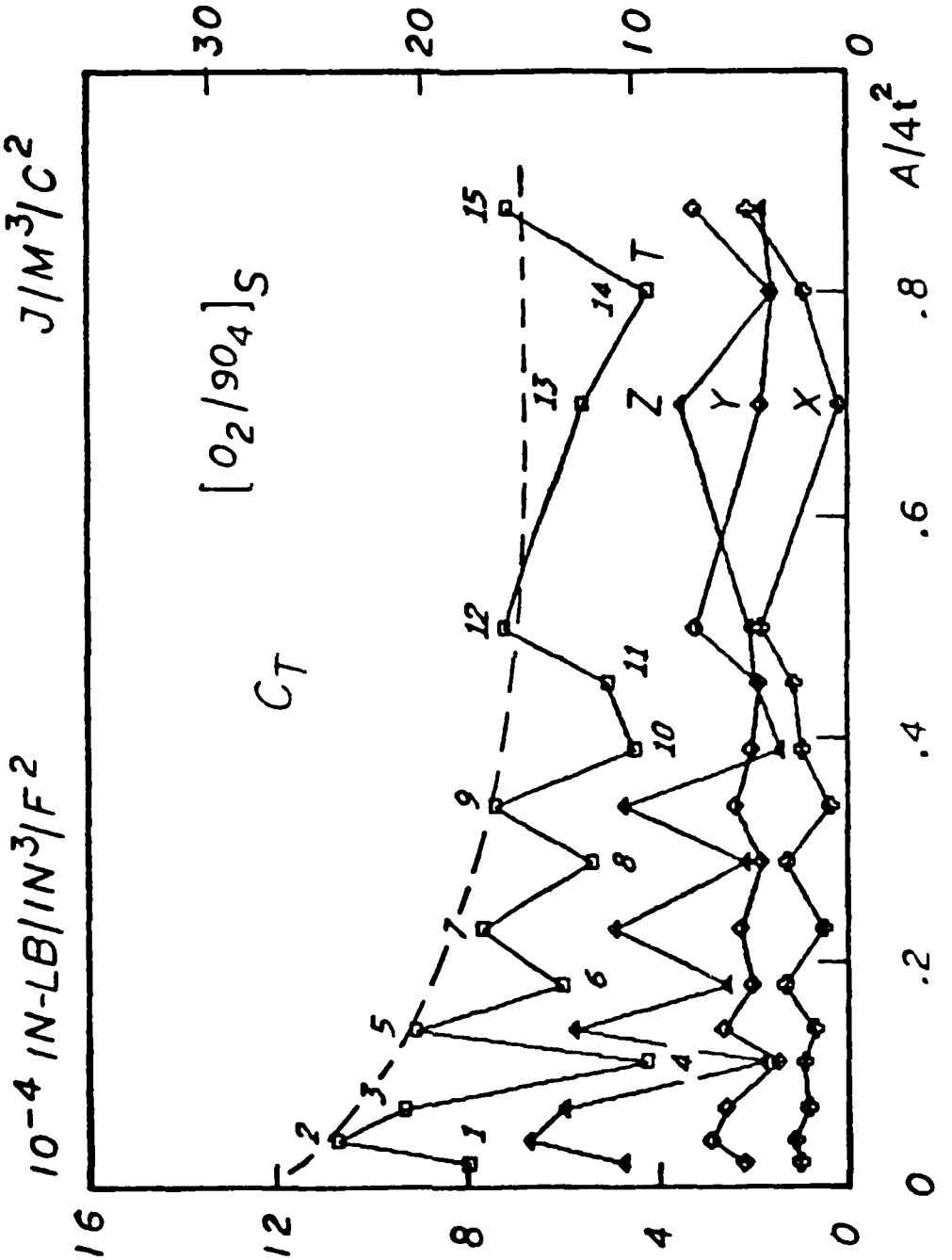

Figure 4.15 Strain Energy Release Rate Coefficient, C_T, for Delamination at Corner Point $[0_2/90_4]_S$.

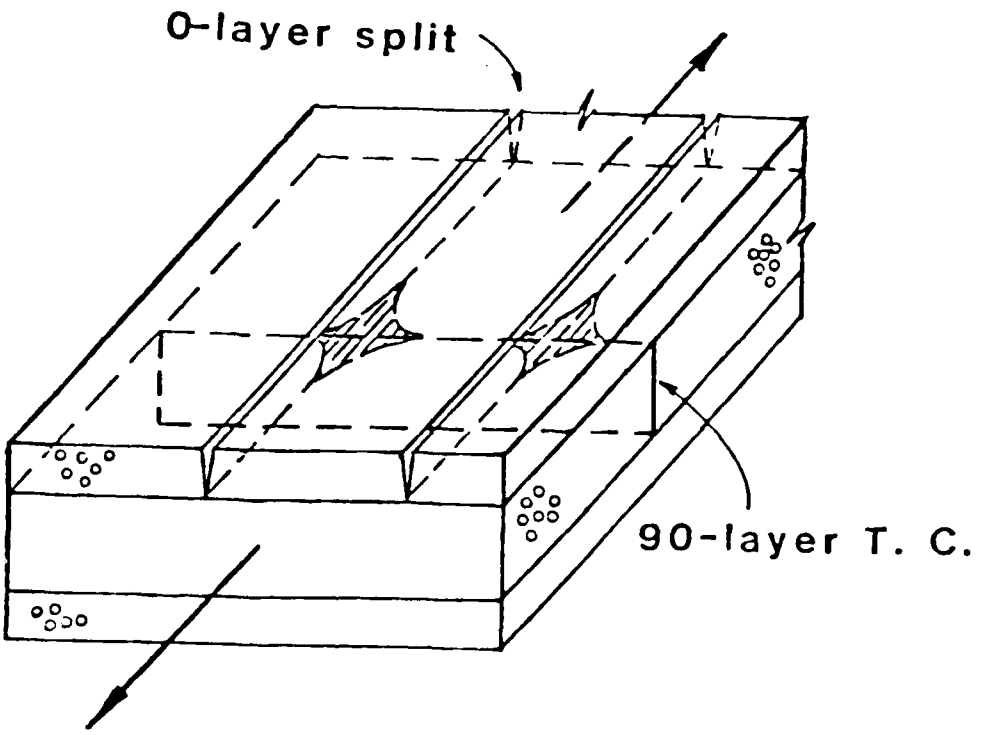

Figure 4.16 Schematic View of Cross Cracks and Delamination at the Cross Cracks.

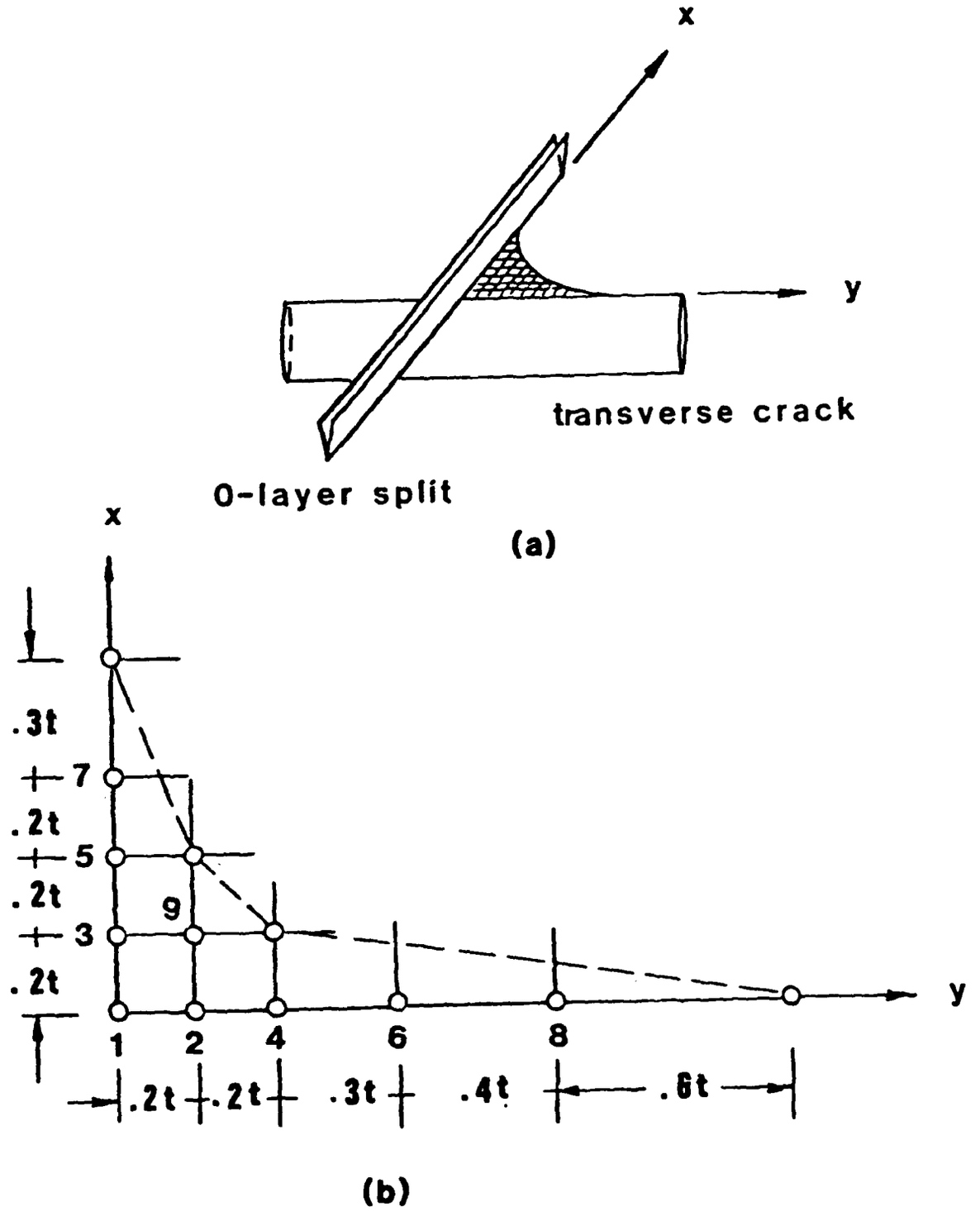

Figure 4.17 (a) Plane of Delamination at a Pair of Cross-Cracks.
(b) Nodal Release Sequence for Simulation.

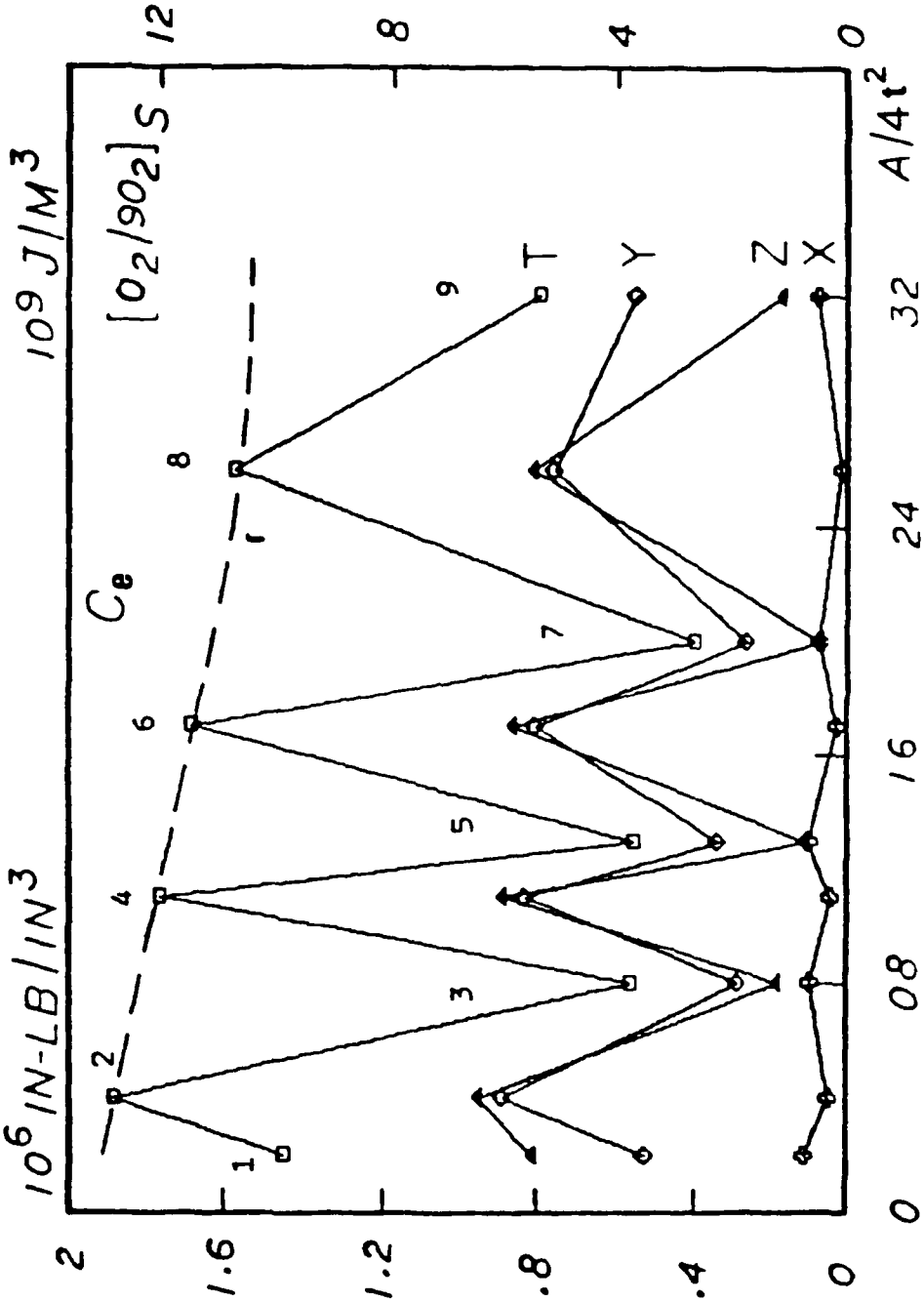

Figure 4.18 Strain Energy Release Rate Coefficient, C_e, for Delamination at Cross-Cracks $[0_2/90_2]_S$.

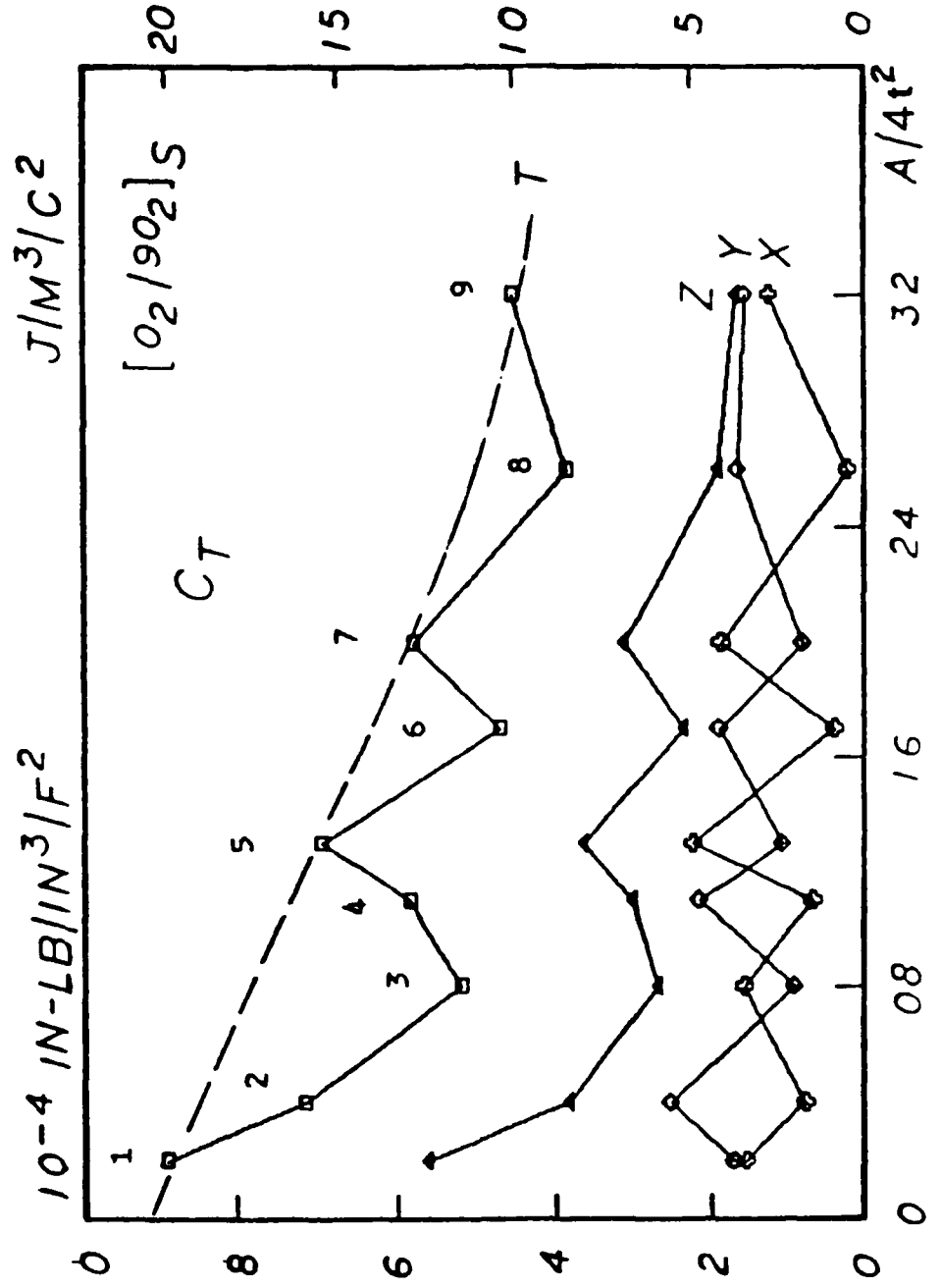

Figure 4.19 Strain Energy Release Rate Coefficient, C_T, for Delamination at Cross-Cracks $[0_2/90_2]_S$.

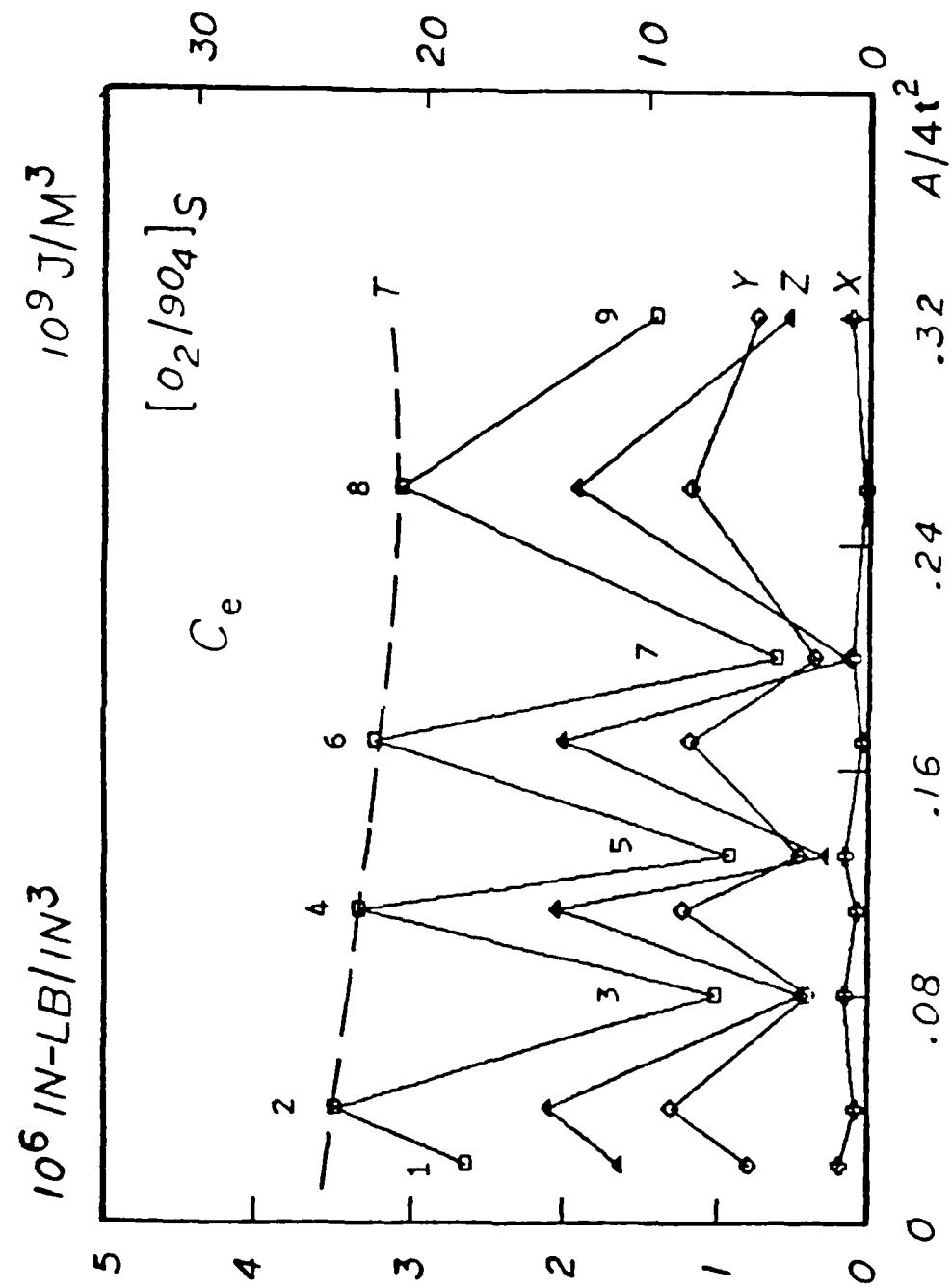

Figure 4.20 Strain Energy Release Rate Coefficient, C_e, for Delamination at Cross-Cracks $[0_2/90_4]_S$.

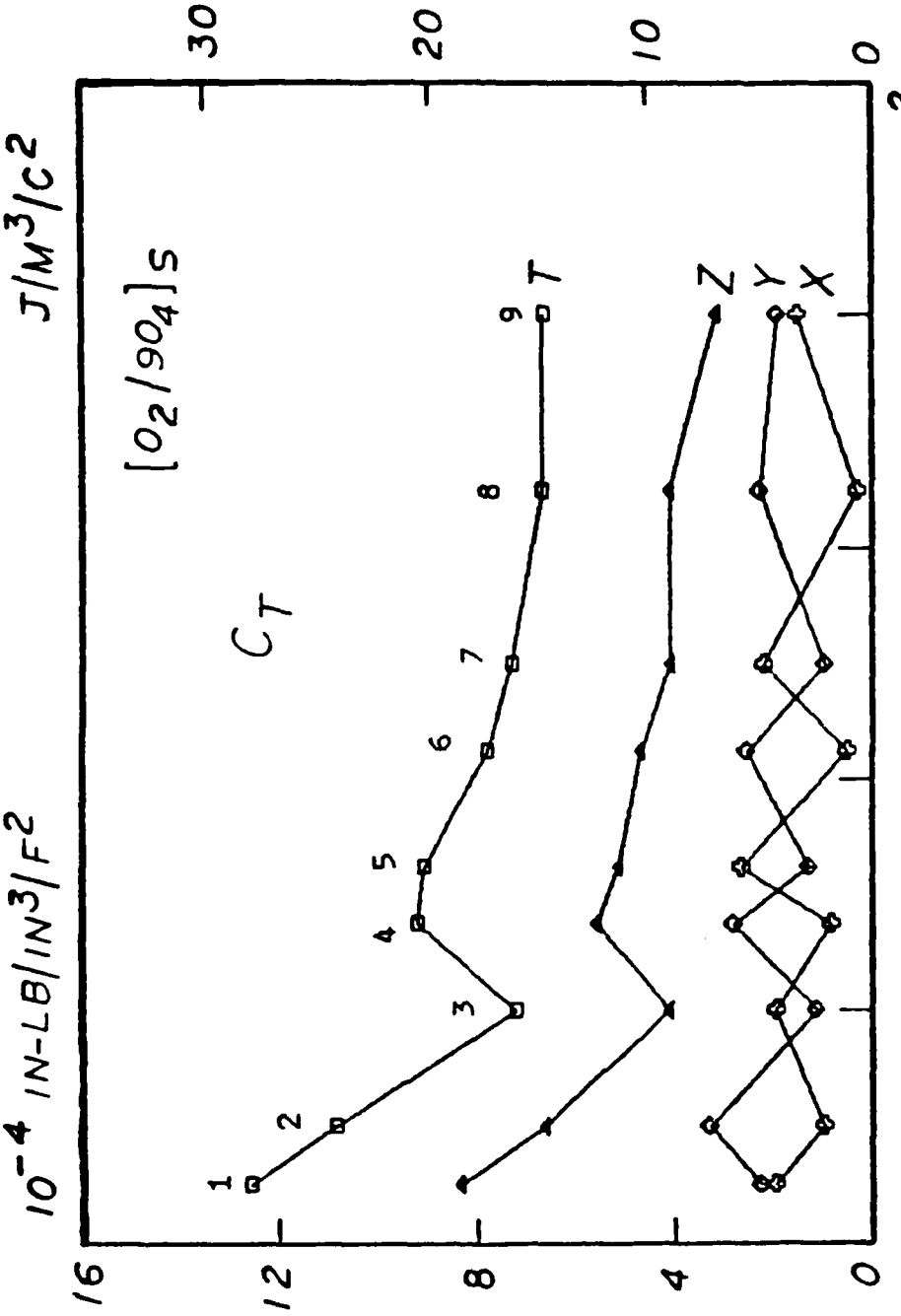

Figure 4.21 Strain Energy Release Rate Coefficient, C_T, for Delamination at Cross-Cracks $[0_2/90_4]_S$.

REFERENCES

[1] Harrison, R. P. and Bader, M. G., "Damage Development in CFRP Laminates Under Monotonic and Cyclic Stressing," Fibre Science and Technology, Vol. 18, 1983, pp. 163 - 180.

[2] Zweben, C., "Fracture Mechanics and Composite Materials: A Critical Analysis," in Analysis of the Test Methods for High Modulus Fibers and Composites, ASTM STP 521, 1973, pp. 65 - 97.

[3] Pagano, N. J., "Exact Solutions for Rectangular Bidirectional Composites and Sandwich Plates," Journal of Composite Materials, Vol. 4, 1970, pp. 20 - 34.

[4] Hashin, Z., "Theory of Fiber Reinforced Materials," NASA CR-1974, March 1972, pp. 11 - 37.

[5] Tsai, S. W. and Hahn, H. T., "Introduction to Composite Materials," Technomics, Westport, CT, 1980.

[6] Whitney, J. M., Daniel, I. M. and Pipes, R. B., "Experimental Mechanics of Fiber Reinforced Composite Materials," Society for Experimental Stress Analysis, 1982.

[7] Flaggs, D. L. and Kural, M. H., "Experimental Determination of the In-Situ Transverse Lamina Strength in Graphite Epoxy Laminates," Journal of Composite Materials, Vol. 16, 1982, pp. 103 - 116.

[8] Phoenix, S. L., "Statistical Aspects of Failure of Fibrous Materials," in Composite Materials: Testing and Design, 5th Conference, ASTM STP 674, 1979, pp. 455 - 483.

[9] Wang, A. S. D. and Crossman, F. W., "Initiation and Growth of Transverse Cracks and Edge Delamination in Composite Laminates: Part 1. An Energy Method," Journal of Composite Materials, Vol. 14, 1980, pp. 71 - 87.

[10] Crossman, F. W., Warren, W. J., Wang, A. S. D. and Law, G. E., "Initiation and Growth of Transverse Cracks and Edge Delamination in Composite Laminates: Part 2. Experimental Correlation," Journal of Composite Materials, Vol. 14, 1980, pp. 88 - 106.

[11] Wang, A. S. D., "Fracture Mechanics of Sublaminate Cracks in Composite Laminates," in Characterization, Analysis and Significance of Defects in Composite Materials," Conference Proceedings 355, NATO AGARD, London, 1983, pp. 15 1 - 19. Also in Composite Technology Review, Vol. 6, No. 2, 1984, pp. 45 - 62.

[12] Wang, A. S. D., Chou, P. C. and Lei, S. C., "A Stochastic Model for the Growth of Matrix Cracks in Composite Laminates," in Advances in Aerospace Structures, Materials and Dynamics, ASME, AD-06, 1983, pp. 7 - 16. Also in Journal of Composite Materials, Vol. 18, 1984, pp. 239 - 254.

[13] Wang, A. S. D., Slomiana, M. and Bucinell, R. B., "A Three Dimensional Finite Element Analysis of Delamination Growth in Composite Laminates Part I. The Energy Method and Case Study Problems," NADC-84017-60, Naval Air Development Center, Warminster, PA, 1983.

[14] Bucci, R. J., Paris, P. C., Landes, J. D. and Rice, J. R., "J-Integral Estimation Procedures," in Fracture Toughness, Part II, ASTM STP 514, 1972, pp. 40 - 69.

[15] Irwin, G. R., "Fracture Dynamics," in Fracturing of Metals, American Society of Metals, Cleveland, OH, 1948, pp. 147 - 186.

[16] Bradley, W. L. and Cohen, R. N., "Matrix Deformation and Fracture in Graphite Reinforced Epoxies," paper presented to ASTM Symposium on Delamination and Debonding of Materials, Pittsburg, PA, November 1983.

[17] Cullen, J. S., "Mode-I Delamination of Unidirectional Graphite Epoxy Composite Under Complex Load Histories," M.S. Thesis, Texas A & M Univeristy, College Station, Texas, 1981.

[18] Williams, D., "Mode-I Transverse Cracking in an Epoxy and a Graphite Fiber Reinforced Epoxy," M.S. Thesis, Texas A & M University, College Station, Texas, 1981.

[19] Griffith, A. A., "The Phenomena of Rupture and Flow in Solids," Phil. Trans. Royal Society, Vol. 221, 1920, pp. 163 - 198.

[20] Cherepanov, G. P., "Mechanics of Brittle Fracture," (English Translation), McGraw-Hill, New York, 1979.

[21] Sih, G. C. and Erdogan, F., "Stress Intensity Factor: Concept and Application," in Linear Fracture Mechanics, Envo Pub. Co., Lehigh Valley, PA, 1975, pp. 85 - 106.

[22] Irwin, G. R., "Fracture," in Handbuch der Physik, Vol. 5, Springer-Verlag, Berlin, 1958, p. 551.

[23] Williams, M. L., "On the Stress Distribution at the Base of a Stationary Crack," Journal of Applied Mechanics, Vol. 24, 1957, pp. 109 - 114.

[24] Wang, S. S. and Choi, I., "The Interface Crack Behavior of Dissimilar Anisotropic Composites Under Mixed-Mode Loading," Journal of Applied Mechanics, ASME, Vol. 50, 1983, pp. 178 - 183.

[25] Knowles, J. K. and Sternberg, E., "On the Singularity Induced by Certain Mixed Boundary Conditions in Linearized and Non-Linear Elastostatics," International Journal of Solids and Structures, Vol. 11, 1975, pp. 1173 - 1201.

[26] Delale, F., Wang, A. S. D. and Binienda, W., "On the Strain Energy Release Rate for a Crack at the Interface of Two Bonded Materials," in Advances in Aerospace Sciences and Engineering, ASME, AD-08, December 1984, pp. 113 - 120.

[27] Rybicki, E. F. and Kanninen, M. F., "A Finite Element Calculation of Stress Intensity Factors by a Modified Crack Closure Integral," Engineering Fracture Mechanics, Vol. 9, 1977, pp. 931 - 938.

[28] Wang, A. S. D., Kishore, N. N. and Li, C. A., "A Three Dimensional Finite Element Analysis of Delamination Growth in Composite Laminates. Part II. The Computer Code, KSAP, User's Manual," NADC-84010-60. Naval Air Development Center, Warminster, PA, 1983.

[29] Bjeletich, J. G., Crossman, F. W. and Warren, W. J., "The Influence of Stacking Sequence on Failure Modes in Quasi-Isotropic Graphite-Epoxy Laminates," in Failure Modes in Composites-IV, AIME, Chicago, 1979.

[30] Pipes, R. B. and Pagano, N. J., "Interlaminar Stresses in Composite Laminates Under Uniform Axial Extension," Journal of Composite Materials, Vol. 4, 1970, pp. 538 - 548.

[31] Wang, A. S. D. and Crossman, F. W., "Some New Results on Free Edge Effects in Symmetric Composite Laminates," Journal of Composite Materials, Vol. 11, 1977, pp. 92 - 106.

[32] Wang, A. S. D. and Crossman, F. W., "Fracture Mechanics of Sublaminate Crack," AFOSR-TR-83-0594, Air Force Office of Scientific Research, Washington, DC, 1983.

[33] Chou, S. D., Brockelman, R., Broz, A., Hinton, Y. and Shuford, R., "Analytical and NDE Techniques for Determining Crack Initiation in Graphite-Epoxy Laminates," ASTM, Symp. Effect of Defects in Composite Materials, San Francisco, 1982.

[34] Juvinall, R. C., "Stress, Strain and Strength," McGraw-Hill, New York, 1967, p. 67.

[35] Daniels, H. E., "Statistical Theory of the Strength of Bundles of Threads-I," Proc. Royal Society of London, Series A, Vol. 183, 1945.

[36] Chou, P. C. and Croman, R., "Certification of Composite Aircraft Structures Under Impact, Fatigue and Environmental Conditions. II. Scale Effect in Fatigue of Composite Materials," NADC-78259-60, Naval Air Development Center, Warminster, PA, 1978.

[37] Wang, A. S. D., "Growth Mechanisms of Transverse Cracks and Ply Delamination in Composite Laminates," Proceedings of ICCM-III, Vol. 1, Paris, 1980, p. 170 - 183.

[38] Crossman, F. W., Warren, W. J. and Wang, A. S. D., "Influence of Ply Thickness on Damage Accumulation and Final Failure," in Adv. Aerospace Structures, Materials and Dynamics, ASME AD-06, 1983, pp. 215 - 226.

[39] Pagano, N. J. and Pipes, R. B., "The Influence of Stacking Sequence on Laminate Strength," Journal of Composite Materials, Vol. 5, 1971, pp. 50 - 57.

[40] Rodini, B. T. and Eisenmann, J. R., "An Analytical and Experimental Investigations of Edge Delamination in Composite Laminates," in Fibrous Composites in Structural Design, Ed. E. M. Lenoe, et. al, Pleum Press, New York, 1978, pp. 441 - 457.

[41] Crossman, F. W. and Wang, A. S. D.," The Dependence of Transverse Cracking and Delamination on Ply Thickness in Graphite-Epoxy Laminates," in Damage in Composite Materials, ASTM STP 775, 1982, pp. 118 - 139.

[42] Wang, A. S. D. and Slomiana, M., "Fracture Mechanics of Delamination-Initiation and Growth," NADC-79056-60, Naval Air Development Center, Warminster, PA, 1982.

[43] Vanderkley, P. S., "Mode-I and Mode-II Delamination Fracture Toughness of a Unidirectional Graphite-Epoxy Composite," M.S. Thesis, Texas A & M University, College Station, Texas, 1981.

[44] Wilkins, D. J., Eisenmann, J. R., Camin, R. A. Margolis, W. S. and Benson, R. A., "Characterizing Delamination Growth in Graphite-Epoxy," in Damage in Composite Materials, ASTM STP 775, 1982, pp. 168 - 183.

[45] Wang, A. S. D., Kishore, N. N. and Feng, W. W., "On Mixed-Mode Fracture in Off-Axis Unidirectional Graphite-Epoxy Composites," Proceedings of ICCM-IV, Vol. 1, Japan Society for Composite Materials, Tokyo, Japan, 1982, pp. 599 - 606.

[46] Russell, A. J. and Street, K. N., "Moisture and Temperature Effects on the Mixed-Mode Delamination Fracture of Unidirectional Graphite-Epoxy," in Delamination and Debonding of Materials, ASTM STP 876, 1985, pp.

[47] Reifsnider, K. L., Stinchcomb, W. W., Henneke, E. G. and Duke, J. C., "Fatigue Damage-Strength Relationship in Composite Laminates," AFWAL-TR-83-3804, Air Force Wright Aeronautical Laboratories, Ohio, 1983.

[48] Jamison, R. D. and Reifsnider, K. L., Advanced Fatigue Damage Development in Graphite-Epoxy Laminates," AFWAL-TR-82-3103, Air Force Wright Aeronautical Laboratories, Ohio, 1982.

DISTRIBUTION LIST (Cont'd.)
REPORT NO. NADC-85118-60

AIRTASK NO. WRO 2303001

	No. of Copies
UNIVERSITY OF OKLAHOMA, Norman, OK 73019	
(Attn: Dr. C. W. Bert, School of AMNE)	1
UNIVERSITY OF WYOMING, Laramie, WY 82017	
(Attn: Dr. D. Adams)	1
VILLANOVA UNIVERSITY, Villanova, PA 19085	
(Attn: Dr. P. V. McLaughlin)	1
VIRGINIA POLYTECHNIC INSTITUTE, Blacksburg, VA 24061	
(Attn: Dr. K. Reifsnider)	1
WASHINGTON UNIVERSITY, School of Engineering and Applied Science, Materials Research Laboratory, Campus Box 1087, St. Louis, MO 63130	
(Attn: T. Hahn)	1

DISTRIBUTION LIST (Cont'd.)
REPORT NO. NADC-85118-60

AIRTASK NO. WRO 2303001

	No. of Copies
DREXEL UNIVERSITY, Philadelphia, PA 19104	
(Attn: Dr. P. C. Chou)	1
(Attn: Dr. A. S. D. Wang)	1
E. I. DuPONT COMPANY, Textile Fibers Department, Chestnut Run Location/CR701), Wilmington, DE 19898	
(Attn: V. L. Bertarelli)	1
FAIRCHILD REPUBLIC CO., Farmingdale, L.I., NY 11735	
(Attn: Mr. Frank Cost)	1
GEORGIA INSTITUTE OF TECHNOLOGY, Atlanta, GA 30332	
(Attn: Prof. W. H. Horton)	1
GENERAL DYNAMICS/CONVAIR, San Diego, CA 92138	
(Attn: D. R. Dunbar)	1
GENERAL DYNAMICS, Fort Worth Division, P.O. Box 748, Fort Worth, TX 76101	
(Attn: J. A. Fant)	1
(Attn: Dr. D. Wilkins, Composite Structures Eng. Dept.)	1
GENERAL ELECTRIC CO., Philadelphia, PA 19101	
(Attn: A. Garber)	1
GREAT LAKES CARBON CORPORATION, New York, NY 10017	
(Attn: W. R. Benn, Manager, Market Development)	1
GRUMMAN AEROSPACE CORPORATION, South Oyster Bay Rd., Bethpage, L.I., NY 11714	
(Attn: R. Hadcock)	1
(Attn: S. Dastin)	1
HERCULES AEROSPACE DIVISION, P.O. Box 210, Cumberland, MD 21502	
(Attn: Mr. D. Hug)	1
HITCO, 1600 West 135th Street, Gardena, CA 90249	
(Attn: N. Myers)	1
ITT RESEARCH INSTITUTE, Chicago, IL 60616	
(Attn: K. Hofar)	1
KAMAN AIRCRAFT CORP., Bloomfield, CT 06002	
(Attn: Technical Library)	1
LEHIGH UNIVERSITY, Bethlehem, PA 18015	
(Attn: Dr. G. C. Sih)	1
LOCKHEED-CALIFORNIA CO., Burbank, CA 91520	
(Attn: E. K. Walter)	1
(Attn: A. Vaughn)	1
(Attn: A. James)	1
LOCKHEED-MISSILES & SPACE CO., 1111 Lockheed Way, Sunnyvale, CA 94086	
(Attn: J. A. Bailie)	1
LOCKHEED-CALIFORNIA CO., Rye Canyon Research Laboratory, Burbank, CA 91520	
(Attn: D. E. Pettit)	1
LOCKHEED-GEORGIA CO., Marietta, GA 30063	
(Attn: Technical Information Dept., 72-34, Zone 26)	1

DISTRIBUTION LIST (Cont'd.)
REPORT NO. NADC-85118-60

AIRTASK NO. WRO 2303001

	No. of Copies
LTV AEROSPACE & DEFENSE CO., Vought Missile & Advanced Program Division, P.O. Box 225907, Dallas, TX 75265-0003	
(Attn: R. Knight)	1
MARCHINSKI, L., 6 East Avenue, Mt. Carmel, PA 17851	1
MATERIALS SCIENCES CORP., Spring House, PA 19477	
(Attn: Dr. B. W. Rosen)	1
McDONNELL DOUGLAS CORP., St. Louis, MO 63166	
(Attn: J. Doerr)	1
(Attn: K. Stenberg)	1
(Attn: R. Garrett)	1
(Attn: R. Riley)	1
McDONNELL DOUGLAS CORP., Long Beach, CA 90846	
(Attn: J. Palmer)	1
MINNESOTA MINING & MANUFACTURING CO., St. Paul, MN 55104	
(Attn: W. Davis)	1
NORTHROP AIRCRAFT CORP., One Northrop Ave., Hawthorne, CA 90250	
(Attn: Dr. M. Ratwani)	1
(Attn: B. Butler)	1
PURDUE UNIVERSITY, School of Aeronautics & Astronautics, West Lafayette, IN 47907	
(Attn: Dr. C. T. Sun)	1
PROTOTYPE DEVELOPMENT ASSOCIATES, INC., 1560 Brookhollow Drive, Santa Ana, CA 92705	
(Attn: E. L. Stanton)	1
ROCKWELL INTERNATIONAL, Columbus, OH 43216	
(Attn: M. Schweiger)	1
ROCKWELL INTERNATIONAL, Los Angeles, CA 90009	
(Attn: Dr. Lackman)	1
ROCKWELL INTERNATIONAL, Tulsa, OK 74151	
(Attn: F. Kaufman)	1
ROHR CORP., Riverside, CA 92503	
(Attn: Dr. F. Riel)	1
SIKORSKY AIRCRAFT, Stratford, CT 06622	
(Attn: J. Ray)	1
(Attn: S. Garbo)	1
J. P. STEVENS & CO., New York, NY 10036	
(Attn: H. I. Shulock)	1
TELEDYNE RYAN AERONAUTICAL CO., San Diego, CA 92138	
(Attn: R. Long)	1
UNIVERSITY OF DAYTON RESEARCH INSTITUTE, 300 College Park Ave., Dayton, OH 45469	
(Attn: Dr. J. Gallagher)	1
UNIVERSITY OF DELAWARE, Mechanics & Aerospace Eng. Dept., Evans Hall, Newark, DE 19711	
(Attn: Dr. R. B. Pipes)	1
(Attn: Dr. J. R. Vinson)	1

DISTRIBUTION LIST (Cont'd.)
REPORT NO. NADC-85118-60

AIRTASK NO. WRO 2303001

	No. of Copies
OFFICE OF NAVAL TECHNOLOGY, 800 N. Quincy St., Arlington, VA 22217	
(Attn: Cdr. R. Fuller, MAT 0711)	1
PLASTEC, Picatinny Arsenal, Dover, NJ 07801	
(Attn: H. Pebly)	1
(Attn: Librarian, Code DRDAR-SCM-O, Bldg. 351-N)	1
U.S. ARMY MATERIALS AND MECHANICS RESEARCH CENTER, DRXMR-PL, Watertown, MA 02171	
(Attn: D. Oplinger)	1
U.S. ARMY APPLIED TECHNOLOGY LABORATORY, USARTL, (AVRADCOM), Ft. Eustis, VA 23604	
(Attn: J. Waller; T. Mazza)	2
U.S. ARMY R&T LABORATORY, (AVRADCOM), Ames Research Center, Moffet Field, CA 94035	
(Attn: F. Immen, DAVDL-AS-MS 207-5)	1
U.S. NAVAL ACADEMY, Annapolis, MD 21402	
(Attn: Dr. R. D. Jamison, Mechanical Engineering Department)	1
DAVID TAYLOR NAVAL SHIP RESEARCH & DEVELOPMENT CENTER, Annapolis, MD 21402	
(Attn: A. Macander; R. Crane, Code 2822)	2
ANAMET LABORATORIES, 100 Industrial Hwy., San Carlos, CA 94070	
(Attn: Dr. R. Arnold)	1
AVCO, Specialty Materials Div., 2 Industrial Ave., Lowell, MA 01851	
(Attn: William F. Grant)	1
BATTELLE COLUMBUS LABORATORIES, Metals and Ceramics Information Center, 505 King Avenue, Columbus, OH 43201	1
BELL AEROSPACE COMPANY, Buffalo, NY 14240	
(Attn: F. M. Anthony, Zone I-85)	1
BELL HELICOPTER CO., Ft. Worth, TX 76101	
(Attn: G. Reis Alsmiller, Jr.)	1
BEECH AIRCRAFT CORP., 4130 Linden Ave., Dayton, OH 45432	
(Attn: M. B. Goetz)	1
BENDIX PRODUCTS, Aerospace Division, South Bend, IN 46619	
(Attn: R. V. Cervelli)	1
BOEING CO., P.O. Box 3707, Seattle, WA 98124	
(Attn: J. McCarty)	1
(Attn: Dr. R. June)	1
BOEING CO., Vertol Division, P.O. Box 16858, Philadelphia, PA 19143	
(Attn: R. L. Pinckney)	1
(Attn: D. Hart)	1
(Attn: C. Albrecht)	1
BOEING CO., Wichita, KA 67277-7730	
(Attn: J. Avery)	1
(Attn: R. Waner)	1
CABOT CORPORATION, Billerica Research Center, Billerica, MA 01821	1
DEPARTMENT OF TRANSPORTATION, Kendall Square, Cambridge, MA 02142	
(Attn: Dr. Ping Tong, DTS 76, TSC)	1

DISTRIBUTION LIST
REPORT NO. NADC-85118-60

AIRTASK NO. WRO 2303001

	No. of Copies
AFWAL, Wright-Patterson AFB, OH 45433	
(Attn: FIBEC, Dr. G. Sendeckyj)	1
(Attn: FIB/L. Kelly, W. Goesch, C. Ramsey)	3
(Attn: FIBCA/C. D. Wallace)	1
(Attn: FIBE/Mr. D. Smith)	1
(Attn: MLBM/Dr. J. Whitney, M. Knight)	2
(Attn: MLB/F. Cherry)	1
(Attn: MBC/Reinhart)	1
(Attn: AFWAL/MLSE/S. Fecheck)	1
DEPARTMENT OF THE AIR FORCE, Bldg. 410, Bolling Air Force Base, Washington, DC 20332	
(Attn: Dr. M. Salkind)	1
DEFENSE TECHNICAL INFORMATION CENTER (DTIC), Bldg. #5, Cameron Station, Alexandria, VA 22314	
(Attn: Administrator)	2
FAA, Washington, DC 20591	
(Attn: J. R. Soderquist)	1
FAA, Technical Center, Atlantic City, NJ 08405	
(Attn: L. Neri, Code ACT-330; M. Caiafa, Code ACT-330)	2
NASA, Washington, DC 20546	1
NASA, George C. Marshall Space Flight Center, Huntsville, AL 35812	
(Attn: E. E. Engler, S&E-ASTN-ES)	1
(Attn: R. Schwinghammer, S&E-ASTN-M)	1
NASA, Langley Research Center, Hampton, VA 23365	
(Attn: Dr. J. R. Davidson, MS 188E; Dr. J. Starnes, MS 190; Dr. M. Mikulus, H. Bohan, and Dr. C. P. Blakenship, MS 188M)	5
NASA, Lewis Research Center, Cleveland, OH 44135	
(Attn: Dr. C. Chamis, MS 49-6; M. Hershberg, MS 49-6)	2
NAVAIRSYSCOM, Washington, DC 20361	
(Attn: AIR-723)	1
NAVAL POSTGRADUATE SCHOOL, Monterey, CA 95940	
(Attn: Prof. R. Ball, Prof. M. H. Bank)	2
NAVSEASYSCOM, Crystal Mall 4, Rm. 109, Washington, DC 20360	
(Attn: C. Zannis)	1
NAVSEC, Arlington, VA 20360	
(Attn: NSEC-6101E)	1
NAVAL SHIP RESEARCH & DEVELOPMENT CENTER, Annapolis, MD 21402	
(Attn: H. Edelstein, Code 2870)	1
NAVAL RESEARCH LAB, Room 866, Crystal Plaza #5, Washington, DC 20360	
(Attn: Dr. I. Wolock; Dr. C. I. Chang)	2
NAVAL SHIP WEAPONS CENTER, White Oak Laboratory, Silver Spring, MD 20910	
(Attn: Dr. J. Goff, Materials Evaluation Branch, Code R-34)	1
(Attn: F. R. Barnet)	1
OFFICE OF NAVAL RESEARCH, 800 N. Quincy St., Arlington, VA 22217	
(Attn: A. Kushner; Y. Rajapakse)	2

END

DTIC

9-86